Spin-Injection into GaAs using ferromagnetic (Ga,Mn)As contacts

Dissertation
zur Erlangung des Doktorgrades der Naturwissenschaften
(Dr. rer. nat.)
der Fakultät für Physik
der Universität Regensburg

vorgelegt von
Andreas Einwanger
aus
Eggenfelden
Mai 2012

Promotionsgesuch eingereicht am: 09.05.2012
Die Arbeit wurde angeleitet von: Prof. Dr. Dieter Weiss
Datum des Promotionskolloquiums: 16.07.2012

Prüfungsausschuss:
Vorsitzender: Prof. Dr. Ingo Morgenstern
Erstgutachter: Prof. Dr. Dieter Weiss
Zweitgutachter: Prof. Dr. Jaroslav Fabian
Weiterer Prüfer: Prof. Dr. Dominique Bougeard

Contents

Keywords

2DEG	**2**-**D**imensional **E**lectron **G**as
2DES	**2**-**D**imensional **E**lectron **S**ystem
AC	**A**lternating **C**urrent
ALD	**A**tomic **L**ayer **D**eposition
AMR	**A**nisotropic **M**agneto**R**esistance
As_{Ga}	Antisites, **As** atoms on **Ga** lattice sites in GaMnAs
BAP	**B**ir-**A**ronov-**P**ikus spin relaxation mechanism
CAIBE	**C**hemical **A**ssisted **I**on **B**eam **E**tching
CIP	**C**urrent **I**n **P**lane configuration
CMR	**C**olossal **M**agneto**R**esistance
CPP	**C**urrent **P**erpendicular to **P**lane configuration
CVD	**C**hemical **V**apor **D**eposition
CZ	Monocrystalline silicon made by the **CZ**ochralski method
DC	**D**irect **C**urrent
DMM	**D**igital **M**ulti**M**eter
DMS	**D**iluted **M**agnetic **S**emiconductor
DNP	**D**ynamic **N**uclear **P**olarization
DP	**D**yakonov-**P**erel spin relaxation mechanism
EBL	**E**lectron **B**eam **L**ithography
E_C	lowest **E**nergy level of **C**onduction band
EMF	**E**lectro **M**otive **F**orce
E_V	highest **E**nergy level of **V**alence band

eV	**E**lectron **V**olt
ETX	2-(2-3-**E**poxypropyloxy) **T**hio**X**anthone
EY	**E**lliot-**Y**afet spin relaxation mechanism
FET	**F**ield **E**ffect **T**ransistor
FOV	**F**ield **O**f **V**iew
FWHM	**F**ull **W**idth at **H**alf **M**aximum
FZ	Monocrystalline silicon made by **F**loat-**Z**one method
GMR	**G**iant **M**agneto**R**esistance
HT	**H**igh **T**emperature
IBE	**I**on **B**eam **E**tching
JMR	**J**unction **M**agneto**R**esistance
LT	**L**ow **T**emperature
LT-MBE	**L**ow **T**emperature **M**olecular **B**eam **E**pitaxy
MBE	**M**olecular **B**eam **E**pitaxy
MIBK	**M**ethyl **I**so**B**utyl **K**etone
Mn-As	Clusters of **Mn** and **As** atoms in GaMnAs crystals
Mn_{Ga}	Substitutional **Mn** on **Ga** lattice site in GaMnAs
Mn_{I}	**I**nterstitial **Mn** off of regular lattice sites in GaMnAs
Mn-Mn	Clusters of **Mn** atoms in GaMnAs crystals
NMR	**N**egative **M**agneto**R**esistance
NVM	**N**ano **V**olt **M**eter
PMMA	**P**oly **M**ethyl **M**ethacryl**A**te
PECVD	**P**lasma **E**nhanced **C**hemical **V**apor **D**eposition
PHE	**P**lanar **H**all **E**ffect
PVD	**P**hysical **V**apor **D**eposition

RHEED	**R**eflected **H**igh **E**nergy **E**lectron **D**iffraction
RIE	**R**eactive **I**on **E**tching
rms	**r**oot **m**ean **s**quare
SFET	**S**pin **F**ield **E**ffect **T**ransistor
SIA	**St**ructure **I**nversion **A**symmetry
SLED	**S**pin **LED**, **S**pin **L**ight **E**mitting **D**iode
SOI	**S**pin **O**rbit **I**nteraction
Spintronic	**Spin** Elec**tronic**
SV	**S**pin-**V**alve
TAMR	**T**unneling **A**nisotropic **M**agneto**R**esistance
TASP	**T**unneling **A**nisotropic **S**pin **P**olarization
TMR	**T**unneling **M**agneto**R**esistance
UHV	**U**ltra **H**igh **V**acuum
V_{Ga}	**V**acancies, not occupied **Ga** sites in GaMnAs crystals
VGF	Monocrystalline silicon made by **V**ertical **G**radient **F**reeze method
VL	**V**acuum **L**evel
VTI	**V**ariable **T**emperature **I**nset

1 Introduction

The invention of the vacuum tube diode 1904 by J. A. Fleming[Flem] and shortly thereafter of the triode (an electronic tube with additional control grid) by L. de Forest[Fore] led to the up growth of electronics, developing out of simple electrical engineering. These new concepts started to give us the ability of controlling electrical device current by an auxiliary gate voltage. This principle was kept in all subsequent enhancements from triodes over the first realized Ge-transistor in the famous Bell-Labs in 1947[Bard] to the integrated silicon circuits nowadays used.

Although surely no one wants to admit it, our everyday life and prosperity are governed by integrated circuits, because they are in toasters, washing machines, car entertainment, smartphones, tablet computers and of course the internet. In these transistors digital information is stored as charge; say "1" implies an existing charge and "0" is denoted by no available charge. Due to the scalar nature of charge – it has only a quantity no direction by itself – the change of logic levels is always connected to a current flow. Associated therewith is inevitably a dissipation of heat[Band]. This thermal output is the biggest menace to Moore's Law, which predicts a doubled transistor density every 18 months[Moor]. Moore's empirical forecast has driven the electronics industry forward for the past decades.

Thankfully, the electron exhibits another elementary feature besides charge, namely its spin, see fig. 1.1. As spin is a vector quantity, its size is defined but its direction can be changed, thus it can be used to encode the digital bits if it's made a bistable system by installing a static magnetic field for example. Due to that the modification of bit information means flipping the spin direction and that needs no physical charge current, which provides us with a potential energy saving of considerable size[Band]. If spintronics can realize this potential of significantly reduced heat dissipation, it has the possibility to sustain Moore's Law and be vividly supported by the well-heeled industry. Although spintronics is a quite new nomenclature, today's research is connected closely to many previous results obtained in various other physical fields like semiconductor physics, magnetism and optics, to name just a few. It is at the very heart of spintronics to investigate and understand the interaction mechanisms of electron spins with its solid state environment and to make useful devices by application of the so gained knowledge[Zuti]. Thereby some fundamental questions have to be answered:

i. How can a spin system be effectively polarized?
ii. What are the timescales the system can remember the spin information?
iii. Is it possible to control the spin information within the system reliably?
iv. Can the existing spin polarization be easily detected?

The generation of a nonequilibrium spin population is the typical case for problem i., the polarization of a spin system. While it is relatively easy to orient spins by optical means, for practical devices an electrical approach would be highly appreciable. This leads us, quasi naturally, to the concept of electrical spin injection. Thereby a magnetic electrode is connected to a nonmagnetic material and an applied bias drives a spin polarized current into the nonmagnetic system to accumulate nonequilibrium spin therein. As intuitive this picture may be, as many practical problems arise at its realization. While a semiconductor based material system would be desirable for easy device integration into existing electronics, the connection of ferromagnetic metals with semiconducting layers leads to severe problems with the conductivity mismatch[Schm] of these substances, extremely limiting the injection efficiencies into the semiconductor. There is more than one possible solution to this problem, e.g. introducing low conductivity ferromagnets, this however renders traditional ferromagnets inapplicable.

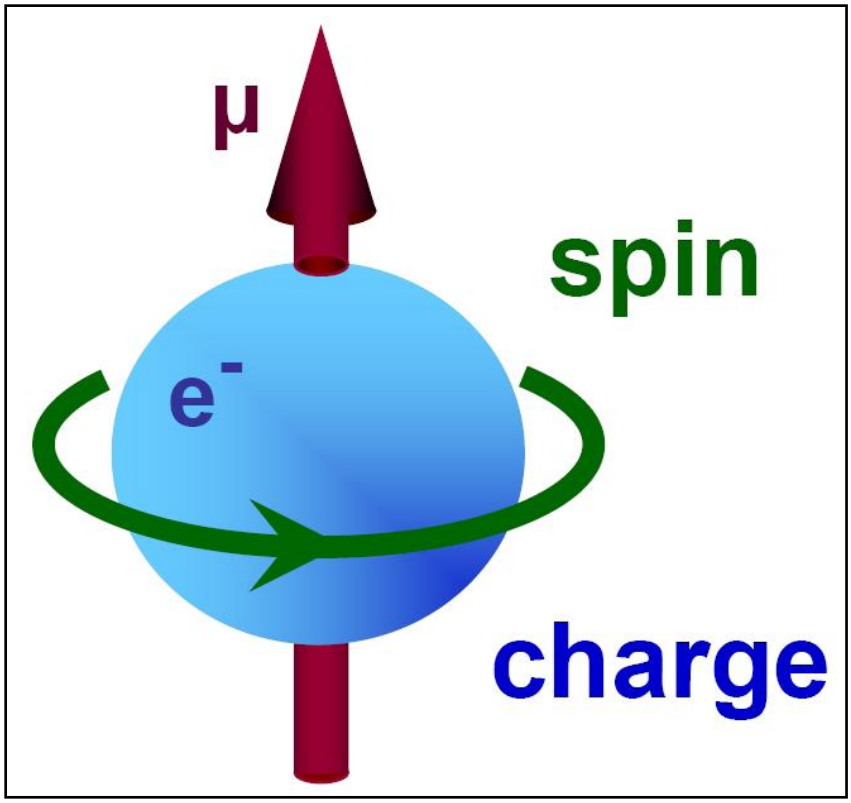

Fig. 1.1: Electrons do have not only scalar quantities like mass and electrical charge, but also possess their own magnetic moment, directly connected to the electron spin, which is a pseudo-vector[Tech].

Once a spin accumulation is generated in the nonmagnetic system, its magnitude depends on two major factors, the effectiveness of the injection process as well as the amount of spin relaxation. The main relaxation mechanisms typically involve spin orbit interaction (SOI) processes in one or the other way and momentum scattering to provide the possibility of equilibrating the spin polarization. Timescales of this point ii. thematic can vary

from picoseconds[Bayl],[Kime] to microseconds[Grae],[Sand] and above but it typically happens in the nanosecond[Ekim],[Guot],[Kik1] range. As long relaxation times are surely preferable, a GaAs-based system would be a good choice, as in these systems relaxation times of 100 ns and more are reliably accessible[Aws1],[Kikk]. These long relaxation times translate into relaxation lengths of several tenths of μm[Lou].

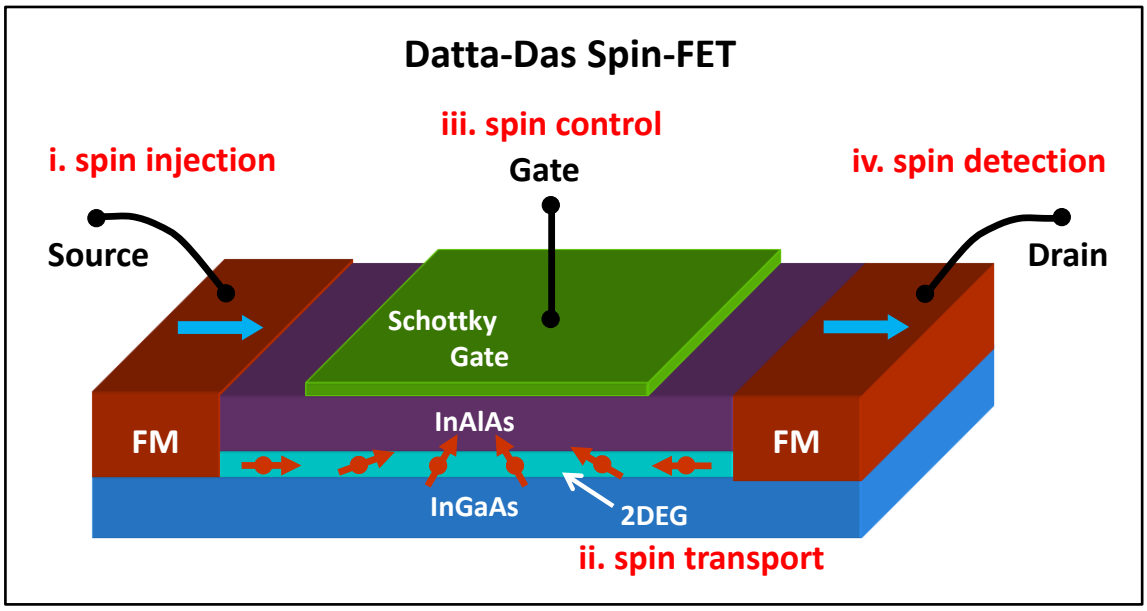

Fig. 1.2: The already famous Datta-Das SFET. Its components are pretty much the same as in a conventional field effect transistor. The information flow from source to drain is controlled by the applied voltage at the gate. The new thing is now the ferromagnetism of the source and drain contacts and the mode of operation of the gate. In this SFET manipulation of information via gating is based on the Rashba term in the Hamiltonian of the system. This allows the manipulation of the spin orientation[Datt].

For question iii., the spin direction within our system can be manipulated with the help of an applied magnetic field $B_{\perp}$, perpendicular to the spin orientation (which lies in the film plane). This field induces a coherent spin precession and can thereby be used to determine the spin orientation of the electrons when arriving at the spin detector. This magnetic field can be just applied externally, although from an application standpoint this is by far the worst realization. In a very sophisticated design this spin precession could be implemented with the help of a built-in structure inversion asymmetry (SIA) field, using a gate electrode to control the effective strength of it[Datt].

Finally point iv. of our list, the spin detection can again be realized in several ways. In recent years many groups employed the nonlocal detection scheme, where the measurement and current excitation paths are spatially separated[Sils],[John],[Lou]. Using this method, no charge current flows at the detection point and thus the measured signal is sensitive to the spin degree of freedom only. Therefore this method eliminates the presence of spurious effects as anisotropic magnetoresistance (AMR) or the Hall effect that could mask or even mimic subtle signals related to successful spin injection[Tang]. A weakness of

this method is the fact, that it is only sensitive to the local spin accumulation and the spin current cannot be measured directly. This ability is made available by the spin current induced Hall effect, the reciprocal of the spin Hall effect[Val1],[Kimu]. This detection scheme uses the conversion of spin current to charge imbalance, thus that an injected spin polarized current induces a lateral voltage between the edges of a nonmagnetic sample.

With their proposed scheme of a spin field effect transistor S. Datta and B. Das designed the prototype of a spintronics device[Datt] already in 1990. This Spin FET in principle combines all four points on our list into a single device, see fig. 1.2. It's based on spin injection and detection with the help of ferromagnetic source and drain contacts, allows the manipulation of spins simply with the help of gate bias, which controls the spin precession rate via changing the Rashba SOI. This Spin FET still lacks a physical realization, as the material choice is the crux of the matter to make this principle work reliably and at sufficiently high temperatures.

Our work presented in this thesis shows a viable route to a possible realization of a future Datta-Das spin transistor. The material system we use bases on the III-V semiconductor GaAs, which can serve us amongst other virtues with a highly developed device technology, long spin relaxation times, and easy tunability of carrier concentration and compound composition. To circumvent the problems of compatibility, low spin polarization and conductivity mismatch, we use a so-called diluted magnetic semiconductor (DMS), namely GaMnAs[1], for spin injection and detection by means of Esaki tunneling contacts. Additionally to the aforementioned benefits, this material's parameters like carrier density or magnitude of the band gap are modifiable in a wide range[Ohno],[Chib],[Chi1]. GaMnAs is to date certainly the best investigated DMS. Here magnetic Mn Ions are randomly distributed in an otherwise nonmagnetic GaAs host crystal. At high enough Mn concentration the material suddenly starts to get ferromagnetic. The biggest problems with this DMS are the still too low Curie temperatures[Wan1],[Wan2] that are despite big improvements still well below room temperature.

This work is structured as follows:

Subsequent to this introduction chapter 2 presents necessary basic knowledge needed for understanding the concepts and materials used. From the energy band diagram of GaAs over the most prominent magnetic classes and effects to the design and behavior of ferromagnetic GaMnAs an overview is given.

[1] We will typically stick to the simpler notation GaMnAs instead of the technically correct $(Ga_{1-x},Mn_x)As$ as the exact concentration of Mn in the GaAs-matrix does indeed change the specific parameters of the material but most characteristics are at least similar if the concentration varies within a not too broad range, see section 2.5.

The following chapter 3 introduces the employed theoretical concepts. From the basic drift and diffusion equations to the standard model of spin injection and spin dynamics everything is touched to sufficient extent.

While chapter 4 showcases the materials used, from the wafer substrate to the specific preparation techniques and manufacturing processes, chapter 5 describes the applied measurement setups and tools we used to gain our results.

In chapter 6 we present our experimental findings and discuss their consequences for further investigations and deeper material insight. For the sake of clarity, some very detailed measurement results are sourced out to the appendix.

Finally chapter 7 summarizes the most important points of the work and gives an outlook on optimized material systems or investigation directions that seem to be reasonable with the gained information.

The added appendices give the interested reader finally more detailed information to the sample preparation and handpicked measurement results.

2 Basics

This chapter gives an overview of the fundamental background needed to get the ideas of this work. Surely, many books dealing with the topics of this chapter in detail can give a much more comprehensive insight. Where applicable, we refer the interested reader to more specific work, done by the according specialists.

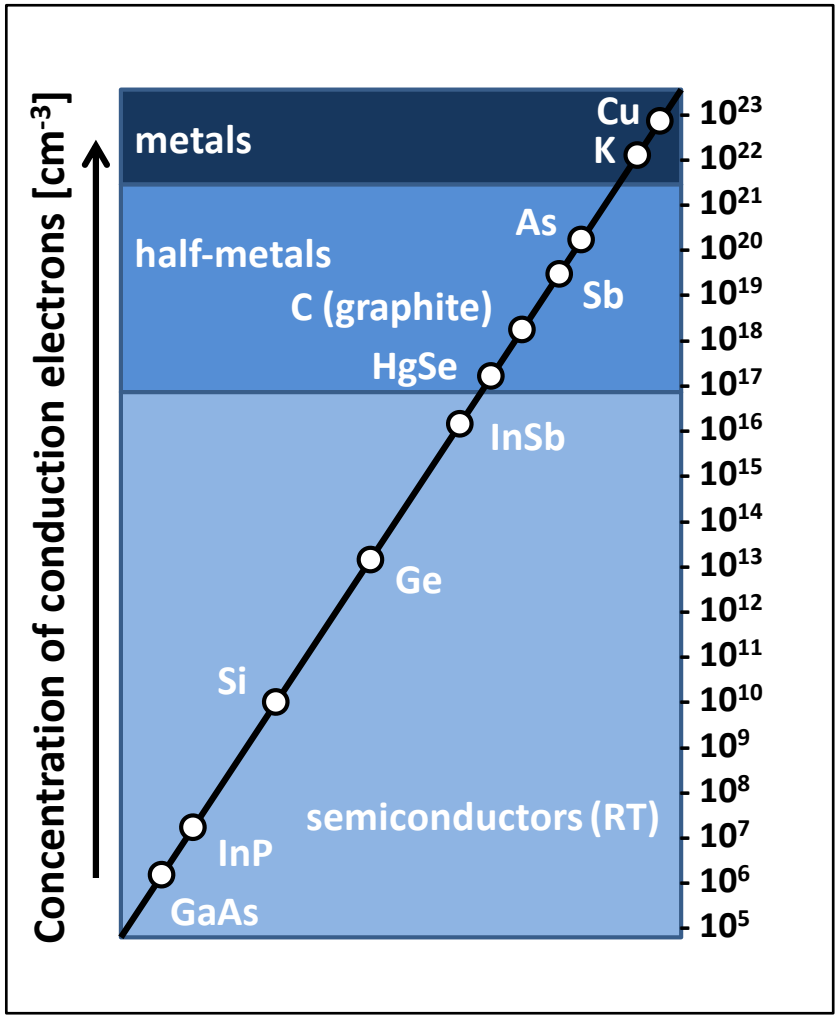

Fig. 2.1: Different materials have different conduction electron concentrations. The higher the concentration, the better the conductivity. The highest concentrations are found in metals, which are then the best conductors, of course. Half-metals are still good conductors, but an increased resistivity is clearly noticeable. The region of semiconducting material is by far the broadest. From InSb down to GaP with its 2 conduction electrons per cm³ it spans over roughly 17 orders of magnitude. (Graph after [Kitt] with additional data from [Ashc] and [Made].)

We are interested in solid phase materials, although exotic proposals of spintronics basing on DNA molecules[Zwol] are very inspiring. Generally there are three types of solid state materials, which are used in electronic circuits.

These are the insulators, semiconductors and conductors. These different types can be readily mixed in electronic devices. However the special device performance is typically determined by layers consisting of semiconducting material. According to that, integrated circuits are normally called semiconducting devices. They possess the most auspicious electronic structure of the three solid state material classes and are therefore the most important and interesting ones for electronics.

2.1 Energy Band Model of Solid State Materials

In a solid state material there are many electrons, ions and neutral atoms present. Typically the number density is around 10^{22} in a volume of one cm^3. Of course these extraordinarily big numbers cannot be described by simple one particle Newton models. Additionally one has to keep in mind that experimental techniques (e.g. resistance measurements) only measure the average values of many particles and not the individual quantum effects of a single one. In electronic applications the most important parameter is the electronic conductivity or resistivity of the solid, of course.

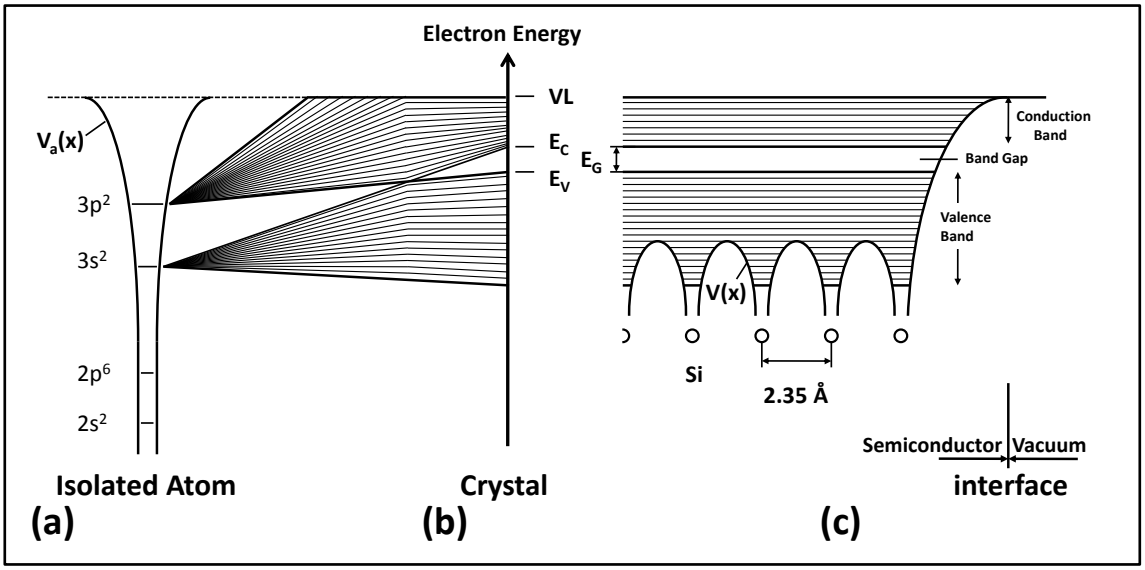

Fig. 2.2: $V_a(x)$ is the atomic potential energy with the electronic energy levels for different states (a). The transition from many isolated atoms to many very densely packed atoms in a crystal leads to broadened energy bands and forbidden zones due to the Pauli Exclusion principle (b). (c) shows the crystalline potential energy $V(x)$ and the energy bands for an electron in a Si crystal[Sah].

The starting point of the energy band model of solid state materials is the potential energy diagram of electrons in isolated and neutral host atoms. The atomic one-electron energy levels and wavefunctions are used as a basis to build up the energy level diagram of a crystal with many atoms and much more electrons. In figure 2.2 one can see a short illustration how the energy levels in an isolated atom develop to the widespread energy bands in crystal structures. The values are given for Silicon, but the principle is also valid for other elemental and compound crystals (e.g. GaAs). In part (a) the energy levels of an

isolated Si atom are given. The energies correspond to the eight electrons in the 2s/2p states and the four valence electrons in the 3s/3p states.

Part (b) shows that the energy levels of the single atom are broadened into energy bands, if one brings more atoms closer together. This is a consequence of the fermionic character of electrons. By definition, fermions are particles that obey Fermi-Dirac statistics: if one swaps two fermions, the wavefunction of the two-fermion system changes sign. This "antisymmetric wavefunction" behavior implies that fermions are subject to the Pauli Exclusion Principle[Paul],[Pau1]. This in turn means that two fermions cannot occupy the same quantum state at the same time. At least one quantum number has to be different, for example their spin. So in a crystal the energy levels of the single atoms are shifted to little bit higher or lower values for each atom and its electrons that are added to the system. In a typical crystal consisting of at least 10^{22} atoms, these steps between the energy levels are so small that one can assume them to be quasi-continuous. These allowed states are called energy bands and they are separated from each other by a forbidden region, the so-called band gap E_G. In the band gap there are no energy levels allowed. Above this gap there is the conduction band, while below it there is the valence band. E_C is the lowest energy level of the conduction band and E_V is the highest energy level that exists in the valence band. In figure 2.2 one can see that the valence band as well as the conduction band of a silicon crystal both arise from the valence electron states in the isolated atom, the two 3s and the two 3p states. Additionally it becomes clear that deeper core energy levels like the $2s^2$ levels are not broadened into energy bands. In part (c) the curves *V(x)* show the potential energy variation seen by an electron due to the Coulomb electrostatic force from Si^{+4} cores and the other valence electrons in the system. One can also see the potential variation at the crystal/vacuum interface. The potential energy rises towards the vacuum level for an electron that wants to move away from the crystal into the free space of the vacuum around it.

As this was only a very qualitative view on the energy bands and their origin, now it is the right time to ask how the electrons fill the states they can occupy[Sah]. To clarify this question, let us look at figure 2.3. It is an expanded and much more precise view on the situation compared to what we show in figure 2.2. Here one can see how the available electrons are distributed onto the existing electronic states. Consider the crystal being composed of N Si atoms. Then there are $14N$ electrons in the system (as a neutral Si atom exhibits 14 electrons). If one now wants to know where the electrons exactly go one has to keep in mind the Pauli Exclusion Principle and look at the $T=0\,K$ case, which simply is the easiest situation we can think of. Because of Pauli two electrons that occupy the same energy level have opposite spin. This level then is full and cannot carry more electrons. Additionally, as we said we are at zero temperature, meaning that the energetically lowest states are preferred by the electrons and no thermally activated configuration exists. So at the beginning

the 1s-like states of the crystal are filled. Accounting for the spin degeneracy, the first 2*N* electrons go to the lowest 1s-like states. The same holds for the next 2*N* electrons that occupy the 2s-like states. As one can see in the sketch the 2p-like levels are filled next by 6*N* electrons. This means that by now already 10*N* of the available 14*N* electrons have found a home. Now we look at the left over 4*N* valence electrons. When the atoms are far away from each other half of them (meaning 2*N*) are in 3s states and the other half are sitting on 3p states. As we have 6*N* available states in the 3p orbitals of the isolated atoms these are the first levels not being completely filled. If now the atoms are brought close together to form a crystal, due to the adjacent atoms the electronic energy levels of isolated atoms are shifted. The larger the orbitals of the individual atoms are the bigger is the effect.

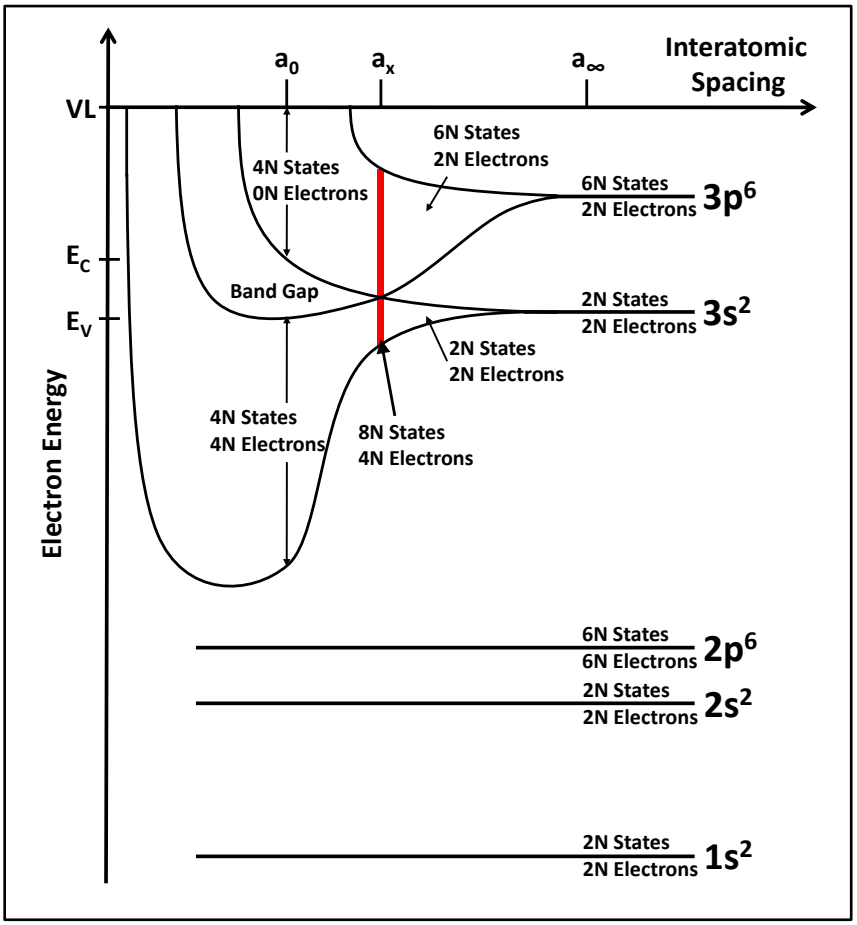

Fig. 2.3: Electron energy levels and their occupation dependent on the interatomic spacing of *N* Si atoms. a_∞ means isolated atoms, while a_x is a hypothetical distance where a Si crystal would be metallic and a_0 is the equilibrium distance between Si atoms in a real crystal[Sah].

In the case of Si these are clearly the 3s and 3p orbitals. The arising forces at the crystal creation perturb the 3p energy levels and remove the configuration degeneracy between $3p_x$, $3p_y$ and $3p_z$. Figure 2.3 shows that, as the assumed interatomic spacing *a* decreases (of course *a* is only a hypothetical variable, its continuous variation is only in mathematical and computer models possible), the shift of the 3s and 3p states increases and they broaden into energy bands of

allowed energies (as described before already). At some specific interatomic spacing a_x the bottom of the 3p-like band and the top of the 3s-like band cross each other. At this point there are two different possibilities for the bands to build linear combinations of the underlying 3s and 3p wavefunctions, which gives two possible distributions of allowed energy levels as a function of electron energy, see figure 2.4:

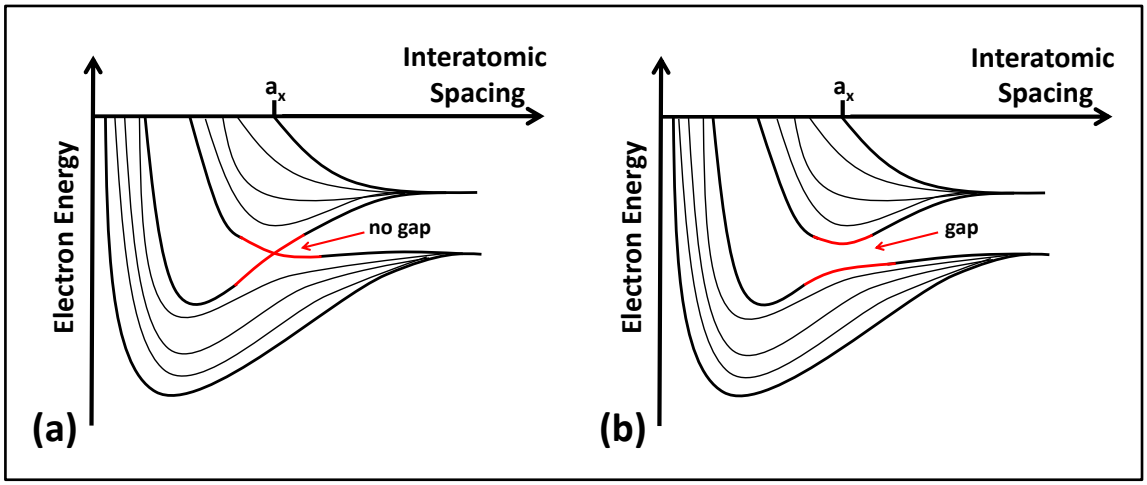

Fig. 2.4: The two possible different linear combinations of atomic orbitals to energy bands. In (a) we have the case of crossing bands, while in (b) the orbitals are combined that way that no crossing appears[Sah].

One distribution does not have an energy gap (attention: the energy gap at interatomic spacing a_x is not the one between conduction and valence band (E_G) at the equilibrium interatomic spacing a_0) as is shown in figure 2.3 and 2.4 (a) the other one has an energy gap in contrast (shown in part (b) of figure 2.4). In both cases one can no longer talk about 3s-like and 3p-like energy levels as from now on there exist only linear combinations of them. Accordingly wavefunctions have both 3s-like and 3p-like components. In the gapless case shown in figure 2.3, the combined band now has $4N$ levels (N from 3s and additional $3N$ from 3p) and correspondingly $8N$ states. As we have only $4N$ electrons left that can be distributed to free electron states, only the lower half of the band can be filled. At this virtual interatomic spacing a_x the Si crystal would be a perfect metal.

As a real Si crystal has the interatomic spacing a_0, which is smaller compared to a_x, one can see that there the band gap again appears (gets wider in the case of 2.4 (b)) and gets bigger the closer the atoms get. This means for the $8N$ possible states that they split equally between the upper and the lower band. Since the lower band of course has the lower energy, all available $4N$ electrons reside now in the so-called valence band, which is fully occupied now, while the conduction band is completely empty.

So what is now the difference between metals, semiconductors and isolators? Why is there such a big difference in their conductivity? The reason behind that is the filling level of the energy bands. If one carefully analyses the creation of

solid state materials out of single atoms, one can see that in metals always partly filled bands exist. This means, that an electron can always find an electronic state in its direct energetic neighborhood which is free. Accordingly it can easily move in the crystal as a quasi-free electron. In the semiconducting case however, the valence band is completely filled, meaning that electrons cannot find free places therein. Completely filled bands do carry no current[Saik]. The same holds for the conduction band, completely empty bands also carry no current, of course, there are no carriers that could do that. The same argument prevents insulators of being conductors, they also have a filled valence band and empty conduction band, only the energy gap between them is even larger as in semiconductors.

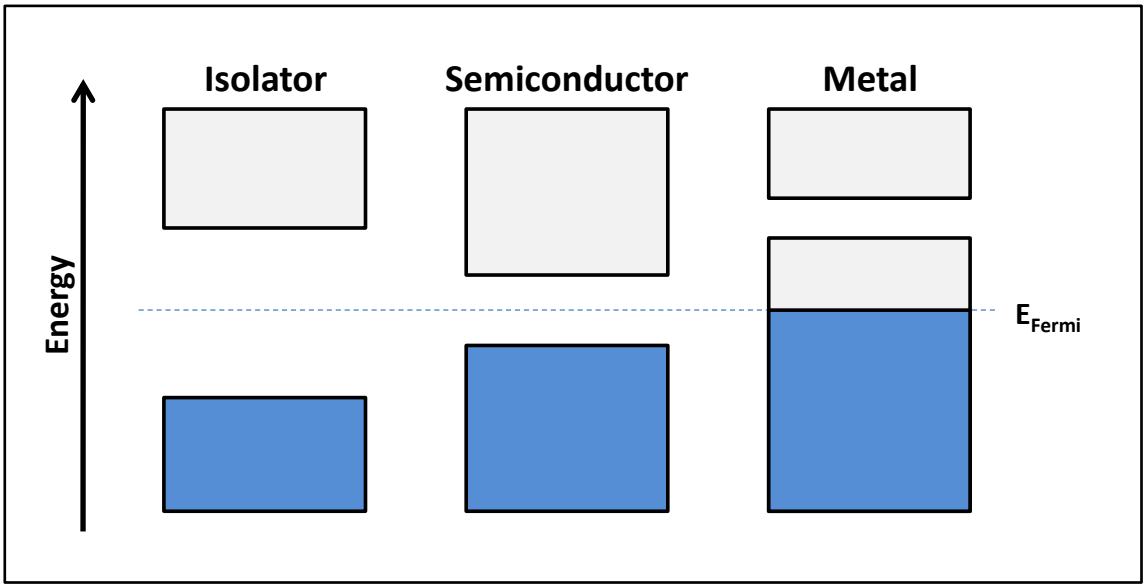

Fig. 2.5: A simplified picture of the energy bands in a solid that allows the three major types of materials to be identified: isolators have a fully filled valence band and an empty conduction band, separated by a big forbidden zone. Semiconductors do have the same band structure but possess a considerably smaller band gap, while metals exhibit a Fermi energy that lies amid of an energy band.

2.2 Semiconductors

The class of semiconducting materials can be divided into two main categories, the elemental semiconductors, e.g. silicon (Si) or germanium (Ge), and the compound semiconductors, e.g. gallium arsenide (GaAs), indium antimonide (InSb) or cadmium telluride (CdTe). As in the previous section said, the distinction between semiconductors and isolators generally is not sharp, but fluent. Only the width of the band gap can be used to distinguish between semiconductor and isolator. As one of the main mechanisms that excite electrons from the valence band across the band gap into the conduction band is the absorption of the energy of a photon, the photonic energy of visible light is generally considered as a rough distinction between semiconductors and insulators. This means band gaps from around 3 eV downwards identify

semiconducting material and everything above 3 eV belongs to the group of insulators.

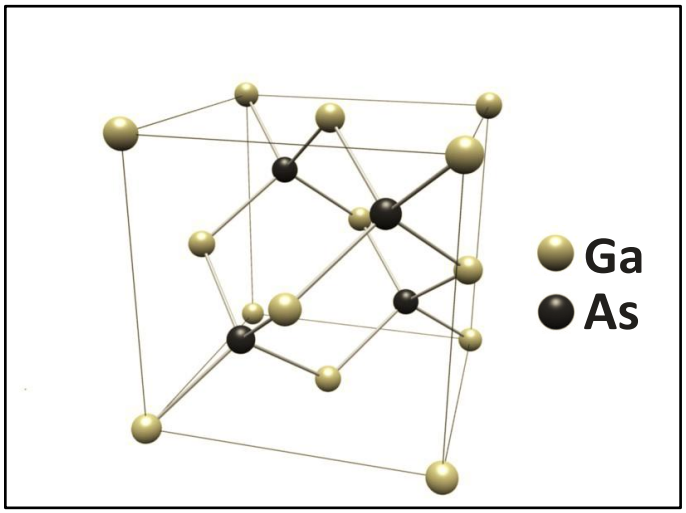

Fig. 2.6: Zinc-blende crystal structure of GaAs. Altogether, the arrangement of atoms is the same as in a diamond cubic structure, but with alternating types of atoms at the sites of the different sub lattices.

2.2.1 Intrinsic Semiconductors

Typical energy gaps at room temperature of the most prominent semiconductors are 1.12 eV, 0.66 eV and 1.42 eV for Si, Ge and GaAs respectively[Thus]. At absolute zero temperature there's no difference between semiconductors and isolators. The valence band is completely filled with electrons and the conduction band is completely empty. Hence, in the valence band there are no free states for the electrons to move and in the conduction band there's plenty of room, but there are no electrons, see figure 2.7. So at 0 K pure intrinsic semiconductors cannot conduct any electricity.

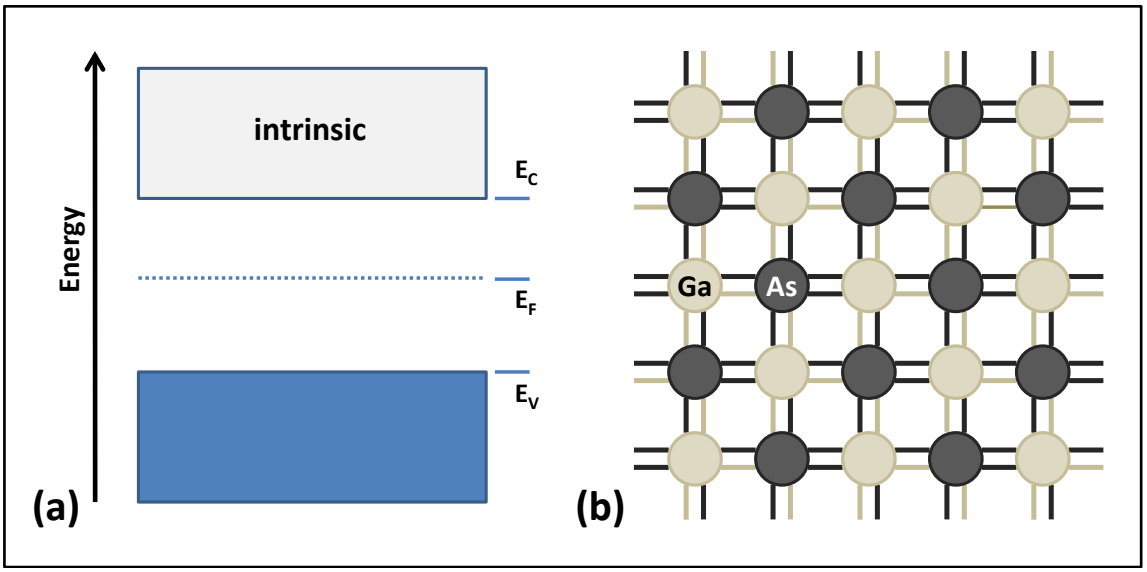

Fig. 2.7: Band structure of an intrinsic semiconductor at 0 K or very small finite temperature (a). The band gap is too big to allow electrons being thermally excited into the conduction band in noteworthy numbers. The GaAs lattice (b) shows that all three valence electrons from Ga atoms and the five from As are tied in the crystal bonds.

If the temperature now is significantly above 0 K, electrons can be lifted up in the conduction band by thermal excitation (the second mechanism of elevating carriers across the band gap). This means, that these electrons can now easily move in the conduction band and also the electrons in the valence band have some room, as each uplifted electron has left a hole in its former place in the valence band. These holes are normally described as if they were positively charged carriers, just for simplicity. The complete band structure is very complex, but fortunately the electronic attributes of semiconductors are mainly dictated by electrons in the conduction band minimum near E_C and holes in the valence band maximum in the vicinity of E_V, see figure 2.8.

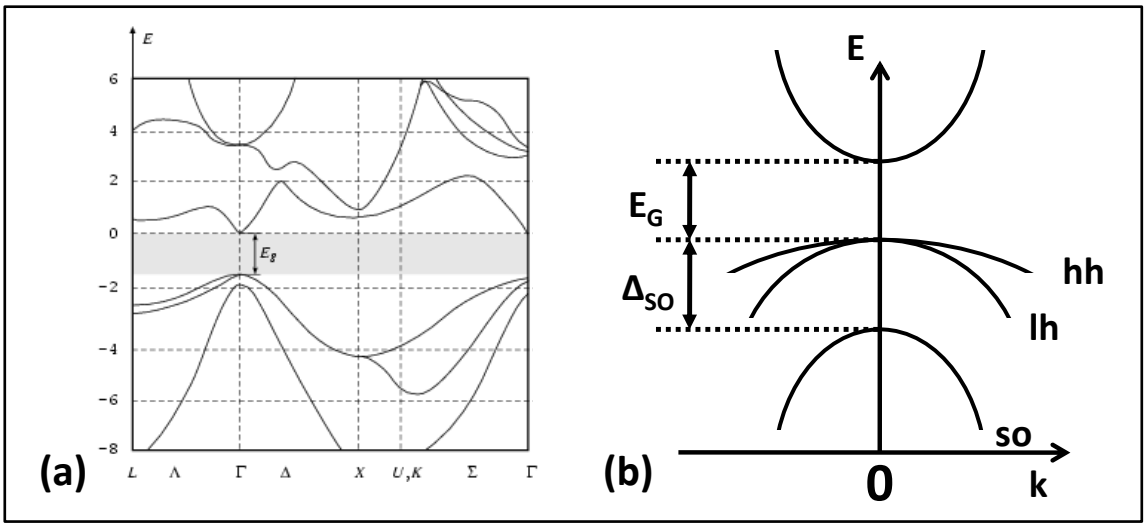

Fig. 2.8: Complete band diagram of a GaAs crystal (a)[Tboo]. (b) Most important for transport are the parabolic regions of the conduction as well as the different (heavy hole, light hole and split-off) valence bands. Within these parabolic areas the equations of motion are formally equal to the dispersion relation of free electrons[Kitt]. Therefore transport in a GaAs crystal can be described similar to free electrons only with the introduction of an effective electron mass.

In these regions the dispersion relation for the electrons is in good approximation quadratic as for free electrons. This means that the equations of motion for crystal electrons can be formulated in the same manner, accounting for the crystal environment simply by establishing a different effective mass than for free electrons[Sah].

2.2.2 Doped Semiconductors

An intrinsic semiconductor is more or less irrelevant for two reasons. Firstly, for real applications its conductivity is often much too low to be of any use (except for application where high tunnel resistances are needed, see chapter 2.4.2) and secondly, it's very challenging to produce crystals that show pure semiconducting behavior for today's technology. Absolutely clean GaAs, Si and Ge crystals have charge carrier concentrations of 2×10^6, 7×10^9 and 2×10^{13} per cm^3 [Thus]. This means that every electrically active impurity that has a concentration between 10^6 and $10^{13}\,cm^{-3}$ (dependent on the semiconductor)

already destroys the real semiconducting behavior. In the easiest case of Ge this still means that only one different atom in one billion Ge atoms is allowed. Yet it is possible to generate ultra-pure Ge, with impurity concentrations of one per 10^{11} Ge atoms[Hall], that shows intrinsic behavior but in GaAs for example one impurity atom has to be surrounded by 10^{16} lattice atoms, still impossible to generate in industrial dimensions and at reasonable prices.

This handicap in fact turns into the biggest advantage of semiconductors, however. By doping those materials with an adequate atomic species the electronic properties can be tuned almost arbitrarily. If one uses Si as a dopant for a GaAs crystal for example, the silicon atoms prefer to be embedded into the crystal at Ga sites (this in fact depends on the crystal orientation, in [001] GaAs the preferred place is a Ga site, while in [311] GaAs it can be controlled by growth conditions if it's a Ga or an As site[Saka]). As the trivalent Ga atom is replaced by the Si atom with four valence electrons, only three electrons are needed for the bonds to the neighboring atoms. That means that one electron stays unpaired and is now only weakly bound to its host Si atom (see fig. 2.9 (b)).

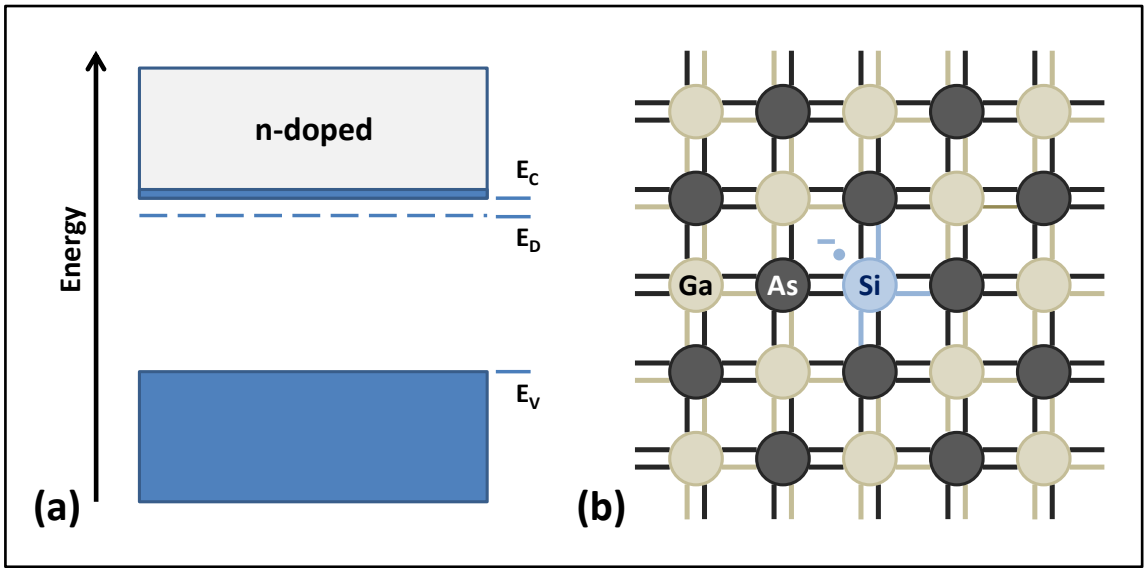

Fig. 2.9: (a) Band structure of a n-doped semiconductor at finite temperature. The donor energy levels are so close to the conduction band that an eminent number of electrons are thermally excited into the conduction band. The lattice schematic (b) shows that the Si atom uses only three of its four valence electrons for the crystal bonds and the now weekly bound fourth one can very easily move around in the crystal.

In part (a) of fig. 2.9 the dashed line E_D indicates the energy levels that are introduced by atomic species that generate n-doped GaAs. These are elements that have one valence electron more than the atom they replace. This gives these dopants their general name as donors, because they donate to the system one (or more) additional electron that can be used subsequently for electrical conduction. The energy levels of donors can be calculated quite easily. If we take the Si^+ ion as a core and look at the weakly bound electron orbiting around it we can use Bohr's standard model for a hydrogen atom[Kitt]. Therefore, the

only adaptations we have to make are the substitution of the free electron's mass m_0 with the effective mass in the crystal m_e (as we have parabolic band bending in the relevant region of the filled states we can describe the electron's motion by an effective mass m_e) as well as the amendment of the dielectric vacuum constant ε_0 with the material constant ε_{GaAs} (the Bohr radius of a donor state is typically large enough to justify this approach as we will see later). As the conduction band levels can be considered as the free and unbound states in the crystal, the binding energy of an electron to its donor level is the difference between donor energy level and lowest state in the conduction band E_C. This means the binding energy is given by

$$E_{bind} = E_C - E_D = \frac{1}{2}\frac{e^2}{4\pi\varepsilon\varepsilon_0 a_e} = 13.6eV \cdot \frac{\left(\frac{m_e}{m_0}\right)}{\varepsilon^2}. \tag{2.1}$$

The Bohr radius of the ground state can be calculated similarly by expanding Bohr's model for the hydrogen atom to

$$a_e = \hbar^2 \cdot \frac{4\pi\varepsilon\varepsilon_0}{m_e e^2} = a_B \frac{\varepsilon}{\left(\frac{m_e}{m_0}\right)} = 5.29\frac{\varepsilon}{\left(\frac{m_e}{m_0}\right)} \cdot 10^{-11} m. \tag{2.2}$$

We have only to fill in the right values for GaAs into the equations. The effective electron mass in GaAs is $m_e = 0.066\, m_0$[Thus], the dielectric constant $\varepsilon_{GaAs} = 13.13$[Kitt]. This gives us an ionization energy for the Si donor of 5.2 meV as well as a donor Bohr radius of 10.5 nm. This means we have about 65'000 crystal atoms within a sphere of this radius in GaAs, which clearly justifies the use of the static dielectric constant ε_{GaAs} to account for the screening of the Coulomb force, which the impurity ion exerts on the weakly bound electron. Furthermore with this large donor radii we can say that already at quite low concentrations (compared to the 10^{22} cm^{-3} host atoms) the distance between the impurities decreases so much that their wavefunctions can overlap. Then an impurity band develops[Kitt], which due to the random distribution of impurities, has band edges with tails. For even higher doping concentrations the impurity band overlaps with the conduction band completely and the semiconductor behaves like a metal. This so-called metal-insulator transition was discussed in detail by Mott[Mot2],[Mot3],[Gebh]. The formation of the impurity band leads to a reduced ionization energy for the impurities and at a critical doping concentration N_C the activation for the carrier concentration completely disappears. The critical density can be estimated from the Mott criterion when the distance of the impurities becomes comparable to their Bohr radius:

$$a_e N_C^{1/3} \approx 0.24. \tag{2.3}$$

For GaAs this yields a value of $N_C = 1.2 \times 10^{16}$ cm^{-3}, which agrees well with experiment, see table 2.1. The process of impurity band conduction generally

sets in at lower donor concentrations if also acceptor atoms are present, as then some donors are always ionized and this assists the conductivity[Kitt]. An equivalent treatment can be applied to so-called acceptor impurities. These are atoms that do have less valence electrons than the lattice atom they replace. Typical acceptors are for example Boron in Si or Carbon in GaAs (on an As lattice site). Now there is one electron missing that would be needed to build the regular lattice bonds. This means that electrons from the surrounding atoms can easily jump into this hole.

Host material	x-type (dopant)	N_C [cm^{-3}]
Ge	n (As)	1.5×10^{17}
Si	n (P)	1.3×10^{18}
Si	p (B)	6.2×10^{18}
GaAs	n (Si)	1×10^{16}

Tab. 2.1: experimentally verified critical doping concentrations for various semiconductors and dopants, values from [Deby], [Pear] and [Stil].

The energy levels of acceptors are just above the valence band edge E_V. If one electron is elevated from the valence band into such a level the remaining electrons in the valence band can start to move because this emerged hole creates some free space. This single missing electron is typically treated as a particle with a positive charge, as it's just the easiest way to deal with it. Figure 2.10 gives an overview of the situation. The energy gap between the valence band edge and the acceptor levels is comparable to the ionization energies for donors; table 2.2 gives some experimental values for different impurities.

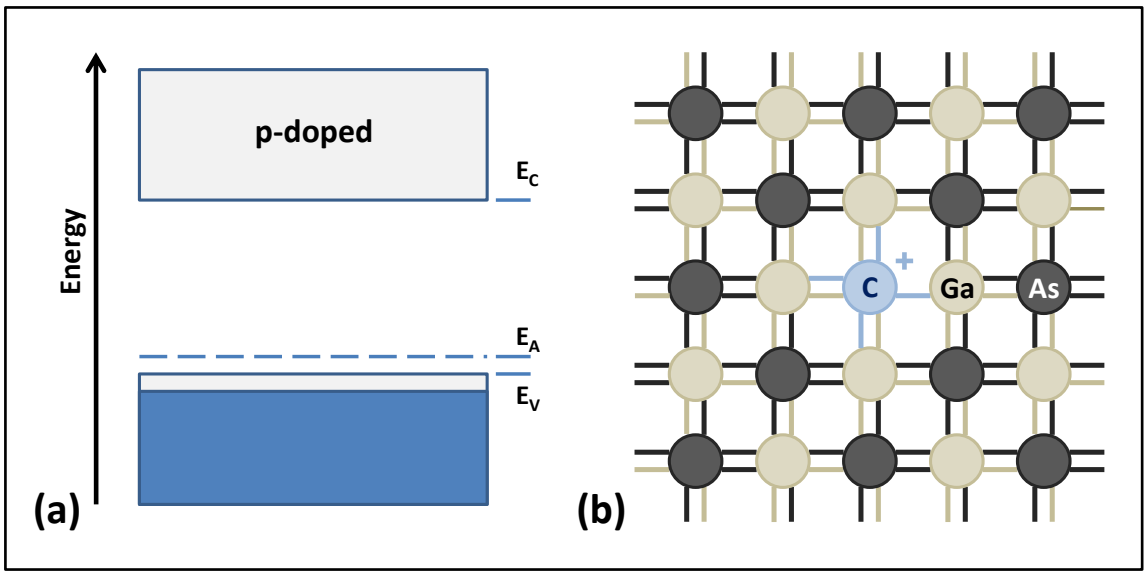

Fig. 2.10: (a) Band structure of a p-doped semiconductor at finite temperature. The acceptor energy levels are so close to the valence band that electrons can be thermally excited into the acceptor levels very easily. The lattice schematic (b) shows that the C atom offers one valence electron less than would be necessary for the crystal bonds. This means there exists a hole that can be filled by other valence electrons, which generate thereby new holes on their original positions.

Host crystal	Donor levels Ionization energy [meV]			Acceptor levels Ionization energy [meV]			
	P	As	Sb	B	Al	Ga	In
Si	45	54	39	45	67	74	160
Ge	12	12	9.6	10	10	10	11
	S	Te	**Si**	C	Cd	Zn	Si
GaAs	6	30	**5.8**	19	35	31	35

Tab. 2.2: The ionization energies of donor and acceptor levels are typically in the range of 10 meV. For GaAs we get the lowest ionization energies for donors due to the very small effective electron mass in the crystal[Eise],[Kitt],[Sze],[Thus].

2.2.3 Esaki Diodes

Typical electronic devices do not consist of homogeneous semiconductors; an example is a semiconductor diode consisting of two differently doped regions, the pn-junction. For simplicity we assume an abrupt change of doping levels. In the left region we have p-type doping, thus our charge carriers are holes. In the right part we have n-type doping and electrons. At the contact between p- and n-region recombination processes occur. The freely moving electrons flow into the p-type region and the holes into the n-type region. This leads to a depletion layer, a zone (almost) without free charge carriers, where only localized and charged impurities reside. The sudden change of carrier concentrations at the end of the depletion zone leads to further diffusion current I_D into the zone, while an equally big but opposed drift current I_F due to the developing electric field in the depletion layer leads to equilibrium conditions[Sah] (see fig. 2.11).

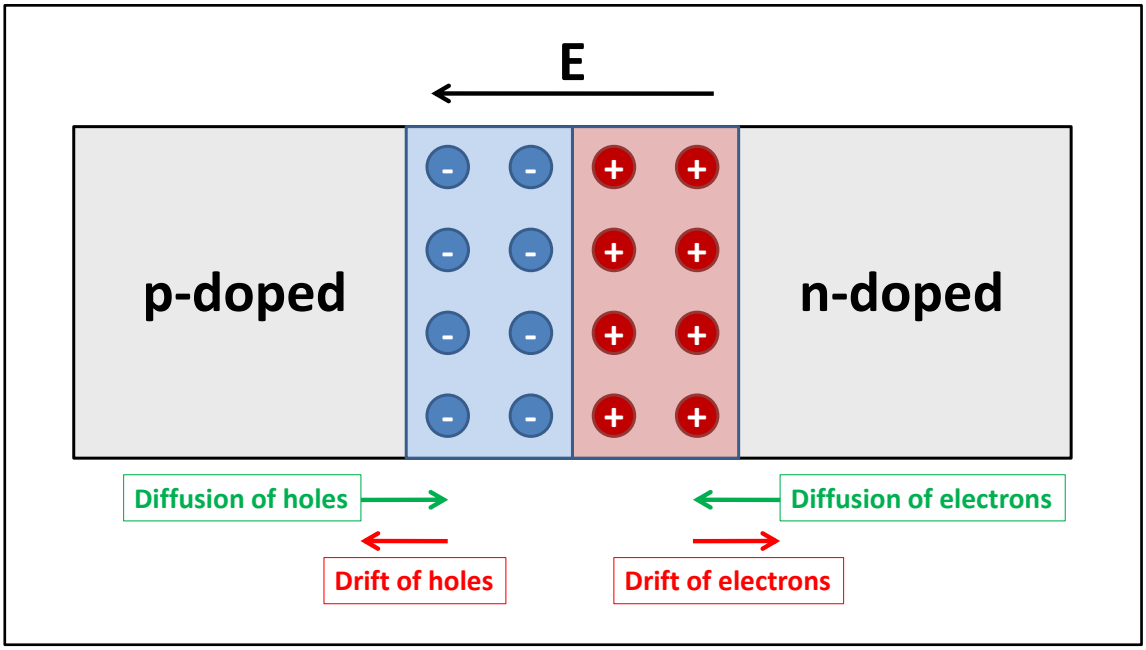

Fig. 2.11: The originally electrically neutral p- and n-doped regions directly at the junction develop the depletion layer/space charge region. The freely movable electrons diffuse in the contact region to the p-doped side and the holes vice versa. Equilibrium condition is reached if the diffusive forces and the built-in potential lead to equally big but opposed currents.

Due to the localized charges in the depletion layer it is also called space charge region. The potential generated by this space charge is called the built-in potential Φ_{bi}. Multiplied with the unit charge of an electron it gives the energy difference of the p- and n-doped sides against each other. This leads to a band bending at the junction, as can be seen in figure 2.12 (a). If one applies a forward bias to the junction, meaning positively biasing p-region with respect to n-doped region, the depletion layer is reduced as electrons are pushed into the n-doped region and holes into the p-doped region. Thus at a voltage comparable to the built-in potential the junction gets conducting. At reverse biased configuration the depletion layer is extended even further and the pn-junction does not carry current until very high voltages are reached where a physical breakdown occurs (see figure 2.12 (b)), which destroys the diode.

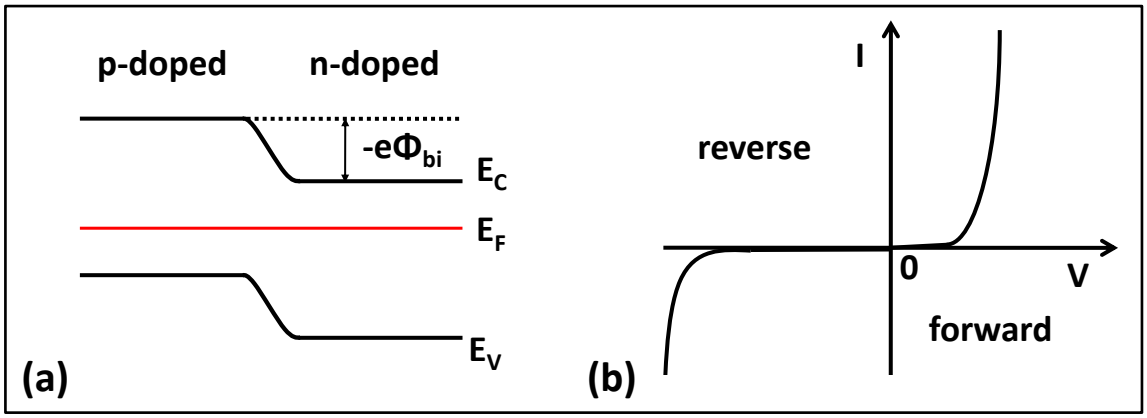

Fig. 2.12: (a) The band structure shows the band bending at the crossover from p- to n-doped region. The built-in potential times electronic charge gives the shift of the bands from one region to another. (b) A sketch of a typical IV-curve of a pn-junction. While at a forward voltage (p-doped side with positive bias voltage compared to n-type region) comparable to built-in potential a reasonable charge current flows in reverse bias regime nearly no current flows until at significantly higher values the breakdown voltage is reached.

If one increases the doping of both regions to degenerate levels (typical $10^{18}\,cm^{-3}$ and more; critically dependent on host semiconductor) the Fermi energy on both sides of the junction lies within the bands. In the p-doped region it lies in the valence band whereas in the n-doped region it is in the conduction band. This gives us an overlap of both bands, meaning the potential drop across the junction is bigger than the band gap:

$$\Phi > \frac{E_G}{e}. \tag{2.4}$$

If no external voltage is applied we have now unfilled states in the conduction band of the n-type region, which are virtually on the same energy level as occupied states in the valence band of the p-doped side. Additionally due to the high impurity concentration the charge density in the space charge region is exceedingly increased and its thickness can be reduced to below 10 nm[Grun]. In a pn-junction with these high doping levels exist not only diffusion and drift

currents like in normal pn-diode but also tunneling currents in both directions can appear, the Zener and Esaki currents[Rost], see figure 2.13.

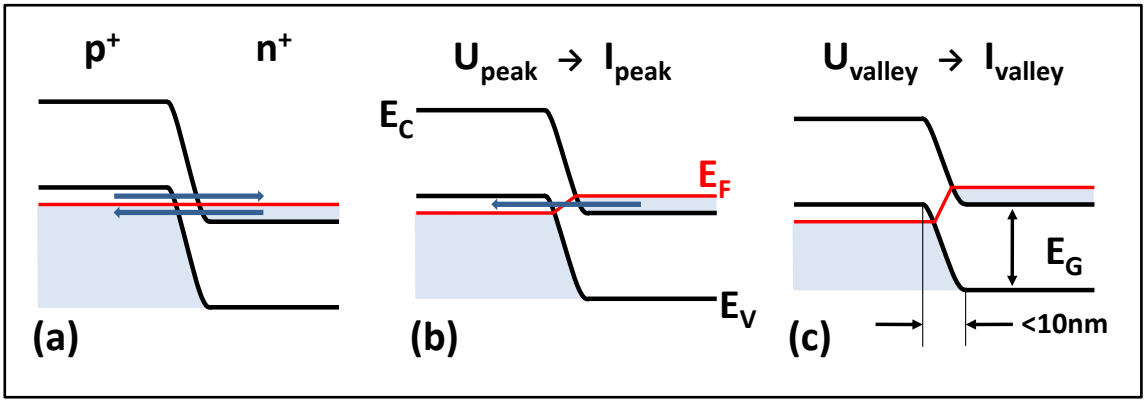

Fig. 2. 13: Energy band model of an Esaki diode (a) without applied field, (b) with forward bias V_{peak} and (c) forward bias V_{valley}. The arrows indicate Esaki (to the left) and Zener (to the right) tunnel currents[Rost].

If an external voltage is applied to the junction these currents develop very differently. Increasing the forward voltage leads to a strongly decreased Zener current while the Esaki current increases until the region between Fermi level and valence band edge in the p-doped region as well as Fermi level and conduction band edge in the n-region are energetically equal. At this voltage the peak current is reached, which decreases at further increased voltage until the Esaki current becomes zero as we do not have a band overlap any more. This is the reason for the characteristic IV-curve of an Esaki diode with the negative differential resistance region as shown in fig. 2.14.

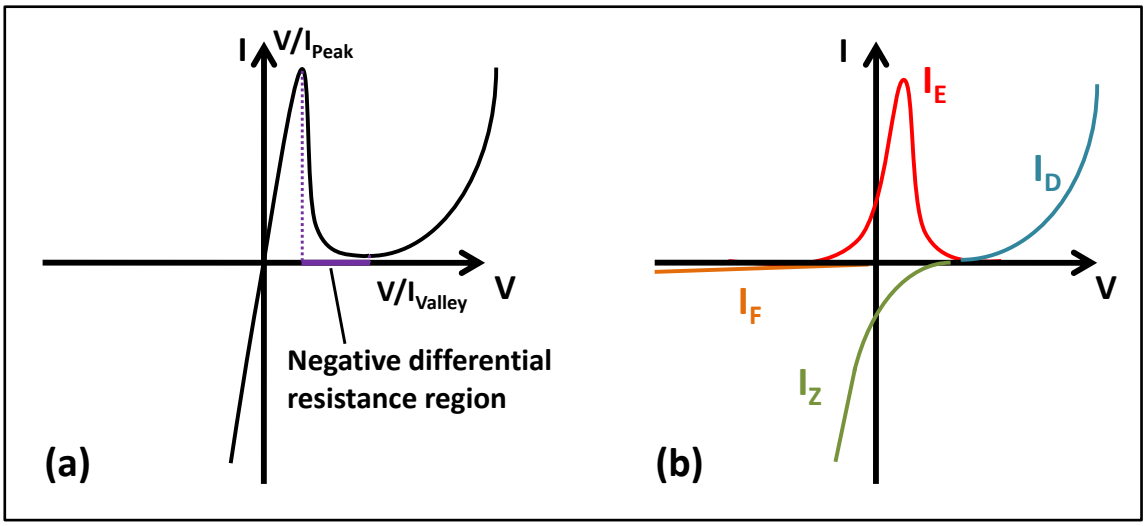

Fig. 2.14: Schematic IV-curve of an Esaki tunnel diode[Rost]. (a) The most interesting part is the region between the voltage of peak current and valley current, where the diode reveals negative differential resistance. (b) The IV-curve can be decomposed to four components. Additional to the normal field and diffusion currents in pn-junctions (I_F and I_D) occur the Esaki as well as the Zener tunnel currents (I_E and I_Z)[Rost].

Now at this voltage we have the valley current. Due to inelastic tunneling processes through states in the band gap the valley current typically does not

go down to zero[Grun]. Above the valley voltage the current increases exponentially as known from a normal pn-junction. In contrast, at a reverse biased Esaki diode the Esaki tunnel current goes down to zero, while the Zener current strongly increases[Rost]. This means that Esaki diodes are also conducting in the reverse biased regime; hence the typical rectifying behavior of a normal pn-junction is lost. The ratio between peak and valley current expresses the quality of an Esaki diode and can reach values of 10 at industrially manufactured Ge Esaki diodes and more than 50 in GaAs based devices[Rost].

2.3 Fabrication of semiconductors

There are several fabrication processes used in industry for the generation of semiconductor wafers. CZ material is fabricated by a method of crystal growth where a seed crystal is dipped into the molten semiconductor material and slowly pulled out of it. The material crystallizes at the seed crystal and maintains the same crystalline direction. The process is named after J. Czochralski, who discovered the method originally through investigations on the crystallization rates of metals[Czoc]. The Bridgman-Stockbarger technique is a method of growing single crystal ingots by involving heating polycrystalline material above its melting point and slowly cooling it from one end of its container, where a seed crystal is located. Single crystal material is progressively formed along the length of the container. The process can be carried out in a horizontal or vertical geometry[Kats],[Birk], where it is typically called the Vertical Gradient Freeze method (VGF). For producing compound semiconductor crystals such as gallium arsenide this procedure is usually preferred as the Czochralski process is more difficult and leads to higher defect concentrations[Lale]. The float zone (FZ) method uses a polycrystalline semiconductor rod, which is passed through a heating coil. This creates a localized molten zone from which the crystal ingot grows. A seed crystal is used at one end in order to start the growth. There are two advantages of the FZ method for Si growth; firstly higher purity and better micro-defect control and secondly faster growth rates and heat-up/cool-down times due to the absences of a crucible and consumable hot-zone parts[Sche]. The semiconductor rod is then cut into thin wafers thereafter and polished. These wafers are the basis for the fabrication method of our specific layer design, the so-called Molecular Beam Epitaxy (MBE). It is a suitable method for the preparation of thin epitaxial structures made of metals, insulators or semiconductors. The quality and purity of the so grown samples are outstanding. For a more elaborate view on this topic the reader is referred to [Lale].

2.3.1 Principle of MBE growth

The growth process is realized in an ultra-high vacuum (UHV) chamber with a base pressure in the order of 10^{-11} mbar, see fig. 2.15. Selected elements, e.g. Ga, As, Al, Mn and others are heated in effusion cells that are attached to the main

chamber. Each material has its own effusion cell and is of extreme purity. The evaporated atoms leave the cells in collimated beams and impinge on a heated surface of a mono crystalline target wafer, the substrate, which is mounted on a sample holder in the middle of the chamber. The holder can be rotated, tilted and heated, to reach best possible growth conditions. The composition and the doping level of the grown epilayers depend, to make a long story short, on the relative arrival rates of the constituent elements and dopants. These rates can be controlled by the temperature of the effusion cells, as this changes the evaporation rate. Typical working temperatures of the effusion cells depend on the materials used inside, these are e.g. for Ga approximately 1000 °C and for As nearly 300 °C. As the growth rate is very slow, around one atomic monolayer per second, and the substrate temperature is very high, around 600 °C for standard GaAs growth, surface migration of the adsorbed atoms on the substrate is ensured. This leads to very smooth surfaces of the grown films. In front of each effusion cell a mechanical shutter is installed and simply by closing it, the beam flux is interrupted and thus the thickness of the film can be controlled on atomic scale. These possibilities allow the growth of high quality semiconducting heterostructures[Herm].

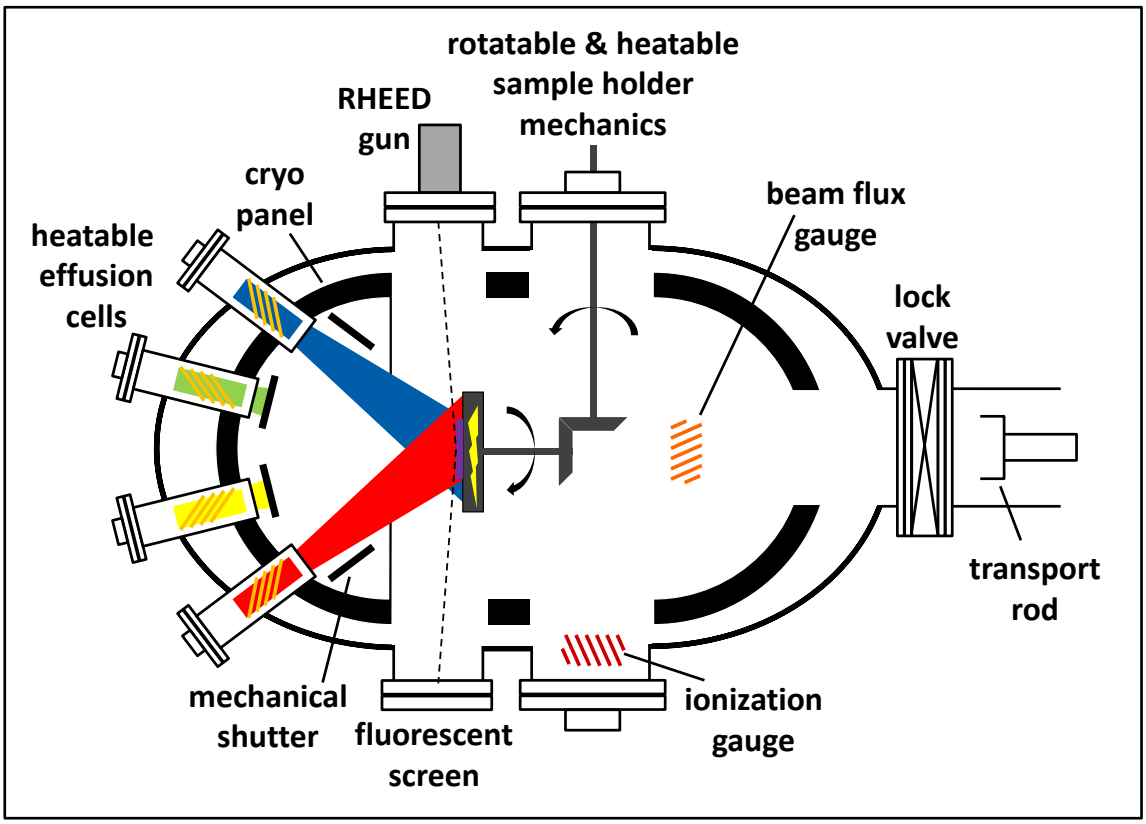

Fig. 2.15: Schematic of an UHV MBE chamber. The different effusion cells with the pure source material for growth of various different layers are attached at the left side. By heating the evaporation rate can be controlled, by closing the mechanical shutters the growth rate can be stopped abruptly. This allows the construction of heterostructures on atomic scale. The wafer holder can be rotated and heated. By opening the lock valve the wafer can be transferred to other chambers connected to the MBE.

2.3.2 Layer Growth Monitoring

The chamber is equipped with some other accessories, as well. The most important ones are an electron gun and the corresponding fluorescent screen. This gun is used for RHEED (reflection high energy electron diffraction) measurements, where an electron beam of typically 5-40 keV is directed at a low angle of 1-3° to the substrate surface[Herm]. The corresponding de-Broglie wavelength is in the range of 0.1 Å and the beam penetration is restricted to few outermost atomic layers. In particular, RHEED can be used for monitoring of the surface morphology, orientation and most important the smoothness of the topmost surface layer. If we think of the initial, perfectly smooth substrate surface, the intensity of the reflected beam has a maximum, corresponding to the high surface reflectivity. Any roughening during the growth, related to local cluster building leads to a decrease in intensity. If a layer is completed by filling the cavities between the clusters, a smooth surface is reconstructed and intensity reaches a new maximum. So, one complete oscillation in the RHEED pattern corresponds exactly to one grown monolayer, see figure 2.16.

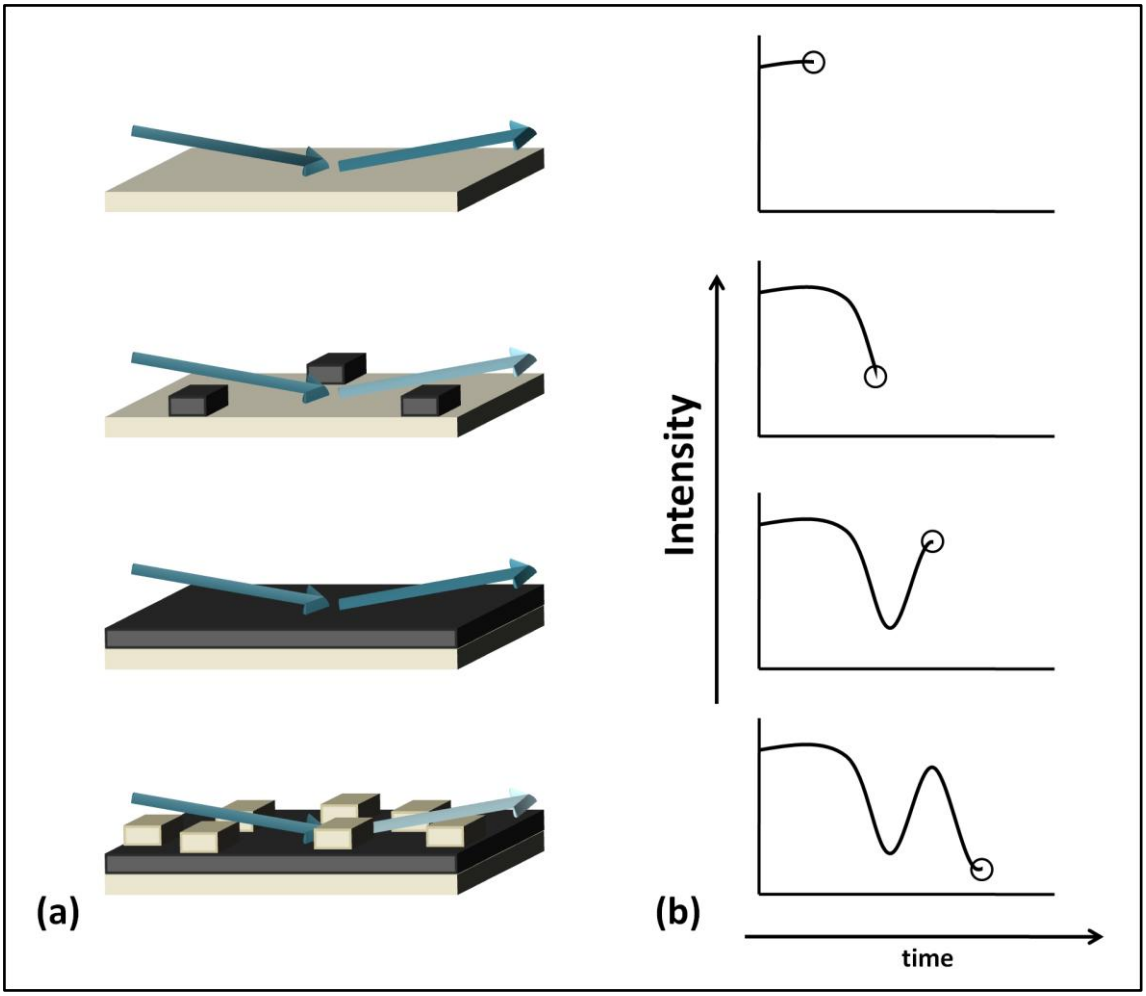

Fig. 2.16: (a) MBE growth of subsequent atomic layers in the desired 2D growth mode and RHEED oscillations during the generation of new monolayers (b). A complete layer gives a maximum signal while a fragmented surface leads to damped intensity of the RHEED signal[Lale].

2.4 Magnetism

Magnetism is a fascinating as well as incredibly widespread subject. To emphasize this fact, the history of magnetism in Europe goes back to the documented use of Lodestone (an iron ore found to be "magnetic") for navigation already around 1300 A.C. at latest[Getz], in China even some hundred years earlier. Really a lot has happened since. Therefore we will give only a short overview of some important subfields and refer the interested reader to the corresponding literature for deeper insight[Coey],[Crai],[Cull],[Getz],[Stöh].

Classically the magnetic moment $\boldsymbol{\mu}$ can be explained by thinking of a current loop. A current I flowing through an infinitely small loop of area dA gives a magnetic moment $d\mu$. More of those can be summed up by integration to a loop of finite size where only the perimeter of the resulting loop counts because the currents of neighboring infinitely small loops cancel out each other:

$$d\boldsymbol{\mu} = I d\mathbf{A} \tag{2.5}$$

$$\boldsymbol{\mu} = \int d\boldsymbol{\mu} = I \int d\mathbf{A} \tag{2.6}$$

The right-hand rule gives the direction of the vector. A magnetic dipole can now be interpreted as a very small loop with still finite magnetic moment. The energy of a magnetic moment can be written as

$$E = -\mu_0 \boldsymbol{\mu} \cdot \boldsymbol{H} = -\mu_0 \mu H \cos\theta \tag{2.7}$$

with θ being the angle between magnetic moment $\boldsymbol{\mu}$ and magnetic field $\boldsymbol{H}$, while μ_0 is the permeability of vacuum.

The magnetization $\boldsymbol{M}$ is simply the total magnetic moment per volume unit and its magnitude M can be written as

$$M = \mu \frac{N}{V}. \tag{2.8}$$

Magnetic induction or flux density $\boldsymbol{B}$ is the response of a material to an external magnetic field $\boldsymbol{H}$. Each material exhibits a characteristic dependency between $\boldsymbol{H}$ and $\boldsymbol{B}$. In free space the correlation is just linear

$$\boldsymbol{B} = \mu_0 \boldsymbol{H}. \tag{2.9}$$

Inside magnetic materials the equation has to be corrected by the influence of the magnetization $\boldsymbol{M}$

$$\boldsymbol{B} = \mu_0 (\boldsymbol{H} + \boldsymbol{M}). \tag{2.10}$$

We will refer to both $\boldsymbol{B}$ and $\boldsymbol{H}$ as "magnetic field" in the following, as its common usage in the literature, although not perfectly correct.

If we investigate so-called "linear magnetic materials" then the relationship between magnetization and external field can be written with the help of the magnetic susceptibility χ as

$$\boldsymbol{M} = \chi \boldsymbol{H} . \tag{2.11}$$

2.4.1 Classification of magnetic material

Matter can be categorized into three classes with the help of the magnetic susceptibility.

Diamagnetism

All existing materials exhibit diamagnetic behavior. Thereby an external magnetic field induces magnetic dipoles, which are due to Lenz's rule anti-parallel oriented to the exciting field. Therefore χ^{dia} is negative and as a pure induction effect independent of temperature

$$\chi^{dia} = const. < 0 . \tag{2.12}$$

The absolute value of χ^{dia} is small compared to the susceptibilities of paramagnets and collective magnetism, thus only purely diamagnetic materials show this behavior like Hg, Ag, He, Xe, many organic substances or superconductors, which are ideal diamagnets with $\chi^{dia} = -1$ (Meißner-Ochsenfeld effect)[Getz].

Paramagnetism

Existing permanent dipoles, which are oriented in the external field $\boldsymbol{H}$ are a necessary precondition for paramagnetism. The degree of this orientation is influenced by thermal fluctuations, thus leading to the following characteristic of the susceptibility

$$\chi^{para} = \chi^{para}(T) > 0 . \tag{2.13}$$

The permanent magnetic moments can be of localized or itinerant nature:

Localized moments

Partially filled inner electron shells are the reason for these localized moments, typical examples are 4f-electrons in rare earth metals or 5f-electrons in actinides. This so-called Langevin paramagnetism is temperature dependent and can be described by the Curie law at high temperatures

$$\chi^{Langevin}(T) = \frac{C}{T} \tag{2.14}$$

Itinerant moments

The Pauli-paramagnetism is quasi temperature independent, as it bases on nearly free electrons in the valence band. Each electron has a magnetic moment of exactly one Bohr magneton μ_B.

$$\frac{\partial \chi^{Pauli}}{\partial T} \simeq 0 . \tag{2.15}$$

The Pauli-susceptibility is much smaller than the Langewin-susceptibility[Getz].

Collective magnetism

The collective magnetism can only be explained by quantum mechanics and is a result of the exchange interaction between permanent magnetic dipoles combined with the Pauli Exclusion Principle for fermions. The susceptibility is complicated and depends on more than one parameter

$$\chi^{coll} = \chi^{coll}(T, \boldsymbol{H}, magnetic\ history) . \tag{2.16}$$

For all materials showing collective magnetism a critical temperature T^* can be defined below that a spontaneous magnetization is present without the need of applying an external magnetic field. Collective magnetism can again be divided into three subclasses.

Ferromagnetism

The critical temperature T^* is called Curie temperature T_C. The behavior of a ferromagnet can be simply divided into the three temperature regimes

$T = 0$: all magnetic moments are aligned parallel

$0 < T < T_C$: the magnetic moments exhibit a preferential direction

$T > T_C$: the thermal fluctuations are so strong that they destroy the coupling of the magnetic moments and the material acts as a paramagnet.

Ferrimagnetism

In these materials the lattice can be divided into two different ferromagnetic sublattices for $T < T_C$:

$$\boldsymbol{M}_A \neq \boldsymbol{M}_B \tag{2.17}$$

$$\boldsymbol{M}^{Ferri} = \boldsymbol{M}_A + \boldsymbol{M}_B \neq 0 \tag{2.18}$$

Antiferromagnetism

This is a special case of ferrimagnetism. The critical temperature of an antiferromagnet is called Néel temperature T_N. The magnetizations of the two sublattices have the same absolute values, but the opposite direction

$$|\boldsymbol{M}_A| = |\boldsymbol{M}_B| \neq 0 \tag{2.19}$$

$$\boldsymbol{M}_A = -\boldsymbol{M}_B \tag{2.20}$$

This means that an external observer does not see any global magnetization, it is only visible if one looks into the substructure of an antiferromagnet[Getz].

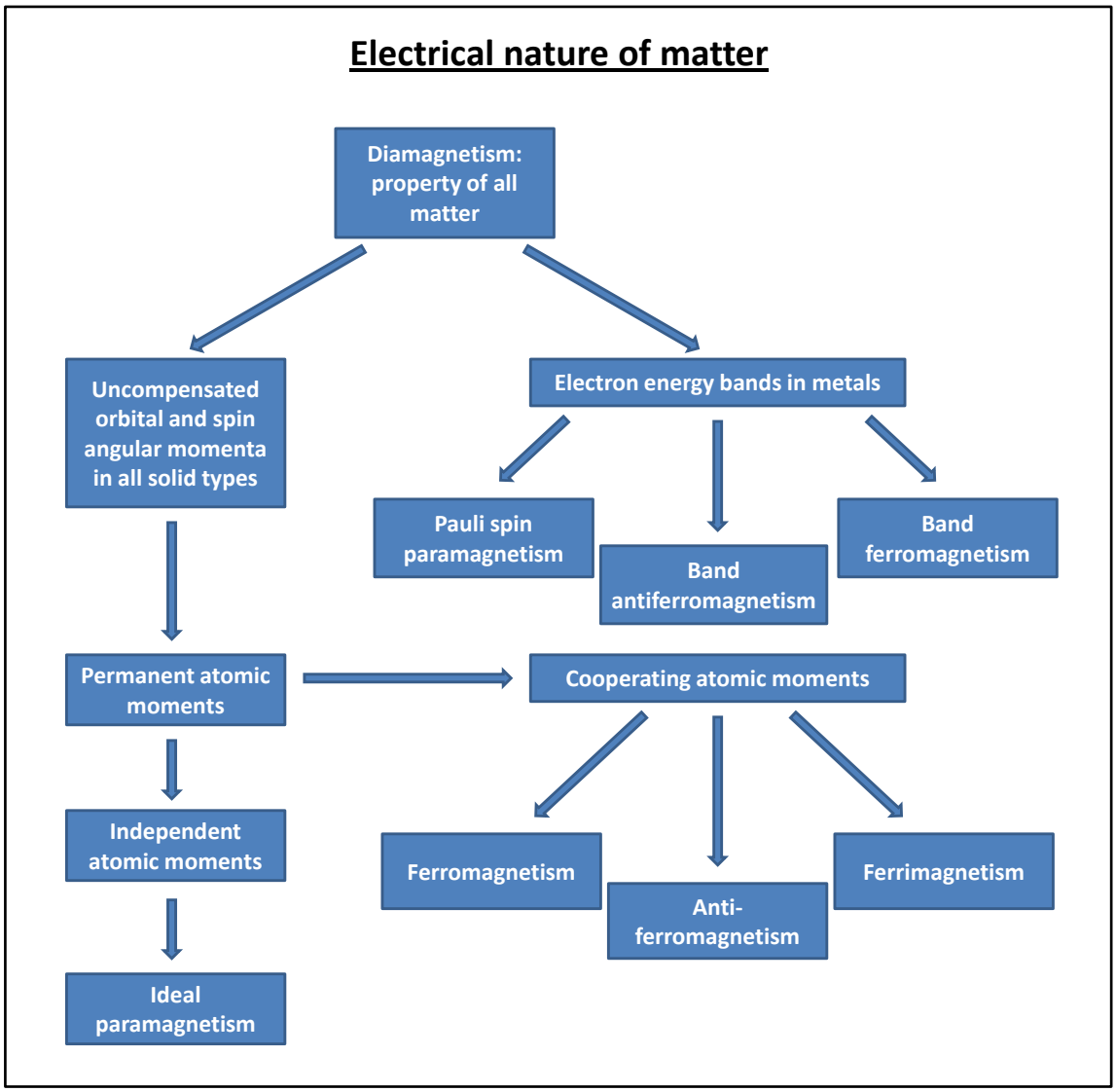

Fig. 2.17: There are different mechanisms that can lead to the same sort of magnetic behavior. This means for example that independent spins at atomic ground states can lead to paramagnetic behavior as well as spins of conduction electrons in metals. This gives a small hint on how complex the magnetic properties of matter really are. (Sketch was reproduced from [Meye].)

Bohr-van Leeuwen Theorem

N. Bohr (1911) and J. H. van Leeuwen (1919) proved independently from each other in their particular dissertations this now well-known theorem for classical and non-relativistic electrons, by using the Maxwell-equations and statistical mechanics. In words, this theorem is:

"At all finite temperatures and in all finite electric or magnetic fields the net magnetization of an ensemble of electrons in thermal equilibrium is identical zero."[Bohr],[vLee],[vFle]

The relevancy of this theorem is that it demonstrates exactly, that without quantum mechanics (taking the electron's spin to be a quantum mechanical phenomenon) there is no finite thermal equilibrium magnetization possible. As the free energy F does not depend on $\boldsymbol{H}$, then the magnetization (which can be written as $\propto \partial F / \partial H$) must always vanish, thus no ferromagnetic materials as iron for example would exist. Responsible for the formation of magnetically ordered structures is the so-called exchange interaction between the existent permanent magnetic dipoles. This interaction can only be explained on a quantum mechanical basis. It is based on a combination of the Coulomb interaction and the Pauli Exclusion Principle. The Heisenberg model is a fairly easy way of describing the interaction:

$$E = -2J_{ij}S_i \cdot S_j. \tag{2.21}$$

Here the so-called exchange integral J_{ij} characterizes the orbital overlap of atoms i and j while S_i and S_j denote their spin. For a parallel alignment of neighboring spins J_{ij} is positive while negative values lead to antiparallel alignment.

Direct exchange is very dominant in materials of very densely packed magnetic atoms like in iron. However the direct exchange interaction is very weak, if the magnetic atoms in a material are far apart from each other due to being randomly distributed in a host matrix. In these cases indirect exchange can lead to an interaction without an orbital overlap of the magnetic atoms itself. Three major mechanisms exist, namely super exchange, double exchange and Ruderman-Kittel-Kasuya-Yosida (RKKY) exchange. We will have a closer look only on the RKKY-interaction in chapter 2.5.2. It was developed to describe the indirect exchange between localized magnetic moments in metals, which is mediated by itinerant charge carriers. This kind of indirect exchange is also made responsible for the appearance of ferromagnetism in GaMnAs[Ohn2].

2.4.2 Anisotropy

Up to here we did not consider any direction dependency of our magnetic systems, i.e. all physical properties were identical for every direction in space. However, the energy of a system as a function of the magnetization can be critically dependent on the orientation of $\boldsymbol{M}$. We will give a short overview of some important magnetic anisotropies:

magneto crystalline anisotropy

This is the most important type of anisotropy. It originates in the spin orbit interaction (SOI) of the electrons. The SOI couples the electron spin to the magnetic field generated by the orbital movement of the electron around the ion. As the orbitals are closely linked to the crystallographic structure this leads to a preferred alignment of the spins along well defined crystallographic axes. Since a magnetic crystal is not isotropic, this leads to the existence of easy magnetization axes, crystal directions in which the material is easier to magnetize than in others, the hard magnetization axes. The SOI can be evaluated either from basic principles or easier from using power series expansions that take crystal symmetries into account and gaining the coefficients from experiments[Getz].

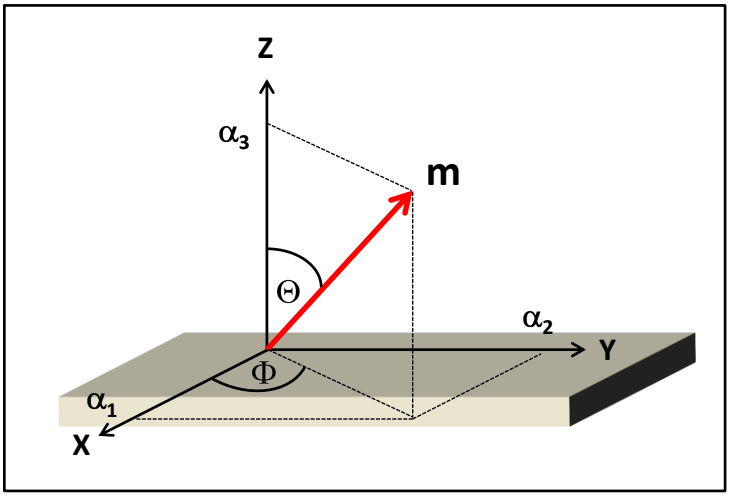

Fig. 2. 18 The magnetization direction *m* can be defined using the direction cosine α_i[Getz].

Relative to the coordinate axes the magnetization direction $\boldsymbol{m} = \boldsymbol{M}/|\boldsymbol{M}|$ can be described by the direction cosine α_i as $\boldsymbol{m}=(\alpha_1, \alpha_2, \alpha_3)$. Thereby the α_i stand for

$$\alpha_1 = \sin\theta\cos\phi \tag{2.22}$$

$$\alpha_2 = \sin\theta\sin\phi \tag{2.23}$$

$$\alpha_3 = \cos\theta. \tag{2.24}$$

Fortunately this definition fulfills the condition

$$\alpha_1^2 + \alpha_2^2 + \alpha_3^2 = 1. \tag{2.25}$$

The magneto crystalline energy E_{crys} can now be expanded into a power series, thereby neglecting usually very small terms of order (α^5) or higher by writing

$$E_{crys} = E_0 + \sum_i b_i\alpha_i + \sum_{i,j} b_{ij}\alpha_i\alpha_j + \sum_{i,j,k} b_{ijk}\alpha_i\alpha_j\alpha_k + \sum_{i,j,k,l} b_{ijkl}\alpha_i\alpha_j\alpha_k\alpha_l. \tag{2.26}$$

As the energy for systems magnetized in opposite directions is the same, i.e.

$$E(\alpha_i) = E(-\alpha_i) \tag{2.27}$$

only even terms of α_i occur in the power series and the expression can be simplified to

$$E_{crys} = E_0 + \sum_{i,j} b_{ij}\alpha_i\alpha_j + \sum_{i,j,k,l} b_{ijkl}\alpha_i\alpha_j\alpha_k\alpha_l. \tag{2.28}$$

This very general equation for the magneto crystalline energy can now be further modified for special crystallographic systems with e.g. cubic or hexagonal symmetry. Often these equations are denoted using the magneto crystalline anisotropy constants K_i, which are only functions of the $b_{ij...}$s, however.

Despite the fact that the magneto crystalline energy is typically small compared to the exchange energy it nevertheless governs the magnetization direction due to the fact that the exchange energy prefers only parallel magnetic moments, not specific crystallographic directions[Getz].

Shape anisotropy

In polycrystalline samples typically global easy and hard axes do exist. Only spherically shaped samples feature isotropic behavior. Due to the polycrystalline nature magneto crystalline anisotropy cannot be the source of this direction dependence. To gain deeper insight into this behavior, one has to deal with stray- and demagnetizing fields. In finite samples $\boldsymbol{B}=\mu_0(\boldsymbol{H}+\boldsymbol{M})$ has to be corrected for the poles at the sample surface that lead to stray fields outside of it. The existence of stray fields is connected to demagnetizing fields inside of the sample. The sample energy in its own stray field is

$$E_{stray} = -\frac{1}{2}\int \mu_0 \boldsymbol{M}\cdot\boldsymbol{H}_{demag} dV \tag{2.29}$$

Here E_{stray} is the stray field energy and $\boldsymbol{H}_{demag}$ the demagnetizing field within the sample. For arbitrarily shaped objects it is very complicated to evaluate E_{stray}, for the simple case of an infinitely wide and very thin plate one can write it as

$$E_{stray} = K_0 + K^V{}_{shape}\, sin^2\theta \tag{2.30}$$

with $K^V{}_{shape} \propto -M^2 < 0$. This means that the stray field energy reaches its minimum for $\theta = 90°$ and therefore shape anisotropy favors a magnetization direction of thin magnetic films within the film plane.

Magnetic surface and interface anisotropies

If one deals with low dimensional systems, e.g. thin films or thin wires, the anisotropy related to the surfaces or interfaces cannot be neglected. At these interfaces the anisotropy energy contains terms with lower order in alpha, which do not occur in three dimensional systems, due to the broken symmetry at the sample surface. The effective anisotropy constant K_{eff} can be divided into the volume part K_V and a contribution from the surface K_S, reading as

$$K_{eff} = K_V + 2K_S / d. \tag{2.31}$$

The factor of two accommodates the creation of two surfaces on top of and below the film while the inverse dependence on the film thickness d is due to the decreasing importance of K_S for thicker films. (2.31) can be rewritten as

$$d \cdot K_{eff} = d \cdot K_V + 2K_S \tag{2.32}$$

and plotted as a $dK_{eff}(d)$ diagram[Broe]. There K_V is the slope and $2K_S$ the zero crossing of the graph. At the critical thickness d_c, defined by $-(2K_S/K_V)$ the sign of K_{eff} changes and at thicker layers the volume contribution dominates whereas at thinner layers the surface part controls the magnetic behavior, respectively.

2.4.3 Magnetoresistivity

The static magnetic properties of solid magnetic materials influence the dynamic motion of electrons in it. An external magnetic field changes these magnetic properties what results in a modified electron mobility and therefore a magnetic field dependent variation of the resistance occurs, which is known as magnetoresistivity. With $R(H)$ being the resistance in an external magnetic field H the magnitude of an arbitrary magnetoresistive effect XMR can be defined as

$$XMR = \frac{R(H) - R(H=0)}{R(H=0)} = \frac{\Delta R}{R}. \tag{2.33}$$

Normal/Positive MagnetoResistance and Negative MagnetoResistance

The most general situation is a nonmagnetic metal within an applied magnetic field. As a consequence of the Lorentz force the resistance increases, therefore this is called positive or normal magnetoresistance. The mean free path of the electrons is thereby reduced as the external field forces them on spiral trajectories[Getz]. Nonmagnetic transition metals like Pd generally show a higher resistance as magnetic ones like Ni below T_C if one compares the normalized resistance curves (see fig. 2.19). As the current in transition metals is mainly carried by s-electrons due to their small effective mass, the resistance can be described by scattering of these s-electrons into empty d-states near the Fermi energy E_F. Transition metals own very large d-band DOS leading to a large

scattering cross section. For a nonmagnet the spin up and spin down electrons can be easily scattered into d-states while in the ferromagnetic case due to the exchange splitting one spin species does not have free d-states any more. This leads to an increased mobility and reduces resistance. An external magnetic field increases the spin order even further and reduces the resistance even more. Therefore in ferromagnetic transition metals we observe a negative magnetoresistance.

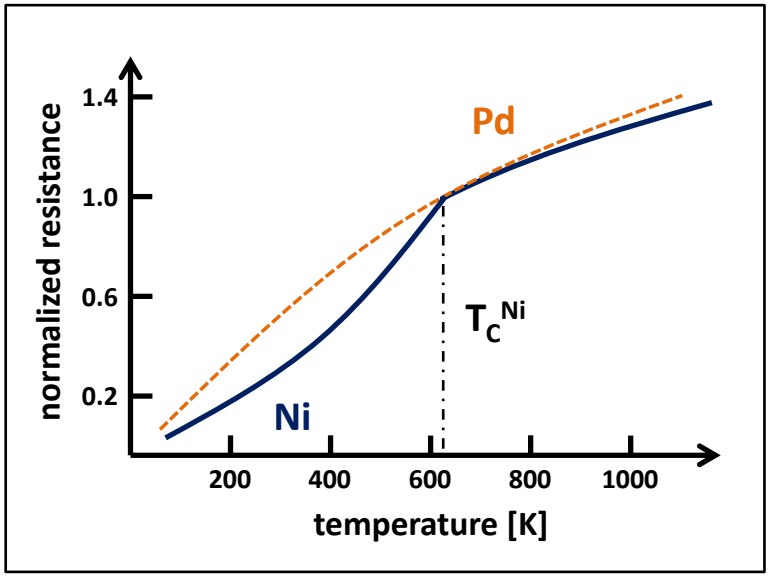

Fig. 2.19: Resistance curves of Pd and Ni normalized to T_C of Ni. Below T_C the resistance of Ni is significantly reduced compared to the paramagnetic Pd[Cole].

Mott introduced a very intuitive model by explaining the total resistance R_{total} as a parallel connection of resistors for majority and minority electrons[Mott] $R_\uparrow$ and $R_\downarrow$:

$$R_{total} = \frac{R_\uparrow \cdot R_\downarrow}{R_\uparrow + R_\downarrow}. \tag{2.34}$$

If one uses the method of describing a variation of magnetic order by the parameter a with inverse proportional and proportional behavior of $R_\uparrow$ and $R_\downarrow$, R_{total} can be rewritten:

$$R_\uparrow = \frac{1}{a}R \tag{2.35}$$

$$R_\downarrow = aR \tag{2.36}$$

$$R_{total} = \frac{\frac{1}{a}R \cdot aR}{\frac{1}{a}R + aR} = R \cdot \frac{a}{1+a^2}. \tag{2.37}$$

The maximum total resistance can easily be evaluated and is reached for $\alpha = 1$, what corresponds to vanishing magnetic order. (This negative MR behaves isotropically.[Getz])

Anisotropic MagnetoResistance (AMR)

Spin Orbit coupling of the 3d-orbitals is the physical origin of the AMR effect in ferromagnetic metals like Co[Getz]. For finite SOI spin flip scattering is allowed and majority s-electrons can be scattered into empty minority d-states. Due to the orbital anisotropy of the empty d-states the scattering cross section is different for parallel and perpendicular orientation between magnetization and current direction. The magnitude of the AMR effect depends on the angle between the magnetization $M(\theta_M)$ and the electric current $I(\theta_I)$ with respect to a given direction. In a ferromagnetic thin film the resistance quickly splits when applying a magnetic field perpendicular or parallel to the current[Getz].

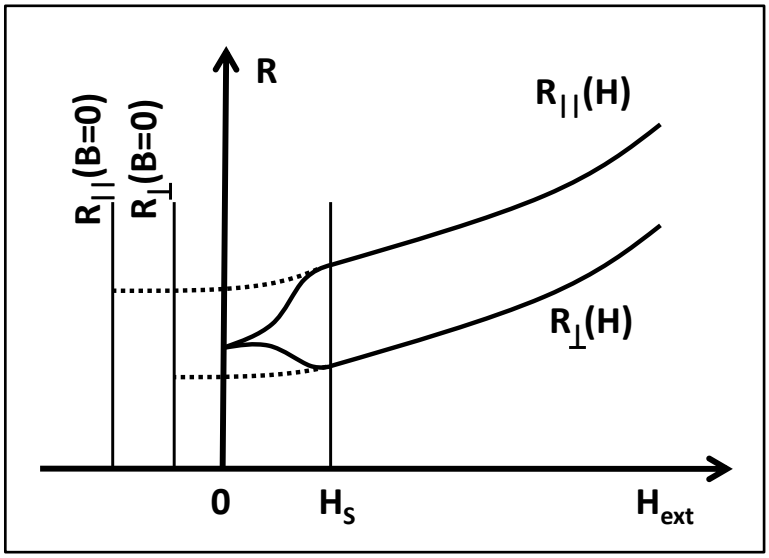

Fig. 2.20: Resistance as a function of external magnetic field. The difference between parallel and perpendicular orientation of the field relative to the current direction rises to its maximum already at H_S[Getz].

The difference between $R_{||}(H)$ and $R_{\perp}(H)$ quickly reaches its maximum at H_S. Above H_S positive or negative MR occurs, dependent on the material[Gros]. The angular dependence of the resistance change due to AMR can be written as

$$R(\theta) = R_{\min} + \Delta R_{AMR} \cdot \cos^2(\theta_M - \theta_I) \tag{2.38}$$

with ΔR_{AMR} being the resistance change because of the AMR effect. This equation can be rewritten as

$$\begin{aligned} \Delta R_{AMR} &= R_{\parallel} - R_{\perp} \\ R_{\min} &= R_{\perp} \\ R(\theta) &= R_{\perp} + (R_{\parallel} - R_{\perp}) \cdot \cos^2(\theta_M - \theta_I). \end{aligned} \tag{2.39}$$

$R_{\parallel}$ and $R_{\perp}$ can be evaluated by extrapolating $R_{\parallel}(H)$ and $R_{\perp}(H)$ to their minima with vanishing slopes, as can be seen in fig 2.20.

Giant MagnetoResistance (GMR)

The GMR effect only occurs in metallic systems of thin magnetic layers separated by nonmagnetic or antiferromagnetic thin films. The resistance of the multilayer systems is low for parallel aligned magnetizations of neighboring magnetic layers and vice versa. So the resistance of antiferromagnetically coupled multilayers can significantly be reduced by the application of an external magnetic field. The size of the effect is defined by

$$GMR = \frac{\rho_{ap} - \rho_p}{\rho_p} = \frac{\sigma_p}{\sigma_{ap}} - 1 \tag{2.40}$$

with $\rho_{p(ap)}$ the resistivity for parallel (antiparallel) aligned neighboring magnetizations and the corresponding equally defined specific conductance $\sigma_{p(ap)}$. The remarkable size of the effect in the pioneering work done by P. Grünberg and A. Fert of ≈ 80 % gave rise to the name "Giant" MR[Bina],[Baib].

Mott's spin channel model can again give us deeper insight into this behavior. The scattering cross section is different for parallel and antiparallel spin orientation with respect to the layer magnetization, thus $\rho^+ \neq \rho^-$. If one assumes only two parallel aligned magnetic layers and neglects the nonmagnetic interlayer, then the resistivity ρ_p is given by

$$\rho_p = \left(\frac{1}{2\rho^+} + \frac{1}{2\rho^-} \right)^{-1} = \frac{2\rho^+\rho^-}{\rho^+ + \rho^-}. \tag{2.41}$$

In the antiparallel case we get

$$\rho_{ap} = \left(\frac{1}{\rho^+ + \rho^-} + \frac{1}{\rho^- + \rho^+} \right)^{-1} = \frac{\rho^+ + \rho^-}{2}. \tag{2.42}$$

The evaluation of ρ_{ap}-ρ_p shows that the antiparallel case cannot have a lower resistivity than the parallel one. We can modify the GMR formula to

$$GMR = \frac{(\rho^+ - \rho^-)^2}{4\rho^+\rho^-} \tag{2.43}$$

and see the bigger the difference in the scattering cross sections between parallel and antiparallel case, the bigger the magnitude of the GMR effect. Until now we assumed a configuration of a current flowing perpendicular to the multilayer planes (CPP configuration) but many experiments make also use of the current in plane (CIP) configuration. The GMR effect is larger for CPP configuration as in the CIP, because in CPP each spin current has to travel through the whole stack while in CIP every single layer can shunt the effect. The configuration change from antiparallel oriented magnetic layers to parallel orientation caused by an external magnetic field is the characteristic of the GMR. Therefore the origin of the antiferromagnetic coupling in the beginning is not important and the spin dependent scattering that causes the GMR effect occurs only at the interfaces[Getz].

Colossal MagnetoResistance (CMR)

This effect was found in mixed valence Manganese oxides exhibiting Mn ions in various oxidation states and localized magnetic moments. With increasing external field the resistance gets smaller due to spin order effects. Adding for example Sr to $LaMnO_3$ results in a new compound with the oxidation states $La^{3+}_{1-x}Sr^{2+}_{x}Mn^{3+}_{1-x}Mn^{4+}_{x}O^{2-}_{3}$, thus the Mn valences Mn^{3+} and Mn^{4+} occur[Gros]. The electronic transport in this compound type can be explained as a hopping mechanism of the remaining and mobile 3d-electrons of the Mn^{3+} ions via the O^{2-} ions to neighboring Mn^{4+} ions. This changes the oxidation states of both Mn ions vice versa and the hopping can go on, leading to relatively high electron mobility.

Due to Hund's rule the remaining 3d-electrons at the Mn ions have parallel spins. Therefore hopping only occurs if the localized spins of neighboring Mn ions are parallel. Therefore the resistance decreases if an external field is applied and supports a ferromagnetic arrangement of neighboring Mn atoms[Getz].

Tunneling MagnetoResistance (TMR)

The situation here is somehow similar to the GMR, but the metallic spacer layer is now replaced by an insulator between both magnetic films. The thickness of the spacer is also restricted to dimensions where the quantum mechanical tunneling can occur. In this discussion we assume that the tunneling process is spin conserving.

Similar to the GMR effect the resistivity of a TMR stack is lower for parallel aligned magnetic layers than for antiparallel alignment. Contrary to GMR, where spin dependent scattering at the interfaces occurs TMR is a band structure effect relying on the spin resolved DOS at the Fermi energy. Julliere's model[Jull] assumes a spin conserving tunnel process and proportionality of $DOS^{\uparrow}$ and $DOS^{\downarrow}$ to the tunneling current. The current for parallel magnetization can be written as[Getz]

$$I^{\uparrow\uparrow} \propto n_1^{\uparrow} n_2^{\uparrow} + n_1^{\downarrow} n_2^{\downarrow} \tag{2.44}$$

and for antiparallel magnetization as

$$I^{\uparrow\downarrow} \propto n_1^{\uparrow} n_2^{\downarrow} + n_1^{\downarrow} n_2^{\uparrow} \tag{2.45}$$

with $n_i^{\uparrow\downarrow}$ being the $DOS^{\uparrow\downarrow}$ at electrode *i*. The number of majority electrons in electrode *i* is $a_i = (n_i^{\uparrow} / n_i^{\uparrow} + n_i^{\downarrow})$ and therefore the minority electrons are 1-a_i. This leads to a spin polarization P_i of

$$P_i = \frac{n_i^{\uparrow} - n_i^{\downarrow}}{n_i^{\uparrow} + n_i^{\downarrow}} = 2a_i - 1. \tag{2.46}$$

With this the differential conductance for parallel aligned magnetic layers can be written as

$$G^{\uparrow\uparrow} = G_p \propto a_1 a_2 + (1-a_1)(1-a_2) = \frac{1}{2}(1+P_1P_2) \tag{2.47}$$

and for the antiparallel case as

$$G^{\uparrow\downarrow} = G_{ap} \propto a_1(1-a_2) + (1-a_1)a_2 = \frac{1}{2}(1-P_1P_2). \tag{2.48}$$

The magnitude of the TMR can be defined as

$$TMR = \frac{G_p - G_{ap}}{G_{ap}} = \frac{R_{ap} - R_p}{R_p}. \tag{2.49}$$

Using the spin polarization *P* this equation can be expressed as

$$TMR = \frac{\Delta R}{R_p} = \frac{2P_1P_2}{1-P_1P_2}. \tag{2.50}$$

Additionally a junction magnetoresistance JMR can be defined by normalizing the two differential conductances to the parallel case:

$$JMR = \frac{G^{\uparrow\uparrow} - G^{\uparrow\downarrow}}{G^{\uparrow\uparrow}} = \frac{G_p - G_{ap}}{G_p} = \frac{R_{ap} - R_p}{R_{ap}} = \frac{\Delta R}{R_{ap}} = \frac{2P_1P_2}{1+P_1P_2}. \tag{2.51}$$

For 100 % spin polarized contacts the JMR reaches 100 % while the TMR diverges to infinity. This FM-I-FM setup can be used to determine the tunneling spin polarization of a specific material ($P_1 = P_2 = P$) if the conductance for parallel/antiparallel cases can be determined:

$$P = \sqrt{\frac{G_p - G_{ap}}{G_p + G_{ap}}}\,. \tag{2.52}$$

Using this further with one material of known polarization P_2 of a second one can be evaluated. The TMR significantly depends on temperature and bias voltage. Additionally the barrier is a very crucial component. Obviously its size and width change the TMR, but also its quality (e.g. impurity atoms, magnetic or not) has a big influence on the magnitude of the TMR[Getz].

Tunneling Anisotropic MagnetoResistance (TAMR)

As opposed to the normal TMR, the TAMR does not rely on the relative orientation of two ferromagnetic electrodes against each other, but strongly depends on the absolute magnetization direction within a ferromagnetic layer relative to the crystal orientation[Brey],[Goul],[Rüst],[Sait]. Therefore TAMR can be observed in tunnel stacks that contain only a single ferromagnetic layer, e.g. GaMnAs/Al_2O_3/Au[Goul] or Fe/GaAs/Au[Mose],[Lobe], and do not show a conventional TMR effect.

Brey et al. investigated the tunneling magnetoresistance in GaMnAs/GaAlAs/ GaMnAs tunnel junctions theoretically and foretold that, as a result of the strong spin-orbit interaction, the tunneling magnetoresistance should depend on the angle between the electrode magnetization and the current flow. The difference between in-plane and out-of-plane configurations was predicted by them to be 6 % at most. For in-plane rotation of the magnetization one can easily define the effect to be

$$TAMR_{[ref]} = \frac{R(\Phi) - R(ref)}{R(ref)} \tag{2.53}$$

where *(ref)* is the crystallographic direction taken as reference and $R(\Phi)$ is the tunneling resistance measured with magnetization at an angle Φ relative to *(ref)*. Gould et al.[Goul] were the first to demonstrate in-plane TAMR experimentally with a measured size of 2.7 %. The experiments typically show mild temperature dependence with decreased effects at higher temperatures. This dependence is extremely exaggerated at GaMnAs/GaAs/GaMnAs stacks investigated by Rüster est al.[Rüst]. The jump in effect size from few hundred percent at 4 K to exceptionally 150000 % at 1.7 K was attributed to the opening of an Efros-Shklovskii gap when crossing the metal-insulator transition. This investigation has been supported by results published from Pappert et al.[Papp].

Material System	TAMR [%]	Temperature [K]	Reference
(Ga,Mn)As/AlOx/Au	2.7 0	4.2 30	[Goul]
(Ga,Mn)As/AlOx/(Ga,Mn)As	150000 300	1.7 4.2	[Rüst]
(Ga,Mn)As/ZnSe/(Ga,Mn)As	10 8.5	2 20	[Sait]
Fe/GaAs/Au	0.4 0.3	4.2 100	[Mose] [Lobe]

Tab. 2.3: The achieved TAMR ratios of different groups depend clearly on the used material combinations and temperatures. All data is valid for vertical TAMR stacks. Quintessentially for TAMR is the fact that for single magnetic layers as well as for double layer stacks an effect is observable[Zuti].

2.4.4 Magnetic domains

At temperatures below the specific Curie point of a ferromagnetic material the permanent electronic magnetic moments are essentially parallel on microscopic scale. However, the whole ferromagnet typically exhibits its saturation moment only if an external magnetic field is applied. The reason is that a ferromagnet usually consists of many smaller regions in which the local magnetization is saturated, called domains. The magnetization direction prevailing in different domains needs not to be parallel to each other. Therefore the net magnetization of the ferromagnet itself is typically much smaller than the saturation magnetization and can even be zero. The domain structure maybe simple or very complex, but it has its origin always in the possibility of lowering the energy of a system by going from a saturated configuration with high magnetic energy to a domain configuration with lower energy. Landau and Lifshitz showed that domain structure is a natural consequence of the various contributions to the total energy of a ferromagnetic crystal, namely the exchange, anisotropy and magnetic energies[Land]. Single domain bodies form magnetic poles on their surfaces, what leads to very high magnetic energies. Increasing the number of domains lowers this energy term, in some configurations even domains of closure appear and no magnetic flux penetrates the crystal surface. Of course the number of domains cannot increase indefinitely, as the generation of a domain wall costs also a certain amount of energy. All effects combined lead to the resulting domain structure, which's exact form depends on temperature, ferromagnetic material, geometrical form of the crystal and magnetocrystalline anisotropy[Kitt].

2.5 (Ga,Mn)As, a ferromagnetic semiconductor

In the past there was a clear distinction between traditional ferromagnets (e.g. Fe or Ni) and semiconductors (e.g. GaAs). But in recent years a class of materials has arised that perfectly fits in this gap and brings both traditional physical fields together. The so-called Diluted Magnetic Semiconductors (DMS).

These are compounds where the cations of a host semiconductor AB are partly substituted by magnetic impurities M to get a ternary alloy $(A_{1-x}M_x)B$. These materials have attracted a lot of attention in the recent years, as one expects them to contribute to the field of spintronics in a major way[Zuti]. As DMSs are generated by "slightly" modifying standard semiconductors they have a major advantage over conventional ferromagnetic metals - the easy integration into existing semiconductor technology. Additionally the electric and magnetic characteristics can be easily changed by electrical fields[Ohno],[Chib],[Chi1].

As it was used exclusively in our work, we will focus on the GaAs-based GaMnAs, which is to date certainly the most studied DMS. The first who succeeded in the growth of ferromagnetic GaMnAs was H. Ohno in 1996[Ohn1], only some years after H. Munekata was the first one to fabricate ferromagnetic InMnAs in 1989[Mune].

2.5.1 Crystal structure

Since GaMnAs is based on a normal GaAs crystal (it can be seen after all as very heavily Mn doped GaAs) it has the same crystalline structure. Both materials crystallize in the so-called zinc-blende structure. This means that Ga as well as As build up their own face centered cubic (fcc) lattices that are displaced from each other by one quarter of a body diagonal. Each Ga atom is surrounded by four equally distant As atoms and vice versa (see figure 2.21).

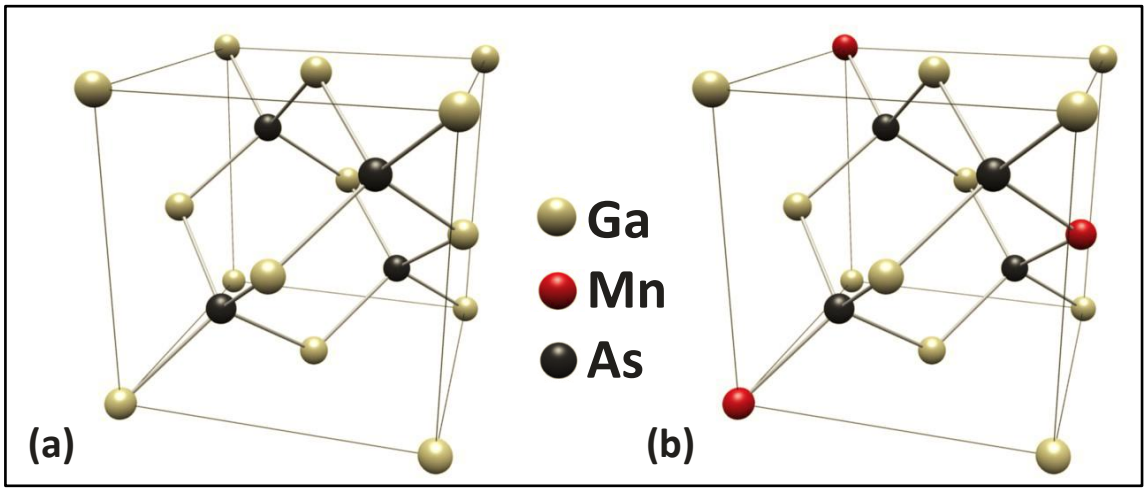

Fig. 2.21: The left side shows a normal zinc-blende GaAs lattice (a), while the right hand side depicts an ideal GaMnAs crystal lattice with Mn atoms only incorporated on substitutional Ga sites (b).

So, where do all the Mn atoms go? Ideally (meaning ideal for ferromagnetism and conductivity) Mn is incorporated into the lattice on Ga sites. This gives exactly one defect-electron per Mn atom, because of the electronic configuration of Ga and Mn (see table 2.4). This means that GaMnAs is a very highly p-doped material for typically used Mn concentrations (in standard material around 5 % of the Ga atoms are replaced by Mn atoms, which gives theoretically ideal hole densities of roughly $5 \times 10^{20}\,cm^{-3}$). So GaMnAs is extremely degenerately doped

and exhibits clearly metallic behavior with very good conductivity down to the lowest temperatures.

Material	Electronic configuration
Ga	[Ar] $3d^{10}$ $4s^2$ $4p^1$
Mn	[Ar] $3d^5$ $4s^2$
As	[Ar] $3d^{10}$ $4s^2$ $4p^3$

Tab. 2.4: The electronic configurations of Ga, Mn and As. One can easily see that the 3d shell of Mn is only filled by 5 electrons, which have unpaired spins according to Hund's rule. Contrary to the completely filled 3d shells of Ga and As this gives 5 times the Bohr Magneton per Mn atom.

However, the growth of GaMnAs is not as easy as the one of GaAs, because of the low solubility limit of the Mn impurities in the host crystal, which is in the range of 10^{18} cm^{-3}[Ohn3]. For ferromagnetic GaMnAs a concentration of at least 10^{19} cm^{-3} is needed, for metallic behavior even more. Under equilibrium growth conditions (roughly 600 °C substrate temperature) the incorporation of such high Mn concentrations into GaAs leads, due to the solubility limit, to the generation of an energetically much more stable phase, ferromagnetic MnAs[Ohn1]. It crystallizes in the hexagonal nickel arsenide structure and has T_C values of 313 K. Thus, a new technique had to be invented to overcome these problems. The solution was the introduction of non-equilibrium, low temperature molecular beam epitaxy (LT-MBE). A significant reduction of the substrate temperature T_S during growth (between 150 °C and 300 °C, dependent on the desired Mn concentration) was the key to suppress the formation of thermodynamically stable compounds such as MnAs and to realize a uniform alloy. Thereby, the substrate temperature is still sufficiently high to provide enough thermal energy for surface migration of the impinging atoms and thus to grow epitaxially on a convenient substrate. LT-MBE growth of GaMnAs usually proceeds in the following way. After the native oxide on the substrate surface has been removed thermally inside the MBE-chamber, a thin buffer layer of GaAs or AlGaAs is grown, which is typically between 100 and 400 nm thick[Awsc]. The growth temperature of this buffer is typical for GaAs, so roughly 600 °C. Additionally a GaAs/AlGaAs superlattice can be grown to further perfect the substrate surface. Before GaMnAs growth starts, the substrate temperature is reduced to around 250 °C and possibly a thin layer of low-temperature GaAs is grown. LT-GaAs has a lattice constant that is only a small nuance bigger than the one of normal GaAs and therefore can reduce the strain of the grown GaMnAs a little bit[Andr],[Look],[Liu1]. Now GaMnAs is grown by simultaneously opening the shutters of the Ga and the Mn effusion cells under As-stabilized conditions. The growth rate is roughly between 500 and 1200 nm/h[Awsc]. Although the reproducibility of the growth process is surely not as perfect as with standard GaAs growth, as long as the substrate temperature and furthermore the As overpressure are the same, the results are at least very similar. The incorporation of Mn atoms into the GaAs host crystal leads to a

changed lattice constant. Vegard's law describes the correlation between Mn concentration and the change of the lattice constant not satisfactory enough[Jung],[Rein], basically because the lattice constant is mainly governed by the incorporated lattice defects. These defects not only determine the size of the lattice constant but also are crucial for the magnetic and electronic properties of GaMnAs and will be discussed in the next chapter. Typically the lattice constant of GaMnAs is bigger than the one of GaAs and therefore GaMnAs grows with compressive strain[Ohn3]. If InGaAs is used as a substrate for the growth, its bigger lattice constant leads to GaMnAs with tensile strain[Liu].

2.5.2 Magnetic and Electronic properties

Let's assume now this ideal world scenario of the previous section really exists and all Mn atoms are incorporated only on Ga sites. The magnetic and electronic properties of GaMnAs are directly coupled to each other. Both of them depend strongly on the number of existing defect-electrons in the system. Each substitutional Mn_{Ga} atom provides one hole to the system and due to its electronic configuration possesses a spin moment of 5/2 and directly connected to it a magnetic moment of

$$\mu = \frac{5}{2}\frac{g_s \mu_B}{\hbar}, \tag{2.54}$$

where g_s is the Landé factor (here $g_s \approx 2$[Jung]) and μ_B is Bohr's magneton. If temperature is low enough (typically below 50 K to 150 K) and doping with Mn is high enough (more than 2 %) suddenly spontaneous magnetic ordering appears in the material. The crucial wave functions of the Mn atoms do not overlap in these doping regions (the 3d-shell is not involved in the crystal bonds) and therefore the ferromagnetism of GaMnAs can be described by the aforementioned indirect RKKY-interaction. The RKKY-Hamiltonian can be denoted as follows:

$$H^{RKKY} = -2\sum_{i \neq j} J_{ij}^{RKKY} \vec{S}_i \vec{S}_j, \tag{2.55}$$

with the exchange integral

$$J_{ij}^{RKKY} = -\frac{g_s^2 k_F^6}{E_F} \cdot \frac{\hbar^2 V^2}{P^2 (2\pi)^3} \cdot F(2k_F r_{ij}) \tag{2.56}$$

and the function

$$F(x) = \frac{sin(x) - x \cdot cos(x)}{x^4}. \tag{2.57}$$

We denote the Fermi wave vector by k_F, Planck's constant by $\hbar$, the volume by V, number of charge carriers by P and the distance between the Mn atoms at the positions i and j by r_{ij}. The exchange integral is depicted in figure 2.22.

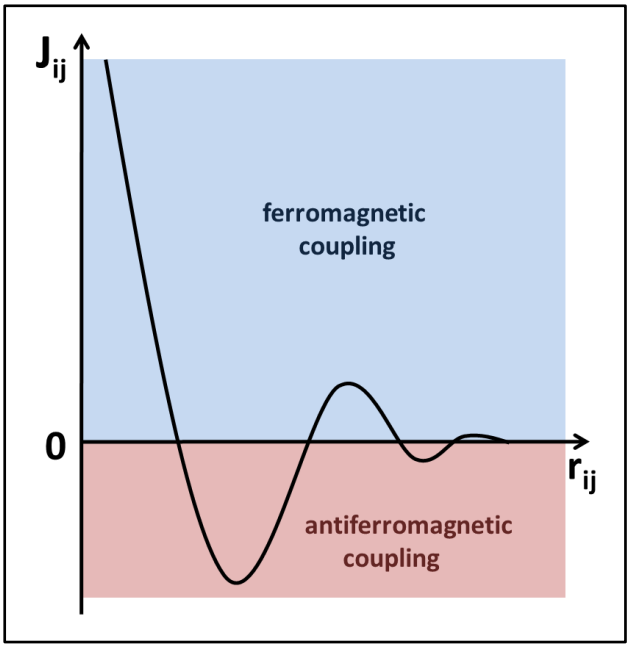

Fig. 2.22: The RKKY-interaction is in first approximation proportional to the exchange integral. If J_{ij} is positive the resulting coupling is ferromagnetic, while it is antiferromagnetic for negative J_{ij}. Typical Mn concentrations occurring in ferromagnetic GaMnAs lead to positive J_{ij}.

Dependent on the distance between two magnetic Mn atoms, its value can be either positive or negative. If we talk about small distances we have a positive region, as we have at typical Mn concentrations above 2 %. In a first approximation the RKKY-interaction goes cubic with the distance r_{ij} while the direct exchange interaction decays exponentially and thus much faster. In GaMnAs the interaction between Mn and an itinerant hole is antiferromagnetic. The hole interacts also antiferromagnetic with another Mn ion and thus the Mn ions are coupled ferromagnetically to each other.

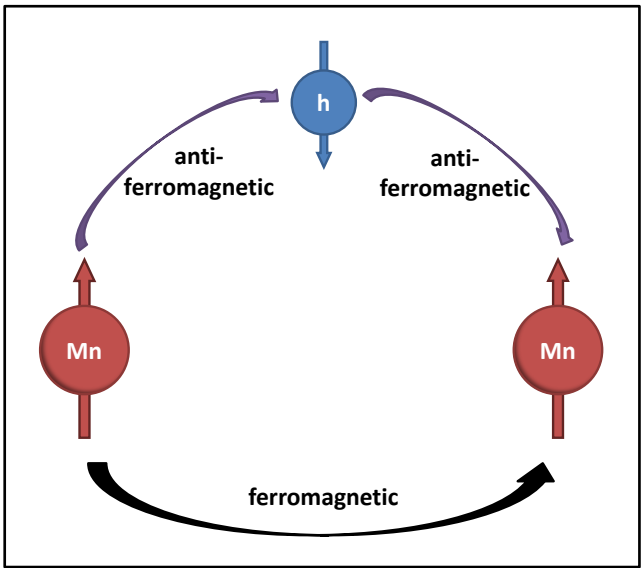

Fig. 2.23: The antiferromagnetic coupling between itinerant holes and Mn atoms leads to a ferromagnetic coupling among the Mn atoms themselves.

Within a molecular field theory it can be shown that the Curie temperature of GaMnAs is proportional to

$$T_C \sim x_{eff} p^{1/3}. \tag{2.58}$$

This means increasing the Curie temperature can be done by increasing the effective Mn concentration x_{eff} (effective means substitutional Mn_{Ga} minus unwanted Mn positions) and the charge carrier concentration p. This simple prediction describes the experimental data quite well[Jun1]. Meanwhile it is possible to grow GaMnAs layers with $T_C \approx 180$ K.

The magnetic anisotropy of GaMnAs is significantly governed by growth-related strain. Compressive strain, which occurs while growth on [001] GaAs substrates, leads to two easy axes in-plane, in [100] and [010] directions[Welp]. If GaMnAs is grown on InGaAs, which has a slightly bigger lattice constant, tensile strain leads to an easy out-of-plane axis alongside [001] direction[Mats],[Ohn3].

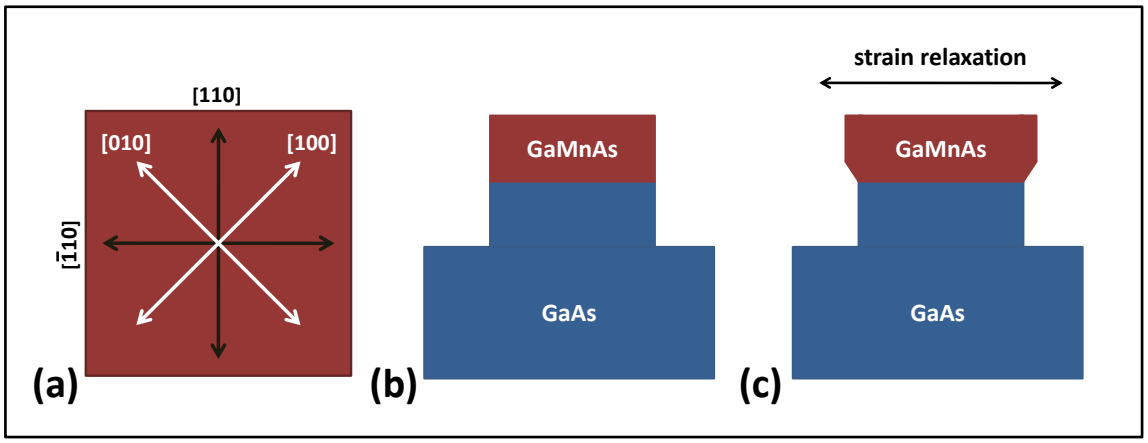

Fig. 2.24: (a) The easy axes of GaMnAs when grown on GaAs are shown in white. Black arrows give the hard axes and are at the same time the preferential breaking directions of the crystal. (b) Sideview of an etched structure that can relax (c) into its own lattice constant after the etching process[Weni].

In regular ferromagnets like Fe or Co, it is possible to design structures with the easy axes in any desired direction by the help of shape anisotropy. In GaMnAs this is not possible due to its very low magnetization and corresponding small stray field anisotropy. Despite this fact, it is still possible to get some kind of shape anisotropy in GaMnAs. Producing very small GaMnAs structures with one side laterally confined below 1 µm leads to a lattice relaxation in this direction. This has been shown by X-Ray diffraction[Weni] and combined ferromagnetic resonance as well as time-resolved Kerr microscopy techniques[Hoff]. If the structure now is long enough in one dimension and narrow enough in the other, this leads to a uniaxial behavior.

Despite intensive theoretical as well as experimental research the form of the band structure of GaMnAs is still not known exactly[Diet]. There exist optical absorption measurements that suggest a so-called impurity band[Burc] in

GaMnAs while other measurements imply a Fermi energy level in the valence band, at least at Mn concentrations above 2 %[Jun2].

As one can easily see, all the magnetic and electric properties depend on the Mn content in GaMnAs. However, the effective Mn concentration that can greatly differ from the nominal concentration due to defects during the crystal growth is the critical parameter. Therefore we give an overview of the most important growth-related defects in GaMnAs.

As antisites (As_{Ga})

As atoms that are incorporated on Ga lattice sites act as deep double donors. Because of the low temperature growth in the range of roughly 250 °C the density of these defects can reach numbers up to 10^{20} cm^{-3}[Avru] and therefore compensate the same amount of holes donated to the system by the good Mn_{Ga} [Myer]. Post-growth annealing at temperatures above 450 °C leads to vanishing As antisites, but would build up MnAs clusters and destroy the GaMnAs crystal structure. So the growth conditions have to be optimized to prevent the formation of these defects.

Mn interstitials (Mn_I)

The zinc-blende lattice allows for several different interstitial positions, meaning positions between the regular Ga and As sites[Glas], which all have relatively low binding energies[Maše]. Typically the interstitials in GaMnAs act as double donors and additionally couple antiferromagnetically to the good Mn_{Ga}.

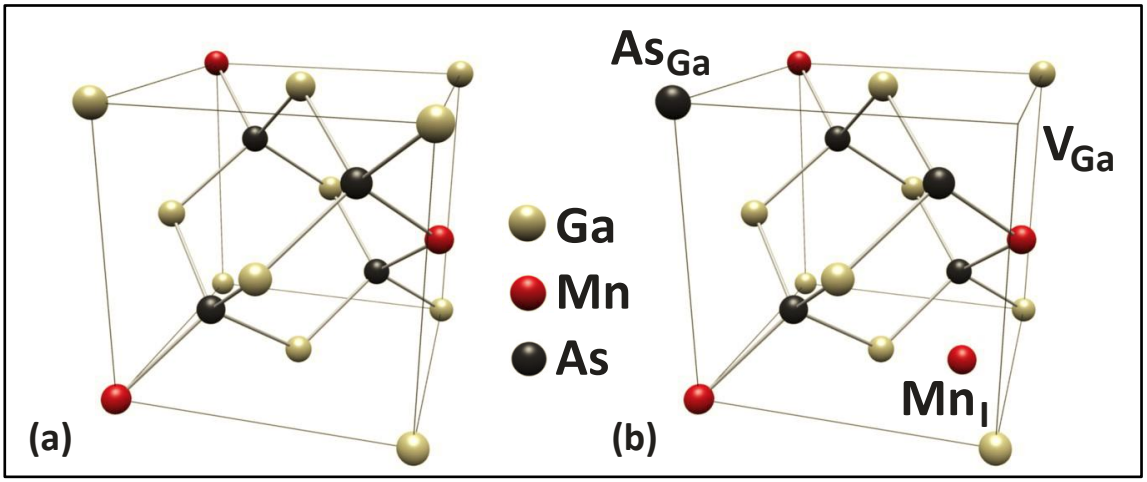

Fig. 2.25: (a) A desired perfect GaMnAs lattice. (b) A more realistic GaMnAs crystal in the as-grown state. Mn is not only incorporated on Ga sites, but also in a significant amount at interstitial positions. Due to the low-temperature-growth also Ga vacancies and As antisites may be built up.

This reduces the ferromagnetic coupling in GaMnAs by diminishing the ferromagnetic interaction mediating holes as well as by adding an antiferromagnetic component. The good thing about the interstitials is that due to their weak binding they can be removed from the crystal by post-growth annealing. The temperatures for that process typically are around 200 °C and

therefore do not destroy the GaMnAs lattice. The interstitials diffuse to the surface in that process and are there passivated by the oxygen of the air. This leads to an amorphous manganese oxide layer at the surface of GaMnAs[Adel],[Edmo].

Mn-Mn and Mn-As clusters

Both, the Mn-Mn as well as the Mn-As clusters, reduce the effective Mn concentration of GaMnAs and therefore the charge carrier density. Hence this results in reduced exchange interaction and therefore reduced Curie temperature[Wurs].

Vacancies (V_{Ga})

If no atom sits on a Ga site, this is called a Ga vacancy. With an approximate concentration of roughly 10^{18} cm^{-3}[Raeb] this is a defect of secondary importance.

3 Spin Theory

In this section we introduce the standard formalism of spin injection theory. Generally a ferromagnetic electrode is used as a spin-aligner contact and spins are injected into a nonmagnetic conductor. In our work GaMnAs and n-doped GaAs take the place of the ferromagnetic contact and the nonmagnetic conductor, respectively. If not otherwise mentioned, we follow the path of [Fabi], where a simplified approach is considered, by focusing on situations where the spins travel mainly in one dimension. To be able of giving a thorough overview, we present the necessary background related to particle drift, diffusion, chemical potentials and charge transport. For spin-transport the additional parameters spin current, spin accumulation, spin relaxation and spin dynamics are introduced. As this work is not intended to be a theoretical work on spin phenomena, for a complete overview on this topic the interested reader is referred to [Fabi], [Fab1], [Fert], [Fer1], [Hers], [Rash], [Ras1], [Schm], [Vale], [Vign], [vSon] and [Zut1].

3.1 Particle drift and diffusion

Consider electrons that are moving basically in one direction, which is defined by the conducting channel. Electrons that move in a diffusive material undergo some kind of random walk. For a specific time τ (the momentum relaxation time) they move a distance l (the mean free path) with a velocity v until they are scattered off impurities or phonons.

$$\tau = \frac{l}{v} \tag{3.1}$$

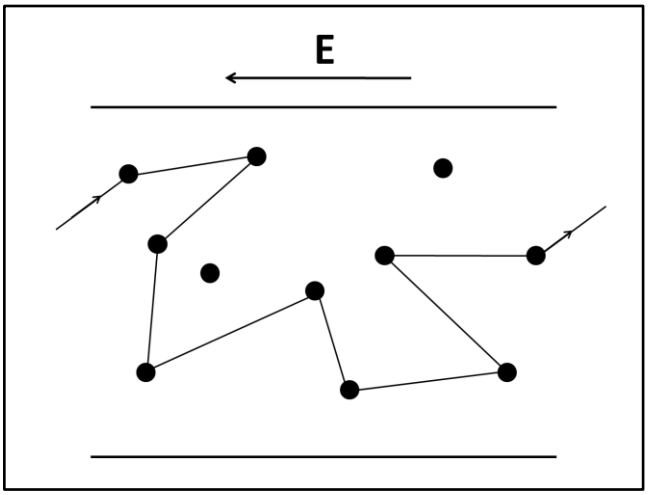

Fig. 3.1: Illustrative picture of the drift-diffusive transport of electrons in a disordered semiconductor with small applied electric field. Scattering events cause the electrons to change their original moving direction while the applied external electric field forces them eventually in one direction.

If we apply a small electric field E that is too weak to significantly change velocity v the electrons undergo a biased random walk. Therefore the electric field E has to fulfill the condition

$$|\Delta v| = \left|\frac{eE\tau}{m}\right| \ll v, \tag{3.2}$$

with e is the electronic charge and m is the electron mass. This is already a good first approximation for one dimensional drift-diffusive transport of electrons in a semiconductor if an external electric field is present (see fig. 3.1). If one is interested in the average macroscopic electronic velocity v_{av}, which is substantially different from the microscopic one v, one can use the simple formula

$$\dot{v}_{av} = -\frac{eE}{m} - \frac{v_{av}}{\tau}. \tag{3.3}$$

Here the last term describes frictional scattering effects. v_{av} is called the drift velocity v_d if we are looking to a steady state regime, where of course the time derivative of v_{av} equals zero. Then equation (3.3) reads as follows:

$$v_d = -\frac{e\tau}{m}E. \tag{3.4}$$

The requirement of a biased random walk is fulfilled, if one thinks of the typical values of v_d, of roughly 1 cm/sec and v_{Fermi} that is several orders of magnitude higher in doped semiconductors, considering that Δv and v_d are of the same size.

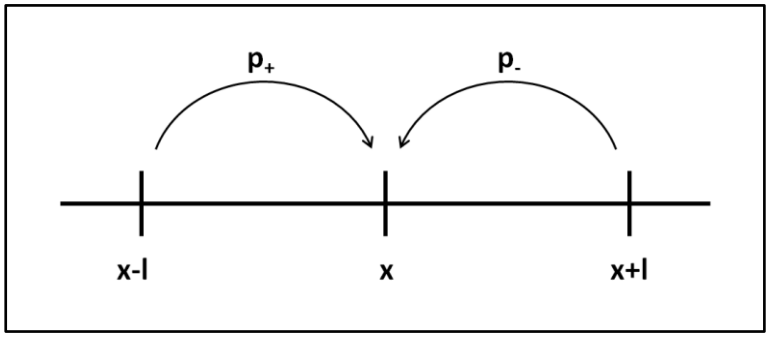

Fig. 3.2: The probabilities of moving left (p_-) and right (p_+) represent the biased random walk in our simple model. The size of each step is l and the time step is τ.

Now we analyze time evolution of the spatial profile of the electron density in our model. We consider N_0 electrons and make the simplifying assumption of number retention (not necessarily given in semiconductors). If the density at time t and position x is $n(x,t)$, these conditions make the normalization equation

$$N_0 = \int_{-\infty}^{+\infty} n(x,t)dx \tag{3.5}$$

valid at all times. If one looks at fig. 3.2 it becomes clear, that the density of electrons at position x at time t is determined by the electron densities at positions $x-l$ and $x+l$ one time step before. Assuming that p_+ and p_- are the

probabilities of electrons moving to the right or to the left and $p_+ + p_- = 1$ the following balance equation holds:

$$n(x,t) = n(x-l, t-\tau)p_+ + n(x+l, t-\tau)p_-. \tag{3.6}$$

In our biased case the probabilities p_+ and p_- are differing from each other (contrary to the case of unbiased random walk where they would both be equal to 0.5). The difference is denoted as $\Delta p = p_+ - p_-$. Expanding the right-hand side of equation (3.6) into a Taylor series around (x,t) for infinitesimal l and τ, and keeping terms up to the orders of l^2 and τ one gets:

$$n(x,t) = n(x,t) - l\Delta p\frac{\partial n(x,t)}{\partial x} + \frac{1}{2}l^2\frac{\partial^2 n(x,t)}{\partial x^2} - \tau\frac{\partial n(x,t)}{\partial t}. \tag{3.7}$$

This gives us directly that

$$\tau\frac{\partial n(x,t)}{\partial t} = \frac{1}{2}l^2\frac{\partial^2 n(x,t)}{\partial x^2} - l\Delta p\frac{\partial n(x,t)}{\partial x}. \tag{3.8}$$

We introduce the diffusion coefficient, which is defined as

$$D = \frac{1}{2}\frac{l^2}{\tau} = \frac{1}{2}v^2\tau. \tag{3.9}$$

D describes the rate of electron diffusion; its units are m^2s^{-1}. If we use the interpretation of

$$\frac{l}{\tau}\Delta p = v\Delta p = v_d$$

we can get to the drift-diffusion partial differential equation, which describes the time evolution of the electron density profile n:

$$\frac{\partial n(x,t)}{\partial t} = D\frac{\partial^2 n(x,t)}{\partial x^2} - v_d\frac{\partial n(x,t)}{\partial x} \tag{3.10}$$

The nomenclature drift-diffusion equation can be justified by looking into the physical behavior. By using the average electron position in the form of

$$\bar{x}(t) = \frac{1}{N_0}\int_{-\infty}^{+\infty} x n(x,t)dx \tag{3.11}$$

it can be shown that

$$\dot{\bar{x}}(t) = v_d. \tag{3.12}$$

Thus, the average position of the electron density moves with the drift velocity v_d. Furthermore can be shown that the variance of the density evolves linearly with time, as proof of diffusion:

$$\sigma^2 = \overline{x^2} - (\bar{x})^2 = 2Dt. \tag{3.13}$$

The standard deviation of the average electron position is then of course

$$\sigma = \sqrt{2Dt}. \tag{3.14}$$

Considering that the number of steps is $N=t/\tau$ and $D = l^2/2\tau$ this conforms to the fact that usually the variance after N steps in random walks behaves like

$$\sigma^2 = 2Dt = 2 \cdot \frac{l^2}{2\tau} \cdot N\tau = l^2 N. \tag{3.15}$$

So the time evolution of the electron density shows a constant drift due to the accelerating electric field and the decelerating frictional scattering effects, which balance each other out in steady state regimes. Additionally one can see diffusion as well, due to thermal movement and the scattering alone. Solving the diffusion equation (i.e. simply the drift-diffusion equation with v_d set to zero) with the initial condition $n(x,0) = N_0\delta(x)$ leads us to the result

$$n(x,t) = \frac{N_0}{\sqrt{4\pi Dt}} e^{-\frac{x^2}{4Dt}}. \tag{3.16}$$

The form of the solution is that of the normal Gaussian probability distribution with variance $\sigma^2 = 2Dt$. The electric field enters only through the drift velocity v_d, which we have found to be proportional to E in our simple model:

$$v_d = -\frac{e\tau}{m} E. \tag{3.17}$$

We define the proportionality coefficient by the following equation:

$$\mu = \frac{e\tau}{m}. \tag{3.18}$$

The units of μ are m^2/Vs. With the help of the diffusion and mobility coefficients we can now rewrite the drift-diffusion equation in the following form:

$$\frac{\partial n}{\partial t} + \frac{\partial}{\partial x}\left[-\mu n E - D\frac{\partial n}{\partial x} \right] = 0. \tag{3.19}$$

The expression in the brackets can be identified as the electron particle current J,

$$J = -\mu n E - D\frac{\partial n}{\partial x} \tag{3.20}$$

where the first term again describes drift and the second one represents the diffusion. One can multiply the particle current with the electronic charge e and define this way the electrical charge current j:

$$j = -eJ = \sigma E + eD\frac{\partial n}{\partial x}. \tag{3.21}$$

Here $\sigma = e\mu n = 1/\rho$ was used, which is called the conductivity and is equal to the inverse resistivity. One can now put everything together and gets with

$$\frac{\partial n}{\partial t}+\frac{\partial J}{\partial x}=0 \tag{3.22}$$

the continuity equation, expressing conservation of particles. Particles can only accumulate in a certain volume if more current is flowing into that area than out of it. This treatment basically goes back to the Drude theory of metallic conduction released back in 1900[Drud].

3.2 Spin drift and diffusion

At this point we have to consider spin dependent effects in our theory. Again the total number of electrons is constant as in the previous chapter. However from now on one can distinguish between two different electron species, spin up and spin down. The total particle density is the sum of the spin-up and spin-down densities

$$n=n_{\uparrow}+n_{\downarrow}, \tag{3.23}$$

while the spin density is the difference of up and down densities

$$s=n_{\uparrow}-n_{\downarrow}. \tag{3.24}$$

Now that we have spin-up and spin-down electrons that undergo a random walk, things are getting slightly more complicated of course. We have to find a similar drift-diffusion equation for *s* as we did for *n* before. If a spin-up electron is scattered on a defect there is the possibility of its spin being flipped to a down-spin. This probability we call ω. Now we can define the spin flip rate by ω/τ. Fig. 3.3 briefly recapitulates the just said.

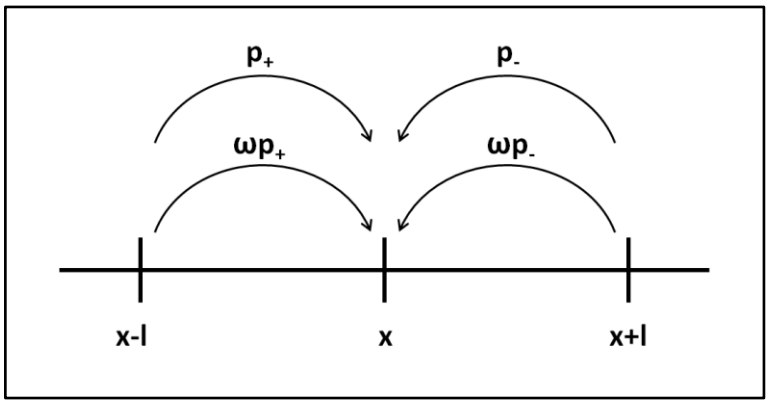

Fig. 3.3: Simple one dimensional random walk model with different spin species. The probability ω is introduced to account for spin flip processes during scattering events.

In fact $\omega << 1$ holds for conduction electrons. They have to be scattered thousands of times to lose their spin information[Dzhi]. We can again write the balance equation for spin-up and down densities and make the Taylor expansions around *(x,t)* as before. For spin up we get:

$$\begin{aligned} n_\uparrow(x,t) &= n_\uparrow(x-l,t-\tau)(1-\omega)p_+ + n_\uparrow(x+l,t-\tau)(1-\omega)p_- \\ &\quad + n_\downarrow(x-l,t-\tau)\omega p_+ + n_\downarrow(x+l,t-\tau)\omega p_- \\ &\overset{Taylor}{\approx} n_\uparrow(1-\omega) - l\frac{\partial n_\uparrow}{\partial x}\Delta p + \frac{1}{2}l^2\frac{\partial^2 n_\uparrow}{\partial x^2} - \tau\frac{\partial n_\uparrow}{\partial t} + n_\downarrow\omega. \end{aligned} \tag{3.25}$$

Analogous operations can be performed for $n_\downarrow$. This again leads to the drift-diffusion equations:

$$\frac{\partial n_\uparrow}{\partial t} = D\frac{\partial^2 n_\uparrow}{\partial x^2} - v_d\frac{\partial n_\uparrow}{\partial x} - \omega(n_\uparrow - n_\downarrow), \tag{3.26}$$

$$\frac{\partial n_\downarrow}{\partial t} = D\frac{\partial^2 n_\downarrow}{\partial x^2} - v_d\frac{\partial n_\downarrow}{\partial x} - \omega(n_\downarrow - n_\uparrow). \tag{3.27}$$

Adding these two equations gives us the previously encountered equation (3.10), but subtracting (3.26) and (3.27) will lead to the desired drift diffusion equation for the spin density *s*:

$$\frac{\partial s}{\partial t} = D\frac{\partial^2 s}{\partial x^2} - v_d\frac{\partial s}{\partial x} - \frac{s}{\tau_s}. \tag{3.28}$$

Here τ_s is the spin relaxation time. One has to take into account that spin relaxation is twice as large as spin flip, because each spin flip accounts for relaxation of both spin species and due to that spin relaxation happens twice as fast. So in this case

$$\frac{1}{\tau_s} = \frac{2\omega}{\tau} \tag{3.29}$$

correctly describes the spin relaxation. One can write the drift-diffusion equation again in terms of mobility and gets

$$\frac{\partial s}{\partial t} = D\frac{\partial^2 s}{\partial x^2} + \mu E\frac{\partial s}{\partial x} - \frac{s}{\tau_s}, \tag{3.30}$$

which can be written again in the form of a continuity equation

$$\frac{\partial s}{\partial t} + \frac{\partial}{\partial x}\left(-\mu E s - D\frac{\partial s}{\partial x}\right) = -\frac{s}{\tau_s}. \tag{3.31}$$

Analogously to equation (3.19) the expression within the brackets can be identified as the spin particle current

$$J_s = -\mu E s - D\frac{\partial s}{\partial x} \tag{3.32}$$

and so one can write the spin continuity equation as

$$\frac{\partial s}{\partial t} + \frac{\partial J_s}{\partial x} = -\frac{s}{\tau_s}. \tag{3.33}$$

Contrary to the particle continuity equation (3.22) the spin at a given place can not only be changed by a spin current flowing into or away from that area, but also by spin relaxation. Obviously the right hand side of the equation represents the spin relaxation rate. Analogously to above one can introduce now a spin charge current by defining

$$j_s = -eJ_s = \sigma_s E + eD\frac{\partial s}{\partial x}, \tag{3.34}$$

where the spin conductivity is defined by

$$\sigma_s = e\mu s. \tag{3.35}$$

We also define two polarizations, namely the density spin polarization P_n as

$$P_n = \frac{n_\uparrow - n_\downarrow}{n} = \frac{s}{n} \tag{3.36}$$

and the current spin polarization P_j as

$$P_j = \frac{j_\uparrow - j_\downarrow}{j} = \frac{j_s}{j}. \tag{3.37}$$

3.3 Quasichemical Potentials μ and μ_s

The density n_0 of a Fermi gas in equilibrium is determined by the chemical potential η. If one postulates the minimum band energy to be $\varepsilon = 0$, the electron density can be expressed (keeping the spin degeneracy in mind) by

$$\begin{aligned} n_0 &= 2\frac{1}{V}\sum_k f_0(\varepsilon_k - \eta) = 2\frac{1}{V}\frac{V}{(2\pi)^3}\int d^3k f_0(\varepsilon_k - \eta) \\ &= \int_0^\infty d\varepsilon f_0(\varepsilon - \eta)\frac{2}{(2\pi)^3}\int d^3k\,\delta(\eta - \varepsilon_k) = \int_0^\infty d\varepsilon g(\varepsilon) f_0(\varepsilon - \eta). \end{aligned} \tag{3.38}$$

Thereby f_0 is the Fermi-Dirac distribution function given by

$$f_0(\varepsilon - \eta) = [\exp((\varepsilon - \eta)/k_B T) + 1]^{-1} \tag{3.39}$$

and $g(\varepsilon)$ expresses the density of states per unit volume

$$g(\varepsilon) = \frac{2}{(2\pi)^3}\int d^3k\,\delta(\varepsilon - \varepsilon_k). \tag{3.40}$$

$\varepsilon_F \approx \eta$ holds for a degenerate Fermi gas and the Fermi-Dirac distribution looks like the ordinary step function

$$\begin{aligned} f_0(\varepsilon - \eta) &\approx \Theta(\eta - \varepsilon), \\ -\frac{\partial f}{\partial \varepsilon} = \frac{\partial f}{\partial \eta} &\approx \delta(\varepsilon - \eta). \end{aligned} \tag{3.41}$$

As $\varepsilon >> \eta + k_B T$ holds for a nondegenerate Fermi gas, the Fermi-Dirac distribution passes into the form of Maxwell-Boltzmann statistics

$$f_0(\varepsilon-\eta)\approx exp(-(\varepsilon-\eta)/k_BT). \tag{3.42}$$

So generally we can state that for the functional form of n_0 applies

$$n_0 = n_0(\eta). \tag{3.43}$$

Now we generalize the above situation to a very slight nonequilibrium. Assume a static electric field $E = -\nabla\Phi$ in our conductor but still no current flow. The system itself stays at equilibrium. This is of course not possible in metals, but in doped semiconducting material, for sure. The chemical potential is constant, as we're in equilibrium, but how does the electron density change? Solely the electron's energy changes, this is expressed by the Fermi-Dirac distribution. The band states ε are occupied by the electrons with the density of states $g(\varepsilon)$ but the total electron energy now is $\varepsilon - e\Phi$

$$n(\vec{r}) = \int_0^\infty d\varepsilon g(\varepsilon) f_0(\varepsilon - e\Phi - \eta), \tag{3.44}$$

what can be abbreviated as

$$n(\vec{r}) = n_0(\eta + e\Phi). \tag{3.45}$$

This functional form has a very important consequence:

$$j = \sigma E + eD\nabla n = -\sigma\nabla\Phi + eD\frac{\partial n_0}{\partial\eta}e\nabla\Phi = \nabla\Phi\left(-\sigma + e^2D\frac{\partial n_0}{\partial\eta}\right). \tag{3.46}$$

As the electric current has to disappear in equilibrium, this implies

$$\sigma = e^2D\frac{\partial n_0}{\partial\eta}. \tag{3.47}$$

This is a fluctuation-dissipation relation[Marc], namely the general form of Einstein's relation[Eins],[Smol]. This type of equations describes the linear relationships between fluctuation (here the diffusivity D) and dissipation strengths (in this case the conductivity σ).
Allowing a current flow means that the chemical potential is not constant any more. Most often we can nevertheless assume that the nonequilibrium electron distribution function f will depend on the electron state only through its energy and not its momentum[Fabi]. This temporal coarse graining allows us to write in the momentum space

$$f_k \approx f(\varepsilon_k) = f_0(\varepsilon_k - e\Phi - \eta - e\mu), \tag{3.48}$$

with $\mu = \mu(x)$ being a spatially dependent addition to the chemical potential. μ is often called quasichemical potential. Therefore we can now try to make the transformation

$$\eta \to \eta + e\mu(x) \tag{3.49}$$

and this leads to the position dependent electron density

$$n(x) = n_0(\eta + e\mu + e\Phi). \tag{3.50}$$

The current can be expressed therewith as

$$j = -\sigma\nabla\Phi + eD\nabla n = \nabla\Phi\left(-\sigma + e^2 D\frac{\partial n_0}{\partial \eta}\right) + e^2 D\frac{\partial n_0}{\partial \eta}\nabla\mu. \tag{3.51}$$

If we now make use of Einstein's relation we can finally write

$$j = \sigma\nabla\mu. \tag{3.52}$$

This means that the gradient of the quasichemical potential drives the current through the system and both drift and diffusion terms are described by it. This specific formulation greatly simplifies the problem of electrical spin injection.

In ferromagnetic conductors the difference between the densities of states at the Fermi level ($g_\uparrow$ and $g_\downarrow$) as well as the Fermi velocities for both spin species ($v_{F\uparrow}$ and $v_{F\downarrow}$) is essential. These deviations lead to the spread in relaxation times, mean free paths as well as in mobilities, diffusivities and conductivities. If one allows also the quasichemical potential to be spin dependent, then we can write

$$j_\uparrow = \sigma_\uparrow\nabla\mu_\uparrow, \tag{3.53}$$

$$j_\downarrow = \sigma_\downarrow\nabla\mu_\downarrow. \tag{3.54}$$

We additionally define now for simplicity the following:

$$g = g_\uparrow + g_\downarrow, \quad g_s = g_\uparrow - g_\downarrow \tag{3.55}$$

$$\sigma = \sigma_\uparrow + \sigma_\downarrow, \quad \sigma_s = \sigma_\uparrow - \sigma_\downarrow \tag{3.56}$$

$$\mu = \frac{1}{2}(\mu_\uparrow + \mu_\downarrow), \quad \mu_s = \frac{1}{2}(\mu_\uparrow - \mu_\downarrow) \tag{3.57}$$

$$D = \frac{1}{2}(D_\uparrow + D_\downarrow), \quad D_s = \frac{1}{2}(D_\uparrow - D_\downarrow). \tag{3.58}$$

These definitions let us write the charge and spin currents in the following way:

$$j = j_\uparrow + j_\downarrow = \sigma\nabla\mu + \sigma_s\nabla\mu_s \tag{3.59}$$

$$j_s = j_\uparrow - j_\downarrow = \sigma_s\nabla\mu + \sigma\nabla\mu_s. \tag{3.60}$$

This directly shows that in a ferromagnetic material an applied bias leads to a spin current and a nonequilibrium spin gradient lets a charge current flow, just because $\sigma_s \neq 0$. We now can write

$$n_\uparrow = n_{\uparrow 0}(\eta + e\mu_\uparrow + e\Phi) \approx n_{\uparrow 0} + \frac{\partial n_{\uparrow 0}}{\partial \eta}(e\mu_\uparrow + e\Phi), \tag{3.61}$$

$$n_\downarrow = n_{\downarrow 0}(\eta + e\mu_\downarrow + e\Phi) \approx n_{\downarrow 0} + \frac{\partial n_{\downarrow 0}}{\partial \eta}(e\mu_\downarrow + e\Phi). \tag{3.62}$$

Using the correlation

$$\frac{\partial n_{\uparrow 0}}{\partial \eta} = g_\uparrow \tag{3.63}$$

and

$$\frac{\partial n_{\downarrow 0}}{\partial \eta} = g_{\downarrow}, \tag{3.64}$$

we get

$$n_{\uparrow} = n_{\uparrow 0} + g_{\uparrow} e\mu_{\uparrow} + g_{\uparrow} e\Phi, \tag{3.65}$$

and

$$n_{\downarrow} = n_{\downarrow 0} + g_{\downarrow} e\mu_{\downarrow} + g_{\downarrow} e\Phi. \tag{3.66}$$

The sum of equations (3.65) and (3.66) gives us the electron density by

$$n = n_{\uparrow} + n_{\downarrow} = n_0 + eg(\mu + \Phi) + eg_s\mu_s. \tag{3.67}$$

From now on we assume local charge neutrality, namely $n = n_0$, which eliminates the electrical potential from the equation by connecting it to the quasichemical potentials:

$$g(\mu + \Phi) + g_s\mu_s = 0. \tag{3.68}$$

In a nonmagnetic conductor $g_S = 0$ and we get automatically $\mu = -\Phi$, the most obvious condition for charge neutrality. We can now look at the spin density and get

$$s = s_0 + eg_s(\mu + \Phi) + eg\mu_s = s_0 + 4e\mu_s \frac{g_{\uparrow} g_{\downarrow}}{g}. \tag{3.69}$$

Consequently we now have

$$\delta s = s - s_0 = 4e\mu_s \frac{g_{\uparrow} g_{\downarrow}}{g} \tag{3.70}$$

for the nonequilibrium spin density δs, which is proportional to the spin quasichemical potential μ_S. We call μ_S the spin accumulation. In the case of a nonmagnetic conductor we get the number of electron states in the interval of $e\mu_S$ at the Fermi level by $\delta s = s = e\mu_S g$.

Subsequently we will concentrate on the current spin polarization $P_j = j_S/j$, contrary to the density spin polarization $P_n = s/n$ and the conductivity spin polarization $P_\sigma = \sigma_S/\sigma$. A simple transformation of equation (3.59) gives us

$$\nabla\mu = \frac{1}{\sigma}(j - \sigma_s \nabla\mu_s). \tag{3.71}$$

Substituting this into (3.60) brings us to the following:

$$j_S = \sigma_S \nabla\mu + \sigma\nabla\mu_S = P_\sigma j + 4\nabla\mu_S \frac{\sigma_{\uparrow}\sigma_{\downarrow}}{\sigma}. \tag{3.72}$$

This leads us to the equation for the current spin polarization:

$$P_j = P_\sigma + \frac{1}{j} 4\nabla\mu_s \frac{\sigma_{\uparrow}\sigma_{\downarrow}}{\sigma}. \tag{3.73}$$

This shows that a large gradient in the spin quasichemical potential is essential for significantly high values of the current spin polarization.
Remember the spin continuity equation (3.33) we derived earlier in a steady state regime reads as

$$\nabla j_s = e\frac{s}{\tau_s}. \tag{3.74}$$

This describes the nonequilibrium spin s in a normal conductor. A valid discussion of ferromagnets needs a small modification:

$$\nabla j_s = e\frac{\delta s}{\tau_s}. \tag{3.75}$$

This describes the decay of the nonequilibrium spin density δs in the ferromagnet. This can be further transformed to

$$\nabla j_s = e\frac{\delta s}{\tau_s} = 4e^2\mu_s\frac{g_\uparrow g_\downarrow}{g}\frac{1}{\tau_s} = \nabla\left(P_\sigma j + \nabla\mu_s\frac{4\sigma_\uparrow\sigma_\downarrow}{\sigma}\right) = 4\frac{\sigma_\uparrow\sigma_\downarrow}{\sigma}\nabla^2\mu_s. \tag{3.76}$$

We used equation (3.70) and the continuity of the electric current in steady state regimes for it. This gives us the desired diffusion equation for μ_S:

$$\nabla^2\mu_s = \frac{\mu_s}{L_s^2}, \tag{3.77}$$

where the generalized diffusivity

$$\bar{D} = \frac{g}{g_\uparrow/D_\downarrow + g_\downarrow/D_\uparrow} \tag{3.78}$$

is used to define the generalized spin diffusion length L_s by

$$L_s = \sqrt{\bar{D}\tau_s}. \tag{3.79}$$

In a normal conductor the diffusivity and the generalized diffusivity are equal. In this formalism L_s is a phenomenological parameter.

3.4 Standard model of spin injection: F/N junctions

This so-called standard model bases originally on proposals of Aronov made in 1976[Aron]. The thermodynamics and a Boltzmann like transport model for spin injection have been developed by Johnson and Silsbee in 1987[Joh1] and 1988[Joh2]. The theory of spin injection has been further developed by many other groups (see introduction of chapter 3). The following bases originally on treatments of Rashba[Rash],[Ras1] using the notation from Žutić et al.[Zuti].

Fig. 3.4 shows the underlying scheme behind the spin injection geometry. The ferromagnetic region F is connected to the nonmagnetic conductor N through the infinitesimal contact region C. We assume the ferromagnetic as well as the nonmagnetic conductors to be much longer than the corresponding spin

diffusion lengths. We are interested in the current spin polarization $P_j(0)$, because it determines the spin accumulation $\mu_{sN}(0)$ in the nonmagnetic semiconductor.

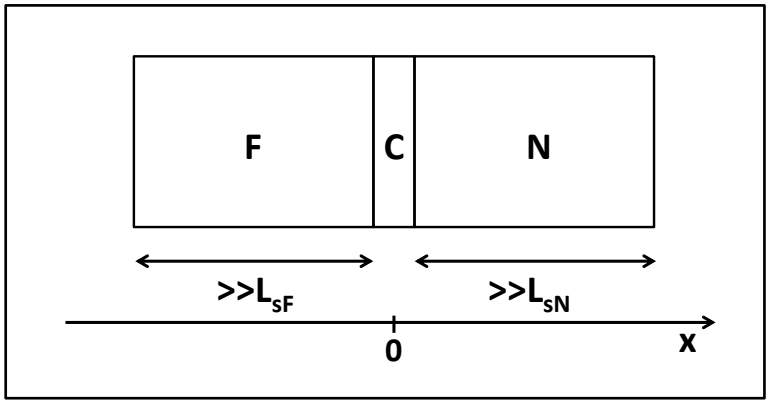

Fig. 3.4: Schematic of the spin injection geometry. The ferromagnet F forms an infinitely thin contact region C with the nonmagnetic conductor N. C represents a discontinuity at $x = 0$.

3.4.1 Ferromagnet

According to equation (3.73) the current spin polarization at $x = 0$ in the ferromagnet can be written as

$$P_{jF}(0) = P_{\sigma F} + \frac{1}{j} 4 \frac{\sigma_{F\uparrow}\sigma_{F\downarrow}}{\sigma_F} \nabla \mu_{sF}(0). \tag{3.80}$$

We have to look at the diffusion equation in the ferromagnet to discover $\mu_{sF}(0)$:

$$\nabla^2 \mu_{sF} = \frac{1}{L_{sF}^{\ 2}} \mu_{sF}. \tag{3.81}$$

The solution of this equation with the correct boundary condition ($\mu_{sF}(-\infty) = 0$) is

$$\mu_{sF}(x) = \mu_{sF}(0) e^{\frac{x}{L_{sF}}}, \tag{3.82}$$

which gives us altogether

$$\nabla \mu_{sF} = \frac{1}{L_{sF}} \mu_{sF}. \tag{3.83}$$

So the spin polarization of the current can be written as

$$P_{jF}(0) = P_{\sigma F} + \frac{1}{j} \frac{\mu_{sF}(0)}{R_F}, \tag{3.84}$$

where an effective resistance of the ferromagnetic region was introduced by

$$R_F = \frac{\sigma_F}{4\sigma_{F\uparrow}\sigma_{F\downarrow}} L_{sF}. \tag{3.85}$$

R_F is an effective resistance that appears in the spin polarized transport. It is not the electrical resistance but as a guideline one can say that it is comparable to the actual resistance of the region of size L_{sF}[Fabi].

3.4.2 Nonmagnet

Of course also in the nonmagnetic region we are interested in the current spin polarization. Here things get much easier, as $P_\sigma = 0$ and $\sigma_{N\uparrow} = \sigma_{N\downarrow} = \sigma_N/2$. So in the end we get for the semiconductor

$$P_{jN}(0) = \frac{1}{j}\sigma_N \nabla \mu_{sN}(0). \tag{3.86}$$

Again we have to find a solution for the diffusion equation

$$\nabla^2 \mu_{sN} = \frac{1}{L_{sN}^{\ 2}} \mu_{sN}. \tag{3.87}$$

For the boundary condition in the nonmagnetic region ($\mu_{sN}(\infty) = 0$) we get the solution:

$$\mu_{sN}(x) = \mu_{sN}(0) e^{\frac{-x}{L_{sN}}}, \tag{3.88}$$

and thus the gradient reads as

$$\nabla \mu_{sN} = \frac{1}{L_{sN}} \mu_{sN}. \tag{3.89}$$

This leads us to an expression for the current spin polarization in the nonmagnetic region

$$P_{jN}(0) = -\frac{1}{j}\frac{\mu_{sN}(0)}{R_N}, \tag{3.90}$$

where

$$R_N = \frac{L_{sN}}{\sigma_N} \tag{3.91}$$

is analogously to the ferromagnetic region the effective resistance of the nonmagnetic semiconductor side. If we are able to determine $P_{jN}(0)$ we of course also know the spin accumulation, as

$$\mu_{sN}(0) = -jP_{jN}(0)R_N. \tag{3.92}$$

As one can easily read off equation (3.92), spin accumulation is proportional to the spin current, which pumps the spin into the system – $j_{sN}(0) = jP_{jN}(0)$ – as well as to the effective resistance. This shows that the greater the spin diffusion length in the semiconductor, the greater the achievable spin accumulation.

3.4.3 Contact

There are different ways of describing the spin transport in spintronics devices. The biggest advantage of the quasichemical potential method over continuous drift-diffusion equations for charge and spin current surely lies in its easy way of characterizing spin-polarized transport across the contact region at $x = 0$. As it is impossible to define gradients in a single point for description of the currents, we have to stick to another method. We use the discontinuity of the chemical potential at the contact and write:

$$j_\uparrow = \Sigma_\uparrow \left[\mu_{\uparrow N}(0) - \mu_{\uparrow F}(0) \right] = \Sigma_\uparrow \Delta\mu_\uparrow(0), \tag{3.93}$$

$$j_\downarrow = \Sigma_\downarrow \left[\mu_{\downarrow N}(0) - \mu_{\downarrow F}(0) \right] = \Sigma_\downarrow \Delta\mu_\downarrow(0). \tag{3.94}$$

In these formulae we have introduced spin dependent contact conductances $\Sigma_\uparrow$ and $\Sigma_\downarrow$, contrary to the conductivities in the extended regions of the ferromagnet and the nonmagnetic conductor. Now we can write for charge and spin currents

$$j = \Sigma \Delta\mu(0) + \Sigma_s \Delta\mu_s(0), \tag{3.95}$$

$$j_s = \Sigma_s \Delta\mu(0) + \Sigma \Delta\mu_s(0). \tag{3.96}$$

Again the conductance Σ and spin conductance Σ_s are defined similar to above quantities:

$$\Sigma = \Sigma_\uparrow + \Sigma_\downarrow ; \; \Sigma_s = \Sigma_\uparrow - \Sigma_\downarrow . \tag{3.97}$$

We can eliminate $\Delta\mu(0)$ from the equation for the charge current j and use the result in equation (3.96) to get

$$j_s = P_\Sigma j + \frac{\Delta\mu_s(0)}{R_C}, \tag{3.98}$$

where we analogously to the ferromagnetic and nonmagnetic parts have defined the conductance spin polarization and the effective resistance of the contact by

$$P_\Sigma = \frac{\Sigma_\uparrow - \Sigma_\downarrow}{\Sigma} \quad and \quad R_C = \frac{\Sigma}{4\Sigma_\uparrow \Sigma_\downarrow}. \tag{3.99}$$

Finally we get as a result for the current spin polarization j_s/j at the contact

$$P_{jC} = P_\Sigma + \frac{1}{j} \frac{\Delta\mu_s(0)}{R_C}. \tag{3.100}$$

3.4.4 Spin injection and spin extraction

Now we have three equations, which all describe the current spin polarization directly at the contact ($x = 0$). If we look at these equations [(3.84), (3.100) and (3.90)] we have five unknown parameters, namely $P_{jF}(0)$, $P_{jC}(0)$, $P_{jN}(0)$, $\mu_{sF}(0)$ and $\mu_{sN}(0)$. We have to eliminate at least two of them to evaluate the whole equation system. This we can do by the physical assumption that spin current continuity at the contact is given. In reality this is only an approximation, because there

will certainly occur spin flip processes in the contact region, but as we measure at very low temperatures, we are not too far off reality[Gali],[Bass]. So with this we can write:

$$P_j = P_{jF}(0) = P_{jC}(0) = P_{jN}(0). \tag{3.101}$$

If we now put everything together the final result of our algebraic system reads as:

$$P_j = \frac{R_F P_{\sigma F} + R_C P_\Sigma}{R_F + R_C + R_N} = \langle P_\sigma \rangle_R . \tag{3.102}$$

This means that the spin injection efficiency is the averaged conductivity spin polarization of the three regions, weighted by the effective resistances. In our simple approach we are within a linear regime and spin injection efficiency does not depend on the current. In the experimental part we will see that in reality this is only valid for small biases, see chapter 6.2.5. For higher currents this model is too simple, mainly because with increasing current electrons from deeper levels play a more pronounced role in the transport and there the ratio from spin up and spin down electrons is significantly different from the levels at the Fermi edge. The standard model of electrical spin injection gives us equation (3.102) as its central result. With that result we can now evaluate the spin accumulation in the nonmagnetic region:

$$\mu_{sN}(0) = -jP_j R_N . \tag{3.103}$$

If electrons flow from the ferromagnetic part into the nonmagnetic one, we speak of spin injection, j is negative. Accordingly spin extraction means that we extract spins from the nonmagnetic region and j is positive. So the spin accumulation $\mu_{sN}(0)$ is positive if we inject spins into the semiconductor and negative if we take spins away from it, a quite reasonable nomenclature. If we look at the density spin polarization in the nonmagnetic region, we get

$$P_n(0) = e\mu_{sN}(0)\frac{g_N}{n} = -jeR_N \frac{g_N}{n} P_j . \tag{3.104}$$

This means P_n is approximately equal to the fraction of electrons in the energy interval of jeR_N (that is the voltage drop at the distance of L_{sN}) times P_j. As the injected spin polarization is proportional to the charge current j within our simple model, the electrical spin injection is an example of spin pumping.

3.4.5 The equivalent circuit

The equivalent circuit diagram given by figure 3.5 summarizes the standard model of spin injection very

briefly. As in the original Julliere model[Jull] there are two parallel electric current channels for spin up and spin down electrons in our considered sample. Each of the six regions can be characterized by its own effective resistance, which was deducted in the previous sections.

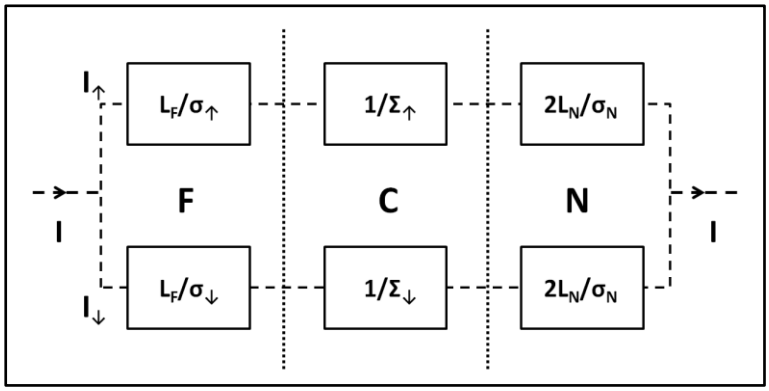

Fig. 3.5: The equivalent circuit of the standard model of spin injection for ferromagnetic injectors F attached to nonmagnetic conductors N. The contact region is denoted by C. If current flows through the circuit there are parallel channels for spin up and down electrons and every part of the circuit has its own characteristic resistance[Fabi].

3.4.6 Quasichemical potentials, nonequilibrium resistance and spin bottleneck

Equation number (3.100) shows that there is a drop in the spin quasichemical potential at the contact:

$$\Delta\mu_s(0) = \mu_{sN}(0) - \mu_{sF}(0) = jR_C(P_j - P_\Sigma). \tag{3.105}$$

This drop changes its sign if the current direction is reversed, as P_j is a parameter of the material itself.

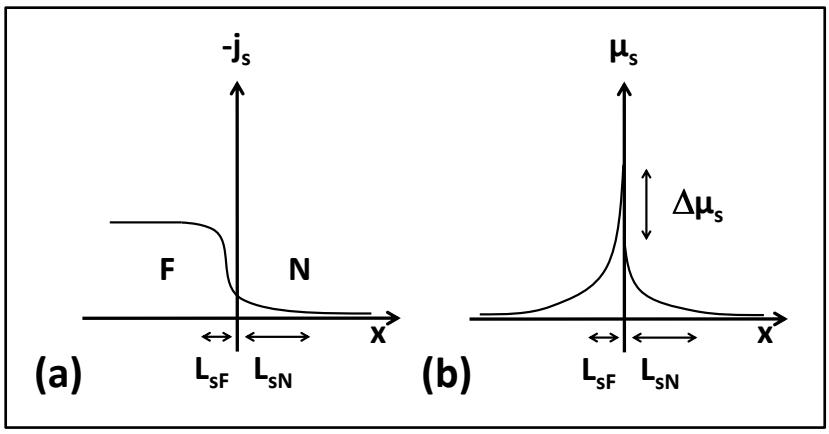

Fig. 3.6: The spin current j_s is depicted on the left hand side for spin injection (a). Its nonequilibrium properties decay on length scales defined by the appropriate spin diffusion lengths of the materials. The right graph shows the spin quasichemical potential for the same situation (b). While the spin current is continuous at the contact, μ_s exhibits a discontinuity at $x = 0$. The size of $\Delta\mu_s$ is proportional to the current, contact resistance and spin current polarization[Fabi], see text.

Previously we dropped the charge quasichemical potential μ for local charge neutrality and concentrated on the spin quasichemical potential μ_s. We have already deduced in (3.71) that

$$\nabla\mu = \frac{1}{\sigma}(j - \sigma_s\nabla\mu_s) = \frac{j}{\sigma} - P_\sigma\nabla\mu_s. \tag{3.106}$$

For the ferromagnetic region we get

$$\nabla\mu_F = \frac{j}{\sigma_F} - P_{\sigma F}\nabla\mu_{sF}, \tag{3.107}$$

while in the nonmagnetic region the simplified

$$\nabla\mu_N = \frac{j}{\sigma_N} \tag{3.108}$$

is the valid expression. The equations for μ_F and μ_N can be integrated to get the following:

$$\mu_F(-\infty) - \mu_F(0) = -j\tilde{R}_F - P_{\sigma F}[\mu_{sF}(-\infty) - \mu_{sF}(0)], \tag{3.109}$$

$$\mu_N(\infty) - \mu_N(0) = j\tilde{R}_N. \tag{3.110}$$

Here we defined $\tilde{R}_F$ by:

$$\tilde{R}_F = \int_{-\infty}^{0} dx \frac{1}{\sigma_F} \equiv \frac{L_F}{\sigma_F}, \tag{3.111}$$

which is the actual resistance of a unit cross sectional area of the ferromagnetic region of size $L_F >> L_{sF}$, taken as infinitely big in the arguments of the quasichemical potentials. The equivalent definition holds for the nonmagnetic part:

$$\tilde{R}_N = \int_{0}^{\infty} dx \frac{1}{\sigma_N} \equiv \frac{L_N}{\sigma_N}. \tag{3.112}$$

By subtracting equation (3.109) from (3.110) and the assumption of lacking spin accumulation at the left end of the ferromagnet (that means $\mu_{sF}(-\infty) = 0$) we get

$$[\mu_N(\infty) - \mu_F(-\infty)] - [\mu_N(0) - \mu_F(0)] = j\tilde{R}_N + j\tilde{R}_F - P_{\sigma F}\mu_{sF}(0). \tag{3.113}$$

Now think of Ohm's law and what you would expect for our junction:

$$\mu_N(\infty) - \mu_F(-\infty) = j\left(\tilde{R}_N + \tilde{R}_F + \frac{1}{\Sigma}\right). \tag{3.114}$$

This is the total drop of the quasichemical potential (as we have assumed charge neutrality this equals the voltage drop) which is given by the product of the flowing charge current times the serial resistance of the three regions. However, if spin accumulation is present, the resistance of the junction gains an additional correction of δR that modifies Ohm's law:

$$\mu_N(\infty) - \mu_F(-\infty) = j\left(\tilde{R}_N + \tilde{R}_F + \frac{1}{\Sigma} + \delta R\right). \tag{3.115}$$

We can substitute this into equation (3.113) to obtain

$$j\left(\frac{1}{\Sigma} + \delta R\right) = -P_{\sigma F}\mu_{sF}(0) + \mu_N(0) - \mu_F(0). \tag{3.116}$$

Thus at the contact we get an additional resistance due to the spin accumulation $\Delta\mu_s(0)$:

$$\Delta\mu(0) = \mu_N(0) - \mu_F(0) = \frac{j}{\Sigma} - P_\Sigma \Delta\mu_s(0). \tag{3.117}$$

As we have shown previously [equation (3.105)] that $\Delta\mu_s(0)$ is proportional to the current j the quasichemical potential drop at the contact is

$$\Delta\mu(0) = \frac{j}{\Sigma} - jP_\Sigma(P_j - P_\Sigma)R_C. \tag{3.118}$$

Substituting this now into equation (3.116) gives us the additional resistance due to nonequilibrium spin accumulation:

$$\delta R = -P_\Sigma(P_j - P_\Sigma)R_c - P_{\sigma F}R_F(P_j - P_{\sigma F}). \tag{3.119}$$

If we now replace spin injection efficiency P_j with equation (3.102), we finally get

$$\delta R = \frac{R_N(P_\Sigma^2 R_c + P_{\sigma F}^2 R_F) + R_F R_c (P_{\sigma F} - P_\Sigma)^2}{R_F + R_c + R_N}. \tag{3.120}$$

The most important thing about this additional resistance is that δR is always positive. The nonequilibrium spin that is existent in the ferromagnet as well as in the normal conductor due to spin injection leads to spin diffusion, which drives the spin away from the contact. As we have nonvanishing P_σ in the ferromagnet and the contact any spin current gives rise to a charge current. This electron flow is always oriented against the external battery and thus manifests itself as an additional resistance. This is called the spin bottleneck effect[Joh3].

3.4.7 Transparent contact

This section deals with a very important limit of the spin injection model. The limit of transparent contacts is applicable if the following condition is valid:

$$R_C \ll R_N, R_F. \tag{3.121}$$

This means we have effectively no contact resistance in our sample, the ferromagnetic and nonmagnetic resistances completely dominate. Now the F/N junction can be characterized by the following equations:

$$P_j = \frac{R_F}{R_N + R_F} P_{\sigma F}, \tag{3.122}$$

$$\delta R = \frac{R_N R_F}{R_N + R_F} (P_{\sigma F})^2, \tag{3.123}$$

$$P_{nN}(0) = -ejR_N \frac{g_N}{n_N} P_j. \tag{3.124}$$

If the effective resistances of the ferromagnetic and the nonmagnetic region are comparable, $R_N \approx R_F$, then the spin injection efficiency is high:

$$P_j \approx P_{\sigma F}. \tag{3.125}$$

This means that the spin injection efficiency into the nonmagnetic region is a significant fraction of the spin splitting in the ferromagnet. This is valid for example if one injects from iron or cobalt into aluminum. Knowing that we can easily understand why the early attempts of injecting spins from ferromagnetic metals into semiconductors were foredoomed. As the semiconductor has a much smaller carrier density, it follows automatically that $R_N >> R_F$ and this gives us

$$P_j = \frac{R_F}{R_N + R_F} P_{\sigma F} \approx \frac{R_F}{R_N} P_{\sigma F} \ll P_{\sigma F}, \tag{3.126}$$

$$\delta R = \frac{R_N R_F}{R_N + R_F} (P_{\sigma F})^2 \approx R_F (P_{\sigma F})^2 \approx R_F, \tag{3.127}$$

$$P_{nN}(0) = -ejR_N \frac{g_N}{n_N} P_j \approx -ejR_N \frac{g_N}{n_N} P_{\sigma F} \approx \frac{eV_F}{\varepsilon_{FN}} P_{\sigma F}, \tag{3.128}$$

where is the voltage drop in F along L_{sF} is V_F and ε_{FN} is the Fermi energy of the nonmagnetic conductor. One can very easily see at equation (3.126) that the spin injection efficiency is dramatically reduced in this configuration. This effect is now well known as conductivity mismatch problem[Schm]. It can be very nicely illustrated by the equivalent circuit shown in figure 3.7.

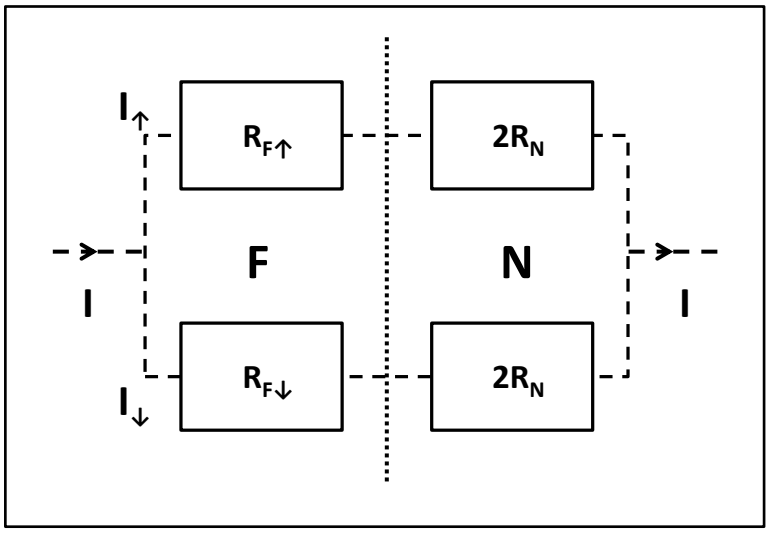

Fig. 3.7: In the equivalent circuit for a transparent contact R_C can be completely neglected against R_F and R_N. If additionally R_N dominates the junction, the two spin currents are brought more and more into line with each other the higher R_N gets[Fabi].

As R_N is dominating the resistance of the junction, the resulting voltage drop can be very accurately approximated by $V \approx 2R_N I_\uparrow \approx 2R_N I_\downarrow$ as the difference in resistances is several orders of magnitude and the spin splitting of conventional ferromagnets does not exceed a factor of two. Altogether we get an adaption of the flowing spin currents, $I_\uparrow \approx I_\downarrow$. So we easily see that this spin injection scheme is very inefficient.

3.5.8 Tunnel contacts

There of course has to exist another important limit in the spin injection model. This limit is a clearly dominating contact resistance R_C, called tunnel contact. In this case the following equations describe the spin injection:

$$P_j = P_\Sigma, \tag{3.129}$$

$$\delta R = \frac{R_N R_C P_\Sigma^{\,2} + R_F R_C (P_{\sigma F} - P_\Sigma)^2}{R_C}, \tag{3.130}$$

$$P_{nN}(0) = -ejR_N \frac{g_N}{n_N} P_\Sigma. \tag{3.131}$$

All quantities depend clearly on P_Σ. The tunnel contact employs a spin filter function. Now let us look again at the conductivity mismatch case, but now with tunnel contacts:

$$P_j = P_\Sigma, \tag{3.132}$$

$$\delta R = R_N P_\Sigma^{\,2}, \tag{3.133}$$

$$P_{nN}(0) = -ejR_N \frac{g_N}{n_N} P_\Sigma \approx -\frac{eV_N}{\varepsilon_{FN}} P_\Sigma. \tag{3.134}$$

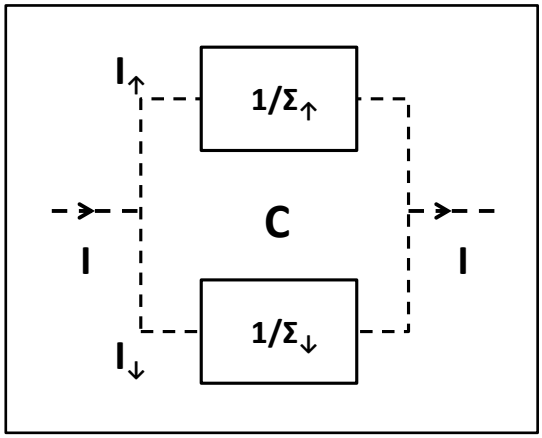

Fig. 3.8: The equivalent circuit model of a spin injection experiment with dominating contact resistances. Apparently nearly all of the voltage drop appears directly at the tunneling contact and the resistances of the ferromagnetic injector and the nonmagnetic conductor can be neglected.

3.5.9 Johnson-Silsbee spin charge coupling

The basic idea behind the electrical spin injection is of course to generate a spin accumulation in the nonmagnetic conductor by driving a spin polarized current over the junction. But vice versa current is initiated if a ferromagnetic contact is attached to a nonmagnetic conductor in the vicinity of nonequilibrium spin accumulation. If there is no closed circuit, e.g. a voltmeter is attached between the ferromagnetic contact and the nonmagnetic region, one can measure an electromotive force (*emf*). This inverse effect to the spin injection is called the Silsbee-Johnson spin charge coupling[Sils],[John].

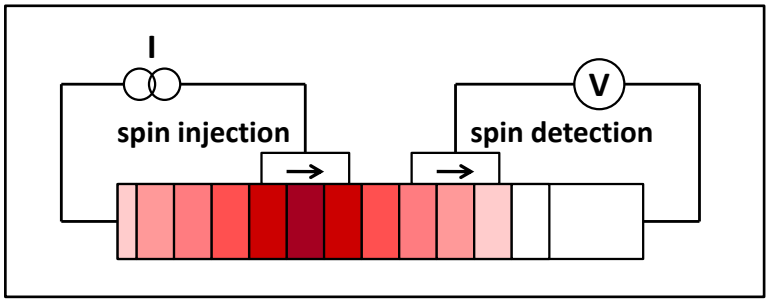

Fig. 3.9: The non-local spin injection and detection scheme, after Johnson and Silsbee. If the injected spins diffuse far enough in the nonmagnetic conductor, a second ferromagnetic contact can be used to detect a spin related signal[John].

The system is schematically depicted in figure 3.9. Spin is injected into the nonmagnetic conductor by the left ferromagnetic electrode. The charge current flows from the ferromagnet across the contact region and directly to the left end of the conductor. However, we do have a system where diffusive transport is dominating. This leads to the fact, that additionally spins are diffusing away from the contact to the right. This nonequilibrium spin accumulation reaches the second ferromagnetic electrode on the right hand side and here it produces a measurable *emf* via the spin charge coupling. It is possible to calculate the arising *emf* resulting from the spin-charge coupling using the previously developed model of spin injection.

Consider the following boundary conditions:

$$\mu_{sN}(\infty) \neq 0 \tag{3.135}$$

and

$$\mu_{sF}(-\infty) = 0. \tag{3.136}$$

This means that at the far right end of our nonmagnetic conductor a nonequilibrium spin is maintained (we do not specify the source of this nonequilibrium spin) while at the far left end of our ferromagnet the spin is in equilibrium. We want to calculate the induced *emf*, which simply can be defined by

$$emf = \mu_N(\infty) - \mu_F(-\infty). \tag{3.137}$$

We want to point out that in this case the basic condition of an open circuit holds, namely:

$$j = 0. \tag{3.138}$$

The drop of the quasichemical potential μ across the junction is represented by the *emf*. In electrical and spin equilibrium this potential drop vanishes. The local charge neutrality led us to equation (3.68) before, what gives us

$$\Phi(x) = -\mu(x) - P_g \mu_s(x). \tag{3.139}$$

In the ferromagnet we have

$$\Phi_F(x) = -\mu_F(x) - P_{gF} \mu_{sF}(x), \tag{3.140}$$

while in the normal conductor P_{gN} vanishes and we therefore get

$$\Phi_N(x) = -\mu_N(x). \tag{3.141}$$

Thanks to our initial boundary condition of equilibrium spin at the far end of the ferromagnet we can write

$$emf = \mu_N(\infty) - \mu_F(-\infty) = \Phi_F(-\infty) - \Phi_N(\infty). \tag{3.142}$$

Thus, the emf can be detected as a voltage drop. From the drift diffusion model and the condition of an open circuit we get

$$\nabla\mu_F = \frac{j}{\sigma_F} - P_{\sigma F}\nabla\mu_{sF} = -P_{\sigma F}\nabla\mu_{sF}. \tag{3.143}$$

Integrating this for the ferromagnetic region gives us

$$\mu_F(-\infty) - \mu_F(0) = -P_{\sigma F}[\mu_{sF}(-\infty) - \mu_{sF}(0)] = P_{\sigma F}\mu_{sF}(0), \tag{3.144}$$

while in the nonmagnetic part we get

$$\mu_N(\infty) - \mu_N(0) = 0. \tag{3.145}$$

Substituting this into equation (3.142) gives us

$$emf = \mu_N(\infty) - \mu_F(-\infty) = \Delta\mu(0) - P_{\sigma F}\mu_{sF}(0). \tag{3.146}$$

Remember that $\Delta\mu(0)$ is the drop of the quasichemical potential across the contact region. We need to know $\Delta\mu(0)$ as well as $\mu_{sF}(0)$ to calculate the emf. First we look at the drop of the electrostatic potential across the contact. From charge neutrality we can deduce that

$$\Delta\Phi(0) = \Phi_N(0) - \Phi_F(0) = -\Delta\mu(0) + P_{gF}\mu_{sF}(0). \tag{3.147}$$

Remember for the drift diffusion model at the contact:

$$j = \Sigma\Delta\mu(0) + \Sigma_s\Delta\mu_s(0), \tag{3.148}$$

$$j_s = \Sigma_s\Delta\mu(0) + \Sigma\Delta\mu_s(0). \tag{3.149}$$

If one eliminates $\Delta\mu_s(0)$ from the second equation, substitutes for the first one and uses the condition of an open circuit (thus $j = 0$) the quasichemical potential drop at the contact can be obtained:

$$\Delta\mu(0) = -R_c P_\Sigma j_s(0). \tag{3.150}$$

This gives us now

$$\Delta\Phi(0) = R_c P_\Sigma j_s(0) + P_{gF}\mu_{sF}(0). \tag{3.151}$$

This equation is of significant importance, as it connects the voltage drop across the contact to the spin current as well as the spin accumulation of the ferromagnet directly at the contact. Using the boundary condition of nonequilibrium spin at the far end of the normal conductor we can describe the spatial profile of μ_s by

$$\mu_{sN}(x) = \mu_{sN}(\infty) + [\mu_{sN}(0) - \mu_{sN}(\infty)]e^{-x/L_{sN}}. \tag{3.152}$$

Admittedly, we still have to determine the exact value of $\mu_{sN}(0)$. From the above equation we can get

$$\nabla\mu_{sN}(0) = -\frac{1}{L_{sN}}[\mu_{sN}(0) - \mu_{sN}(\infty)]. \tag{3.153}$$

Using the open circuit condition $j = 0$ again we receive the following three equations for the spin currents in the different regions directly at the contact:

$$j_{sN}(0) = -\frac{1}{R_N}[\mu_{sN}(0) - \mu_{sN}(\infty)], \tag{3.154}$$

$$j_{sF}(0) = -\frac{1}{R_F}\mu_{sF}(0), \tag{3.155}$$

$$j_{sc}(0) = \frac{1}{R_c}\Delta\mu_s(0). \tag{3.156}$$

The assumption of spin current conservation across the interface leads us to the equality of j_s, $j_{sF}(0)$, j_{sc} *and* $j_{sN}(0)$. Therewith we can transform equation (3.151) into

$$\Delta\Phi(0) = \left(\frac{R_c P_\Sigma + R_F P_{gF}}{R_F}\right)\mu_{sF}(0). \tag{3.157}$$

Also the quasichemical potential $\mu_{sF}(0)$ can be obtained now from the set of equations for the spin currents at the contact to be

$$\mu_{sF}(0) = \frac{R_F}{R_F + R_c + R_N}\mu_{sN}(\infty) < \mu_{sN}(\infty). \tag{3.158}$$

Now we can write the spin current at the contact as

$$j_s(0) = \frac{1}{R_F + R_c + R_N}\mu_{sN}(\infty). \tag{3.159}$$

In combination with equation (3.150) we can write now for the quasichemical potential drop

$$\Delta\mu(0) = -\frac{R_c P_\Sigma}{R_F + R_c + R_N}\mu_{sN}(\infty). \tag{3.160}$$

This means that the spin filtering effect of the contact is the reason for the drop of the quasichemical potential across the contact. A spin independent contact conductance would lead to a continuous quasichemical potential at $x = 0$. Furthermore we can combine equations (3.157) and (3.158) to write

$$\Delta\Phi(x) = \frac{R_c P_\Sigma + R_F P_{gF}}{R_F + R_c + R_N}\mu_{sN}(\infty). \tag{3.161}$$

This means that the electrostatic potential drop across the contact arises due to the spin polarization of the ferromagnet, P_{gF}, as well as due to the spin filtering

effect of the contact, P_Σ. Now we can finally give the formula for the spin induced emf. Using equations (3.158) and (3.160) to concretize equation (3.146) finally gives us

$$emf = -\frac{R_F P_{\sigma F} + R_C P_\Sigma}{R_F + R_C + R_N} \mu_{sN}(\infty) = -P_j \mu_{sN}(\infty). \tag{3.162}$$

Remember equation (3.102), where we defined the spin injection efficiency P_j, which is the conductivity spin polarization P_σ averaged over the three regions F, C and N, weighted by the effective resistances of them. Let us now introduce an external spin injection circuit to our system that maintains a positive spin accumulation μ_{sN} at $x = \infty$, what means electrons are flowing from F to N in the external circuit and from N to F through our system completing the circuit. Assuming a positive P_j this leads to a negative *emf*. Switching P_j leads to a sign reversal of the *emf*, switching also μ_{sN} gives us the original value again. This essentially can be done by different coercive fields of F_{inj} and F_{det} and sweeping an external magnetic field. Typically one uses shape anisotropy effects to get different switching fields of nanopatterned magnets. Altogether this means if we do an in-plane field sweep we would get a spin-valve-like signal.

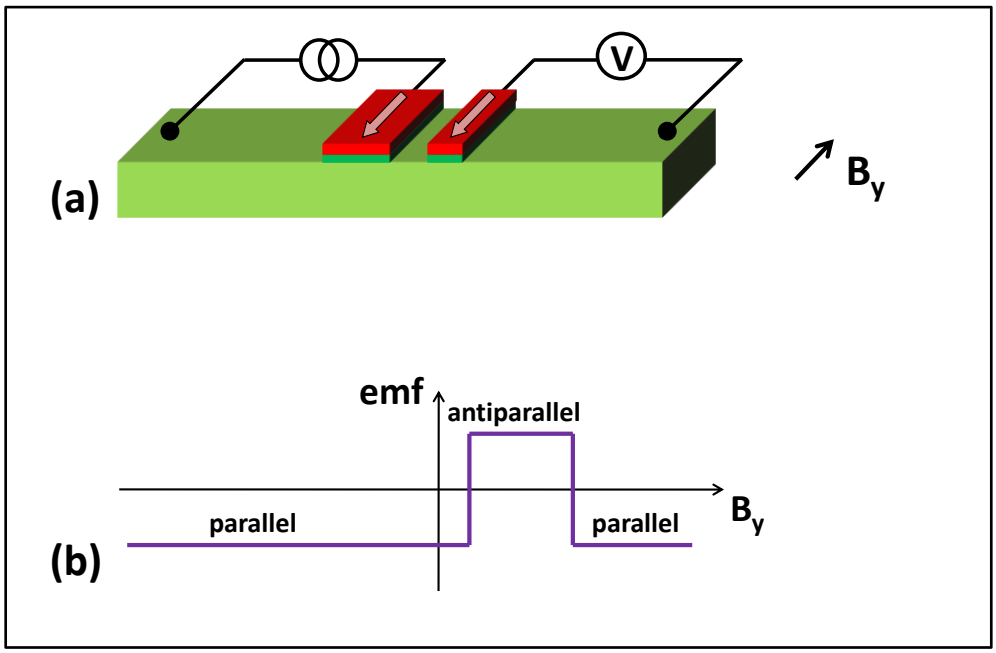

Fig. 3.10: The simplified principle of an in-plane spin-valve measurement. The parallel configuration of injector and detector ferromagnets leads to a certain emf at the detector. An external magnetic field is swept to change the magnetizations. While passing the coercive field of the injector contact its magnetization switches 180° and thus μ_{sN} changes its sign. At coercive field of the detector its P_j changes sign and the original *emf* value is restored.

3.6 Spin dynamics

3.6.1 Drift diffusion model for spin dynamics

Now think back of our random walk model we introduced previously. Electrons are scattered on their way through the conductor and can change their direction of movement on each scattering event. In a second step we added spin flip processes. Now we want to generalize this model by introducing the possibility of an electron spin rotation due to the presence of an external magnetic field B. A spin s precesses around the external field as is described by

$$\frac{ds}{dt} = s \times \omega_0, \tag{3.163}$$

where $\omega_0 = \gamma B$ is the directed Larmor frequency, with the gyromagnetic ratio γ. We imply that for one single time step $\tau << 1/\omega_0$ holds. If at time t the spin is s, at time $t+\tau$ the spin will be

$$s(t+\tau) = s(t) + s(t) \times \omega_0 \tau. \tag{3.164}$$

The change of the spin is proportional to the product of precession time and Larmor frequency. The absolute value of the product gives us the phase change of a spin precessing transverse to the magnetic field.

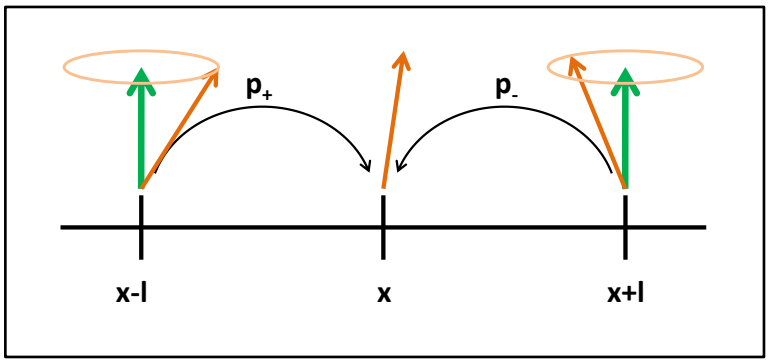

Fig. 3.11: Random walk with allowed spin precession. Probabilities $p_{+/-}$ are well known by now. The big green arrows represent an applied magnetic field. The electrons' spins precess around that field. The resulting spin at x is a weighted average of the spin at x -/+ l at the time of the scattering event[Fabi].

Staying in our random walk model, the spins at point x at time $t+\tau$ are given by the sum over the spins one time step earlier located at $x-l$ and $x+l$ each rotated about $\omega_0\tau$ and decreased by τ/τ_s due to the spin relaxation (see fig. 3.11):

$$\begin{aligned} s(x,t+\tau) = p_+ &\left[s(x-l,t) + s(x-l,t) \times \omega_0 \tau - s(x-l,t)\frac{\tau}{\tau_s} \right] \\ + p_- &\left[s(x+l,t) + s(x+l,t) \times \omega_0 \tau - s(x+l,t)\frac{\tau}{\tau_s} \right]. \end{aligned} \tag{3.165}$$

Again p_+ and p_- denote the jumping probabilities to the right and to the left. We expand the left side of equation (3.165) into a Taylor series around t and the right side into a series around x and obtain after evaluation:

$$\frac{\partial s}{\partial t} = s \times \omega_0 + D\nabla^2 s + \mu E \nabla s - \frac{s}{\tau_s}. \tag{3.166}$$

This is the so-called drift diffusion equation for spin dynamics. The terms on the right hand side describe spin precession, spin diffusion, spin drift and spin relaxation, respectively. Now we want again a continuity equation for spin, this time including spin dynamics. Again we suppose charge neutrality (i.e. constant electric field) and rewrite equation (3.166) the following way:

$$\frac{\partial s}{\partial t} - \nabla[\mu E s - D\nabla s] = s \times \omega_0 - \frac{s}{\tau_s}. \tag{3.167}$$

Just as in the chapters before the expression inside the brackets can be identified by the generalized spin current

$$J_s = -\mu E s - D\nabla s. \tag{3.168}$$

The appropriate spin charge current then is

$$j_s = -eJ_s = e\mu E s + eD\nabla s. \tag{3.169}$$

Altogether the continuity equation now looks like

$$\frac{\partial s}{\partial t} + \nabla J_s = s \times \omega_0 - \frac{s}{\tau_s}. \tag{3.170}$$

The first term on the right hand side represents the spin dynamics.

3.6.2 Hanle effect

Think of the following situation: a ferromagnetic contact injects spins s_y that are aligned along the y-direction of the coordinate system. They diffuse in the nonmagnetic conductor in the x-direction (we stick to our simple one-dimensional model). In some distance that still allows the measurement of the *emf* due to spin charge coupling a second ferromagnetic electrode exists. This detector measures the average spin signal of all incoming spins underneath it. If we now apply an external magnetic field in z-direction the electron spins start precessing around it. As different electrons do have different transit times, due to the diffusive character of the channel, they will have different precession angles when arriving at the detector. Generally the Hanle effect now refers to the magnetic field dependence of the spin accumulation in the nonmagnetic channel. While at small magnetic fields the accumulation decreases very quickly with increased out-of-plane fields, at elevated fields decaying coherent oscillation of the signal can be observed. If the difference in transit times of

diffusing electrons becomes comparable to the Larmor period the spin signal vanishes due to a completely dephased electron ensemble.

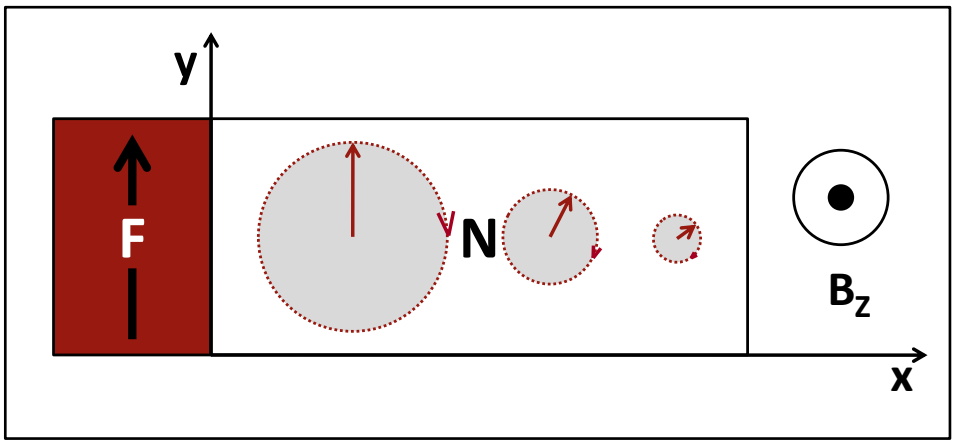

Fig. 3.12: The spin injection scheme at the Hanle setup. The channel is oriented along x-direction. The injected spins point along the y-axis, while the external field is applied along the out-of-plane z-direction.

Typically for analyzing Hanle measurements a combination of spin diffusion, spin precession and spin relaxation is used to describe the spin density at a certain distance from the injector. The average electron arrives at the detector after $t = x/v_d$. If we use the electron diffusion constant D, drift velocity v_d and the Larmor frequency ω_0 the average spin components along x- and y-directions are given up to the overall scale by

$$s_x(x,t) \sim \frac{1}{\sqrt{4\pi Dt}} e^{-(x-v_d t)^2/4Dt}\, e^{-t/T_2}\, \sin(\omega_0 t), \tag{3.171}$$

$$s_y(x,t) \sim \frac{1}{\sqrt{4\pi Dt}} e^{-(x-v_d t)^2/4Dt}\, e^{-t/T_2}\, \cos(\omega_0 t). \tag{3.172}$$

We use T_2 as spin dephasing time as we deal with spin dynamics of transverse spin. The sine and cosine functions correspond to the initial condition of spin aligned in y-direction with vanishing x-component. As we have to take all electrons into consideration at the point of detection we have to integrate over all transport times t for fixed x:

$$s_x(x) \sim \int_0^\infty dt\, s_x(x,t) = \int_0^\infty dt \frac{1}{\sqrt{4\pi Dt}} e^{-(x-v_d t)^2/4Dt}\, e^{-t/T_2}\, \sin(\omega_0 t), \tag{3.173}$$

$$s_y(x) \sim \int_0^\infty dt\, s_y(x,t) = \int_0^\infty dt \frac{1}{\sqrt{4\pi Dt}} e^{-(x-v_d t)^2/4Dt}\, e^{-t/T_2}\, \cos(\omega_0 t). \tag{3.174}$$

We can also integrate $s_{x/y}(x)$ along the probe dimension to get a result suitable for the used detector contact size.

We have to solve the spin dynamics drift-diffusion equation (3.166) with the following boundary conditions:

$$s(\infty) = 0, \tag{3.175}$$

$$j_{sx}(0) = j_{sz}(0) = 0, \tag{3.176}$$

$$j_{sy}(0) = j_{s0}. \tag{3.177}$$

The first one says that at the end of our nonmagnetic channel the spin accumulation has completely vanished, which is valid as the spin relaxation length is much shorter than our sample dimension. Equations (3.176) and (3.177) express the fact that spin current is conserved at the injection contact at $x = 0$ and that only spins oriented along the y-direction are present at the time of injection. j_{s0} is a parameter, but its size does not influence the functional form of the spin profile, which is the most interesting thing in Hanle experiments. Just to give a rough estimate of its actual magnitude, the spin current at $x = 0$ is

$$j_{s0} \approx P_{nF} j. \tag{3.178}$$

Here j is charge current and P_{nF} the density spin polarization in the ferromagnet, respectively. For our analysis we are interested in steady state effects, which means that time derivatives of our spin components can be set to zero. This gives us the three equations

$$\dot{s}_x = s_y\omega_0 + Ds_x'' - v_d s_x' - s_x/\tau_s = 0, \tag{3.179}$$

$$\dot{s}_y = -s_x\omega_0 + Ds_y'' - v_d s_y' - s_y/\tau_s = 0, \tag{3.180}$$

$$\dot{s}_z = Ds_z'' - v_d s_z' - s_z/\tau_s = 0. \tag{3.181}$$

Again we have to consider the boundary conditions for our three spin components

$$s_x(\infty) = s_y(\infty) = s_z(\infty) = 0 \tag{3.182}$$

and as we assumed in our derivation spin current conservation at the contact region

$$-v_d s_x'(0) + Ds_x'(0) = 0, \tag{3.183}$$

$$-v_d s_y'(0) + Ds_y'(0) = j_{s0}/e, \tag{3.184}$$

$$-v_d s_z'(0) + Ds_z'(0) = 0. \tag{3.185}$$

Because the spin component in the z-direction is not coupled to the other two components, the solution for its spin profile is very easily identifiable:

$$s_z(x) = 0. \tag{3.186}$$

This spin profile coincides with the fact that there exists no force that wants to tilt the spin direction out of our sample plane. For further analysis of the two in-plane components we can write the drift-diffusion equation for them in another form:

$$s_x'' - 2\kappa\frac{s_x'}{L_s} - \frac{s_x}{L_s^2} + \frac{s_y}{L_s^2}(\omega_0\tau_s) = 0, \tag{3.187}$$

$$s_y'' - 2\kappa\frac{s_y'}{L_s} - \frac{s_y}{L_s^2} + \frac{s_x}{L_s^2}(\omega_0\tau_s) = 0. \tag{3.188}$$

Here was used that $D = L_s^2\tau_s$ and $\kappa = L_d/2L_s$. κ is a dimensionless parameter that measures the strength of drift over diffusion. The spin drift length is defined by

$L_d = v_d \tau_s$. Now also the equations for the boundary conditions can be rewritten in the same form using κ and L_s:

$$-2\kappa \frac{1}{L_s} s_x(0) + s_x'(0) = 0, \tag{3.189}$$

$$-2\kappa \frac{1}{L_s} s_y(0) + s_y'(0) = \frac{j_{s0}}{eD}. \tag{3.190}$$

We can search for solutions of (3.187) and (3.188) in the form of

$$s_x(x) = A_x \exp(-\alpha x / L_s), \tag{3.191}$$

$$s_y(x) = A_y \exp(-\alpha x / L_s). \tag{3.192}$$

This gives us a quite complicated condition for α:

$$\begin{vmatrix} \alpha^2 + 2\alpha\kappa - 1 & \omega_0 \tau_s \\ -\omega_0 \tau_s & \alpha^2 + 2\alpha\kappa - 1 \end{vmatrix} = 0. \tag{3.193}$$

Solving the determinant equation gives us some complex solutions, where we pick the ones with a real positive part. Solving some more algebraic equations to get $A_{x/y}$ together with applying the right boundary condition equations leads to the spin profiles for $s_{x/y}(x)$:

$$s_x(x) = \frac{-j_{s0} L_s}{eD} e^{-\alpha_1 x / L_s} \left[\frac{2\kappa + \alpha_1}{(2\kappa + \alpha_1)^2 + \alpha_2^2} \sin\left(\frac{\alpha_2 x}{L_s}\right) + \frac{\alpha_2}{(2\kappa + \alpha_1)^2 + \alpha_2^2} \cos\left(\frac{\alpha_2 x}{L_s}\right) \right], \tag{3.194}$$

$$s_y(x) = \frac{-j_{s0} L_s}{eD} e^{-\alpha_1 x / L_s} \left[\frac{2\kappa + \alpha_1}{(2\kappa + \alpha_1)^2 + \alpha_2^2} \cos\left(\frac{\alpha_2 x}{L_s}\right) - \frac{\alpha_2}{(2\kappa + \alpha_1)^2 + \alpha_2^2} \sin\left(\frac{\alpha_2 x}{L_s}\right) \right]. \tag{3.195}$$

with α_1 and α_2 defined by

$$\alpha_1 = \frac{1}{\sqrt{2}} \sqrt{1 + \kappa^2 + \sqrt{(1 + \kappa^2)^2 + (\omega_0 \tau_s)^2}} - \kappa, \tag{3.196}$$

$$\alpha_2 = \frac{1}{\sqrt{2}} \sqrt{-1 - \kappa^2 + \sqrt{(1 + \kappa^2)^2 + (\omega_0 \tau_s)^2}}. \tag{3.197}$$

α_1 thereby is a measure for the effective spin relaxation

$$L_{s,eff} = \frac{L_s}{\alpha_1}, \tag{3.198}$$

while α_2 describes the effective spin precession

$$L_0 = \frac{2\pi L_s}{\alpha_2}. \tag{3.199}$$

Now, after all of these theoretical calculations what signal shape do we have to expect from our experimental non-local Hanle measurements on diffusive GaAs channels? This diffusive condition is generally characterized by

$$\kappa \ll 1. \tag{3.200}$$

This condition converts (3.196) and (3.197) into

$$\alpha_1 = \frac{1}{\sqrt{2}}\sqrt{1+\sqrt{1+(\omega_0\tau_s)^2}}, \tag{3.201}$$

$$\alpha_2 = \frac{1}{\sqrt{2}}\sqrt{-1+\sqrt{1+(\omega_0\tau_s)^2}}. \tag{3.202}$$

At small fields $\omega_0\tau_s<<1$ holds and α_1 converges against 1 while α_2 roughly vanishes. In the high field limit both go as $(\omega_0\tau_s/2)^{1/2}$. This explains the relatively big values at small fields as the effective spin relaxation length is L_s while the effective period length of the Larmor spin precession converges against infinity. At large magnetic fields however, the effective spin relaxation length decreases rapidly due to increasing $\omega_0\tau_s$ and additionally the effective period length decreases proportional to $(1/\omega_0)^{1/2}$. This, one can interpret as a Larmor length, which is the distance of spin diffusion within one Larmor period $2\pi/\omega_0$. Altogether the diffusive regime of the Hanle effect lets us expect curves for the non-local voltage of our detector as shown in figure 3.13.

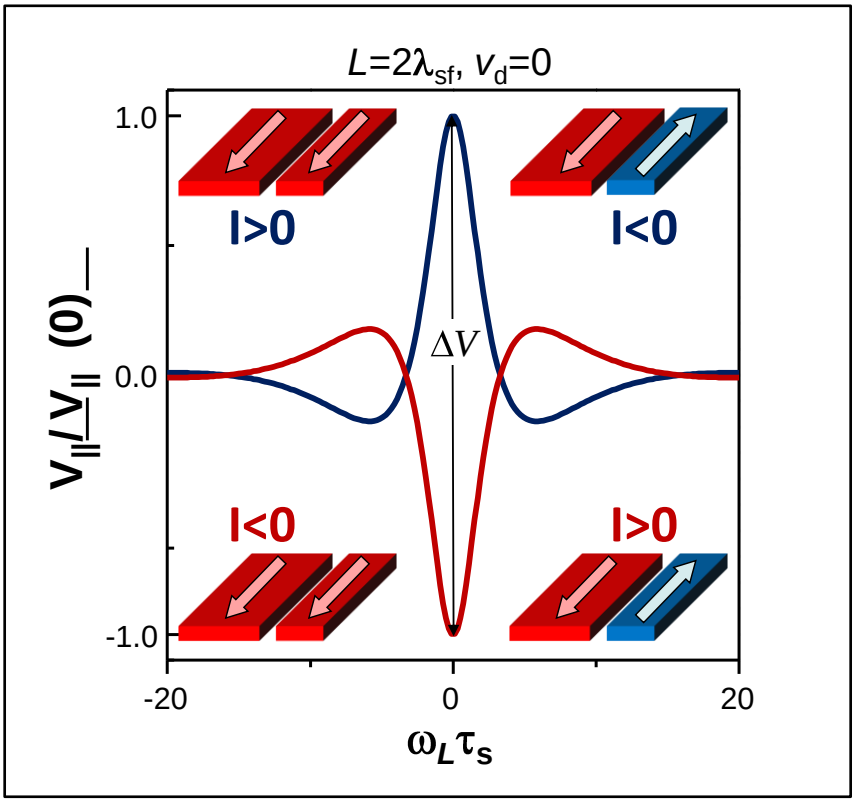

Fig. 3.13: The non-local detector voltage in a diffusive Hanle experiment at varied external out-of-plane field at a constant injector detector spacing of two spin diffusion lengths. Beginning with a relatively high peak/dip the signal rapidly decays and changes sign if the average spin signal over all incoming spins vanishes. Coherent oscillations are visible until the entire spin ensemble is completely dephased. Whether the signal starts with a peak or a dip depends on the experimental conditions, namely the contact magnetizations as well as the current direction.

3.7 Spin relaxation

After all the time we talked about spin drift and diffusion it is time to address one of the most important issues of that topic, i.e. the spin relaxation. It can be seen as the disappearance of initial non-equilibrium spin polarization due to temporally fluctuating magnetic fields, which are most often not real but effective fields originating from spin-orbit or exchange interaction. Two important parameters characterize a randomly fluctuating magnetic field: its amplitude (to be precise its root mean square (rms) value) and its correlation time τ_c, which is the duration the field can be considered as constant[Dya2]. Below we shortly describe the four most important spin relaxation mechanisms.

3.7.1 Elliot-Yafet (EY) mechanism[Elli],[Yafe]

SOI transforms the electrical field accompanying lattice vibrations (phonons) or charged impurities to an effective magnetic field. As a result momentum relaxation should be accompanied by spin relaxation. Spin relaxation by phonons is rather weak at low temperatures as the correlation time is on the order of the inverse frequency of a typical thermal phonon. For impurity scattering, the direction as well as the value of the random magnetic field depends on the geometry of the individual collision. Thus the field cannot be characterized by a single correlation time. Typically an electron undergoes 10^3 to 10^6 scattering events before its spin is flipped[Maek]. The higher the scattering frequency, the faster the spin relaxation happens.

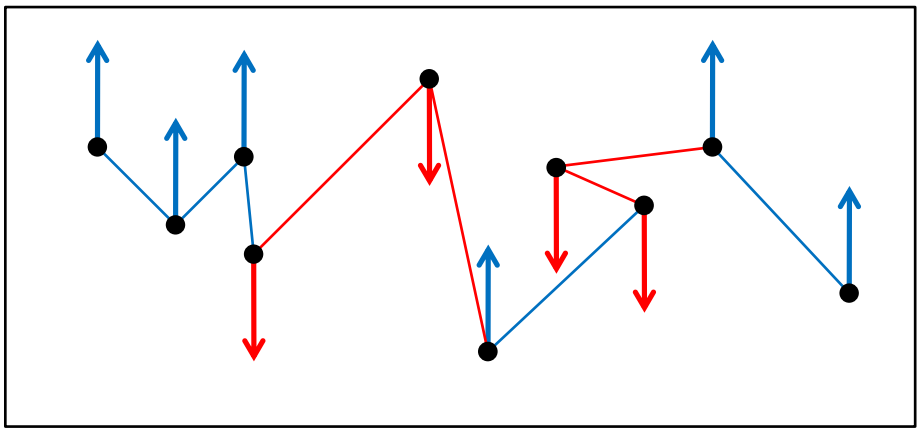

Fig. 3.14: In materials with dominating Elliot-Yafet spin relaxation mechanism the spin can change its direction at each specific scattering event. However, during these events its direction stays constant. This relaxation mechanism is typical for metals and semiconductors with inversion symmetry, like e.g. silicon[Elli].

3.7.2 Dyakonov-Perel (DP) mechanism[Dyak],[Dya1]

In semiconductors without inversion symmetry as in GaAs this relaxation mechanism is related to the spin-orbit splitting of the conduction band. A spin dependent extra term has to be added to the electron's Hamiltonian that can be viewed as the energy of a spin in an effective magnetic field. The effective magnetic field is dependent on the direction of the momentum of the electron

and thus the correlation time is on the order of the momentum relaxation time. In contrast to EY mechanism, the spin rotates not at the time of a collision but between two collisions what means that a faster scattering rate translates into less spin relaxation. This peculiar behavior is known as motional narrowing. DP mechanism is typically the dominant one in bulk III/V and II/VI semiconductors.

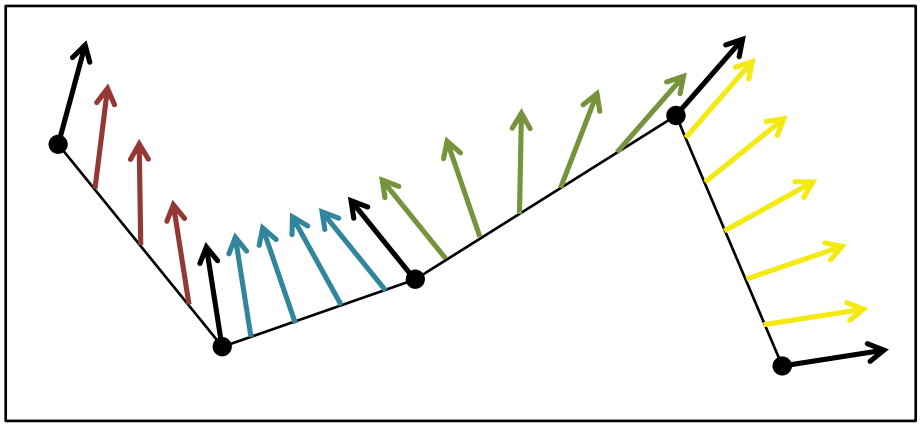

Fig. 3.15: If the Dyakonov-Perel mechanism is primarily responsible for spin relaxation, the spin direction changes during two scattering events, not at a certain collision itself. This is typical for n-type III-V semiconductors as GaAs.

3.7.3 Bir-Aronov-Pikus (BAP) mechanism[Bir]

This mechanism leads to electron spin relaxation due to the exchange interaction between the electron and hole spins. The corresponding relaxation rate is proportional to the number of holes in the valence band and thus may only become the dominant mechanism if one deals with highly p-doped semiconductors.

3.7.4 Hyperfine Interaction (HFI) with Nuclear spins[Dya2]

Typically the lattice nuclei are in a magnetically disordered state and the electron spins interact with the nuclear spins. Thus the nuclei provide directly a random effective magnetic field. The corresponding relaxation rate is quite weak, but for doping concentrations below the metal insulator transition where localized electron states exist or in quantum dots it may become important[Maek].

While in quantum wells there is only very little evidence that spin relaxation mechanisms other than DP are important, in bulk material EY and BAP play also an important role. One of the most important recent measurements of electron spin relaxation in bulk materials is the discovery of a maximum spin relaxation time in n-GaAs at low temperatures at a doping concentration right next to the metal insulator transition[Kikk]. Together with additional measurements done by Dzhioev et al., they are shown in figure 3.16.

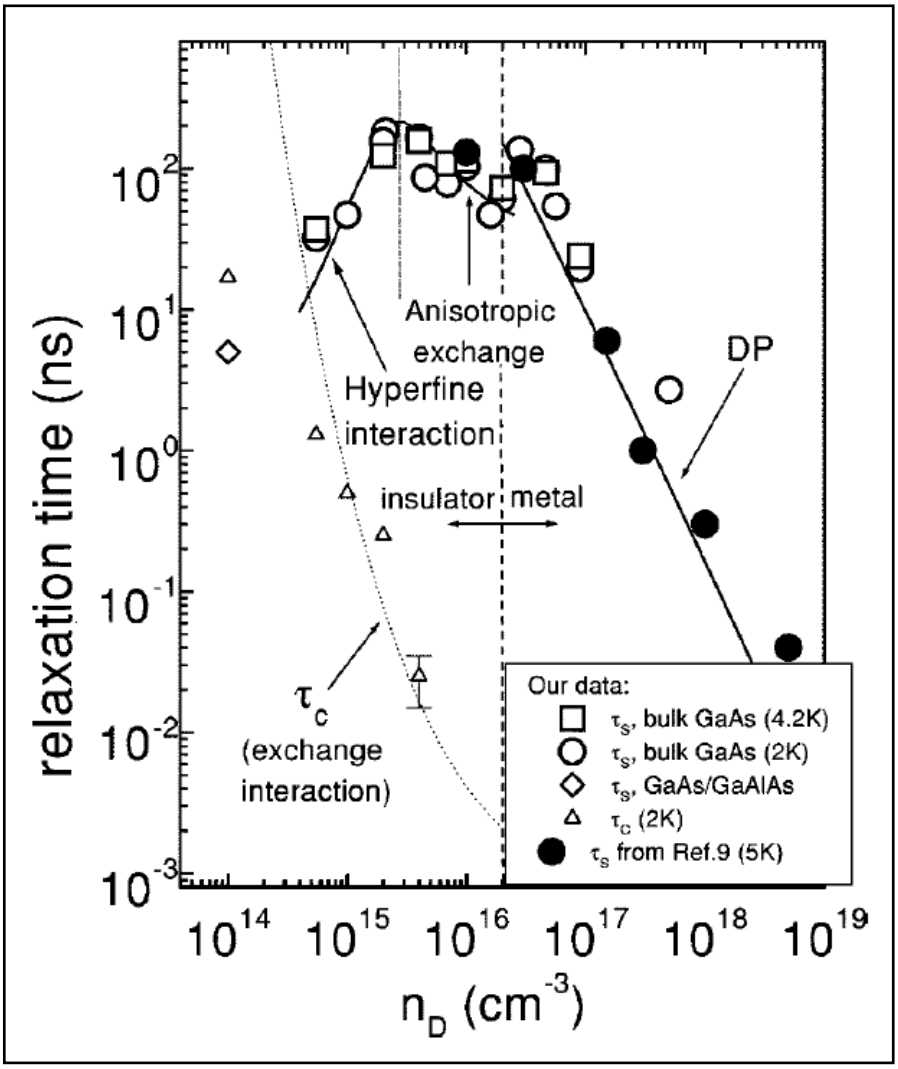

Fig. 3.16: Spin relaxation time for n-doped GaAs. Two peaks are observed at 2×10^{15} and 2×10^{16} cm^{-3}. Below the metal insulator transition the electrons are localized at the donors while at higher concentrations the Dyakonov-Perel mechanism dominates the decrease in spin relaxation time[Dzhi]. It was shown theoretically that this maximum of the spin relaxation time correlates with the onset of degeneracy and decreases at further increased doping levels at zinc-blende semiconductors[Jian].

At doping levels above the MIT of GaAs, so around 2×10^{16} cm^{-3} and more, the electrons are delocalized in the conduction band and τ_s decreases as N_d^2, what is consistent with the DP mechanism induced by ionized impurity scattering. At the MIT the relaxation times reach outstanding 100 ns and above but sadly only in a very limited doping range[Kikk] where the conduction takes place through an impurity band and the electrons are yet bound to the donors. A new relaxation mechanism called anisotropic exchange was suggested to explain this behavior[Kavo]. If one goes to even lower doping densities hopping of electrons is lessened more and more and so HFI of the electron spins with the semiconductor nuclei Ga and As leads to increased spin relaxation. Recent reports on this topic show however, that we do not understand the mechanisms well enough, especially when increased temperatures come into play[Dzh1].

4 Wafer Material and Sample Preparation

The sample preparation consists of many different steps. Beginning from the big dimensions of a whole 2 inch GaAs wafer to the smallest nanostructures variable processes are applied to get a readily processed structure that can be measured in a cryostat. This chapter presents the main tasks in our sample preparation and the according processing methods we used. The explicit process cycles performed for the analyzed structures of chapter 6 can be found in the appendix A. For further information on processing technology itself the reader is referred to the technical literature[Menz],[Widm].

4.1 Wafer material

During our work we have tested several wafers with different layer thicknesses and varying doping densities. Yet the basic design was always the same and is depicted in figure 4.1. On undoped buffer layers and AlGaAs/GaAs super lattices the relatively low doped transport channel was grown. Its doping level was slightly above the metal-insulator transition in the range of $2-6 \times 10^{16}\,cm^{-3}$ to assure long spin lifetimes, according to figure 3.16 above. A transition layer

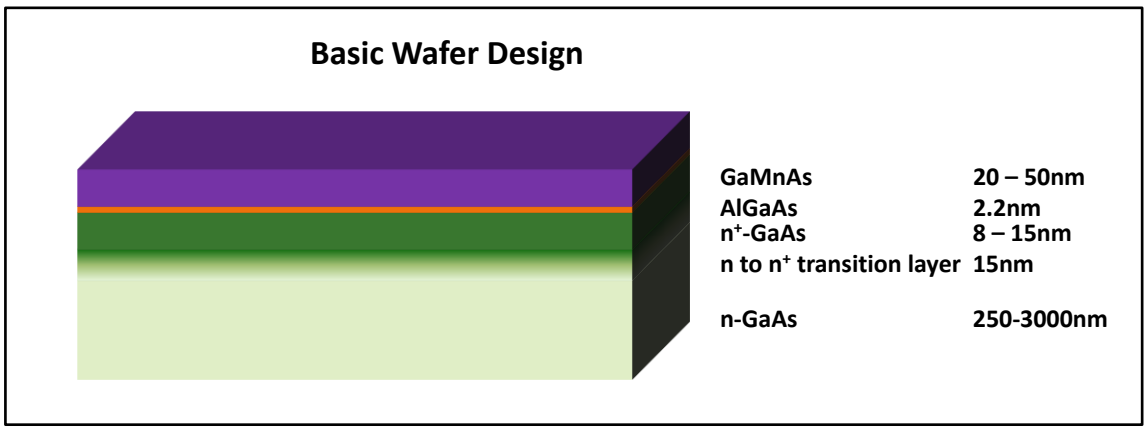

Fig. 4.1: The wafer design was basically the same in all our tested structures. Only the individual layer thicknesses and doping densities were adjusted for each newly designed wafer to test specific characteristics.

consisting of five 3 nm thin steps was subsequently grown to gently adjust the doping level to the highly doped n^+-region. This n^+-layer was very thin, as thicker layers consistently lead to lower spin injection efficiencies due to increased scattering[Koh1]. The directly following very thin low temperature AlGaAs layer was grown to prevent the Mn atoms from diffusing into the n-doped regions[Schu]. The top layer consisted of GaMnAs with around 5 % of Mn. The GaMnAs layer together with the highly n^+-doped GaAs create an Esaki tunneling diode, which is used to convert the spin polarized holes within the GaMnAs into electrons injected into GaAs. This interband tunneling is

necessary to circumvent the extremely short spin lifetimes of holes in GaAs due to spin-orbit interaction[Fabi],[Hilt],[Dya2].

4.2 Wafer preparation

The very first processing step for a freshly MBE-grown wafer is to cover it with an optical resist to prevent the surface from oxidation and mechanical damage. Then we have to remove the gallium from the backside of the wafer, which is used in the MBE chamber for fixing the wafer on the sample holder during growth. This backside cleaning is done with pure HCl, heated to 75 °C. After that the wafer can be cleaved into smaller pieces, to allow a reasonable handling of the samples. Therefore we cut the wafer into 5x5 mm² quadratic pieces. This is done by a small diamond tip that is used to scratch the wafer surface. This scratch defines the predetermined cleaving direction (a GaAs crystal breaks in two preferential directions, namely the [110] and the [1-10] directions). The wafer is subsequently cleaved with the help of a defined sharp edge. One corner of each square piece is marked to be aware of the crystal orientation later on. With every unit of the wafer numbered and marked, a wafer map can be created as the ones shown in figure 4.2. These maps are used for processing purposes and to track the quality of the measured devices. Generally one can say that the outermost regions are not worth measuring, as their quality is very bad. Samples originating in the outer third of the wafer radius were never giving good results in our experiments. Therefore we were using these pieces only for etch tests in the end.

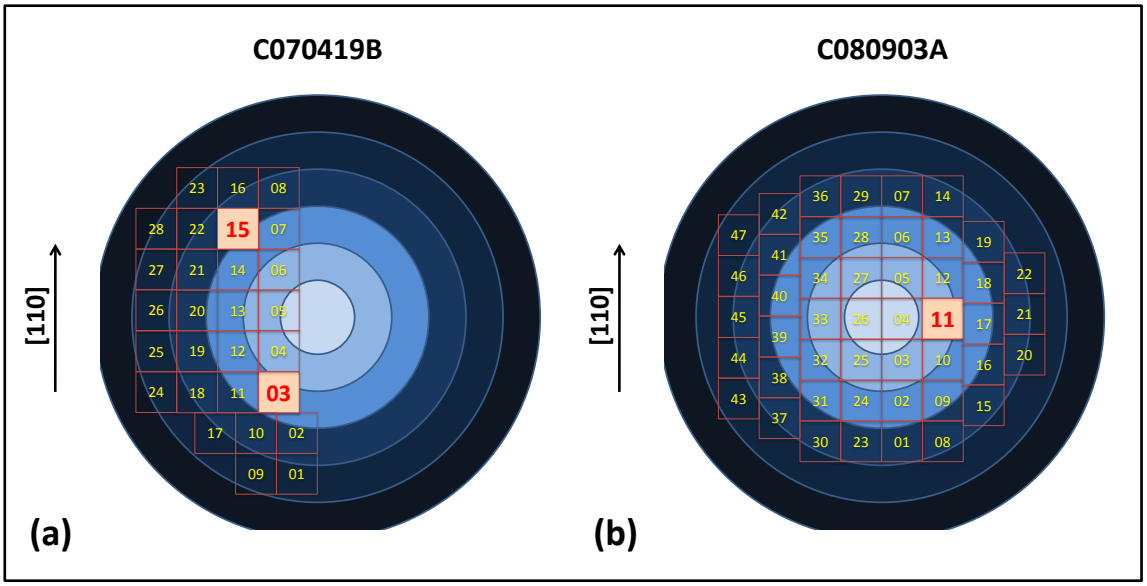

Fig. 4.2: The wafer maps show the location of the structures of which we will present measurements in chapter 6. As one can see the brighter the color, the more central the location on the wafer. In the very outer regions generally temperature during MBE growth is not adequately controllable due to geometrical reasons of the sample holder design and also the layer-thickness calibration is done for the sample center.

4.3 Sample preparation

4.3.1 Cleaning cascade

At the beginning there is the cleaning of the wafer surface by a cleaning cascade. That is 5 minutes in an acetone bath in the ultrasonic cleaner, followed by a new acetone bath and 60 seconds ultrasound and the same again for 30 seconds. After each acetone bath the sample is swilled with fresh acetone from a spray bottle to wash away potentially adherent dirt particles. Subsequently the sample is stored in an iso-propanol bath until the next processing step.

4.3.2 Resist spin-coating

Generally there exist two different resist types, positive and negative. While developing a positive resist, the exposed areas are dissolved. A negative resist behaves the other way round but needs a second processing step, typically a heating step to provide the thermal energy for a cross linking of the resist molecules, to be finished. For covering the samples with different sorts of optical and e-beam resists, we used standard spin-coating techniques. The sample is fixed through a small vacuum pump in the center of the spin-coater plate and the resist is dispersed all over the sample. The spin-coater turns with sufficiently high rotation speeds (some thousand rounds per minute) to distribute an evenly thick layer all over the sample (apart from the edges, where a thicker beading due to surface tension appears). Final thickness depends on the chosen resist, rotation speed and time (see table 4.1).

Resist	Rpm (acc)	Time	Bakeout	Time	Thickness
O:Shipley 1805	6000 (0)	30 sec	90 °C	2 min	500 nm
O:Shipley 1813	6000 (0)	30 sec	90 °C	2 min	1300 nm
O:ARP 3740	3000 (0)/8000 (9)	5/30 sec	110 °C	3 min	1280 nm
O:AZ 5214 E (neg)	6000 (0)	30 sec	90 °C	2 min	1450 nm
E:PMMA 200k (7%)	3000 (0)/8000 (9)	5/30 sec	150 °C	5 min	350 nm
E:PMMA 950k (2%)	3000 (0)/8000 (9)	5/30 sec	150 °C	10 min	85 nm

Tab. 4.1: The processing parameters for optical (O:) and e-beam (E:) resists. AZ 5214 E is the only negative resist that was used by us. The given values for acceleration (acc) describe the parameters for reaching the desired rotation speed, where 0 means quasi instantaneously and 9 only very slowly.

For e-beam lithography usually a two-layer resist system is used, as this gives a clearly superior lift-off behavior compared to single layer resists. The bottom layer is made of the resist with shorter molecule lengths and the topmost layer has longer molecules. This leads to an undercut in the resist structure as the shorter molecules in the bottom layer are better dissolved in the developer and

thus prevent the metallization to stick on the sidewalls during lift-off process. This is a similar effect as appears while using negative optical resists, which makes them superior in lift-off behavior compared to positive ones.

4.3.3 Lithography

For big structures like mesas, Hall-bars or bond-pads standard optical lithography is used. The desired structure of a chrome mask is transferred to the optical resist by means of a mercury vapor lamp in a Karl Suss MJB 3 mask aligner. The emitted light is in the UV-range and its photons deposit enough energy to destroy the resist molecules, what makes them easily dissolvable in an adequate developer. The exposure times depend on the resist, its thickness and the used mask, as the glass substrates of the masks have different thicknesses and therefore the absorption in the glass substrate is different.

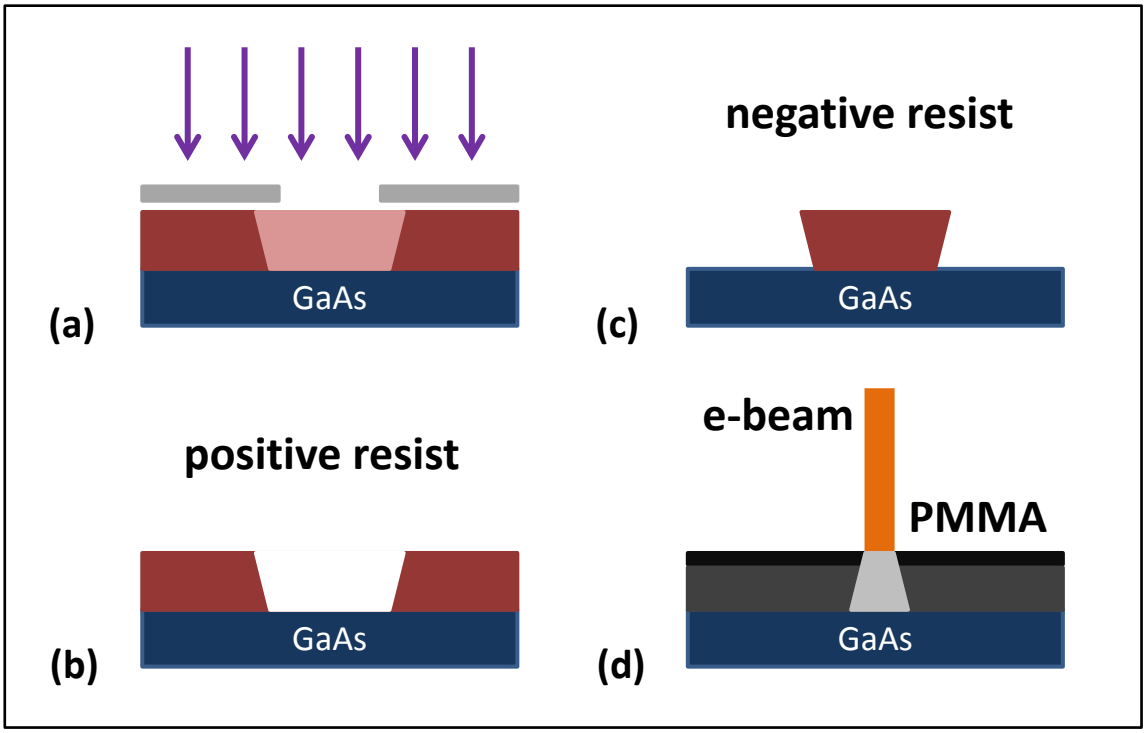

Fig. 4.3: The exposure of an optical resist (a) leads naturally to a broadened structure size due to light diffraction. A positive resist is developed and the resulting angle of the bevel often leads to a bad lift-off behavior (b). Negative resists use a bake out step and the developing removes the not exposed areas (c). Similar to double layer e-beam resists this leads to an undercut (d), what simplifies the lift-off enormously, see section 4.3.2.

For very small structures optical lithography is not applicable as diffraction at the structure edges of the mask limits the achievable lateral resolution (especially with our optical hardware, stability, vibrations, etc.) at long structures to around 2 µm. For smaller structures e-beam lithography (EBL) is the method of choice. The e-beam-sensitive resist is exposed with a focused electron beam using acceleration voltages of 30 kV in a scanning electron microscope (SEM). The beam is moved across the sample in a grid pattern and a beam blanker inhibits the sample from being exposed at unintended places.

Besides the advantage in achievable structure sizes e-beam lithography is much more flexible, as a new mask can readily be made in minutes on a PC[Nano]. The downside is however, that only small structures can be made in reasonable timescales with EBL.

Resist	Exposure	Time	Dose	Depends on
O: Shipley 1805	UV-light	12 sec	---	Used mask/lamp age
O: Shipley 1813	UV-light	55 sec	---	Used mask/lamp age
O: ARP 3740	UV-light	36 sec	---	Used mask/lamp age
O: AZ 5214 E (neg.)	UV-light	40 sec	---	Used mask/lamp age
E: PMMA 200k (7%)	e-beam	---	225-550 μC/cm²	Structure size/acc. voltage
E: PMMA 950k (2%)	e-beam	---	225-550 μC/cm²	Structure size/acc. voltage

Tab. 4.2: The exposure times for the optical resists depend on the used mask and the already completed service life of the used UV-lamp. The critical points for the right exposure dose for e-beam resists are the used acceleration voltage of the electron beam as well as the structure size as this has an immense impact on the proximity effect.

4.3.4 Development

After the resist has been exposed one has to develop it in a convenient chemical dilution. For optical resists usually NaOH based developer solutions are used for that purpose. In the case of PMMA, there can be used different dilutions, e.g. pure iso-propanol, propanol mixed with methylene isobutyl-ketone (MIBK) or 2-(2-3-Epoxypropyloxy) ThioXanthone (ETX, which we avoided as it is very toxic). We used a dilution of one part MIBK for three parts iso-propanol by default.

Resist	Developer	Time	Cleaning	Postbake	Time
O:Shipley 1805	Microposit 351/H_2O (1:4)	27 sec	DI water	110 °C	3 min
O:Shipley 1813	Microposit 351/H_2O (1:4)	40 sec	DI water	110 °C	3 min
O:ARP 3740	AR 300-26/H_2O (1:3)	26 sec	DI water	110 °C	3 min
O:AZ 5214 E (neg)	AZ 351 B/H_2O (1:4)	~4 min	DI water	120 °C	50 sec
E:PMMA 200k (7%)	MIBK/iso (1:3)	20 sec	propanol	---	---
E:PMMA 950k (2%)	MIBK/iso (1:3)	20 sec	propanol	---	---

Tab. 4.3: The developers for optical resists are generally all based on NaOH dilutions. A postbake of PMMA is very critical as the resist starts melting at higher temperatures and the sharp edges start smearing. This is counterproductive for the realization of nanostructures.

After developing the resist the sample is put in deionized water (optical resists) or pure propanol (EBL resists) to stop the chemical reaction and to clean the sample surface as well. Concluding, the optical resist has to be post-baked. In this step the heating removes all humidity from the resist and makes it resistive against physical damage. Additionally the structure edges are also sharpened by the post-bake. After this step the sample is ready for the evaporation of a metallization or an etch step.

4.3.5 Deposition of metallization and isolators

For the deposition of contacting material or isolating dielectrics the readily developed sample is put into the adequate facility. For contacts the appropriate metallization is deposited by a Univex 450 A evaporation system. Typical contacts to GaMnAs layers are made by titanium (alternatively chromium can be used as well) as a thin sticking layer and subsequently a thick gold layer (typically 15 nm Ti and 130 nm Au). Titanium is heated by an electron gun (with 6 kV acceleration voltage) while gold is heated thermally (inside a tungsten crucible and with roughly 140 A heating current). The layer thickness can be controlled with the help of a quartz monitoring system. For contacts to n-type GaAs Pd/Ge or Pd/Ge/Au contacts were used. They have to be annealed after deposition creating an extremely high doped surface layer through Ge indiffusion[Love],[Wang] into the GaAs layer.

Material	Chamber	Current	Rate	Temperature	Thickness
Ti	Univex	45 mA (e-gun)	2 Å/sec	---	15 nm
Au	Univex	140 A (thermal)	2.5 Å/sec	---	150 nm
Pd	Univex	55 mA (e-gun)	1 Å/sec	---	10-45 nm
Ge	Univex	145 A (thermal)	2.5 Å/sec	---	50-111 nm
Cr	Univex	135 A (thermal)	0.3 Å/sec	---	15 nm
AuPd	Univex	130 A (thermal)	2 Å/sec	---	5 nm
SiO_2	PECVD	---	40 nm/min	105-115 °C	250-4000 nm
Si_3N_4	PECVD	---	10 nm/min	105-115 °C	250-700 nm
Al_2O_3	ALD	---	1 Å / 45 sec	100 °C	5-50 nm

Tab. 4.4: The different metallization materials used during this work were evaporated within the Univex chamber. The sample temperature is not known. $Si0_2$ and Si_3N_4 were made with PECVD in a temperature range right above 100 °C. In the ALD chamber this low processing temperature leads to very long pumping cycles that determine the extremely small growth rates. In PECVD and ALD processes the sample plate can be hold at a defined temperature.

For isolating SiO_2 or Si_3N_4 layers the plasma enhanced chemical vapor deposition (PECVD) method is used while Al_2O_3 was deposited in an atomic layer deposition (ALD) chamber. These layers are added to prevent leakage currents between the bond pads or parasitic current flowing between the current feed lines that have physical contact to the mesa sidewalls. After finishing the deposition the sample is placed in a heated (60 to 90 °C) acetone bath to remove the resist together with the deposited material at the covered regions. This is the so-called lift-off process.

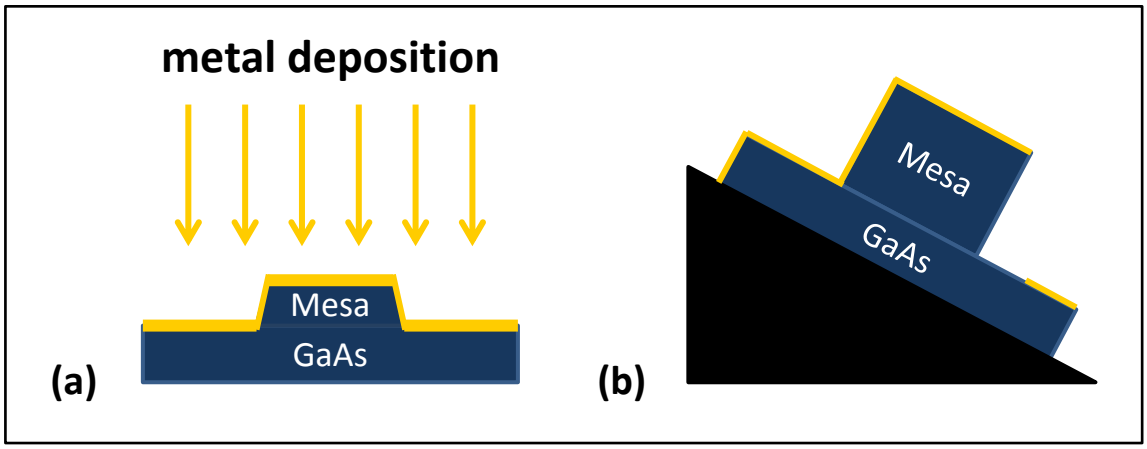

Fig. 4.4: If contact metallization is deposited a small height difference and trapezoidal shape of the mesa make things much easier (a). If the mesa was structured with anisotropic RIE and/or the height step is very large, then a closed metallization layer is not self-evident. Therefore we used small wedges with different angles while evaporating the contacts. Naturally the averted side of the mesa now is shadowed (b).

4.3.6 Etching

The appropriately prepared sample is put either into our chemical assisted ion beam etching (CAIBE) or reactive ion etching (RIE) chamber for physical etching or alternatively etched in an adequate wet chemical solution. The wet chemical etching has the big advantage of generating no physical damage to the sample surface, but on the other hand suffers from severe underetching of the masked structures, which is a big problem at very small structure sizes. The physical etching methods have the advantage of nearly eliminated underetching tendency but harm the sample surface structure through the high kinetic energy and additionally occurring radiation damage. This is not acceptable at very sensitive parts of the sample as the uncovering step of the low doped conduction channel at the end of the processing cycle for example, because the spin relaxation lengths are severely shortened due to highly increased scattering rates. Physical etching creates defects and surface states that can clearly dismantle the measurement results. Table 4.5 summarizes the used recipes and etchants.

After such an etching process the resist can be removed. This again is done in a heated acetone bath, but now this process is called resist striping.

Method	Recipe	Ratio/press/flow/fp	Isotropic	Etch rate
Wet chemical	Acetic acid/H_2O_2/H_2O	5:1:5	yes	≈ 4.65 nm/sec
Wet chemical	Acetic acid/H_2O_2/H_2O	15:3:50	yes	≈ 1.8 nm/sec
Wet chemical	Citric acid/H_2O	3.5-10:1	yes	1.5-3.5 nm/sec
RIE	$SiCl_4$	13mT/4sccm/15W	no	≈ 2.5 nm/sec
RIE	$SiCl_4$	15mT/25sccm/72W	no	≈ 2 nm/sec
RIE	$SiCl_4$	15mT/20sccm/80W	no	≈ 2.5 nm/sec
RIE	$SiCl_4$	15mT/20sccm/120W	no	11- 13 nm/sec
RIE	$SiCl_4$	15-25sccm/72-120W	no	2 to 13 nm/sec
CAIBE	Ar^+		no	< 1 nm/sec

Tab. 4.5: Due to the extreme chemical stability of GaAs even concentrated HCl provides noticeable etch rates not until temperatures of 250 °C. Therefore H_2O_2 is added to the acidic dilution to oxidize the surface, which can then be removed easily by acids at room temperature. In RIE processes radicals and ions are generated in a plasma what results in chemical as well as physical etching. We used only CAIBE processes with pure Ar^+, without adding Cl. This process uses pure physical momentum transfer to strike out surface atoms, thus it is actually an IBE mode etching, to be precise.

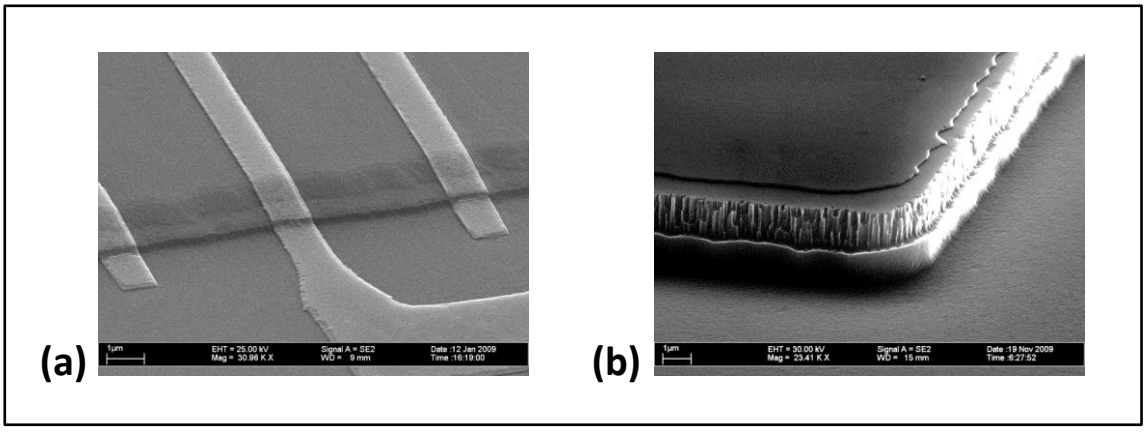

Fig. 4.5: The choice for an etching method has enormous consequences on the further sample processing. The naturally given underetching tendency of wet chemical etchants renders this method unusable for very fine lateral structures. For broad mesa structures, however, this underetching leads to a trapezoidal mesa form (a), which supports easy evaporation of contact metallization, see fig. 4.4. If one has to etch several micrometers deep to isolate the thicker conduction channel of some wafers the RIE method can be used. Though, high power is needed to get reasonable etch rates and this leads to very high sidewall damage (b). The top GaMnAs layer is now hard to contact reliably even with tilted evaporation methods.

4.3.7 Sample preparation Roundup

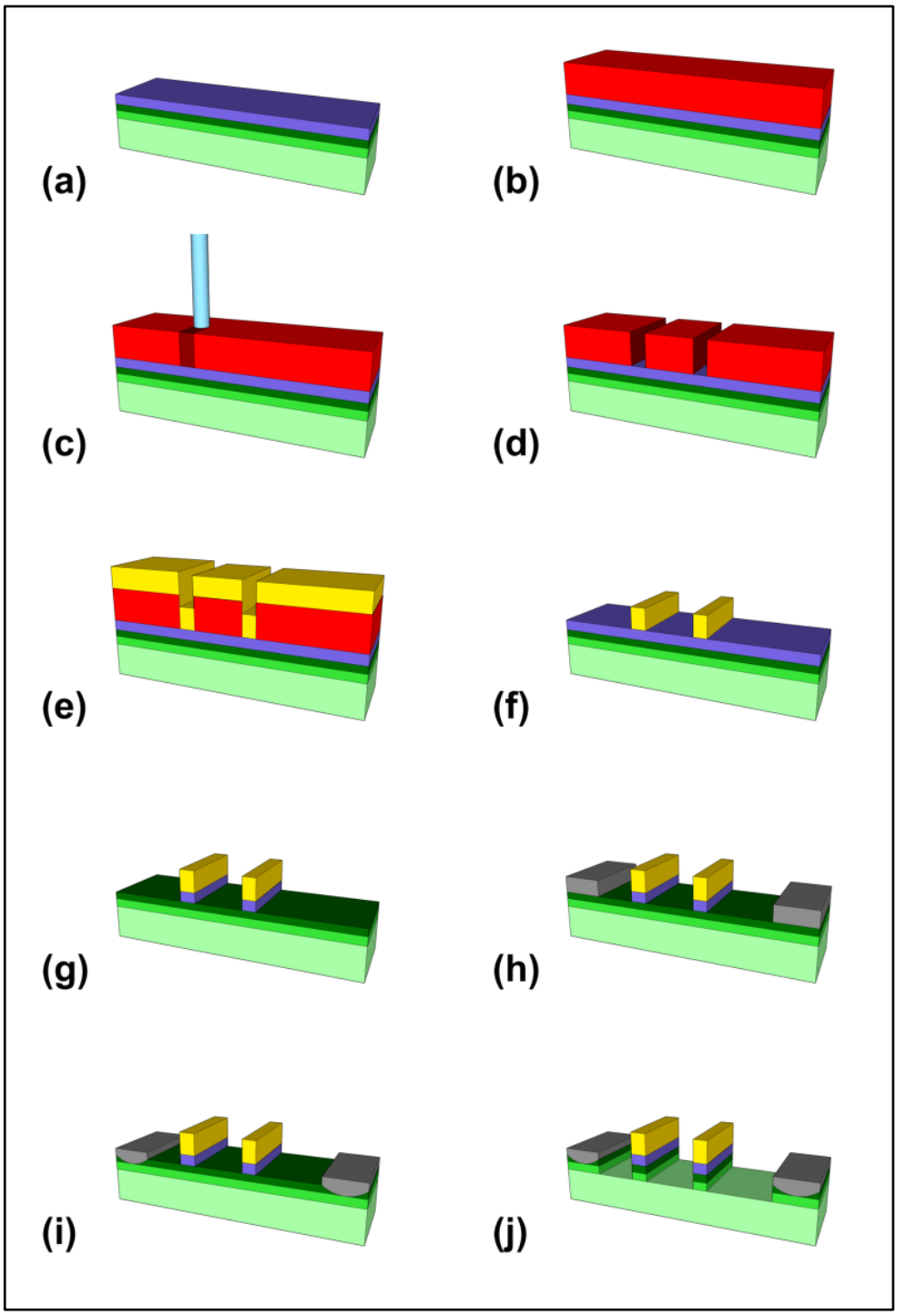

Fig. 4.6 Sketch of the sample processing. (a) A readily etched mesa structure. It is covered by a PMMA e-beam resist (b) whose molecular structure is destroyed by a 30 keV electron beam of a SEM (c). After developing in MIBK/propanol (d) a Ti/Au metallization is evaporated for contacting the GaMnAs layer (e). The lift-off process (f) removes the metallization on top of the resist covered areas and uncovers the desired structures. In a further etch step (g) the highly n^+-doped GaAs layer is uncovered and again contacts are defined by EBL and Pd/Ge(/Au) contacts are evaporated (h). In an annealing process the material diffuses into the semiconductor and creates a heavily doped surface layer that realizes a low resistive ohmic contact (i). In a last etch step the current flow is confined to the low doped channel (j).

5 Measurement Techniques

This section describes the measurement setup used for characterization of the lateral spin-valve structures. All measurements were done at low temperatures (1.5 to 60 K) in ^{4}He Cryostats.

5.1 Cryostat systems

For cooling the samples below their Curie temperatures we used two different ^{4}He cryostat systems. The first one is depicted in fig. 5.1. A big Dewar is designed to hold a liquid helium bath, which is used to keep the superconducting magnet's solenoid below its transition temperature. The double isolated variable temperature inset (VTI) is placed in the middle of the cryostat Dewar and makes it possible to bring the sample in the center of the magnet coil, where the generated magnetic field can be assumed completely homogeneous[Oxfo]. The VTI is connected to the liquid helium bath by a needle valve, which lets one control the amount of helium flowing into the VTI. By pumping the vapor pressure in the VTI can be reduced and so the temperature can be lowered to roughly 1.5 K. By additionally using a heater that is mounted at the bottom of the VTI the sample space can be heated to around 200 K. A temperature sensor that is integrated in the probe, directly beneath the sample, lets one track the sample temperature very precisely.

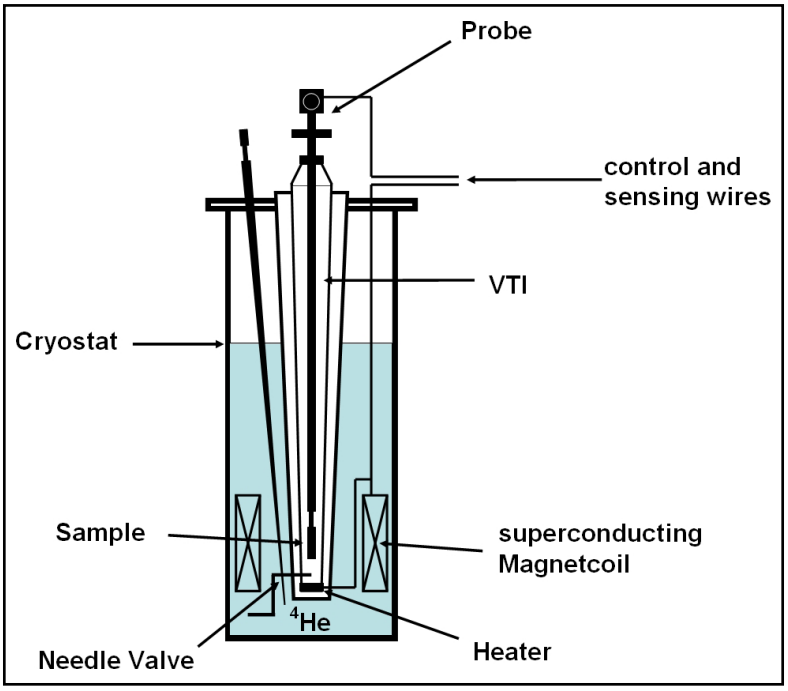

Fig. 5.1: ^{4}He cryostat system from Oxford[Oxfo]. The superconducting magnet coil is immersed in liquid helium all the time. Opening the needle valve lets helium flow into the VTI and cool the sample space.

To perform in-plane and out-of-plane field measurements there are two different sample holders that can be mounted at the end of the probe. The in-plane holder can be rotated by 360 degrees for different angles between the structures and the magnetic field, while the out-of-plane holder can be used to tilt the sample plane out of the magnetic field direction.

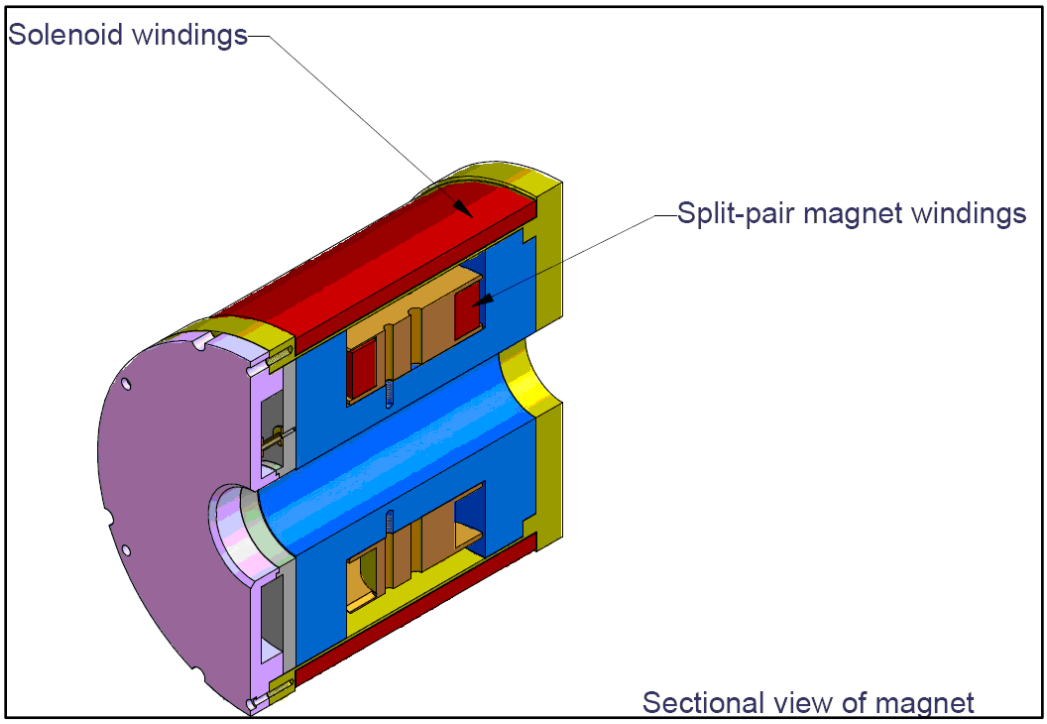

Fig. 5.2: Cross sectional view of the 3D-vector magnet. There are two split pairs to generate fields in the x-y plane while a big solenoid coil generates the out-of-plane fields in z-direction. The probe that contains the samples is inserted into the hole in the middle to provide homogeneous fields in the sample space[Cryo].

The second cryostat system is a 3D-vector magnet made by Cryogenics Limited. The big difference to the Oxford system is the availability of two additional split-pair coils inside the Dewar vessel. Each of the three magnets is specified to reach a field of 1 T. So combining the three individual fields any arbitrary field vector up to an absolute value of 1 T can be achieved (of course the geometrical maximum would be higher, but the system is only specified up to fields of 1 T in arbitrary directions). Contrary to the Oxford system the VTI of the vector magnet cannot be filled with liquid helium but is a gas-flow-only cryostat. So it has to be pumped all the time while measuring. On the other hand this system is capable of operating up to 320 K VTI temperature.

5.2 Measurement setup

Most measurements are done using DC technique. Only for very low injection currents we used AC measurements. All measurement devices were connected to a pin box on top of the probe by coaxial cables to prevent the setup from capturing interfering signals from outside. From the connection box to the sample a wiring inside the probe is used.

5.2.1 DC setup

For DC measurements we used a Keithley 6221 as a constant current source. It was directly connected to the injector contact. At the ohmic contact of the injector circuit we attached an Ithako 1211 current preamplifier that was read out by an Agilent 34410A 6.5 Digit Multimeter (DMM). The voltage drop across the injector circuit was also measured by an Agilent 34410A. For measuring the detector signals we used Nanovoltmeters (NVMs), either Agilent 34420A or Keithley 2182A models. Important to mention is the fact that signals from the three different detectors were measured simultaneously during the same magnetic field sweep and not in different consecutive runs. All measurement devices and the magnets were connected by a GPIB bus to a GPIB-USB-HS adapter that was controlled by a self-made PC program to read out all devices and control the magnetic field.

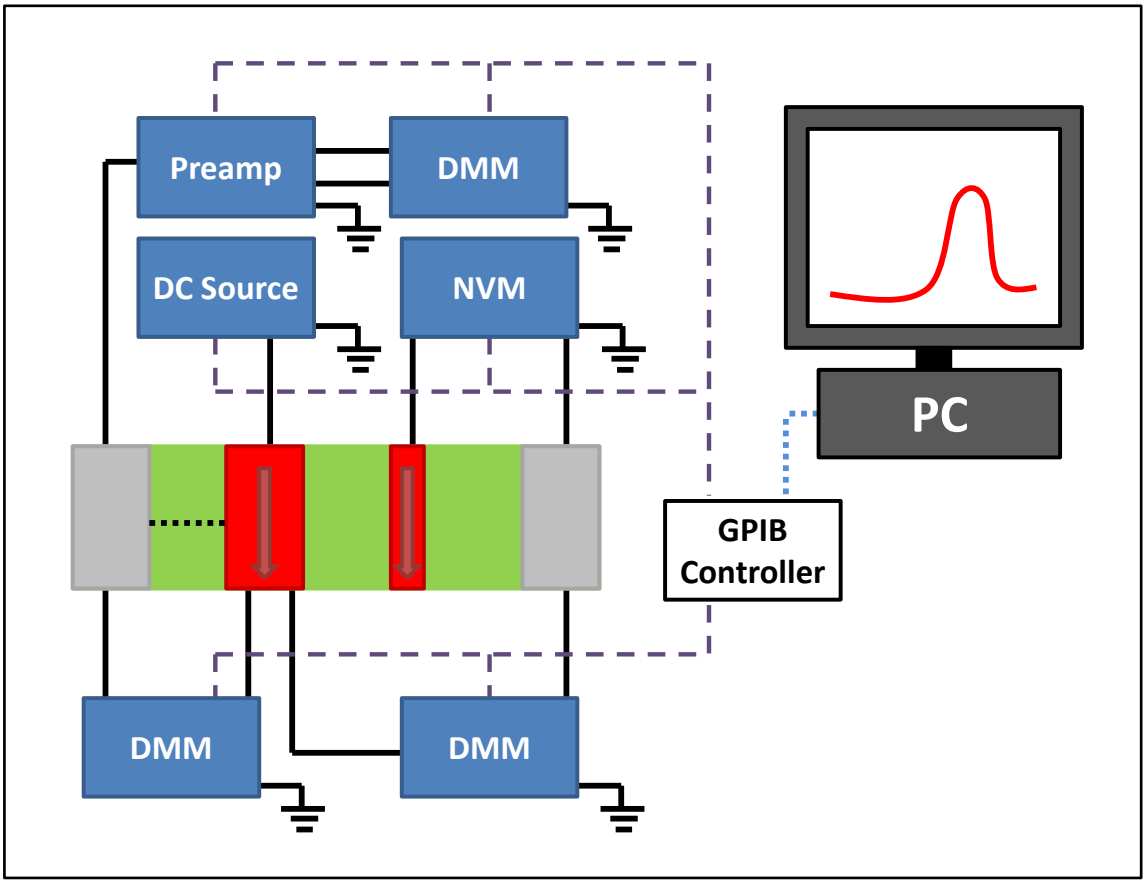

Fig. 5.3: Sketch of the DC measurement setup. We drive a constant current through the injector circuit by a Keithley 6221. The current leaves the system through an Ithako 1211 preamplifier, which converts the current into a voltage that is measured by an Agilent 34410 digital multimeter. The arising voltages in the injector circuit, the 3-point resistance of the injector contact alone and the nonlocal voltages arising between detectors and reference contact are measured with nanovoltmeters or multimeters, dependent on the specific interest and resolution needs. The control and read-out of the measurement equipment is done by a GPIB 488.2 controller, which is directly connected to a PC system by an USB bus.

5.2.2 AC setup

For the AC measurements we used EG&G 7265/7260 DSP Lock-Ins from Signal Recovery. The master lock-in gives the frequency for all other attached lock-ins and the master output "osc out" is connected to a high ohmic resistor of 10 or 100 MΩ. This leads to a constant current measurement setup as the magnetoresistance change of the sample structure itself is many orders of magnitudes smaller than the shunt resistance. As in the DC setup the additional lock-ins are connected between the detector contact and the second ohmic contact to sense the arising *emf* due to spin accumulation in the sample or measure the injector circuit voltage or 3-point injector contact resistance. The lock-in technique is far superior in signal-to-noise ratio compared to DC measurements in the case of low excitation current in the injector circuit. Contrary to DC measurements we lose the information on differences between spin injection and spin extraction, though.

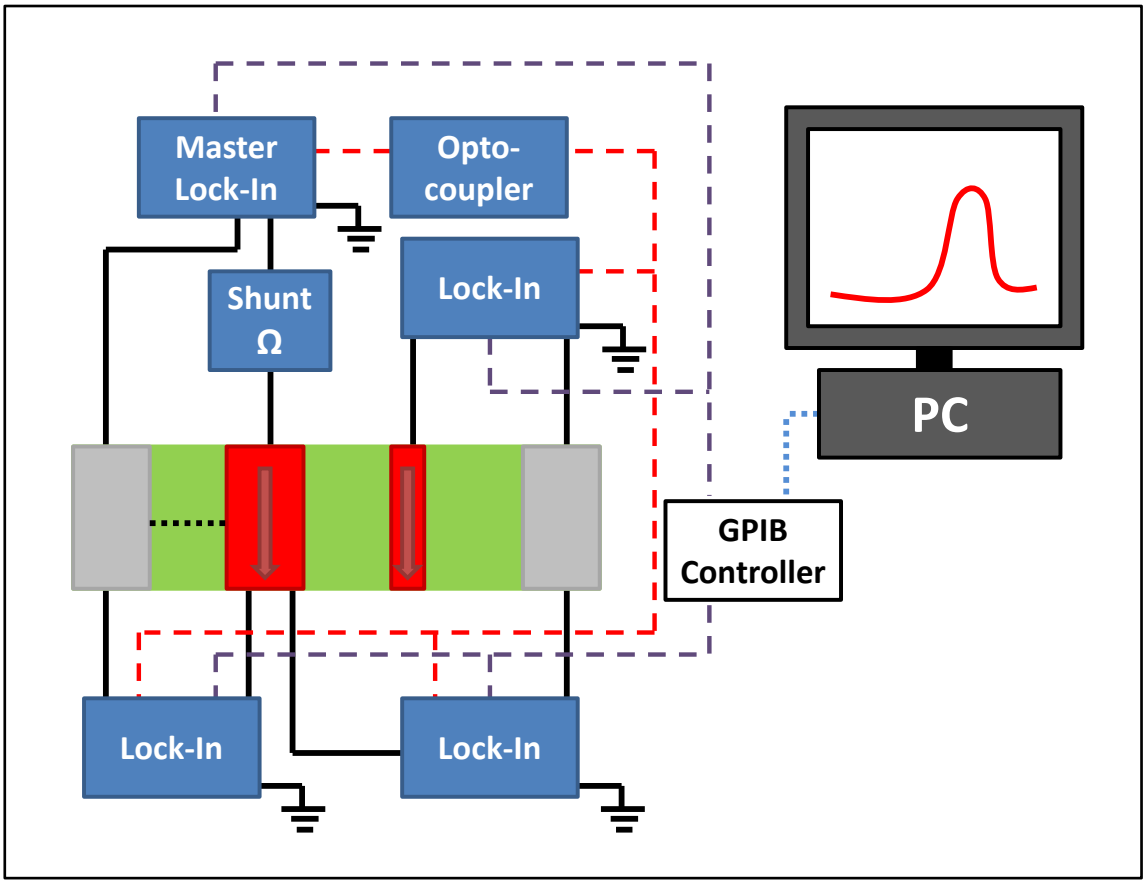

Fig. 5.4: Sketch of the AC measurement setup. The Oscillator output of the master Lock-In applies a voltage to a shunt resistor of 10 or 100 MΩ. This resistance is much higher than the arising electrical resistances of the sample structures. This leads to a constant current measurement, even if field dependent magneto resistances arise. The current flows through the injector circuit and back to the master Lock-In. The AC frequency is synchronized to all other Lock-Ins by means of a galvanically isolated opto-coupler. These Lock-Ins can now be used again to measure the voltage drops across the injector circuit, the 3-point resistance of the injector contact alone and the nonlocal voltages between detector and reference contact. The control and read-out of the measurement equipment is again done by a GPIB 488.2 controller, which is directly connected to a PC system by an USB bus.

Of course also the lock-ins are connected by a GPIB bus to the host PC for control and read out operations, although sometimes a serial RS232 connection is used because some equipment will not work when connected on GPIB altogether.

6. Results and Discussion

Most of the results we present are from structures made of wafer C070419B. Based on the references [Koh1], [Dor2] and [Ade1] a wafer design was developed which should have combined the effective spin injection scheme from p-type GaMnAs into n-type GaAs that has been proven to work in optical spin LED experiments[Kita],[Kohd],[Koh1],[Dor2], as well as the long spin diffusion length in n-doped GaAs as was demonstrated in some different experiments so far[Dzhi],[Kikk]. C070419B was our first fully functional wafer in terms of spin injection and transport. In chapter 6.6 we present measurements done on wafer C080903A that show some of the advantages of its slightly modified layout and therefore give us some evidences how to further improve spin injection devices.

6.1 I-V curves of Esaki diodes (and pn simulation)

We present measurements on structures made of sample number 15 and 03 of wafer C070419B in the following subchapters. The structures differ in their particular crystallographic orientation. While on sample number 15 the mesas are oriented along [010] direction the ones on number 03 are oriented along [100]. The rest is mainly analogous, from a processing standpoint. The only noteworthy difference besides the orientation is the fact that sample #15 exhibits an isolating SiO_2 layer while sample #03 does not (see chapter 4 and appendix A).

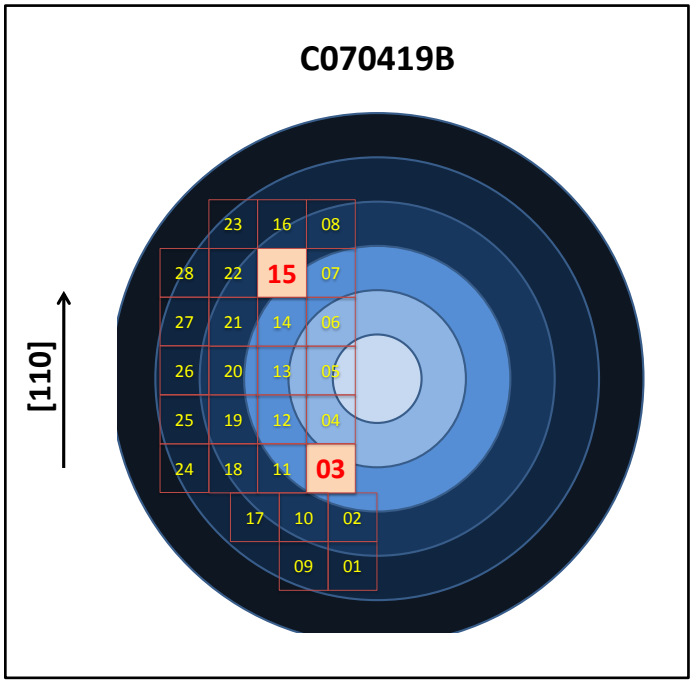

Fig. 6.1: Wafer map of wafer C070419B. The results we discuss here were obtained on two pieces with the numbers 15 and 03 according to the map. You can see the primary (bottom) as well as the secondary flat (left side), which are both used for orientation purposes.

At the beginning we want to present a simple one dimensional simulation of our structure done with the Snider Poisson tool[Snid]. The simulation temperature was set to 4 K. At the GaMnAs side of the junction, we applied the "slope = 0" boundary condition, which is applicable as the high doping lets the GaMnAs act like a metal and we assume a metallic contact on its top. As the band structure of GaMnAs is still not accurately known, the 20 nm thick GaMnAs layer itself is simulated by standard p-doped GaAs. We make use of a virtual p-type dopant with ionization energy of 110 meV, which equals the one from Mn in GaAs host crystals[Linn]. The 2.2 nm thin low temperature AlGaAs layer directly below the GaMnAs is simulated with standard high temperature AlGaAs with the same Al content of roughly 37 %. The subsequent n-type layers are simulated with Si doping and ionization energies of 6 meV. According to the growth protocol of the wafer and a calibration curve of different substrates grown in the MBE chamber we used the following stacking: 8 nm of 6×10^{18} cm^{-3} doping, followed by a transition layer of 3nm thin films doped with 5×10^{18} cm^{-3}, 4×10^{18} cm^{-3}, 2×10^{18} cm^{-3}, 8×10^{17} cm^{-3} and 2×10^{17} cm^{-3}. The lower doped 250 nm thick transport channel finally has a doping of 6×10^{16} cm^{-3}. The transition layer is needed to gently adjust the doping level and prevent spin scattering at interfaces of highly different doping levels. In previous attempts with abrupt changes in the doping concentrations from high n^+ to low n-type doping we could not verify spin transport. We use a step function (that is divided into very fine sections, though) like doping characteristic as a continuous variation of the profile is very difficult to achieve due to the thermal inertia of the silicon filament used for the process of n-type doping in the MBE chamber. The boundary condition for the n-doped epilayers was "ohmic contact", as we use ohmic Pd/Ge contacts for contacting the n-type part of the injection and detection circuits. In figure 6.2 we show the result of a simulation run with a p-type doping concentration in the GaMnAs layer of 5×10^{20} cm^{-3}. This would equal a layer of 5 % Mn content at substitutional Ga lattice sites. As we know the Mn atoms sit also on interstitial places in the crystal, what reduces the effective Mn content as well as the concentration of holes. Both effects change the band structure and as we cannot be sure of the really existing doping profile we additionally calculated the structure with a p-type doping level of 1×10^{20} cm^{-3}. This did not change the qualitative picture of our structure, only the band bending changed a little bit and therefore the thickness of the space-charge region was somewhat different. However, the most important thing is that we do obtain a significant band bending; at the p-doped side the Fermi energy lies in the valence band while in the n-doped region it is in the conduction band. This means that the structure should work as Esaki tunnel diode. An eye-catching effect occurs in part (b) of figure 6.2. The spikes in the conduction as well as the valence band have their origin in the thin undoped AlGaAs layer, as AlGaAs has a bigger band gap than standard GaAs. We introduced this layer because of two reasons. First AlGaAs can be used as an etch stop layer in AlGaAs/GaAs heterostructures when using RIE etching as

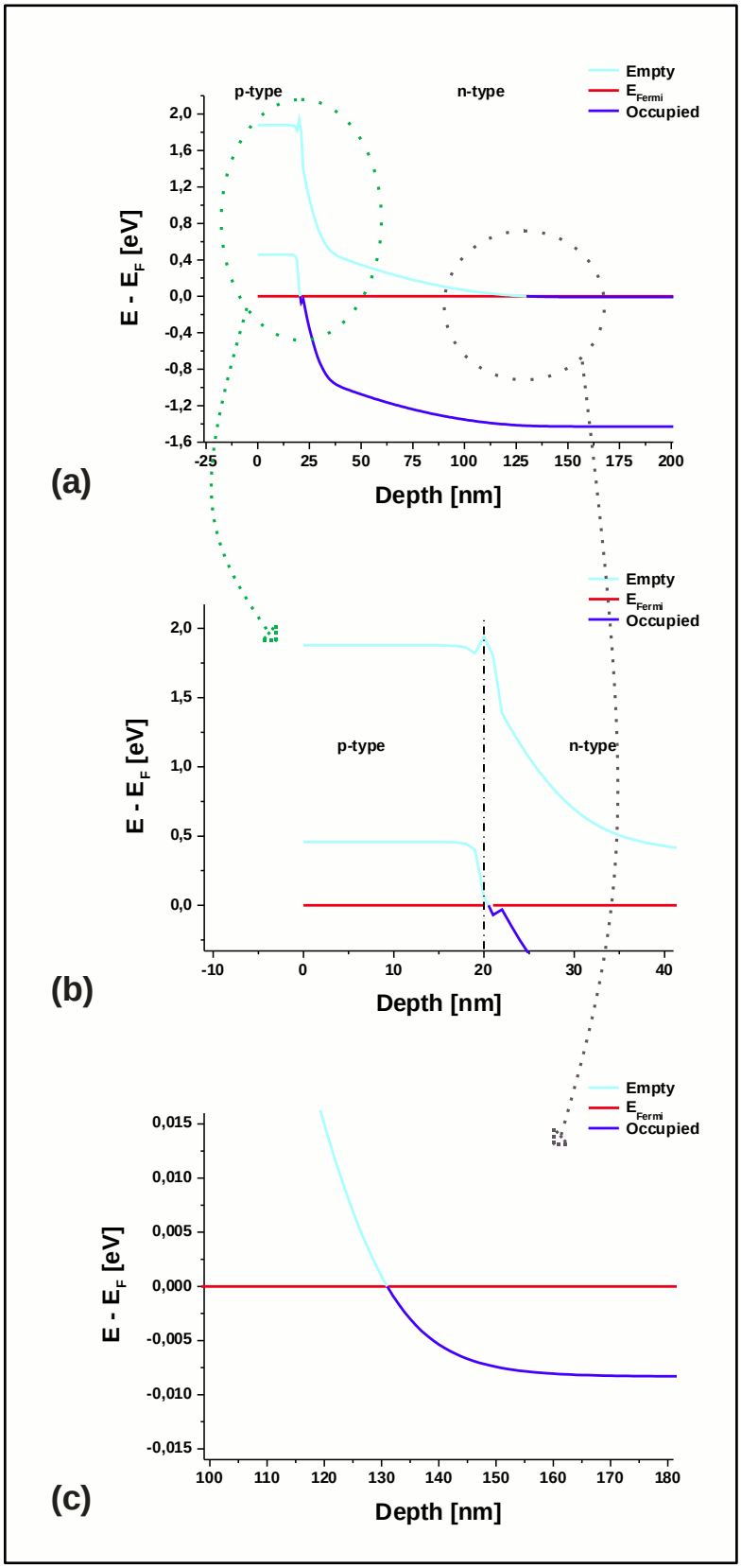

Fig. 6.2: A simple one dimensional simulation of the Esaki diode with the Snider Poisson tool[Snid]. The whole diode with 20 nm p-type GaMnAs on the left side and the n-type GaAs on the right side is shown (a). (b) A closer look at the transition from GaMnAs to GaAs. The cusps in the band structure are due to the thin AlGaAs layer. (c) concludes with the conduction band edge of the n-type GaAs channel, which is below the Fermi level, so interband tunneling between GaMnAs and GaAs can take place.

well as wet chemical etching with the right recipes. Unfortunately the layer was too thin, the Al concentration was too low and we used low-temperature AlGaAs, what altogether made the etch stop layer not working reliably enough. The second and even more important reason was the fact, that low temperature AlGaAs prevents Mn backdiffusion from the GaMnAs layer into the n-type regions what would lead to a compensation of the n^+-doping in the n-type region of the Esaki diode. This effect was discovered by R. Schulz at the chair of Prof. Wegscheider[Schu]. The higher the Al concentration in this layer, the better the diffusion barrier effect. This seems only to work for low temperature AlGaAs, what suggests that the Al atoms that are also integrated on interstitial places in the lattice, due to the low temperature growth, block the diffusion channels for interstitial Mn atoms. We rely on the functionality of Esaki-tunnel diodes for injecting spins into the nonmagnetic GaAs channel via interband tunneling. There, due to the high doping level of both, the p- as well as the n-type region, a small reverse bias leads to the tunneling of electrons from the valence band of p-type region (GaMnAs) to the conduction band of n-type region (Si doped GaAs). This is necessary for the carrier conversion from holes to electrons, as the holes suffer from the extraordinarily high spin-orbit coupling in the valence band and this leads to extremely short (femtosecond scale) spin lifetimes[Hilt],[Dya2]. Therefore we first present a simple I-V curve of an

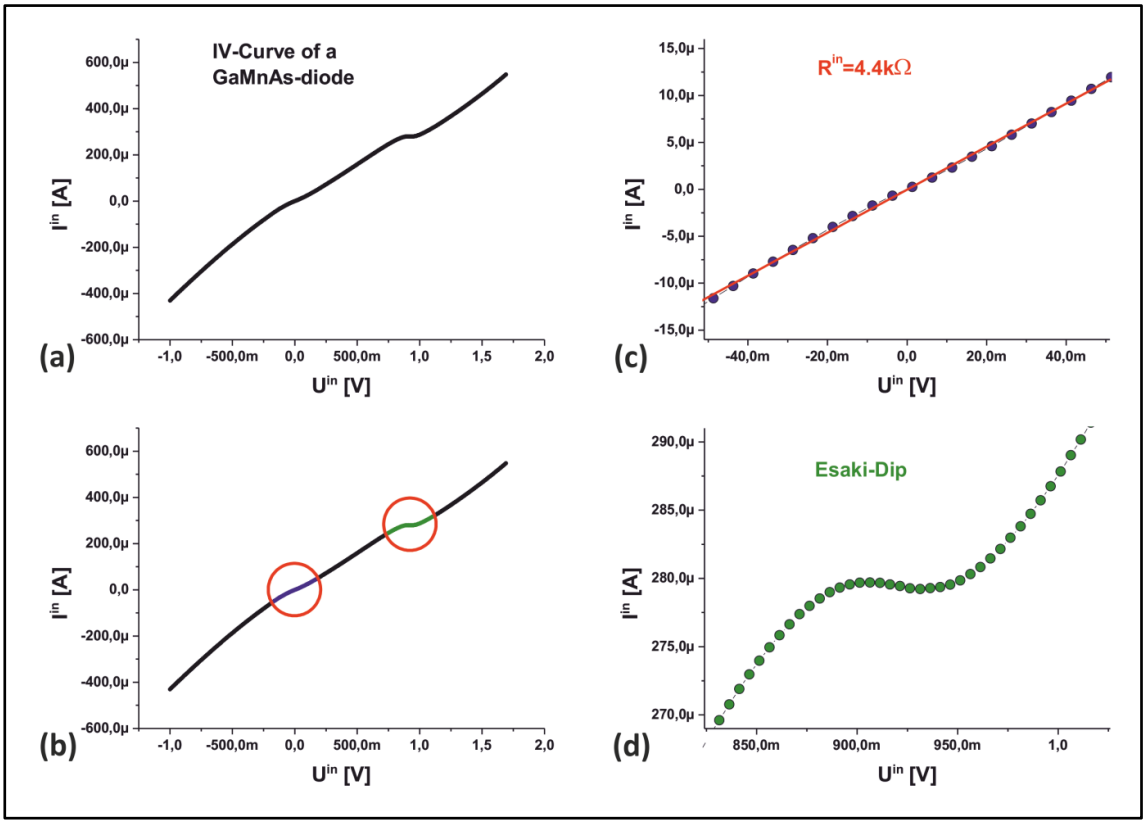

Fig. 6.3: IV-characteristic of a GaMnAs diode contact (a). The two regions of interest are marked in different colors (b). (c) shows the region around zero, which exhibits the characteristic low and nearly linear tunnel resistance of Esaki-tunnel-diodes. Part (d) illustrates the most important characteristic of Esaki tunneling, the Esaki dip. This is a region where a negative differential resistance occurs.

Esaki diode measured at structures made from wafer C070419B. If one looks at the big range curve in figure 6.3 (a), two specific regions are of particular interest, marked in (b). At first the very linear and low resistive region around zero bias voltage, what is typical for Esaki diodes (see figure 6.3 (c)). The second and even more important region is shown in part (d), here we see the negative differential resistance region, a unique feature of Esaki diodes that shows us that we really deal with interband tunneling in our diodes. However, one has to say that this dip only occured at low temperatures, never at room temperature. Additionally it is very dependent on the processing parameters of the structures, especially the annealing time and temperature. This is yet not very surprising, as we do not fabricate perfect industrial-type Esaki diodes and the band structure of GaMnAs is drastically changed by annealing effects. Additionally we certainly introduce some defects within the band bending region through the low temperature AlGaAs layer. As a remark we want to mention, that also Esaki diodes that do not show this dip can work well as spin injection contacts.

6.2 In-plane measurements

In the non-local spin-valve measurement configuration depicted in figure 6.4 one ferromagnetic contact is used as a spin-injector. The applied bias current is driven between the injector and the adjacent non-magnetic ohmic contact through the channel. This spin polarized current creates a nonequilibrium spin accumulation below the injector contact, which diffuses in all directions away from the contact as we deal with a diffusive nonmagnetic conductor. According to the spin injection theory[Fert],[John],[Fabi] presented in chapter 3, this spin accumulation vanishes while diffusing away from the injector due to spin relaxation processes with a characteristic distance called the spin diffusion length. If another ferromagnetic contact is placed on top of the channel where the accumulation has not vanished yet, an *emf* is created that manifests itself in a voltage drop between this detector contact and another ohmic contact to the channel, which is not within the current path. The method is called nonlocal measurement because in the detection circuit no charge current flows contrary to local measurements, where the current is driven between two ferromagnetic contacts and the voltage drop is measured on the same contacts in a simple two point measurement setup. The nonlocal measurement technique highly benefits from minimized spurious effects, e.g. local Hall Effect or magnetoresistance of the contacts[Monz],[Mon1],[Tang] that can influence the measured signal and mimic spin-valve like results we are studying. Following theory one expects a measurable nonlocal voltage at a distance L from the injector equal to

$$V^{nl} = \pm(P_{inj}P_{det}I\lambda_{sf}\rho_N / 2S)exp(-L/\lambda_{sf}). \tag{6.1}$$

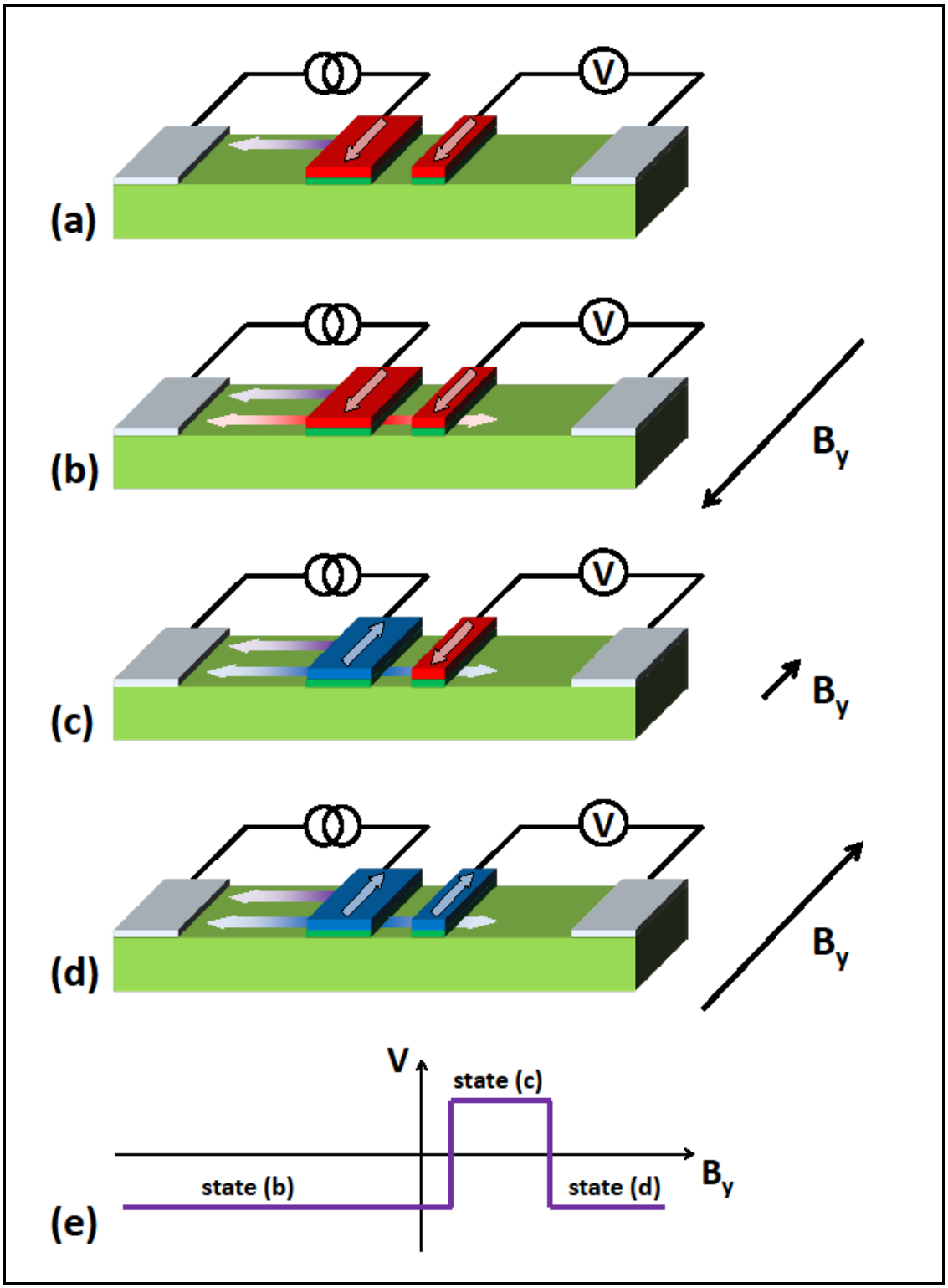

Fig. 6.4: The basics behind the in-plane spin valve measurements. The biased injector generates a (violet shaded) spin polarized current flowing in the injector circuit (a). As we do have a diffusive system, also a pure spin current diffuses in both directions away from the injector ((b), red shaded). An in-plane field B_y can be used to change the magnetization direction of the contacts. At large negative fields both contacts are aligned parallel to the field as well as to each other. Sweeping the external field to positive directions switches at first the magnetization of one contact (shown in (c)) if the field equals its coercive field and then the other contact (d) (the different coercive fields are typically achieved with the help of shape anisotropy). (e) shows the expected non-local voltage measured at the detector; compare to chapter 3.

Thus the nonlocal voltage is determined by the spin injection efficiency of the injector P_{inj} (detector P_{det}), the bias current I, spin diffusion length λ_{sf}, the resistivity of the channel ρ_N and its cross sectional area S. Additionally the signal is damped exponentially the farther away it is measured. + (-) sign corresponds thereby to parallel (antiparallel) configuration of the contact magnetizations. These different states are created by sweeping an external magnetic field in the sample plane. While at high negative B_y field both magnetizations are surely parallel, a reduction of the field strength and following shift of its direction lead to magnetization reversal of the contacts and antiparallel states should be created for field values between the individual coercive fields of both contacts. Further increase of external field again prepares parallel alignment. For achieving different coercive fields one typically makes use of shape anisotropy of the ferromagnetic material. For GaMnAs this is a very critical point as the low magnetization of the material makes this approach difficult. In chapter 6.3.3 we will address this fact in more detail. The factor of ½ in the formula originates from the geometry of our sample design. We make the simplifying assumption of purely one dimensional transport in x-direction and have an injection contact that is placed in the middle of the channel. Therefore the spin accumulation diffuses in both directions of the injector, which makes the detectable accumulation in one direction half the value of the total one. The sample measured is depicted in figure 6.5. The very big contacts 1 and 6 are nonmagnetic ohmic contacts to the GaAs channel, made of annealed PdGe. The inner four contacts are ferromagnetic Esaki diodes capped with TiAu metallization. The long side of the channel (350μm) is structured along [010] direction and its width is 50 μm. The ferromagnetic contacts are each 1 μm wide and 50 μm long, while their center-to-center spacing is 5 μm.

We drive a current from contact 2 to contact 1 with the help of a Keithley 6221 DC current source. Simultaneously we measure the arising nonlocal voltages between contacts 3 and 6, 4 and 6 as well as 5 and 6 using three Agilent 34420A NVMs. We want to emphasize that a reversed configuration, using contact pair 5 and 6 as injector circuit and the others relative to contact 1 as detectors shows the same results, meaning that all measured signals are not bound to artifacts only appearing on one specific contact but are valid for our overall measurement scheme.

6.2.1 Non-local spin-valves and exponential distance dependence

Typical nonlocal spin-valve results are shown in figure 6.6. We show the raw measurement data that are a sum of the spin related non-local signal V^{nl} plus an offset voltage. This offset was also measured by many different groups[Jede],[Lou],[Erve],[Staa] performing nonlocal measurements on different material systems, but its origin is still not well understood. It might be related to some heating effects, because increasing the bias current increases also the offset

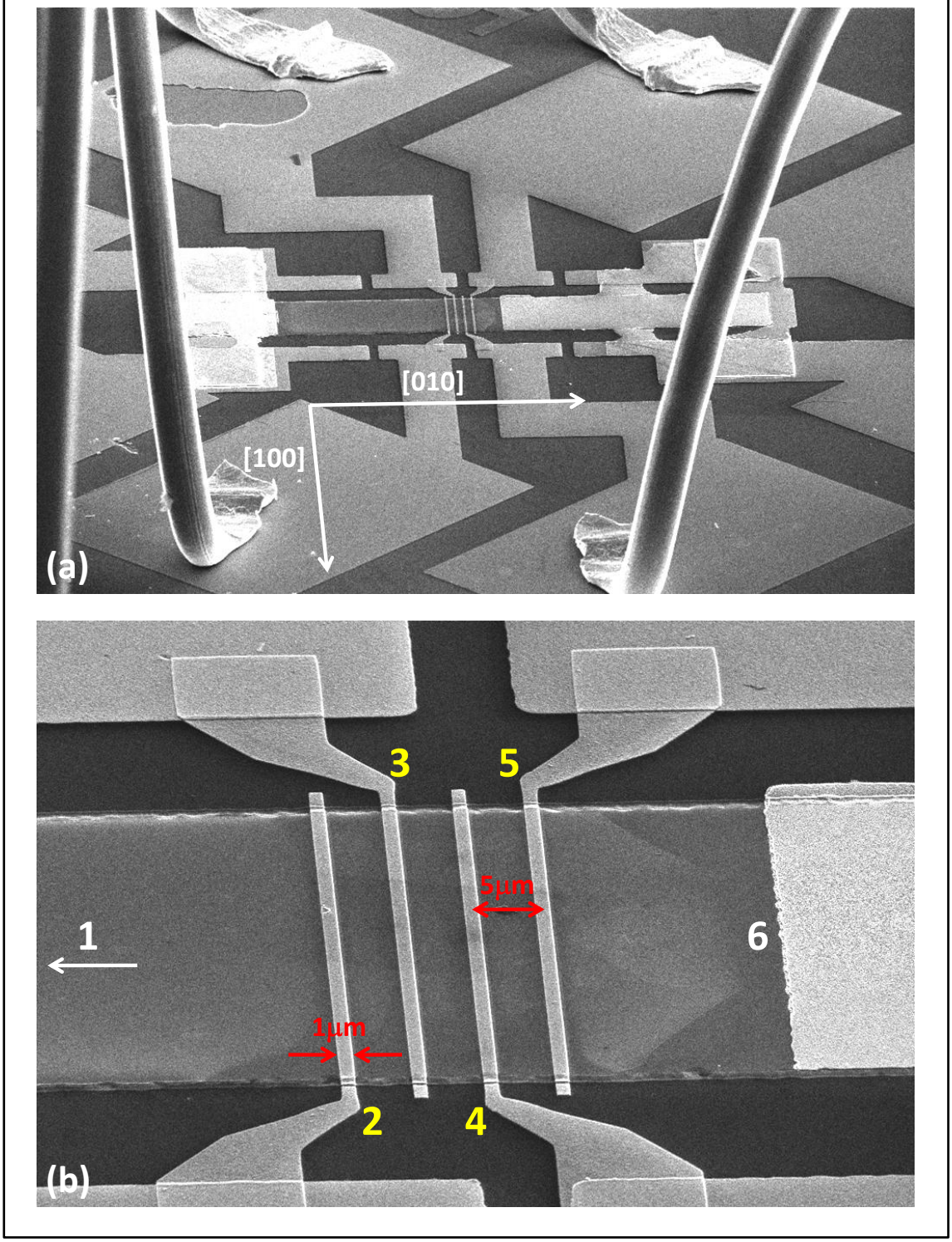

Fig. 6.5: In (a) one can see the bonded sample #15 (tilted view inside of our LEO SEM). The long mesa side (350 µm) is aligned along [010] crystallographic axis, while its short side (50 µm) is parallel to [100]. (b) gives a closer look at the structure. The big ohmic contacts are labeled 1 and 6, while the ferromagnetic Esaki diodes are named 2 to 5. Each of them has a size of 1 x 50 µm² and their center-to-center spacings are 5 µm.

voltage. The measurement results we obtained on sample #15 show a clear spin-valve signal at all three detectors as expected from theoretical predictions. The very peculiar peak at vanishing external fields we will discuss separately in chapter 6.2.4.

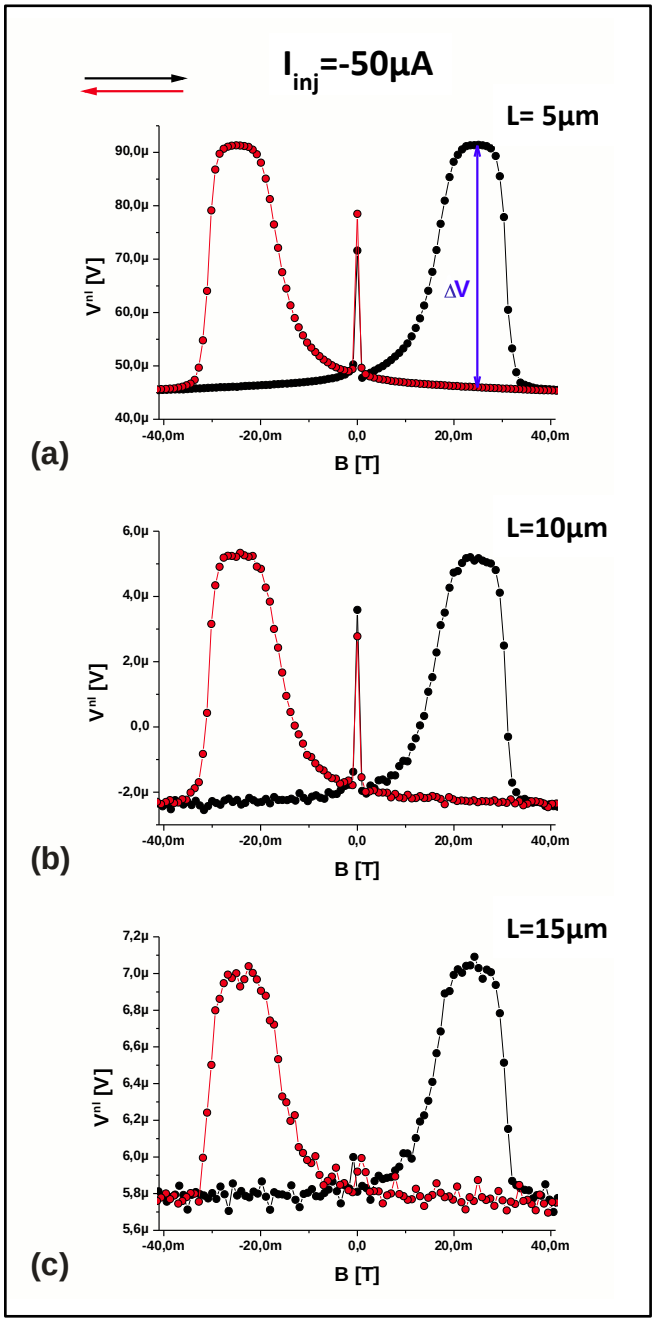

Fig. 6.6: Non-local detector signals. At a bias current of -50 µA we have the case of spin injection. The *emf* due to the diffusing non equilibrium spin accumulation gives rise to a detector signal that is measured in (a) 5 µm, (b) 10 µm and (c) 15 µm distance to the injector contact (all distances are center to center spacings of the ferromagnetic contacts).

If one looks at the ΔV values (see figure 6.6 (a)) of the three detectors one can easily see that the signal amplitudes decrease with injector detector spacing. Extracting these values they can be plotted against the distance from the injector contact and the exponentially damped signal height becomes apparent. Fitting the decay gives us a value for λ_{sf} being equal to 2.79 µm, as can be seen in figure 6.7.

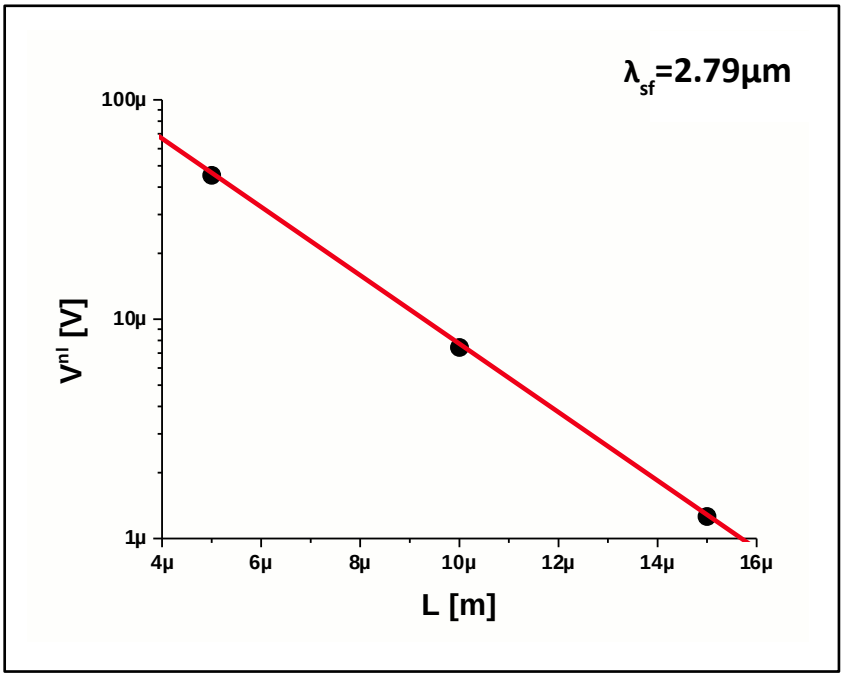

Fig. 6.7: The *ΔV* values that can be extracted from the nonlocal spin-valve measurements shown in figure 6.6 above can be fitted with an exponential decay function. This yields a characteristic decay length of 2.79 µm.

6.2.2 Spin injection and spin extraction

The next experiment one can perform very easily is to use a reversed bias current in the injector circuit. In figure 6.6 we used a negative bias current, which means we dealt with spin injection. If we now reverse the bias we have a positive voltage at the injector contact and we have the spin extraction case (as already explained in chapter 3.4.4). According to equation (6.1) the nonlocal signal should now be turned upside down compared to the case of spin injection, because everything stays the same except the sign of the current changes. Figure 6.8 now shows typical results obtained with a reversed injection current of the same absolute value as in figure 6.6, namely +50 µA. We again measure the nonlocal *emf* arising at three different distances from the injector contact simultaneously. As one can easily see the signal shape now is mirrored upside down but besides that identical to the case of spin injection. Again we can look at the detector signals and extract the signal height *ΔV*. Plotting these values against the distance from the injector we can fit the decay rate and extract a spin diffusion length once again. As we show in figure 6.9 this decay length is very similar to the one extracted from measurements with negative voltage attached to the spin injection contact, namely we get λ_{sf} = 2.75 µm, what is the same within the experimental errors.

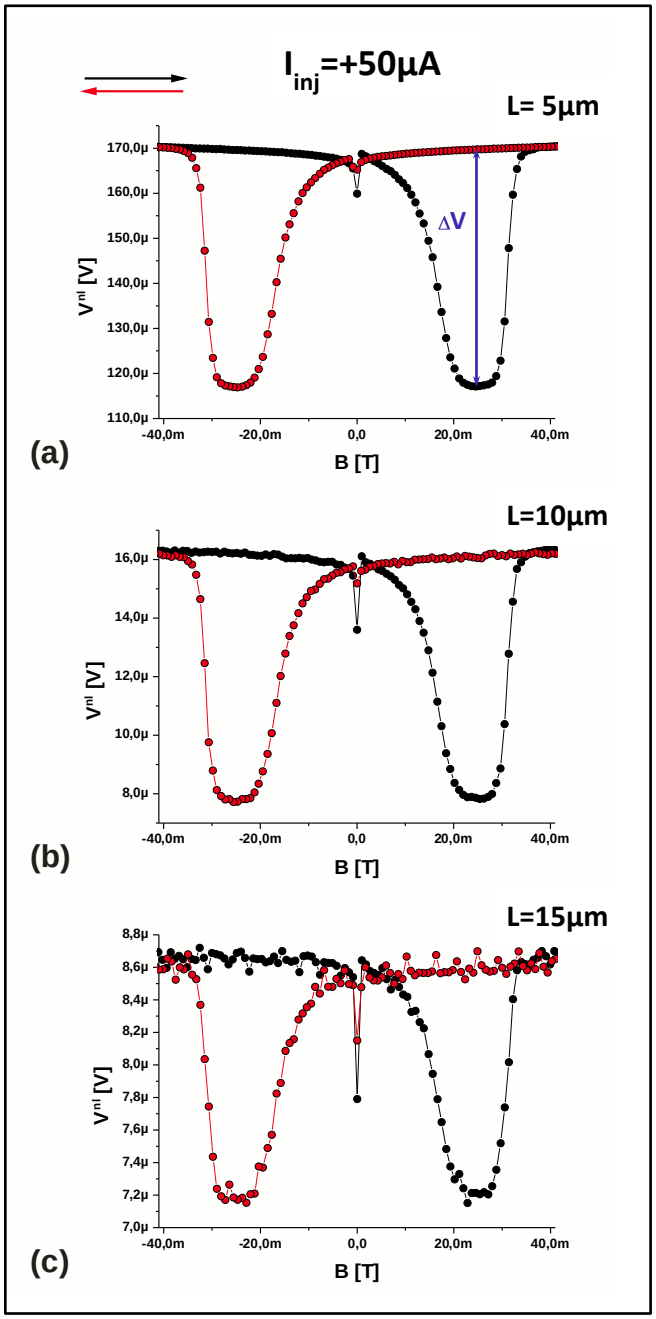

Fig. 6.8: The same measurement as in fig. 6.6, but with reversed current direction. As expected from the spin theory the detector signal is just upside down compared to the first case of spin injection.

6.2.3 Angular dependence of the spin-valve

The shown measurements hint already to a successfully realized spin injection scheme in our samples. As the non-local signals depend critically on changes of the magnetic configuration of the GaMnAs contacts we can expect clearly different signal shapes at different in-plane angles of the external magnetic field. We did measurements all around the sample plane in steps of 15 degrees for negative and positive bias current. The complete recordings are shown in appendix B, while at this point we show only some handpicked curves in fig.

6.11. Additionally this time we show the voltage drop that appears across the injection circuit while driving a constant current through it. The spin valve-like signal observed in these graphs is attributed mainly to the TAMR effect in the injector contact itself.

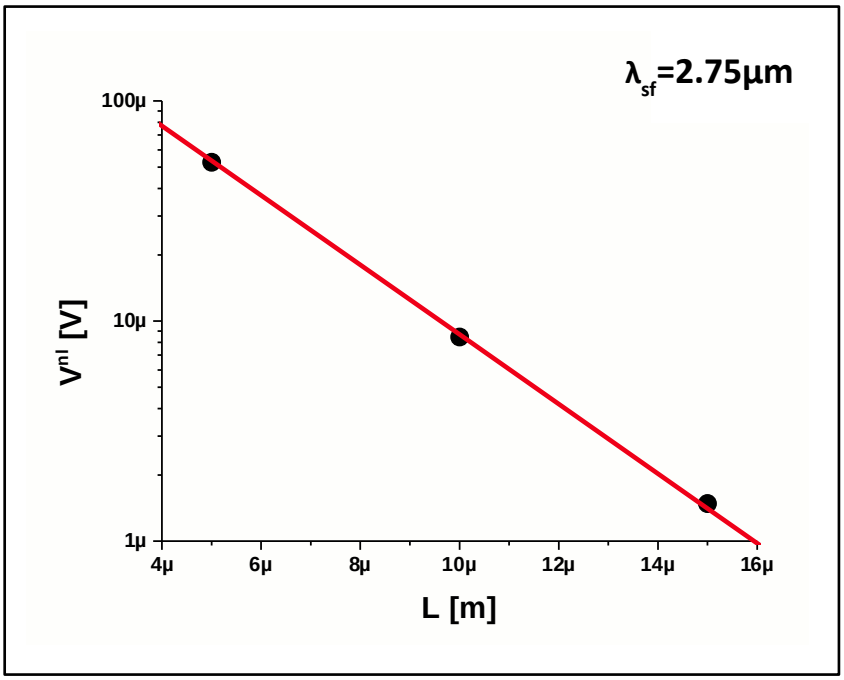

Fig. 6.9: The *ΔV* values that can be extracted from the nonlocal spin-valve measurements in the case of spin extraction show also an exponential decay as in the spin injection case with a nearly identical decay constant of λ_{sf}= 2.75 µm.

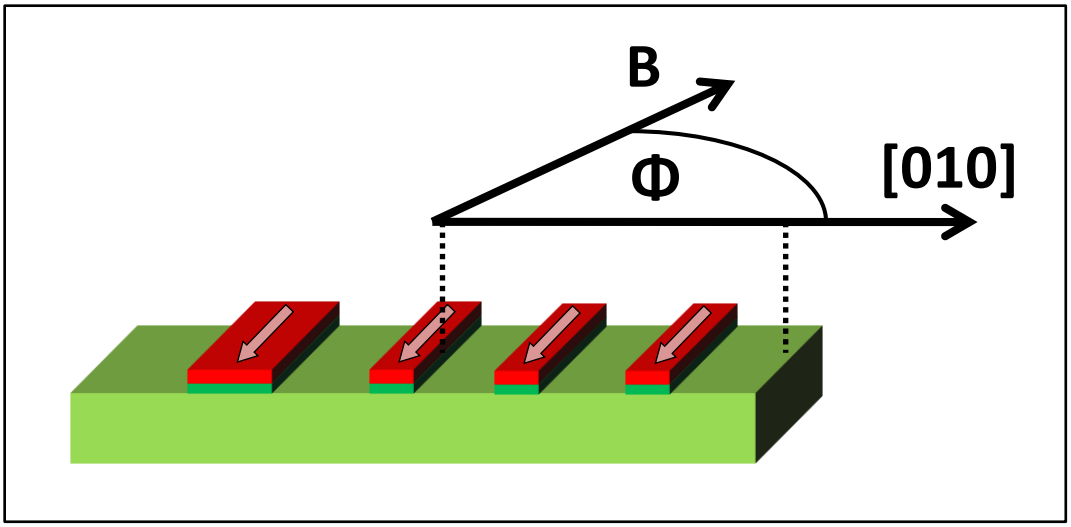

Fig. 6.10: If we change the angle *Φ* between the in-plane magnetic field *B* and the crystallographic axes of our sample we can get an angular dependent set of non-local spin-valve measurements.

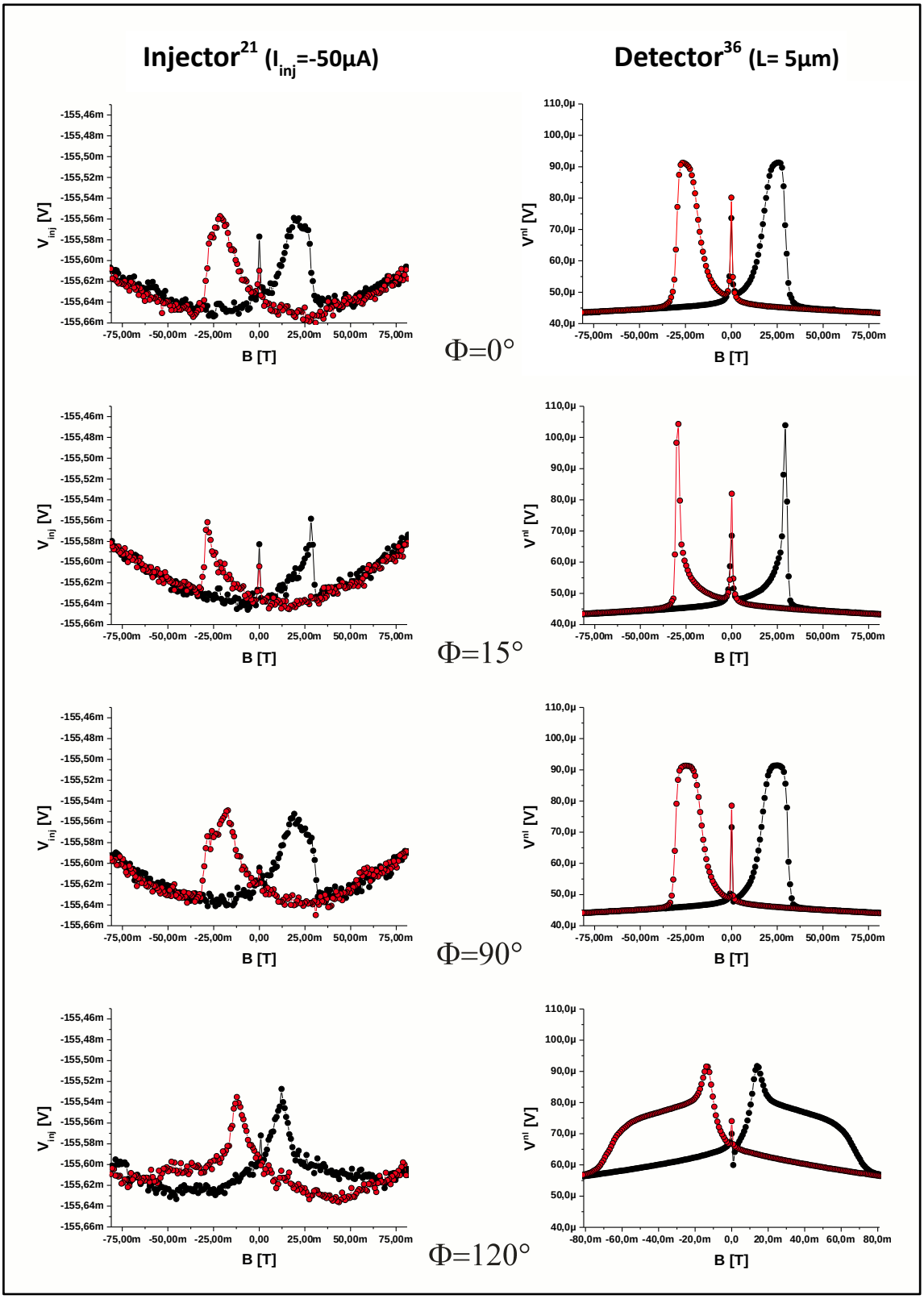

Fig. 6.11: The injector voltage on the left and the nonlocal detector signal in 5 µm distance on the right for the in-plane field angles of $\Phi = 0°$, 15°, 90° and 120°. The injector signal is a combination of channel and contact resistance and its form is in large part attributed to the TAMR of the GaMnAs contact. The non-local detector as well as the injector signal both change their shape dramatically with the field direction.

One again can extract the ΔV values from the non-local spin-valve measurements for all the different angles and look at the decay lengths. In

figure 6.12 one can see the extracted values for the three arbitrarily chosen angles. Fitting exponential decay curves to the data of each different angle gives us values for the spin diffusion length in any case as before. The obtained values are in the very same range as we already evaluated in chapters 6.2.1 and 6.2.2, indeed for all angles.

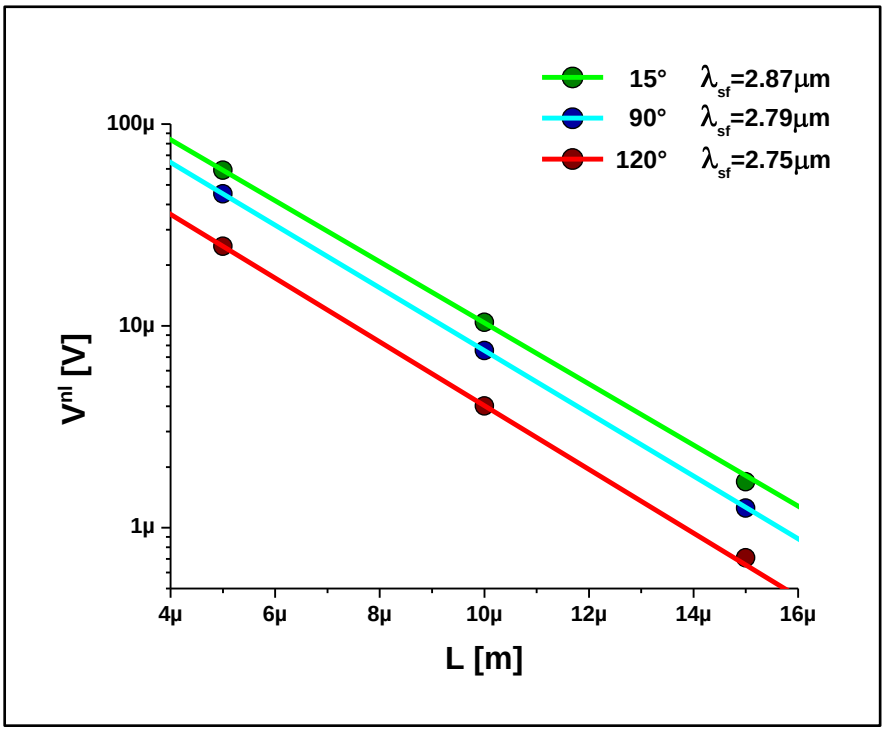

Fig. 6.12: The spin diffusion constant values for three arbitrarily chosen angles are in very good agreement with each other as well as the previously extracted ones. All are within 2.75 to 2.87 µm.

We can analyze now the evolution of the signal shape for all angles in two ways. First we can compare the injector circuit TAMR signal with the non-local spin-valve signals of the detectors. Analyzing the switching fields for all different curves reveals the fact that at the injector and the detectors these switching events always, without any exception, happen at exactly the same field values, at least within the accuracy of our measurement setup. This raises the question about the origin of the spin-valve signal we measure. Expectedly parallel and antiparallel magnetizations of injector and detector contacts should have been the reason for the nonlocal spin-valve like detector signals. However, different switching fields should have been measured if this was the case. For further clarification of this circumstance we refer to chapter 6.3.3. The second thing we can learn from the signal shapes is something about the easy and hard axes of our GaMnAs layers. Typically in GaMnAs there are two easy axes parallel (or at least very close) to [100] and [010] directions, originating from the zinc-blende crystal symmetry. Additionally there exist weaker uniaxial components along [110] or [-110] directions, origin of which is still not clear[Hümp]. A second, very weak uniaxial component along [010] direction can only be observed with the help of very high resolution methods[Goul]. This leads

to a very complicated switching characteristic of GaMnAs contacts that generally is described by a two state switching behavior. Our set of angular dependent in-plane field sweeps verifies that our layers behave the same way as would be expected from this kind of anisotropic energy landscape. For $\Phi = 0°$,

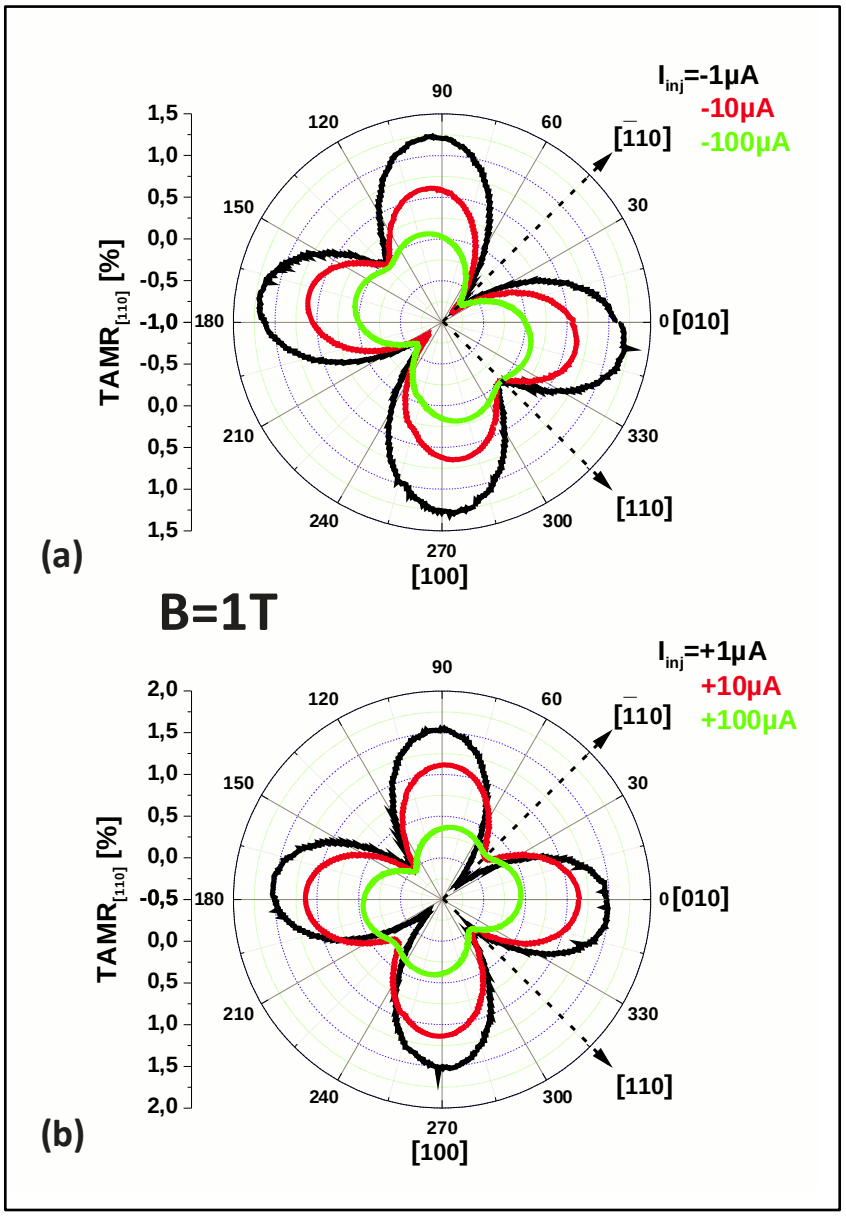

Fig. 6.13: In a circular sweep with prevailing field of 1T, the magnetization of the GaMnAs contacts is surely always parallel to the field. The typical biaxial behavior with slightly modifying uniaxial component can be observed. Graph (a) shows the change of the TAMR curve normalized to [110] for different injection currents, while (b) gives the same for different extraction currents. Comparing the curves for -/+100 µA shows a 90° turned anisotropy characteristic as was observed very similarly in [Mose].

90°, 180° and 270° (thus parallel to [100] and [010] directions) the curves look very similar, as all these measurements are done with external field nearly parallel to easy axes of the material. This additionally means that we did not achieve different switching fields of the contacts by shape anisotropy or rather strain relaxation as the signals not only look similar but really are

interchangeable to each other with external field along short as well as long magnetic contact axes. For the hard axes along the field angles in between the main directions we get a much more comprehensive and complicated switching behavior. For measurements with field in the quadrant of the [1-10] axes ($\Phi = 0°$ to 90° and 180° to 270°) the SV-signals are narrowed to a sharply cusped form, whereas for field angles in the other two quadrants of the [110] axes ($\Phi = 90°$ to 180° and 270° to 360°) the signals evolve to a much more broadened shape. This represents the additional uniaxial magnetization component typical for these GaMnAs layers.

In circular field sweeps, where the absolute value of the external field stays constant and only its angle is varied relative to the crystallographic axes this rich magnetic energy landscape leads to typical fourfold butterfly graphs. This behavior is shown by our samples, too. Additionally one can see that the change of the applied bias changes the anisotropy of the junction (see figure 6.13). For example at -100 µA bias current the [-110] directions reveal negative TAMR while at +100 µA they show positive TAMR relative to the [110] directions. Similar as in the work from Moser et al.[Mose] this could be attributed to a changed Rashba term of the interface. This overall can explain that current changes the behavior of the biased injector contact in contrast to the unbiased detectors. But still the mystery of simultaneous switching as observed in the in plane field sweeps and the origin of the spin valve signal cannot be explained with that.

6.2.4 Dynamic Nuclear Polarization (DNP) effects

We do use superconducting magnets for our measurements, thus we always have to deal with some hysteresis effects of the magnets. So zero field on our display is not really zero field, it is always a little bit shifted dependent on the magnet's sweep history. Figure 6.14 illustrates this issue. Before performing a spin-valve measurement we typically magnetize to a certain in-plane field of -0.5 T to assure complete saturation of the magnetic contacts in field direction. Then we go to small fields of roughly -100 mT and sweep the field slowly to +100 mT for the measurement and then saturate again, this time in opposite direction. Proceeding this way gives us curves as shown in figure 6.14 (a). If one now looks at the very peculiar sharp peaks near to zero fields that appear in all our nonlocal spin-valve measurements, they are clearly shifted against each other for approximately 7 mT. If we now do the same measurement but skip the second saturation magnetization, thus sweep slowly from -100 mT until +50 mT in a first step and then directly sweep back in the other direction you can see that the peaks nearly coincide with each other, see figure 6.14 (b). This means that the hysteresis of the superconducting magnet itself gives us a shift in the measured signal. We compensate for this effect by subtracting the field value of these zero field peaks from the measurement data, therefore all spin-valve measurements shown in this thesis have this peak at zero external field.

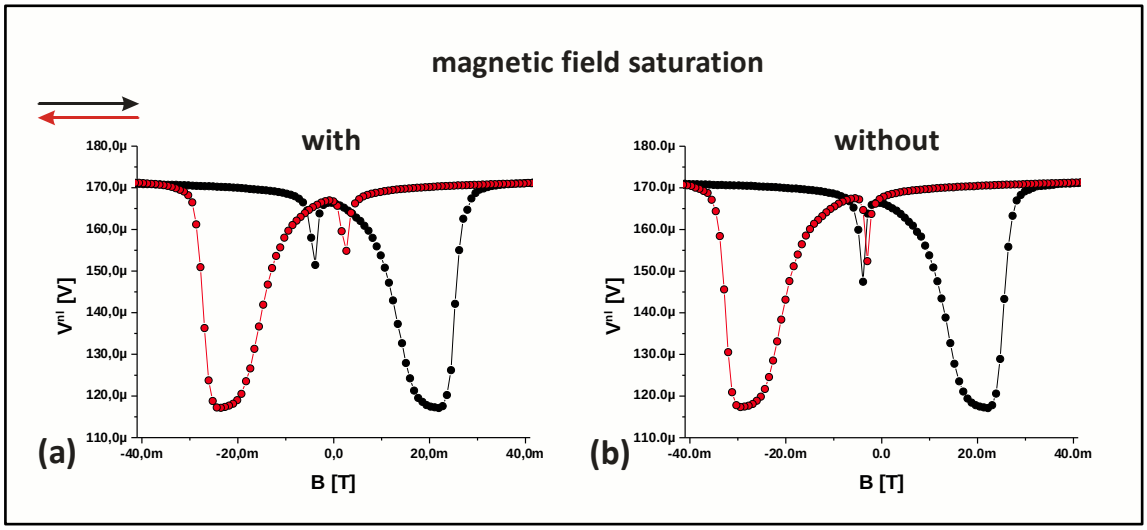

Fig. 6.14: The graphs show the raw data, measured at the first non-local detector. On the left side the magnetic field was driven up to ±0.5 T to completely saturate the contact magnetizations in the field directions. The right hand side shows the same non-local measurement if the field saturation is done before the up sweep but not before the down sweep. The difference between the DNP peaks is reduced from 6.57 mT to 0.9 mT.

The two questions that arise now are the following: What effect causes these zero field peaks and why can we use them to define vanishing external field?

Similar cusps at zero external field were also observed on other spin injection devices based on GaAs investigated by Lou et al.[Lou]. There the authors attributed these peaks to dynamic nuclear polarization of the GaAs nuclei in the channel due to hyperfine interaction with the spins of injected electrons. The

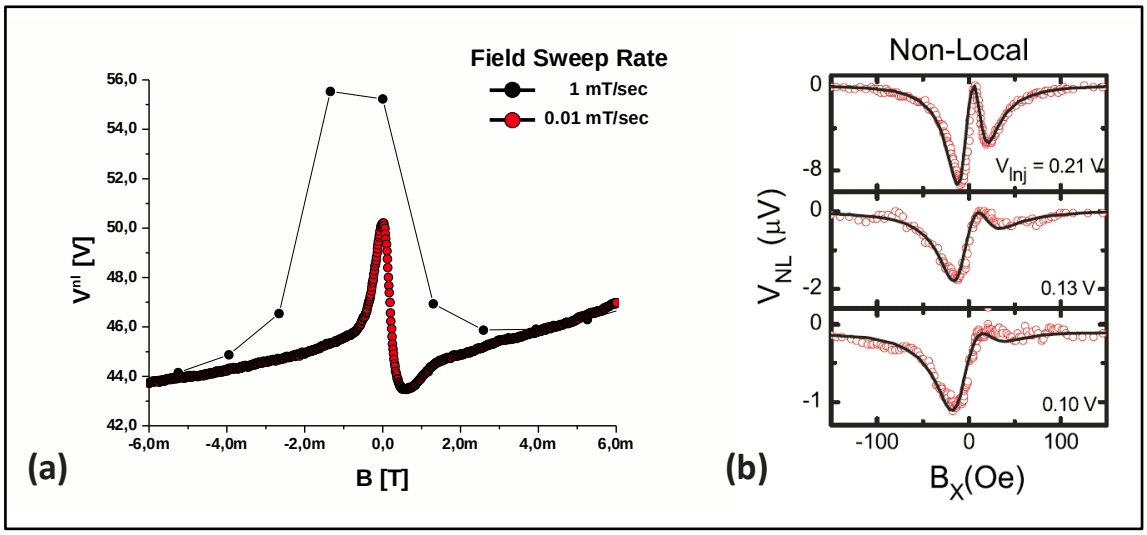

Fig. 6.15: Dependence of the sharp zero field cusp on the sweep rate suggests a correlation to DNP effects[Dorp]. In other groups these DNP effects were very intensely studied on spin injection devices based on GaAs, the form of their resulting curves resembles ours very closely (we used a negative injection current, thus we have reversed sign of our injector voltage, compared to the measurements done in [Chan]. Taking this into account the curves have to be mirrored upside down and then they are a perfect match to each other).

dependence of their exact form on the sweep rate of the magnetic field we observed in our measurements supports this explanation[Dorp]. Closer

investigations that were made on this specific topic done by Chan et al. show very similar curve structures (thereby these cusps always appeared in the direct vicinity of zero field.) and also a dependence on applied bias[Chan] as was discovered in our experiments. Figure 6.15 (a) shows a non-local detector signal typical for our measurements at two different sweep rates. The smaller rate of 10 μT/sec is very close to the minimum rate we can achieve with our cryostat setup. Comparing this sample curve with the ones shown in 6.15 (b), one can see that it closely matches the DNP curves from [Chan], that were made with a corresponding sweep rate of 2.5 μT/sec. Further effects were observed in our work that support the identification of these cusps with DNP effects and are mentioned in chapter 6.3. These are in short sweeping an out-of-plane magnetic field through zero resulted in very asymmetric and also hysteretic behavior, and additionally the linewidth around 0 T in Hanle signals is smaller than expected from theory.

6.2.5 Spin injection efficiency

The theory in chapter 3 assumes being in the linear regime of spin injection. This means; increasing the injection current by a specific factor also increases the measurable non-local signal by the same factor. Now let's have a closer look at this issue. The equation that describes the measured signal in the non-local case again is

$$V^{nl} = \pm(P_{inj}P_{det}I\lambda_{sf}\rho_N / 2S)exp(-L / \lambda_{sf}). \tag{6.2}$$

In this chapter, the size of the injection current is the only factor we change in the experiment. Looking at figure 6.16 (a) and (b) shows us that an increased bias current indeed increases the detectable non-local voltage, for spin injection as well as for spin extraction. However if one looks at the normalized nonlocal resistance values, which means

$$\Delta R = \frac{\Delta V}{I} = \pm\frac{P_{inj}P_{det}\lambda_{sf}\rho_N}{2S}exp\left(-\frac{L}{\lambda_{sf}}\right), \tag{6.3}$$

in part (c) of figure 6.16, one can clearly see that the higher the bias current gets, the smaller the normalized nonlocal resistance is. If one zooms into that graph and looks only to small bias values of ±10 μA or less, a plateau becomes visible, where the nonlocal resistance saturates (fig. 6.16 (d)). This saturation of the nonlocal resistance leads us to the assumption that at small bias currents the spin injection efficiencies of both injector and detector contacts are the same. So we can evaluate the equation for the nonlocal resistance with the help of

$$P_{inj}(|I| \leq 10\mu A) \approx P_{det}, \tag{6.4}$$

which leads us to the fact that we have a peak spin injection efficiency of ≈ 52 % (see figure 6.17). This value is comparable to results that were obtained by

calculations as well as in experiments utilizing spin light emitting diodes (Spin LEDs)[Dor1],[Kohd], where spin injection efficiencies of up to 80 and 85 % were

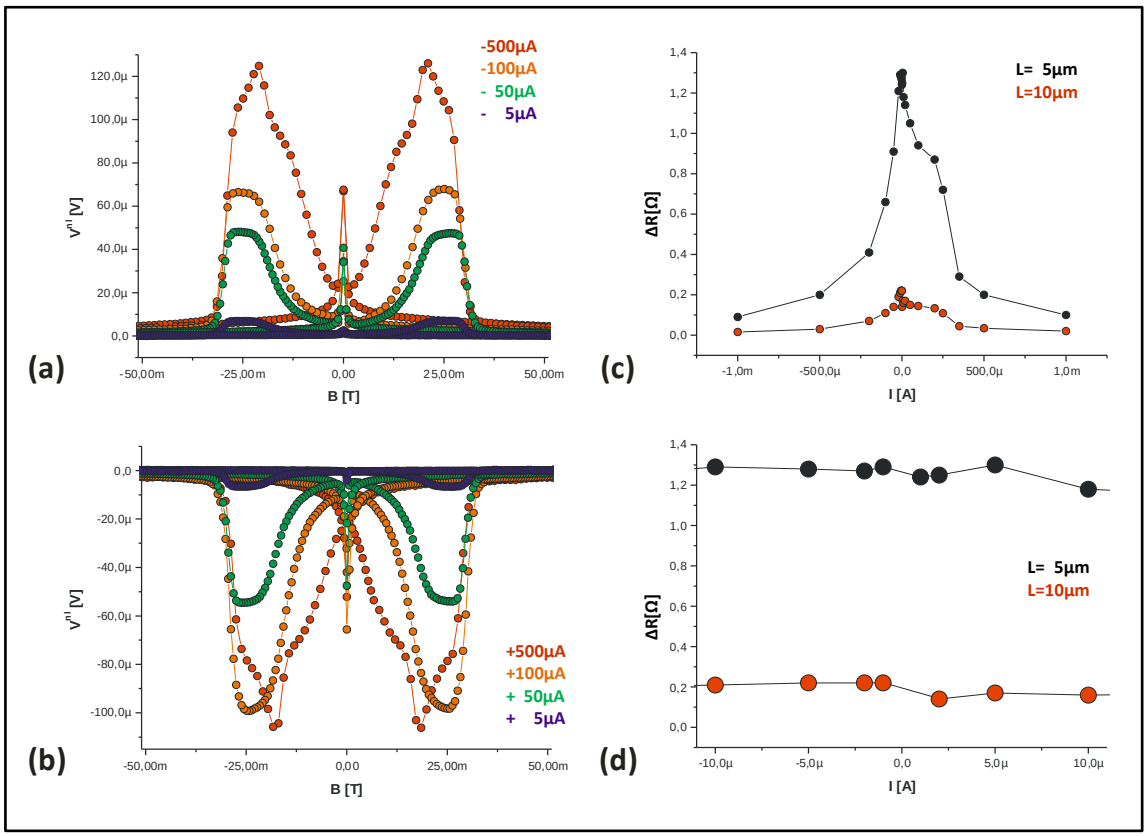

Fig. 6.16: The measurable non-local voltage at various injection currents for spin injection (a), as well as for spin extraction (b). All curves are shifted to zero base levels for easy comparison. (c) shows the normalized nonlocal resistance values, which means *ΔR = ΔV/I*. Looking only at small bias currents of ±10 µA or less, a plateau becomes visible, where the non-local resistance saturates.

found respectively, depending greatly on the thickness of the n^+-layers. The spin injection efficiency dependence on the bias is also consistent with results from these groups. The decrease of spin injection efficiency with increasing reverse bias can be explained by taking the band structure of a ferromagnet into

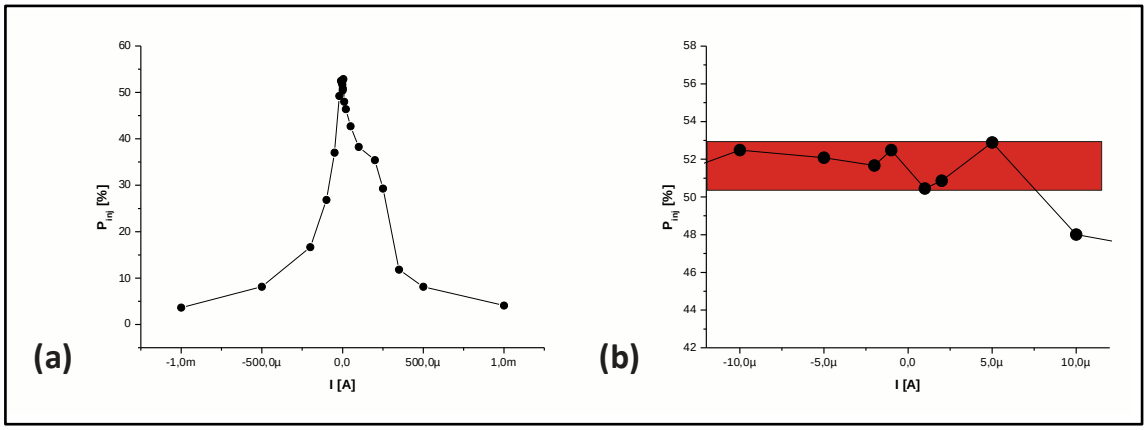

Fig. 6.17: The spin injection efficiency of the injector contact depends on injection current in the same way as the nonlocal resistance (a). In a narrow range the efficiency saturates at a peak value of ≈52 % (b).

account. The higher the bias current is, the higher the bias voltage. Therefore one gets deeper into the bands and the contribution of minority spins gets bigger and bigger. This leads to a mixed spin alignment of majority and minority electrons and therefore to a loss of injection efficiency at higher bias. On the other side of zero, at forward bias, the efficiency also declines significantly but initially much slower than on the negative side. This drop could be explained by occurring inelastic tunneling processes through forbidden states in the band gap[Sze]. The pronounced contribution of such transitions to the total current is supported by the very small peak to valley ratio of the Esaki dip in our measured I-V curves, see figure 6.3. At bias currents exceeding +250 µA the injection efficiency starts dropping significantly. This is in agreement with position of the Esaki dip observed in the I-V curve of the injector contact, which could be explained by the fact that at this specific region the thermal current gets bigger and starts dominating over the tunneling current[Sze].

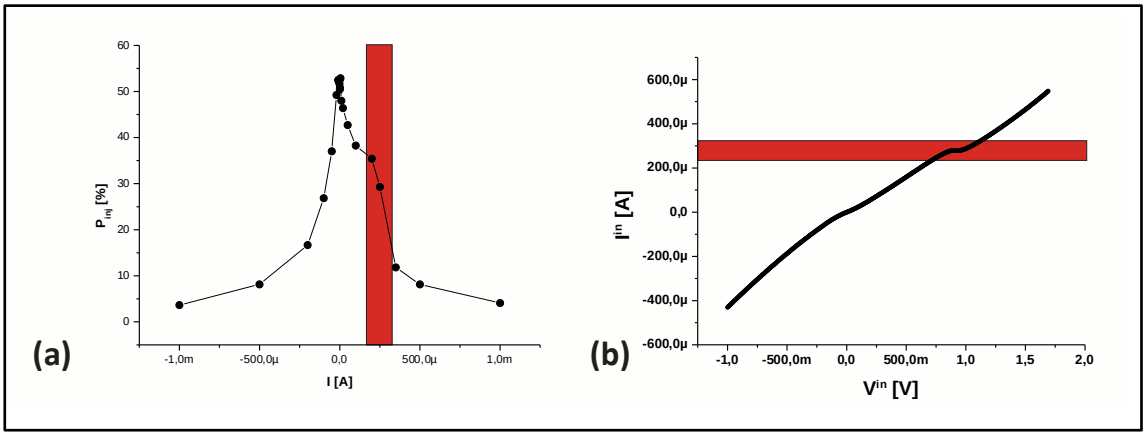

Fig. 6.18: The spin injection efficiency drops initially much slower in the forward bias side, which could be explained with occurring inelastic tunneling processes through forbidden states in the band gap (a). The sudden efficiency drop at +250 to +300 µA corresponds to the negative differential resistance region in the IV of the Esaki diode (b) and shows the onset of dominating thermal current[Sze].

6.3 Out-of-plane measurements

The in-plane spin-valve measurements are sometimes not respected as a hard proof for dealing with spin injection, transport and detection. Therefore another measurement type is used to give conclusive evidence. Here the electrical configuration is the same as in the previous chapter. We have a current carrying path with the spin injection contact and a non-biased detector, so again a non-local setup. The only, yet very important, difference is the direction of the external magnetic field. In this so-called Hanle setup the external field direction is out-of-plane. This gives rise to the fact, that at non vanishing field values the injected spins are precessing around the field vector, as the spin direction is in-plane. This effect leads to a cosine like signal shape, as the detector measures the projection of the incoming spins underneath it onto its own magnetization direction. Together with the diffusive transport mechanism this leads to a

cosine shaped signal that is damped exponentially[Jede],[John],[Fabi]. Figure 6.19 (b) shows the expected signal of the detectors for this measurement configuration.

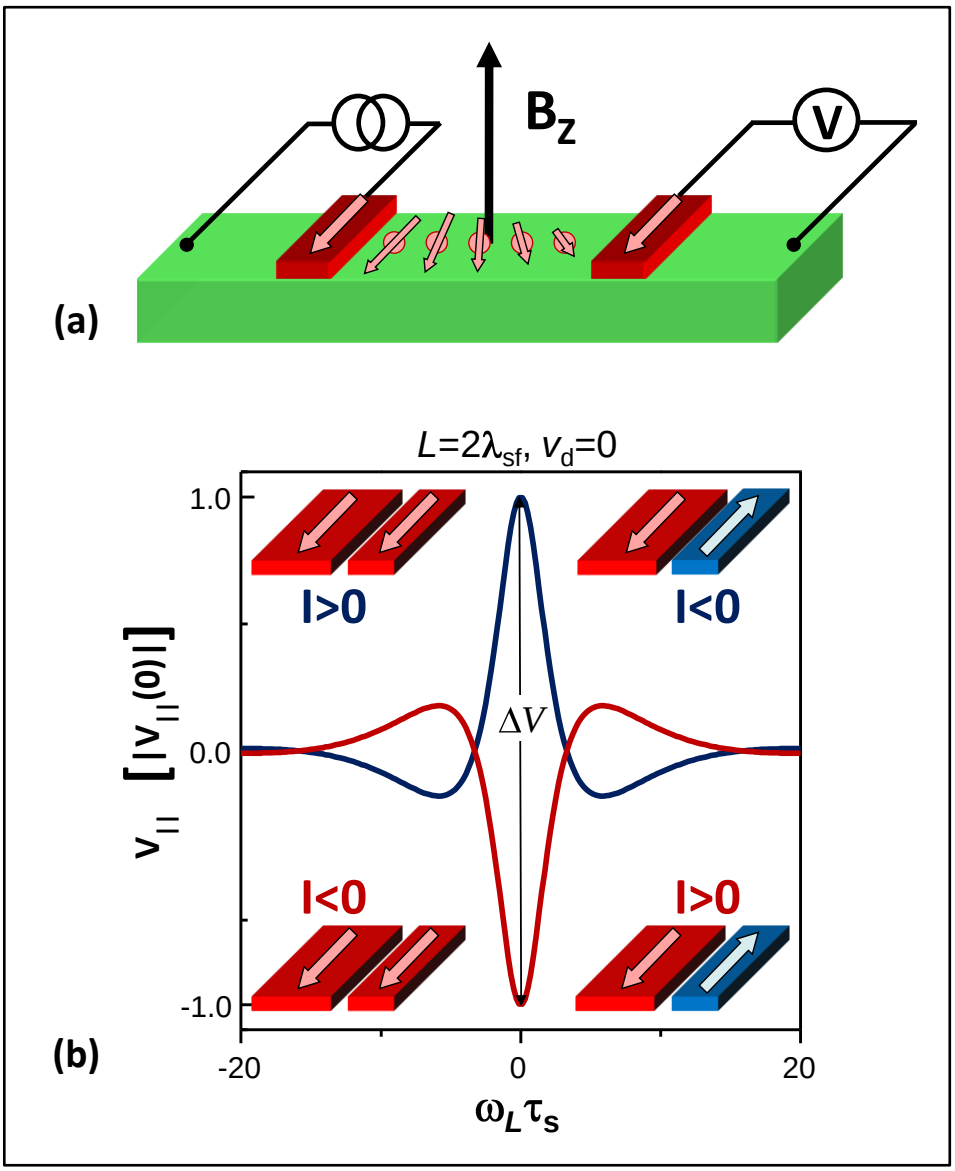

Fig. 6.19: Hanle setup (a). An external magnetic field is swept perpendicular to the sample plane. The electron spins start to precess as soon as the field has a non-zero value. (b) shows the expected signal measured at the detection contacts with respect to the relative magnetization of injector and detector contacts plus current direction.

6.3.1 Hanle measurements

Figure 6.20 shows some measurements on our sample at three different distances from the injection contact. As one can see the curves resemble the ones for spin injection (negative potential at the injector) and parallel magnetizations of the contacts (see figure 6.19 (b), red line). For these measurements we had to prepare the contacts by magnetizing up to 500 mT in-plane (way above the fields necessary for saturation of GaMnAs) and then reduced the field to zero. After that we started to increase an out-of-plane magnetic field. Therefore we had to do this procedure two times to get a

complete curve, with increasing the out-of-plane field in the two different directions of +/-*z*. Going to an out-of-plane field and then sweeping through zero in this configuration resulted in very asymmetric and also hysteretic behavior (see figure 6.21), what also could be attributed to DNP effects playing an important role in our samples[Page].

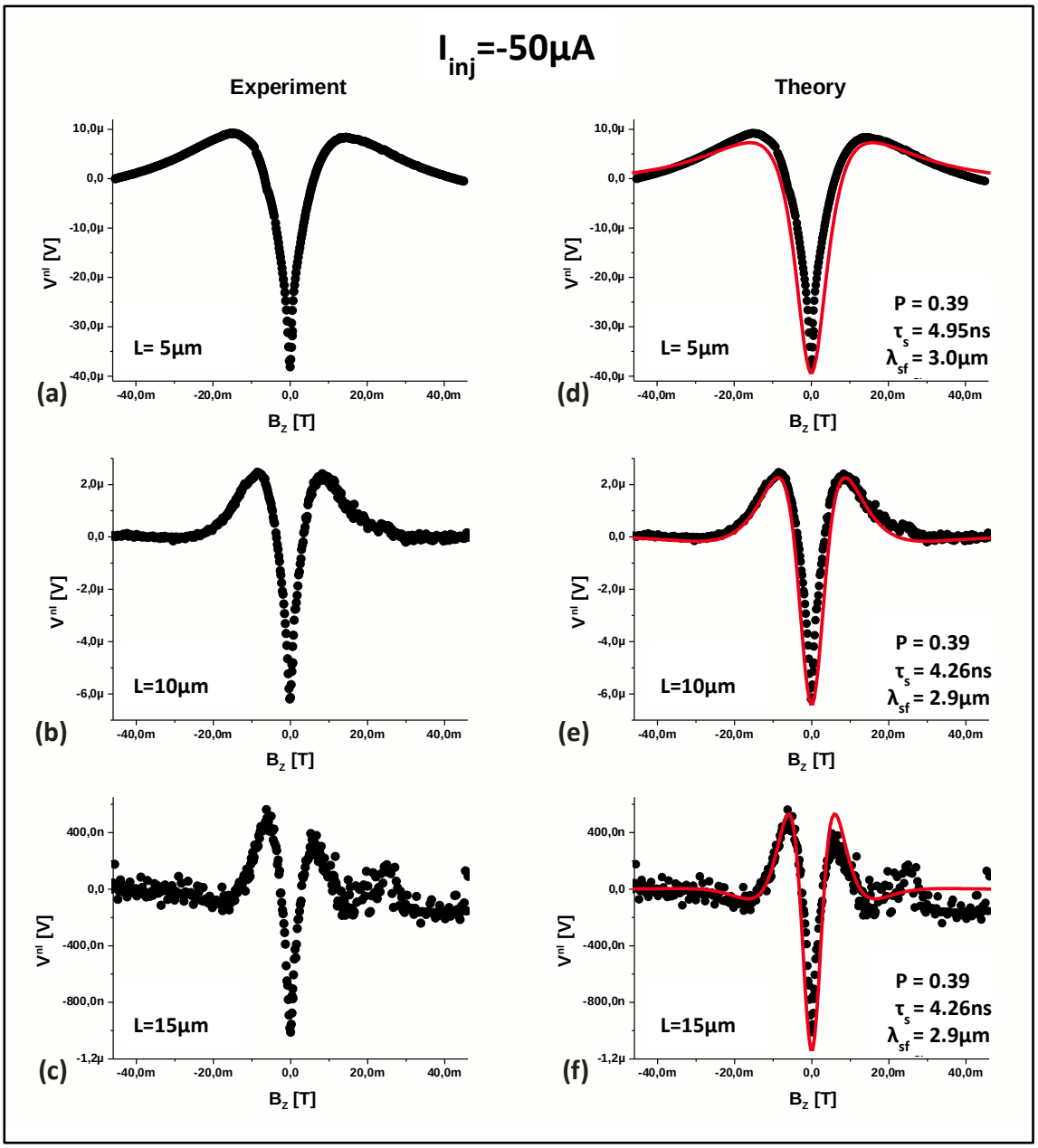

Fig. 6.20: Hanle signals obtained for three different injector-detector spacings. The larger the distance gets the more decreases the signal height and the more oscillations are visible due to the increased time for the spins to rotate ((a) to (c)). The measured Hanle signals can be fitted with equation (6.5). The fit gives us consistent values for all three detectors. We get a spin injection efficiency of 39 % and spin diffusion length of nearly 3 µm what additionally authenticates our values extracted from non-local spin-valve measurements shown in previous chapters.

As one can see, the bigger the distance between injector and detector, the nicer the signal looks regarding clarity of oscillations. This is expected, as the spins

need certain time to precess around the external field. The closer a detector is placed, the shorter the effective precession time is for the spins and therefore fewer oscillations can be observed. On different structures processed in the same way but with injector detector spacings below the spin diffusion length of 3 µm oscillating Hanle signals therefore could never be observed. These measurements can now be fitted with the following equation:

$$V_{\parallel}(x_1,x_2,B)=V_0\int_0^{\infty}\frac{1}{\sqrt{4\pi Dt}}e^{-(x_2-x_1-v_dt)^2/4Dt}\cos(\Omega t)e^{-t/\tau_s}dt \tag{6.5}$$

The fitted curves were obtained by integrating $V_{||}$ over the width of injector and detector with τ_S, λ_{sf} and P^2 being free parameters. We used a value of -0.44 for the g-factor and set the drift velocity to zero, as we operate in purely diffusive regime. If one looks at the linewidth around 0 T of our experimental curves it becomes obvious that theory predicts a broader characteristic. This effect can again be explained with DNP effects, which are known to narrow Hanle signals at very low magnetic fields[Page]. The consistency between theory and experiment increases with injector-detector spacing, smaller bias current or higher temperatures, as can be seen in section 6.4.1.

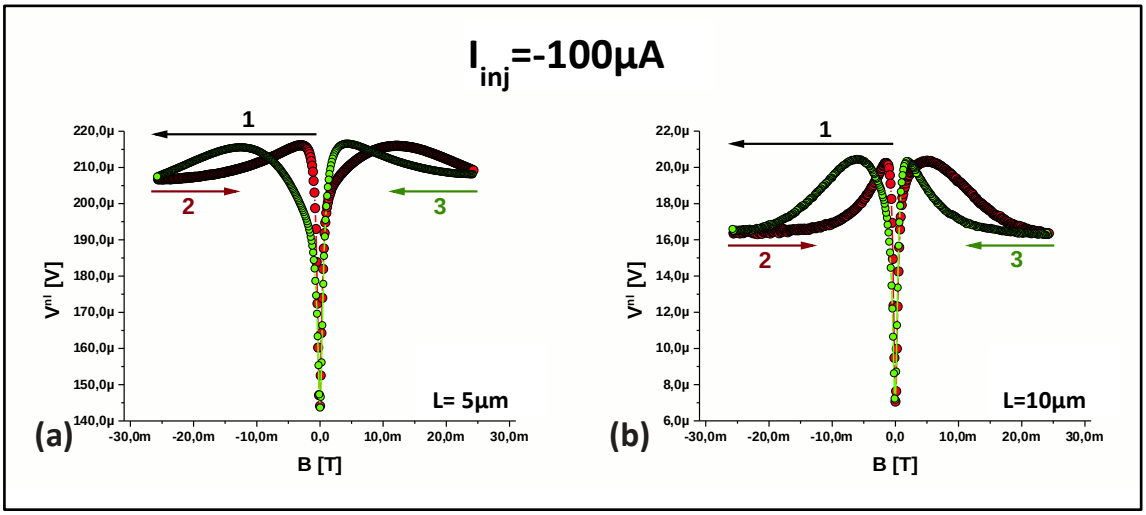

Fig. 6.21: Non-local voltages at the first two detectors. Preparing parallel in-plane magnetizations and then sweeping in out-of-plane configuration to -25 µT gives us a certain voltage level (black arrow, curve not shown). If we then sweep in out-of-plane configuration through zero to +25 mT (the red curve), one can see that the Hanle curve is asymmetrically deformed, what could be attributed to DNP effects[Page]. Reversing the sweep direction once more (green curve) shows again the same, but now mirrored, asymmetric behavior.

The obtained results from the theoretical fits support the values we have extracted from the non-local spin valve measurements. The obtained spin diffusion length λ_{sf} is close to 3 µm and the spin injection efficiency P is 39 %. The spin injection efficiency behaves here in the same way as we already analyzed in section 6.2.5 with the help of the non-local spin valves. The higher the bias current (and the according voltage) the lower the injection efficiency,

thus evaluating Hanle measurements with lower injection current leads to peak efficiencies slightly above 50 %, as seen before.

6.3.2 Hanle signal decomposition

In contrast to the in-plane spin-valve results, Hanle curves we depict for example in fig. 6.20 do not represent as-measured raw data. The reason is that measured signal exhibits some MR contributions that are not due to a rotation of the injected electron spins in the applied external magnetic field. One has to analyze the signal first and decompose it into the relevant elements. From the measured raw signal (shown in figure 6.22 (a)) at first a parabolic background has to be subtracted (see part (b), this background also occurred in other groups' Hanle measurements[Lou]). The result one can see in part (c) and it looks already quite similar to what we want to have. At roughly 70 mT the magnetization is turned out-of-plane and with it the injected spins, what is visible through a step in the non-local voltage. This suggests that different spin injection efficiencies could exist for different spin directions – we will address this specific topic in chapter 6.5. If we finally concentrate onto the inner region below 50 mT where spins are still in-plane, we can fit the non-local detector signal with existing Hanle theory and the nearly perfect match shows that we deal with successful spin injection and detection.

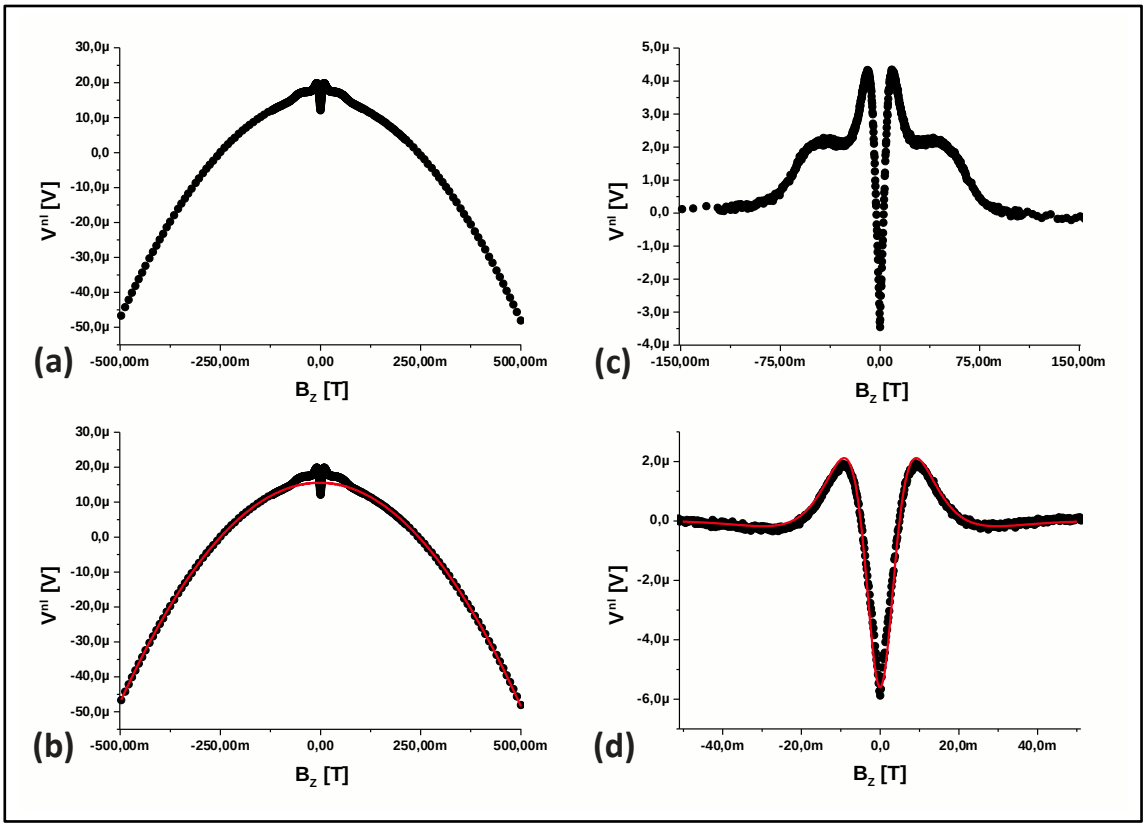

Fig. 6.22: (a) As-measured Hanle curves. The parabolic background can be fitted and subtracted very easily (b). It turns out that the step in the range of 70 mT originates in the spins being tilted out-of-plane (c). Concentrating on the inner region up to external fields of +/-50 mT shows that the pure Hanle spin signal comlies very accurately with theory (d).

6.3.3 Origin of the spin-valve signal

The angular-dependent spin-valve measurements of chapter 6.2.3 showed us that we cannot claim parallel/anti parallel configurations of our GaMnAs contacts. It can easily be seen there that the injector TAMR signal and the detector signals show switching events at the same magnetic fields. This has two important implications. First, we cannot change the coercive fields in samples of this wafer by shape anisotropy, as aspect ratios of 50 (magnetic field parallel to the long contact side) and 0.02 (field parallel to the short side) give exactly the same switching fields. To explain this one has to keep in mind that shape anisotropy does not have an effect on coercive fields of GaMnAs contacts

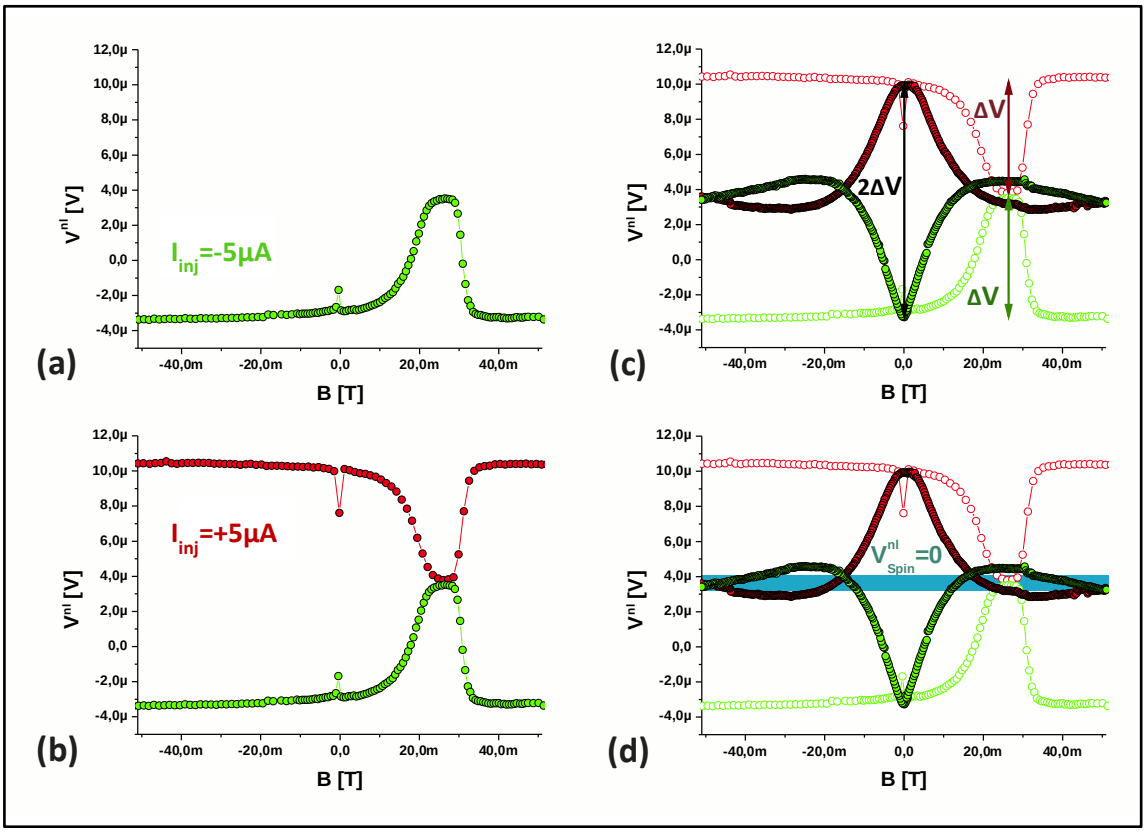

Fig. 6.23: Non-local spin-valve signal as in previous sections, but for smaller injection current (a). After reversing current direction the signal is mirrored (b), but its bottom touches its predecessors top. (c) overlaps these in-plane measurements with out-of-plane Hanle signals for both bias directions. Based on the fact that the spin signal completely vanishes in Hanle measurements at around 50 mT this means the extrema of the spin-valves correspond to zero spin signal (d).

due to stray fields but because of strain relaxation. The reason that we could not achieve this contrary to work done by Wenisch et al.[Weni] and Hoffmann et al.[Hoff] can be the only 20 nm thin GaMnAs layer of our wafer. The other groups made use of at least 50 nm thick GaMnAs layers. Additionally, due to our sample preparation method and electrical setup the strain relaxation in our samples could be inhibited by the top Ti/Au contact as well as the GaAs crystal below the GaMnAs. Both impose the original geometrical size of the crystal before etching upon the GaMnAs contact and therefore lessen its possibility to

relax extremely. Additionally in [Weni] the contacts were thinned laterally to 200 nm, clearly below our 1000 nm wide stripes, while at [Hoff] an effect on coercive fields is already at 1µm wide contacts clearly observable. In chapter 6.6 our measurements on structures made of wafer C080903A will show that probably the layer thickness is the most important factor, as there we used 50 nm GaMnAs and clear effects on the switching fields can be observed by different aspect ratios. So as we know we have not parallel/anti parallel magnetization configuration between injector and detector contacts, we need to clear up the situation why we then observe a spin-valve like signal as expected for contacts with different switching fields.

In figure 6.23 (a) we see a non-local spin-valve signal with negative bias, thus in the spin injection regime. According to spin injection theory the bottom and top signal levels correspond to parallel and antiparallel alignment of the injector and detector magnetizations. Therefore we expect the curve for spin extraction at the same voltage levels but mirrored. Part (b) shows what we do get from a measurement with an injection current of the same absolute value but opposite direction. The curves touch each other at their top (spin injection) and bottom (spin extraction). If we now add Hanle curves with the same injection currents as well as the same injector and detector contacts used to the SV-data into the viewgraph one can make very interesting observations. In the Hanle measurements there occurs a complete spin dephasing at higher magnetic fields. Therefore the spin related signal at roughly +/-50 mT corresponds to a vanishing net spin in our system. If we look at the in-plane spin-valves we can say therefore that at their top values for the injection and bottom values for extraction case the spin related signal is zero and hence the magnetic configuration is surely not antiparallel. A vanishing spin signal could be explained by two possible states of the system: a perpendicular configuration of the magnetic injector and detector contacts or by a decay of the contacts into a magnetic multi-domain state whose net magnetization disappears. Recently the formation of stable multi-domain structures in GaMnAs during the magnetization reversal process was observed using planar Hall effect (PHE) measurements[Shin]. If this multi-domain state is the dominating factor, one would expect on the other hand that the in-plane spin-valve measurements show a dependence on the individual sweep, as the multi domain structure is very unlikely to rebuild the very same domain structure every time again. This effect should express itself in slightly different switching behavior on each consecutive field sweep. We could not identify such behavior in our measurements. Nevertheless this is not an ultimate proof against this multi domain theory, as we have to deal with some amount of measurement uncertainties due to finite sweep rates, limited sampling rates of the nanovoltmeters, hysteresis of the superconducting magnet and so on what could altogether easily lead to a too low resolution to resolve this fact. We simply do not know if these differences are big enough to be visible in our

measurements. Let's come to the second possibility, i.e. the perpendicular magnetizations of injector and detector contact. The existence of perpendicular magnetizations would imply an antisymmetric Hanle curve relative to $B_Z=0$ [Fabi],[Staa]. We tried to reproduce antisymmetric curves by the following procedure. At first we prepared parallel magnetizations with the help of sufficiently high in-plane magnetic fields, as always. After that we reduced the external field, crossed zero and stopped sweeping it at the top of the spin-valve signal (see figure 6.24 (a) 1st arrow). Now we reduced the field to zero (2nd arrow in the figure), switched to the out-of-plane configuration and increased the out-of-plane field to around $B_Z=33$mT (figure 6.24 (b) 1st arrow), a field well below the spins start to rotate out of the sample plane. Subsequently we swept the field through zero in the out-of-plane configuration until $B_Z=-38mT$ (red curve in part (b) of figure 6.24). A clear antisymmetric Hanle curve was observed. The shape is not perfectly antisymmetric due to the always accompanying DNP effects. An immediately executed back sweep (green curve) through zero field shows again a similarly deformed (due to DNP) antisymmetric curve. We want to point out here that this perpendicular configuration appears to be extremely volatile, as we could reproduce this measurement only two more times at the very beginning of the sample's lifetime and never thereafter again. Typically during sweeping back from the top of the spin-valve back to zero in-plane field the non-local voltage starts to resemble the same level as prevails in the parallel configuration. Concluding one has to say that these almost antiparallel Hanle curves are an impressive sign to support the perpendicular magnetizations theory, but we definitely cannot exclude the multidomain structures. In the end one cannot eliminate the possibility of a combination of both alternatives.

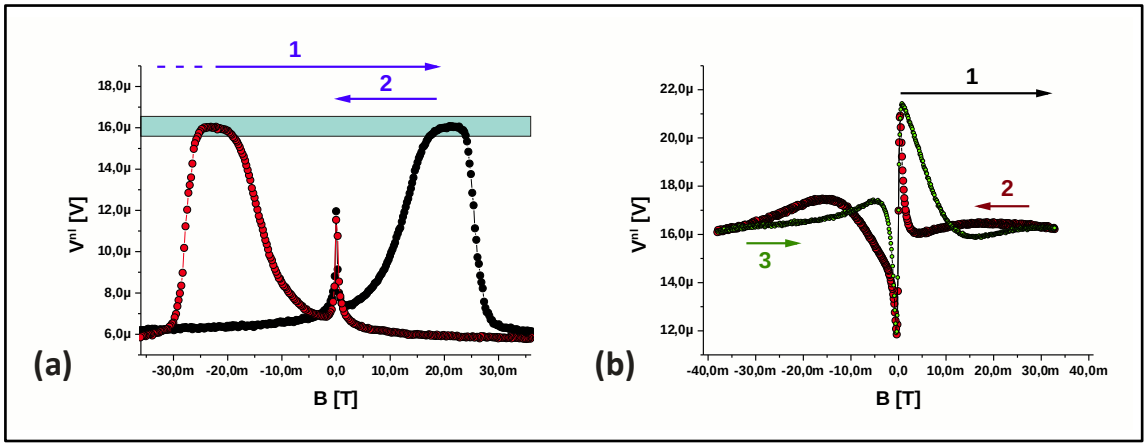

Fig. 6.24: Preparing parallel in-plane magnetization by field saturation and sweeping back through zero field onto the top of the spin-valve signal (arrow 1) before going back to zero (arrow 2) we can test the perpendicular magnetization theory (a). An immediately following out-of-plane sweep to +33 mT (black arrow, data not shown), followed by a sweep until -38 mT (red data) and back again (green data) generates an antisymmetric Hanle curve (b), which is a little bit deformed due to DNP effects.

6.4 Temperature dependent measurements

We also performed temperature dependent spin-valve as well as Hanle measurements. One expects for that type of measurements smaller signals the closer one comes to the Curie temperature of the material, as naturally the magnetization is reduced what directly influences the efficiency of the spin injection. Another factor is the increased

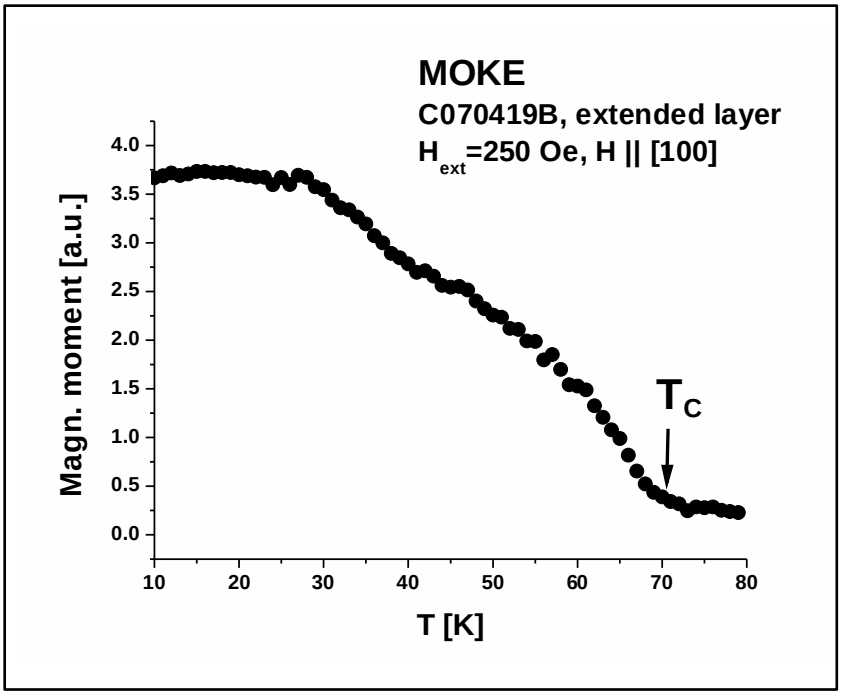

Fig. 6.25: MOKE measurements at an as-grown 5x5 μm² sample from wafer C070419B. The Curie temperature is roughly 70 K. Parasitic magneto-optical effects prevented the signal from vanishing completely above T_C.

spin scattering at higher temperatures especially on phonons. Squid measurements have shown that the wafer itself has a Curie temperature of roughly 70 K, in the as-grown state. Unfortunately we do not have squid measurements of completely processed spin injection samples with GaMnAs contacts of 50 μm² area size as even Squids are dependent on having enough magnetic material to produce results with adequate enough signal to noise ratios. This massive downscaling of lateral dimensions from 5 mm to 1 μm affects the Curie temperature for sure. A second unknown is the effect of the annealing procedure we use for achieving good ohmic contacts to the channel. Nevertheless as the Mn interstitials cannot be passivated after diffusing to the top, because there are our gold contacts, we do not expect a big change of Curie temperature due to the contacts annealing process.

6.4.1 Hanle measurements

Aside of all these aforementioned uncertainties we can look at our results of those temperature dependent Hanle measurements. When increasing the temperature it is observed that the signal amplitude strongly decreases while

the full width at half maximum (FWHM) gets bigger. From these measurements one can quite easily deduce the decreasing spin lifetime and the correlated decrease of spin diffusion length by fitting the results to theory (see figure 6.26). If we assume that the magnetization behaves similar in these structured samples than in the as grown one from fig. 6.25, we can say that probably increased spin scattering at phonons leads to the very rapid loss of signal height while the magnetization reduction due to temperature would be too small to explain the results.

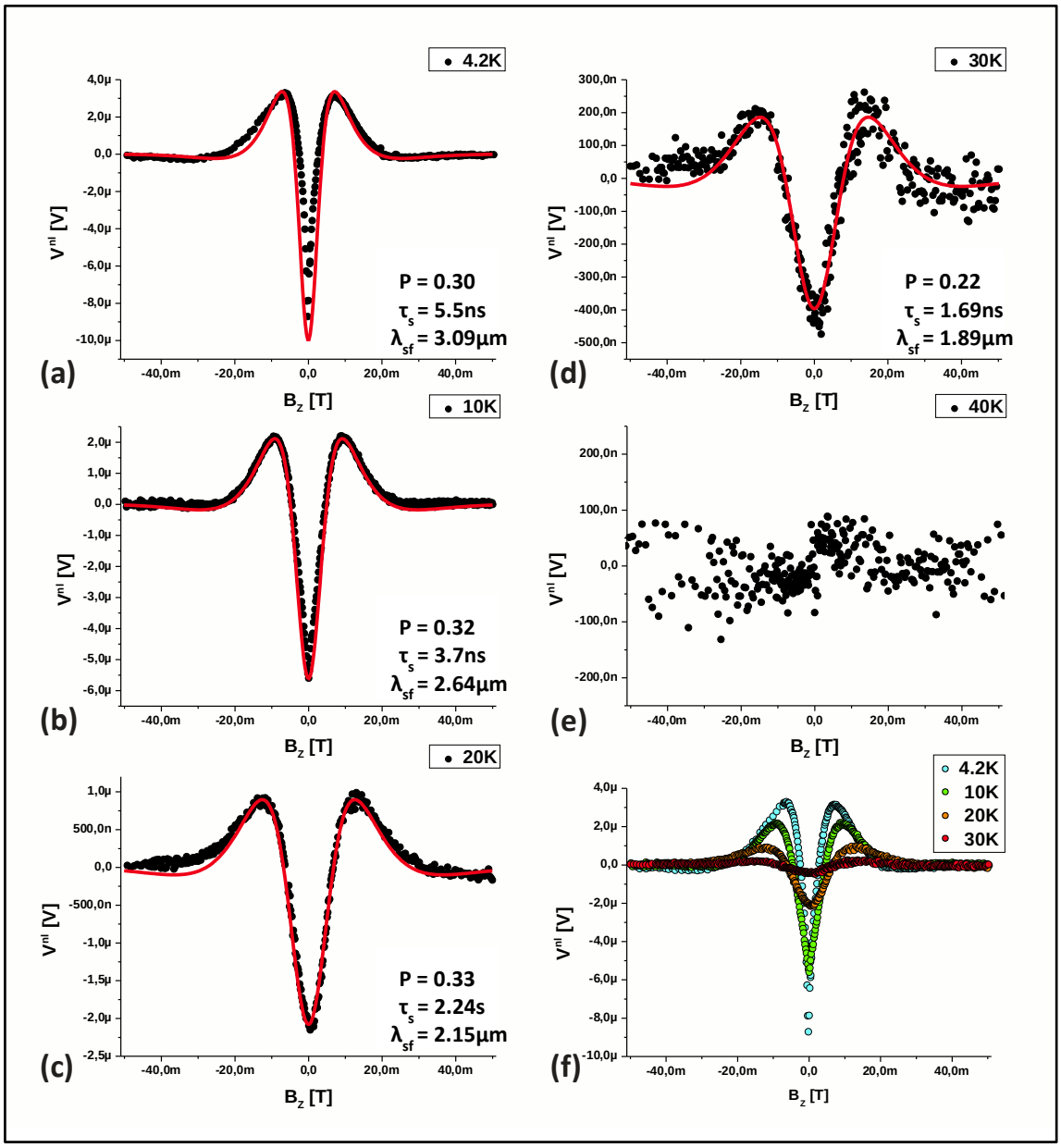

Fig. 6.26: At increasing temperatures the Hanle signal height gets smaller, while the width gets bigger. (a) to (d) show Hanle signals from 4.2 K to 30 K. At 40 K the signal is already so small that it starts disappearing within the noise level of the measurement (e). In part (f) all signals with reasonable size are superimposed in one single plot.

6.4.2 Spin-valve measurements

We also performed standard spin-valve measurements at different temperatures. What is expected is basically the same as in Hanle experiments; reduced signal magnitude the higher the temperature gets due to reduced magnetization in the contacts as well as a shortened spin diffusion length due to increased scattering. Yet it is important to keep in mind that we are limited to three distances of 5, 10 and 15 µm due to our sample geometry. If one now recalls the measurements we presented at the beginning of chapter 6, it is only logical to expect that the already small signals at the third detector at 4 K will very rapidly disappear within the background noise if temperature is raised. Therefore we do not show some exponential fits. Instead we only demonstrate the SV-signal of the first detector, which is clearly decreasing with increased temperature, see figure 6.27.

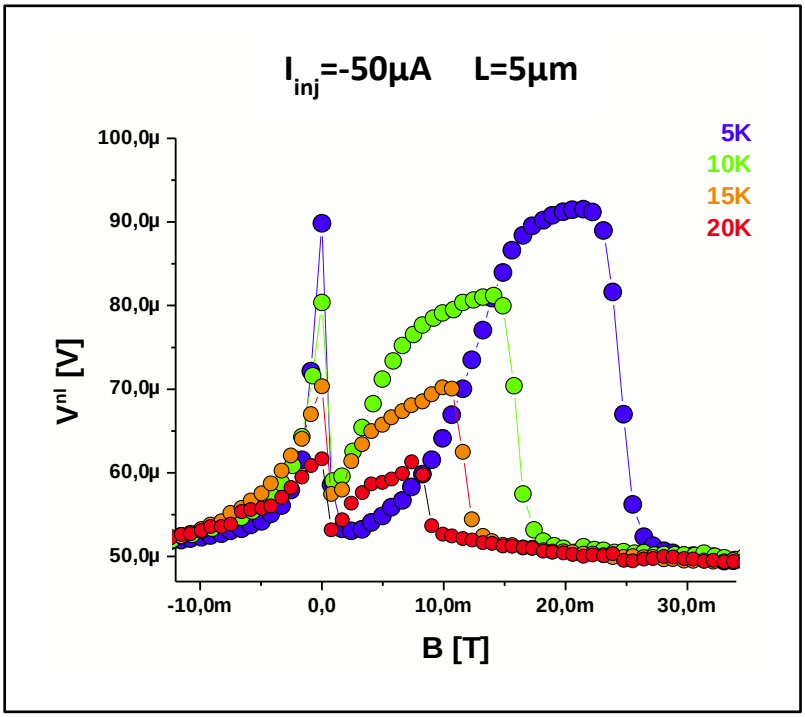

Fig. 6.27: Nonlocal SV-measurements with injector current of -50 µA at different temperatures and shifted to the same background level for easier comparison. The first detector was used for these measurements. The signal decrease coincides with the temperature dependent Hanle measurements.

6.5 Tunneling anisotropic spin polarization (TASP)

As just recently was discovered[Goul], the tunnel resistance in structures with single ferromagnetic GaMnAs layers depends on the relative orientation of the layer magnetization with respect to the crystallographic direction. This effect was called TAMR. Analogously to that, the anisotropy in related polarization of tunneling current can be described as tunneling anisotropic spin polarization (TASP)[Fabi].

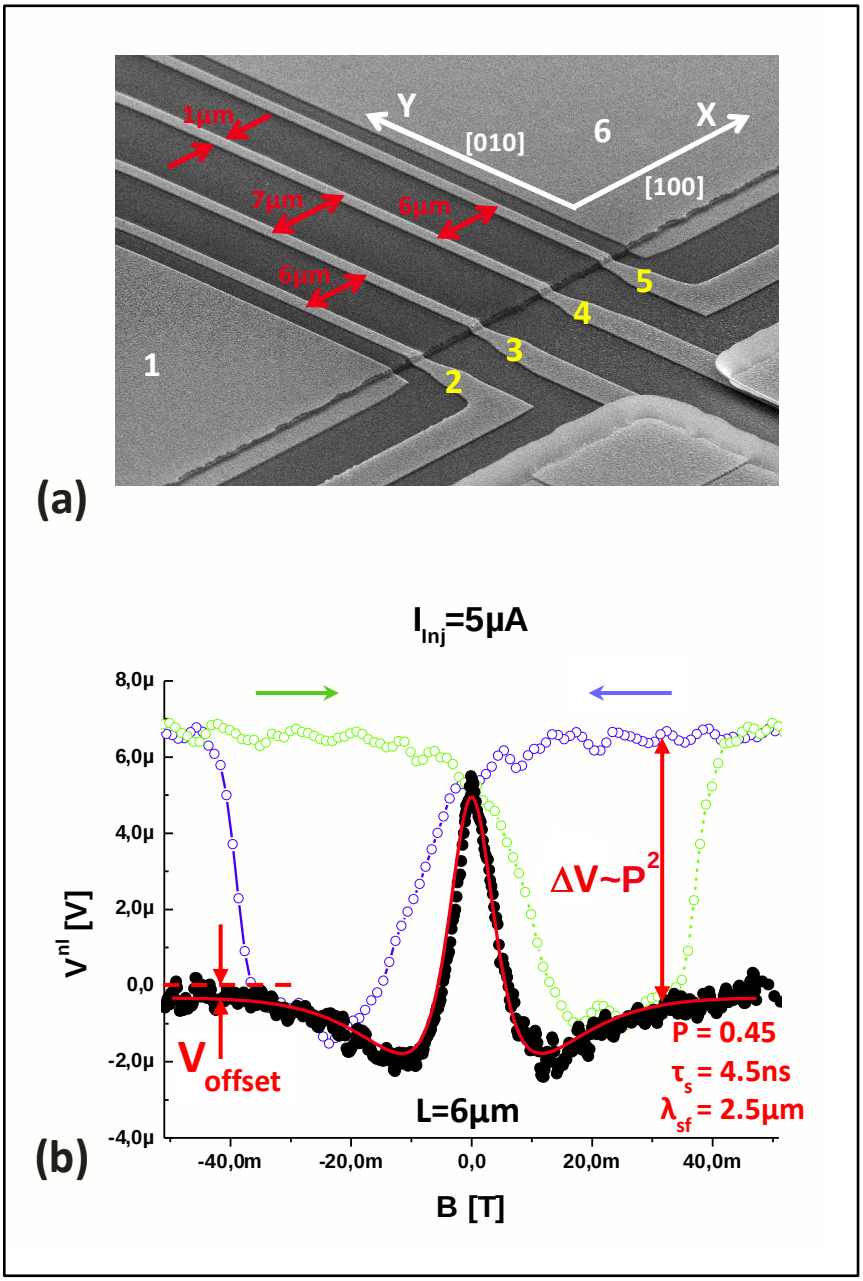

Fig. 6.28: Sample #03 is structured very similar to the previously measured one (a). Main difference is the channel orientation, which is turned by 90° thus parallel to [100] direction. (b) depicts a superposition of in-plane and out-of-plane curves, similar to fig. 6.23.

In this chapter we present the results obtained on a similar device of sample 03 from the same wafer as was characterized before, depicted in figure 6.28 (a). The channel was structured along the [100] direction of the GaAs crystal and is both 350 µm long as well as 50 µm wide again. The center to center spacing of the ferromagnetic contacts is now 6 µm between contact pairs *2-3* and *4-5* as well as 7 µm between the inner pair *3-4*. The injection circuit was again biased with a certain current, while at the detector contacts only the nonlocal voltage was measured with respect to the ohmic contact 6. Additionally the resistance of the injector contact was measured in a 3-point configuration between contacts *2* and *6*. As there is no current flowing between these two specific contacts V_{inj} here only reflects the voltage drop across the interface of the

injector contact 2 without any contributions from the lateral transport channel. Here we limit the bias current to values where $P_{inj} = P_{det}$ holds, as was shown in the previous chapters. Most of the measurements are done with AC lock-in technique and a bias current of $I_{inj} = 5\,\mu A$. AC measurements offer the two main advantages of increased signal to noise ratio for low current measurements and minimized background in our signal, as the background appears to be roughly symmetric with the bias current. The drawback of AC-measurements is however that the information about the difference between injection and extraction of the spins is lost.

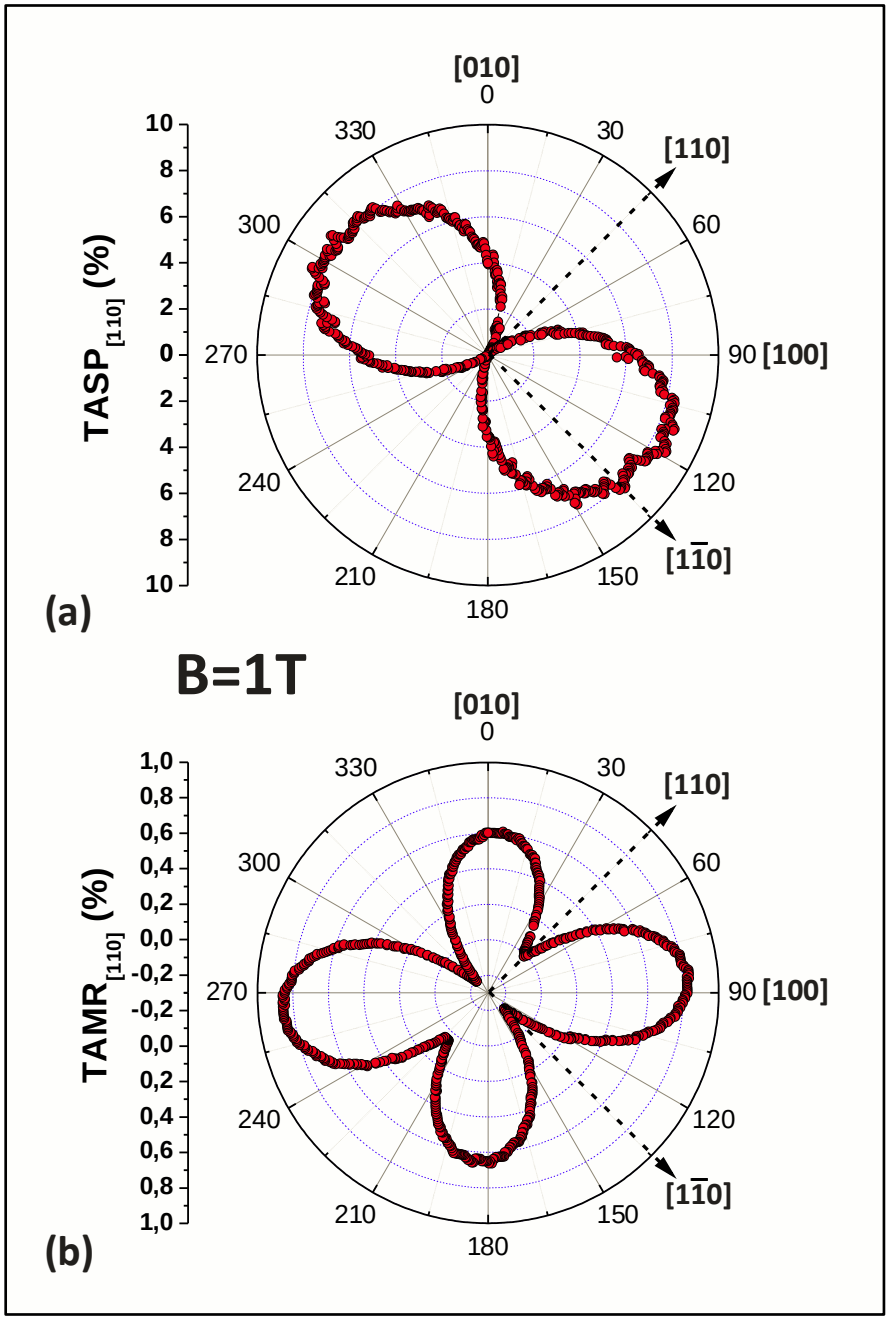

Fig. 6.29: In-plane TASP and TAMR are shown in (a) and (b) respectively. The magnetizations were kept parallel with an in-plane field of 1 T. Contact pair 3-6 was used as injecion circuit, 3-1 for sensing the voltage drop V_{inj} and 2-1 to detect the non-local spin signal.

In figure 6.28 (b) we show typical results of spin-valve measurements for external field swept along B_y direction as well as for Hanle measurements with external field swept along B_z. The combination of the nonlocal detector signals for both configurations in one plot shows that the behavior is the same as in previous chapters with DC measurement techniques. At sufficiently high out-of-plane fields of ≈50 mT the spin signal is completely suppressed and therefore equal to zero (black curve). We now can extract the offset signal as V_{offset}≈-0.4 μV. Fitting these data with theoretical curves gives us a spin injection efficiency of P_{inj}≈45 %, spin relaxation time of 4.5 ns and a corresponding spin diffusion length of 2.5 μm. These results are consistent with the previously obtained values from sample 15, characterized in the chapters before. The curves for the in-plane SV-measurements (blue and green) show typical spin-valve-like behavior with the spin signal reaching zero at the bottom of the spin-valves. We can extract the spin injection efficiency also from these measurements but now get an approximate value of P_{inj}≈51 %. This discrepancy between the values extracted from spin-valve and Hanle measurements could stem from the anisotropy of spin injection efficiency, which results from different orientations of the injected spins with respect to the crystallographic directions. For the P_{inj}-values extracted from spin-valve measurements we used the ΔV signals. These were determined with the magnetizations of the magnetic contacts (and therefore the directions of the injected spins) being parallel to the external magnetic field, i.e. pointing along [010] direction. Contrary to that our Hanle experiments probe the spins injected parallel to the magnetizations of the contacts at B_y=0 T, which do not have to point along [010] at vanishing external field.

For a closer investigation of the in-plane anisotropy of P_{inj}, we performed measurements with an in-plane field of B_{xy}=1 T. This field kept the magnetizations of the magnetic contacts always parallel to its own direction while the sample was rotated in it. The measured voltage is then determined by

$$V^{nl} = \pm(P_{inj}P_{det}I\lambda_{sf}\rho_N / 2S)exp(-L/\lambda_{sf}) + V_{offset} \tag{6.6}$$

and the observed changes in the signal are due to the dependence of the polarization on the crystallographic direction[2]. Typical results of those measurements are shown in figure 6.29 (a). The plotted TASP for spins forming an angle φ with [010] direction is defined, in reference to [110], as

$$TASP_{[110]}(\varphi) = 100\% \cdot [P(\varphi) - P(45°)]/P(45°). \tag{6.7}$$

Between [1-10] direction (ϕ = 135°) and [110] direction (ϕ = 45°) an anisotropy of ≈8 % is observed. These findings are consistent with theoretical results of Sankowski et al.[Sank], assuming a small strain along [110] direction. In 6.29 (b) we plot the anisotropy in tunneling resistance, which is defined in a very similar way as TASP by

[2] We assume isotropic V_{offset}, which was confirmed by measurements on characteristic crystal directions.

$$TAMR_{[110]}(\varphi) = 100\% \cdot [R(\varphi) - R(45°)] / R(45°). \quad (6.8)$$

Here $R = V_{inj} / I_{inj}$ holds. The obtained TAMR curve shows anisotropy both between [010] and [100] directions as well as between [110] and [1-10] directions, as is typically observed in GaMnAs structures[Cior]. If one investigates the behavior along [1-10] direction, it can easily be seen that a positive TASP along this direction corresponds to a negative TAMR, which again is consistent with theoretical predictions[Sank].

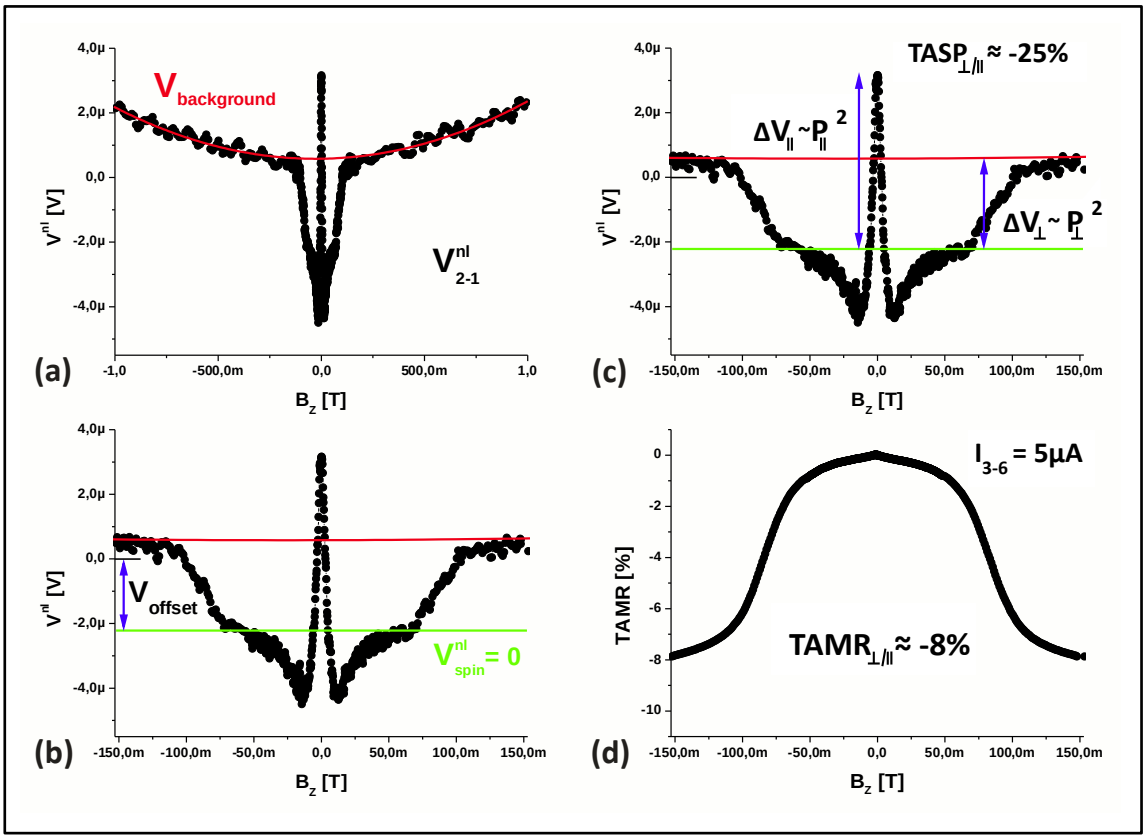

Fig. 6.30: Non-local voltage that was measured between contacts 2 and 1, while excitation current was applied between 3 and 6 (a). The parabolic background was observed also from other groups[Lou] and can be easily fitted. As at sufficiently high out-of-plane fields of 50 mT and above the spin signal vanishes due to dephasing one can extract an offset of -2.2 μV for zero spin signal (b). The voltage drops from zero spin signal to zero external field (ΔV_{II}) and to high out-of-plane field ($\Delta V_{\perp}$) is a measure of the anisotropy of the spin injection efficiency (c). The out-of-plane TAMR at the injector contact is comparable in its size to results of other groups[Gira] (d).

We also investigated the anisotropy of spin injection efficiency between the in-plane and out-of-plane orientations. The value of TASP is obtained from measurements in perpendicular magnetic field, which is shown in figure 6.30 (a). The spin signal again vanishes at out-of-plane fields of ≈ 50 mT due to spin dephasing. We can extract an offset background of $V_{offset} \approx$ -2.2 μV, which is different from the previous value as we used other contact pairs. Increasing the out-of-plane field to ≈ 70 mT and above tilts the magnetizations of injector and detector contacts out-of-plane and the injected spins are again parallel to the external field. In this configuration we again observe a nonzero spin-dependent

signal at the detector. The amplitude of the resulting voltage step in the detector signal we call $\Delta V_\perp$. It is proportional to the square of the spin injection efficiency $P_\perp$ of spins pointing out-of-plane in [001] direction. At higher fields the measured detector signal shows parabolic behavior as was already observed in previous chapters and from other groups[Lou]. This parabolic background is plotted in figure 6.30 as a red line and clearly can be disregarded in the interesting range we show. The difference in the signal registered at high out-of-plane field ($\Delta V_\perp$) and the one at zero external field ($\Delta V_{//}$) is then a measure of the anisotropy of the spin injection efficiency. We define the perpendicular to plane anisotropy as

$$TASP_{\perp/\parallel} = 100\% \cdot (P_\perp - P_\parallel)/P_\parallel \tag{6.9}$$

and obtain a value of roughly -25 %. In figure 6.30 (d) we show the magnetic field dependence of the out-of-plane TAMR of the injector contact. The evaluated value for the

$$TAMR_{\perp/\parallel} = 100\% \cdot (R_\perp - R_\parallel)/R_\parallel \tag{6.10}$$

is almost -8 %, a value that is in the same range as the one in earlier reports on spin Esaki diode contacts[Gira]. Contrary to the in-plane case we discussed just before, the sign of TASP and TAMR is the same in the out-of-plane case.

6.6 Measurements on thicker GaMnAs layers

We have done analogous measurements on many other wafers with similar doping profiles. However the overall results were never as good as with samples made from wafer C070419B. When we had conduction channels with much longer spin lifetimes, we had problems with contacting the material adequately, the homogeneity of the layers was not good enough or the GaMnAs layers had problems. Therefore we only present measurements from one additional wafer, namely C080903A. The wafer map is shown in figure 6.31 (a). The principle wafer design is the same as with wafer C070419B. The only differences are the lower doping level of the n-channel of roughly 2.5×10^{16} cm^{-3} (what should lead to higher spin diffusion lengths) together with an increased thickness of the channel (now 1 µm) and the thickness of the GaMnAs layer was raised as well, which now accounts for 50 nm.

We also had problems contacting the n-doped layers on this wafer. So for these measurements we used Esaki diodes also for the reference contacts. This leads to different effects in the injector and the detector circuit. We apply a constant current in the injector circuit flowing from contact 2 into the sample and at contact 1 out of it. We monitor the voltage drop between contacts 2 and 1, what means we have the configuration of a local spin-valve measurement. Due to the relatively high spin diffusion length in this wafer (from electrical as well as optical measurements on several different samples spin diffusion lengths of around 10 µm were extracted, what is due to the lower n-doping of the channel

compared to the previously characterized samples) and the edge to edge distance between these two contacts of 5 µm we expect spin dependent signals

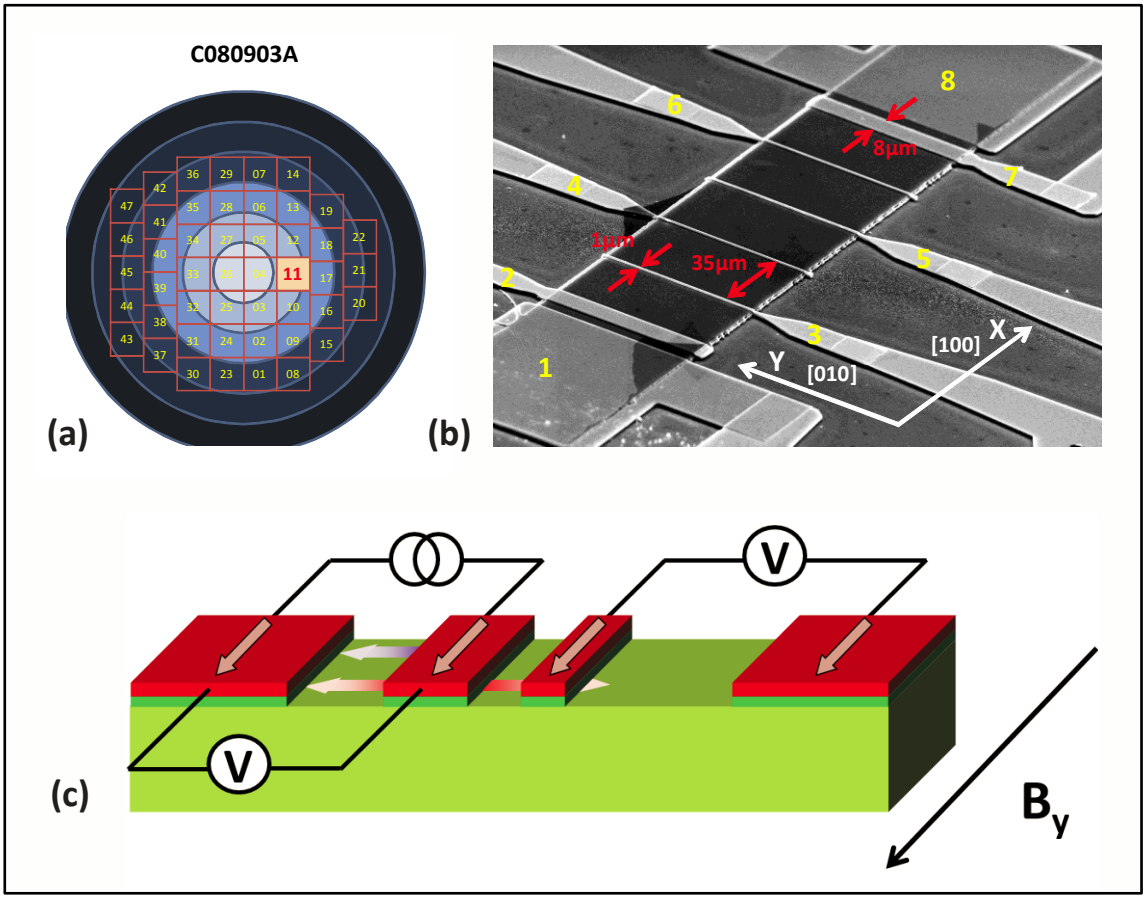

Fig. 6.31: Wafer-map of C080903A (a). In part (b) a SEM picture of a companion structure can be seen. All eight contacts are ferromagnetic Esaki contacts this time. The edge to edge distance of the two injector circuit contacts (number 2 and 1) is roughly 5µm. The spin diffusion length measured on several samples of this wafer is around 10µm, gained from electrical as well as optical measurements. The experimental setup is shown in part (c). In one run a local 2-point as well as a non-local 4-point measurement can be done.

in the local measurements. Additionally we perform non-local 4-point measurements, as always. Therefore we detect the arising voltage between the contacts 3 to 7 and the big reference contact 8. Although the reference contact 8 is a ferromagnetic Esaki contact and not a non-magnetic ohmic one we do not expect problems from that fact, as the distance from the injector is more than 180 µm and therefore the spin accumulation has already vanished much earlier. Therefore we can treat this contact as if it was a standard ohmic one as in the previous chapters[Lou],[Erve].

In figure 6.32 we show measurement results obtained the following way: External field was swept along y-direction (see fig. 6.31 (c)), thus parallel to the long side of the magnetic contacts. We only show field sweeps in positive field direction to simplify matters, but the back sweep signals behave analogously. A constant current of -100 µA was applied at contact 2 and the local voltage between 2 and 1 is shown in part (a) and (c). Obviously the signal in the injector

circuit exhibits three different states, besides the omnipresent DNP peak at zero (these results were not corrected for magnet's hysteresis, only offset to the same background voltage levels). As contact 1 is nearly quadratic with lateral dimensions of 50 µm

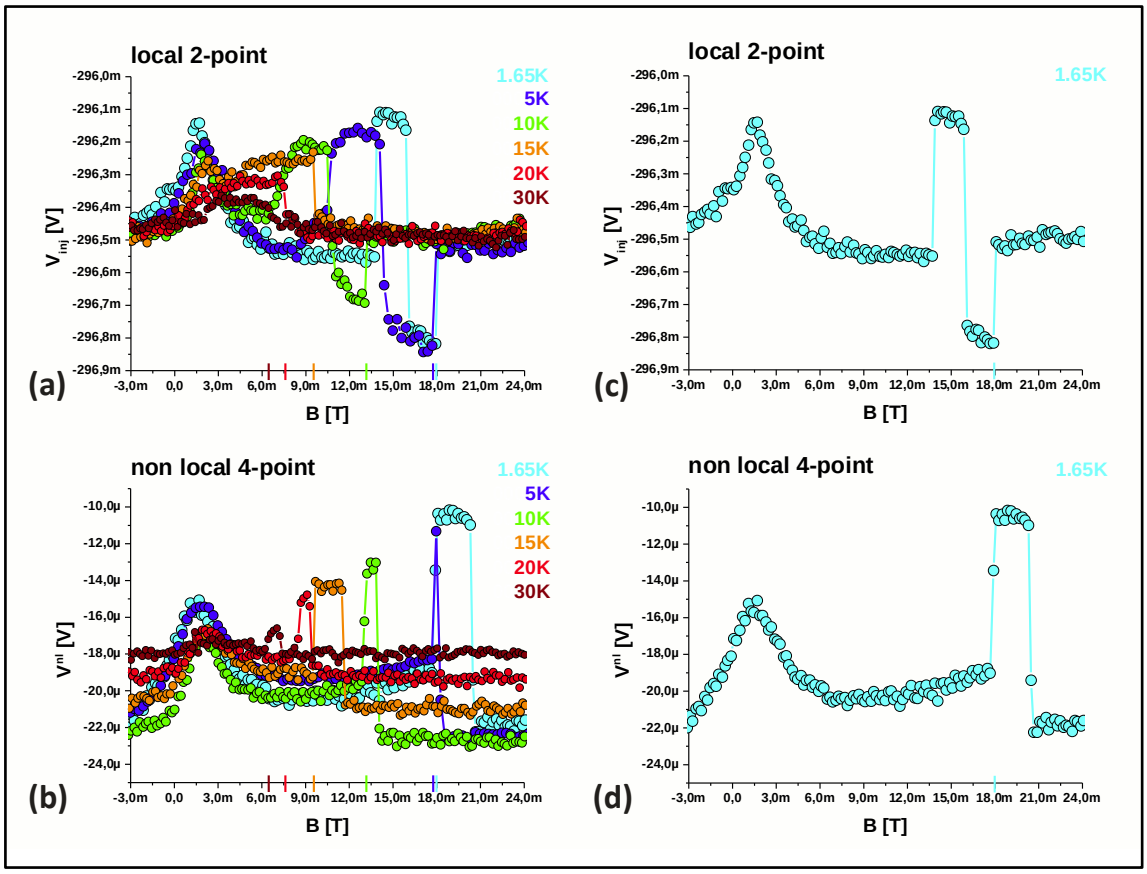

Fig. 6.32: (a) local 2-point spin-valve measurements in the injector circuit at different temperatures. (b) according non-local measurement between contact 3 and 8, which means the detector is 35 µm away from the injector contact. The last jump in the injector circuit is always at the same field value as the first one from the detector. (c) and (d) show the same measurements but only for a single temperature.

and more we can explain the signal as follows: The magnetization of contact 1 behaves as bulk GaMnAs and therefore the magnetization reversal takes place in two steps. At first the magnetization jumps from the [010] easy axis to the [100] easy axis, which gives the first jump in the local signal. The second step can be correlated to the completion of the reversal process if the magnetization jumps from the [100] to [0-10] and is now aligned again parallel to the field. The contact 2 behaves already uniaxial due to its geometrical form and switches after the big contact in a single event. As both contacts are biased (one in reverse the other in forward direction) both imply a spin accumulation into the channel, one through spin injection the other by spin extraction. In the non-local signals that are shown in part (b) and (d) of the figure one can clearly see the footprint of the switching of contact 2. The fact that the two-step switching of contact 1 cannot be seen in the non-local signal can be explained by the bigger distance. As the spin accumulation decays exponentially the dominating

contact is number 2. Its switching can be seen clearly in both signals, as the third event in the local signal can always be seen as first voltage jump in the non-local signal (see the markings at B-axis in figure 6.32). If the external field is swept further the detector contact number 3 switches also in a uniaxial event its magnetization. In the viewgraphs 6.32 (a) and (b) we can see this behavior consistently for different temperatures from 1.65 to 30 K. Every time the third voltage drop in the local signal occurs at the same field value as the first one in the non-local signal. Additionally the signal heights in both measurements decrease with increasing temperature, as expected. This can again be explained by reduced magnetization of the GaMnAs contacts as they approach their Curie temperature as well as increased spin-scattering at higher temperatures. Additionally the switching occurs consistently at lower field values, which can again be explained by lower magnetization values at higher temperatures.

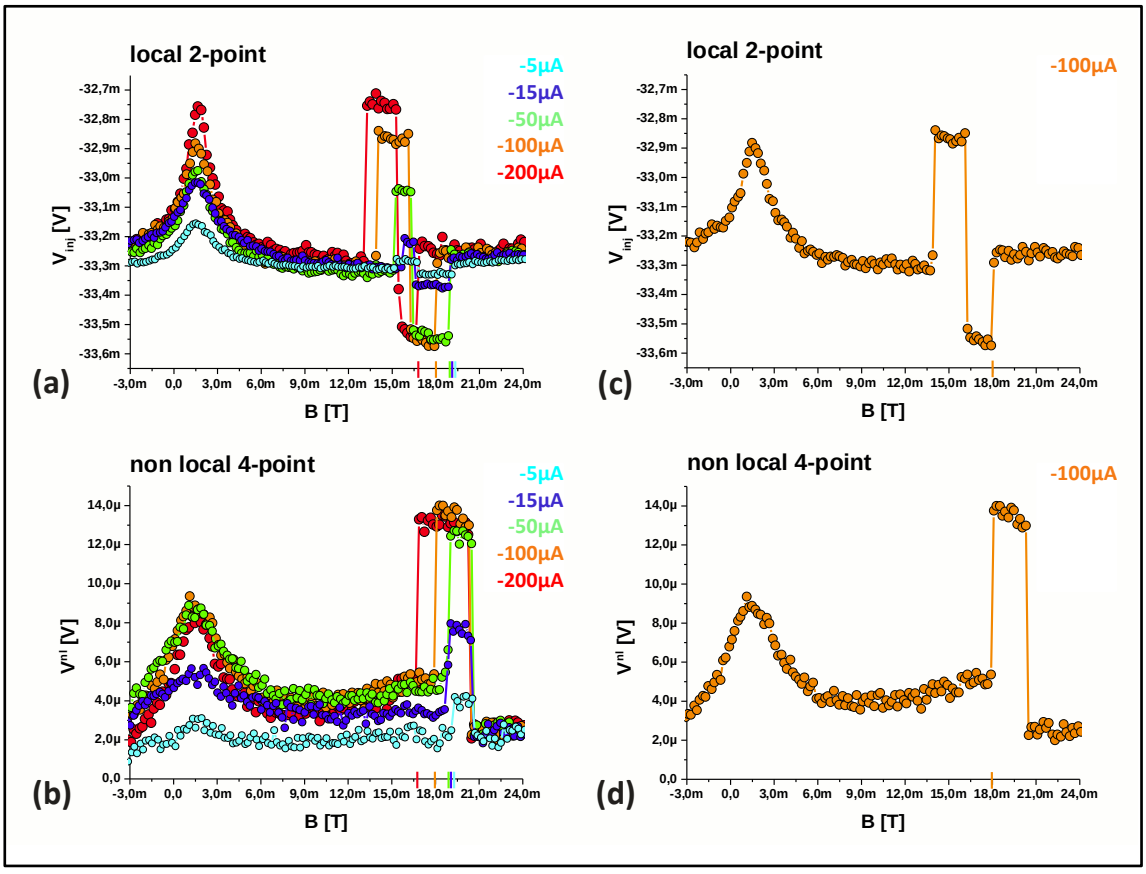

Fig. 6.33: (a) local 2-point spin-valve measurements in the injector circuit at different injection currents. (b) the according non-local measurement between contact 3 and 8. The last jump in the injector circuit is again always at the same field value as the first one from the detector, as in figure 6.32. (c) and (d) show the same measurements only for an injector current of -100 µA.

In figure 6.33 we show the same measurement type again, yet this time with varying injector current at a constant temperature of 1.65 K. In part (a) we see again the three voltage levels as before, which can be explained by the two step magnetization reversal of contact 1 and the uniaxial switching of contact 2. If one increases the injector current from -5 µA to -200 µA the switching fields

decrease. One can explain this very easily by increased Joule's heat deposited in the contacts and the channel. This has the same effect as increasing the overall temperature. If one compares the switching values of the third event from part (a) with the corresponding first voltage jump in part (b), again both always occur at the same external field. Contrary to this the second voltage drop in the non-local signal does not show any dependence on varied injector current. This is expected as it is 35 µm away from the injector circuit and thus an increased current does not change the temperature in this contact. In contrast a change of the overall temperature in fig. 6.32 modifies the switching field of the detector contact very well. These observations support our assertion of the voltage jumps with the according switching events of the magnetic contacts.

Overall these results on wafer C080903A show that here it is very easily possible to change the magnetic behavior of the contacts by structuring. At a comparable Mn amount of roughly 5 % as in the wafer C070419B the only difference is the GaMnAs layer thickness of now 50 nm. Together with observation from other groups we can now put all data together to a complete picture. The first observations of lithographically induced magnetic anisotropies were made on 20 nm thick layers[Hümp] but the nanomagnets were not covered by a metallization and therefore the GaMnAs lattice could easily relax perpendicular to the structures. In other papers to this topic the layers were even thicker with 50 nm[Hoff] and 70 nm[Weni]. In our first only 20nm thin samples we had always a metallization on top of the GaMnAs contacts. This prevented the lattice from relaxing easily as it is strained from top and bottom side (through the GaAs lattice) likewise. Together with the results obtained from the 50 nm thick layers on C080903A we can see that this layer thickness is big enough to allow a relaxation of the GaMnAs lattice in between the GaAs below and the metallization on top to exhibit different coercive fields at varied aspect ratios.

7. Summary and Outlook

In our work we have employed a successful all electrical and all semiconductor spin injection scheme. Our samples base on a new class of so-called diluted magnetic semiconductors, namely its best known representative GaMnAs. As spin injection from metallic ferromagnets into semiconducting material suffers from severe conductivity mismatch, this DMS can help solving these problems in various ways. At first its lower conductivity reduces the gap to semiconductors, while the combination of this naturally p^+-type material with highly n^+-doped GaAs forms an Esaki-tunneling diode which can serve us with very high spin injection efficiencies. As GaMnAs can be grown epitaxially on GaAs it is also the perfect ferromagnet to take advantage of the high spin lifetimes in GaAs layers doped near the metal-insulator transition.

In our experiments we were able to reliably achieve spin injection efficiencies of remarkably high 50% and slightly above. The results obtained from nonlocal in-plane spin-valve measurements were thereby consistent with our out-of-plane Hanle experiments in terms of injection efficiencies as well as spin diffusion lengths. These were roughly 3 μm, what corresponds to a spin lifetime in the range of 5 ns. We additionally investigated the anisotropies of tunneling MR and spin polarization. For in-plane TAMR we gained values of up to ≈1.5 % while for out-of-plane configuration we observed ≈8 %. In the case of in-plane TASP the effect had a magnitude of ≈8% and the out-of-plane TASP reached ≈ -25 %. For a second wafer with slightly lower doping of the conduction channel and thicker GaMnAs the spin diffusion length easily exceeded 10 μm, what was also confirmed by optical measurements.

With this second wafer we have shown that a lithographically induced control of magnetic anisotropies in GaMnAs is possible due to strain relaxation of the GaMnAs layer perpendicular to the structure edges. Due to our sample design and processing methods our GaMnAs contacts are capped with metallic contacts that prevent the strain relaxation as long as the GaMnAs layer is not thick enough for that. Our results show that a GaMnAs layer thickness of 50 nm is nevertheless enough to allow for significant strain relaxation of compressively strained GaMnAs. This is consistent with the results of other groups.

For future experiments there are various possibilities. If sticking to epilayers one could just try to decrease the doping levels of the channel just to the metal-insulator transition of 1×10^{16} cm^{-3}. A second important step seems to be the use of thicker GaMnAs layers, to be able to easily tune the magnetic switching behavior of the GaMnAs contacts. Another promising route would be the

investigation of the same design on a Si-basis, which would have the big advantage of complete compatibility to the dominating semiconductor technology.

The second option would be to go in the direction of 2D electron systems, as there a difference in the spin diffusion lengths could allow infinitely long spin lifetimes or strongly suppressed ones, dependent on the direction[Schl], which could be used for functional design. Additionally it should be possible to use gating to change the spin information while transport in the channel by Rashba interaction what could be used to build a Datta-Das transistor. This would make the use of external magnetic fields dispensable and principally allow for integration of spin-transistors into modern electronics.

A third thing is independent of using 2DES or epilayers. The Curie-temperature of GaMnAs has been substantially increased from the beginning of its investigation until today. But still 180 K is far from being adequate for standard every-day applications. This renders GaMnAs a model system for fundamental research or at best niche applications in satellites or quantum computers. However the combination of GaMnAs with Fe could be a viable route out of this dead-end street. The magnetic coupling of a Fe layer on top of a thin GaMnAs layer could be used to increase the Curie temperature of the system to room temperature and give the possibility of using the system in standard computing applications. First promising results have already been reported in [Song], where T_C could be increased by roughly 40 K.

Appendix A: Preparation Techniques

In this first appendix chapter we want to give deeper insight into our sample preparation techniques and the problems we ran into therewith.

Before you can do anything you need at very first a GaAs wafer substrate with a diameter of 2″. This is bought from an external substrate manufacturer. These substrates are glued onto a wafer holder with liquid gallium (melting point 29.76 °C). This gallium glue provides an excellent thermal coupling to the substrate. Inside of the MBE chamber (in fact more chambers are coupled to a bigger system) the holder can be moved by several manipulators, which are magnetically coupled to the outside world. Exactly 15 wafers were grown over the course of this thesis. While only very few wafers showed both excellent electrical resistances and fine spin effects many of them seemed to have already problems with the substrate material. Some had quite big cracks after lock out from the growth chamber without any further processing. In figure A.1 some optical microscope pictures are shown for very good as well as suboptimal wafer surfaces after growth.

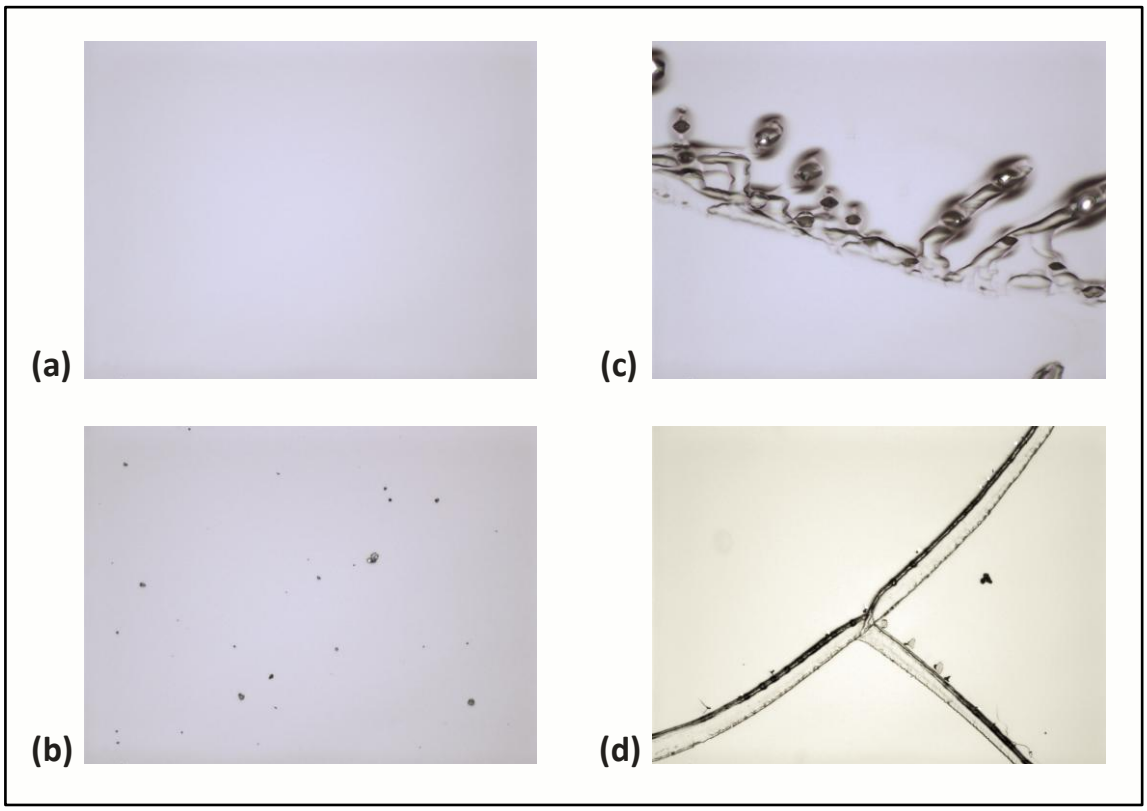

Fig. A.1: Optical microscope pictures from different GaMnAs wafers. A perfectly smooth and clear surface implies a very good crystal structure (a). Many things can lead to crystal defects during the epitaxy such as dirty substrate material, contamination inside the growth chamber, too impure material in the effusion cells, wrong temperature or imperfect, tensed substrates what can culminate in tension cracks during growth (b to d).

The growth of the desired layers in the MBE chamber can be recapitulated on the basis of the growth protocols. For the two wafers we presented measurements of we give the according protocols on the subsequent pages.

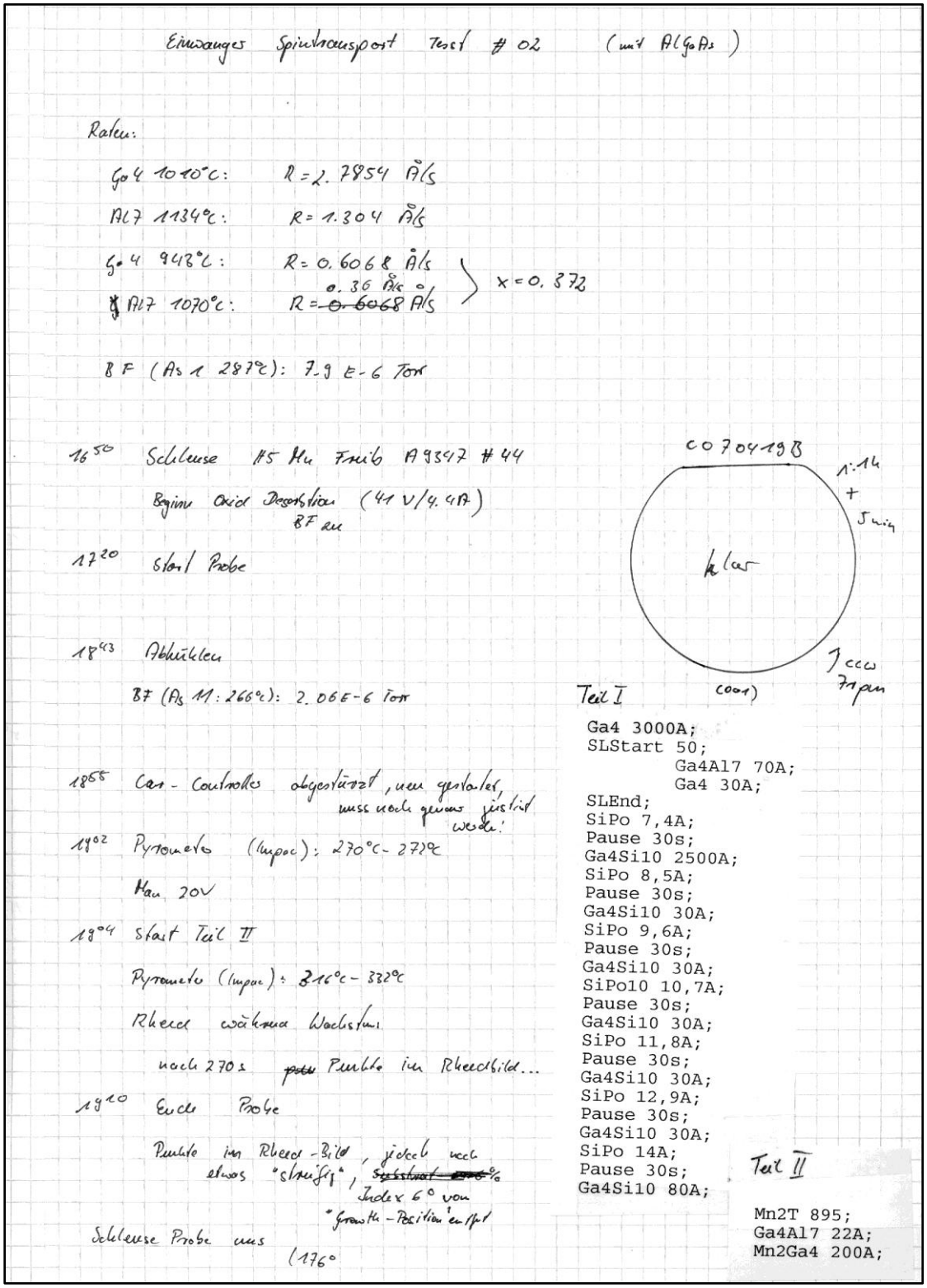

Fig. A.2: MBE growth protocol of wafer C070419B. The rates of Ga and Al on the sample are calibrated before the growth, the temperatures of the effusion cells are measured. Then every timestep is mentioned from the inward transfer of the wafer to the lock out. This wafer was very lucky not to end up at the bottom of the chamber as at 18:55 the car controller crashed.

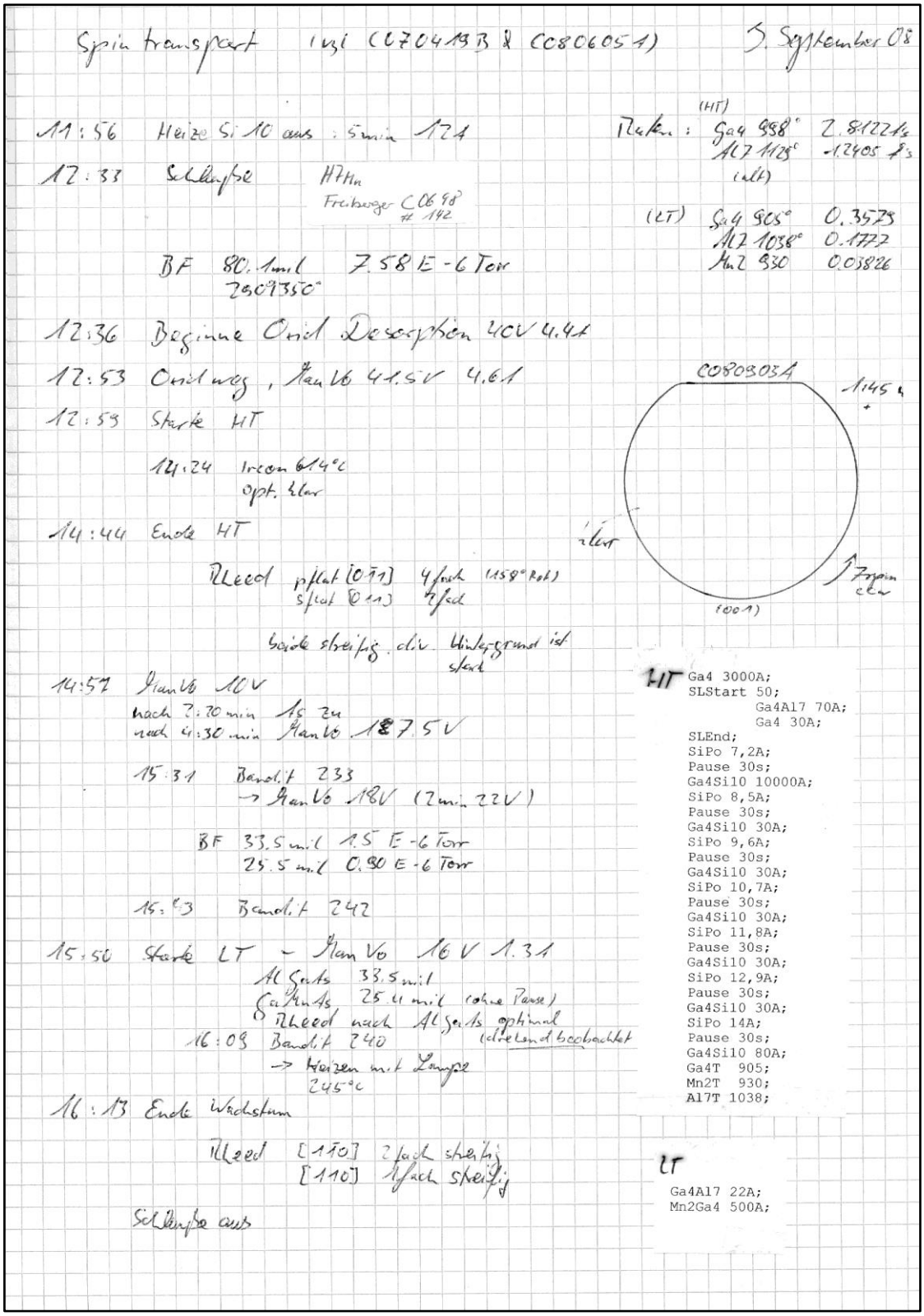

Fig. A.3: MBE growth protocol of wafer C080903A. The growth is just controlled by a simple Lab View program that opens and closes the effusion cell shutters while checking the temperature and wafer rotation. It is always added to the protocol. After the HT steps the wafer has to cool down before the LT growth of the upper AlGaAs and GaMnAs layers can start. This takes at least one hour until the temperature is stable at the desired value.

In the following we illustrate the exact production process of our presented samples. The basic flow is always the same, while single parts have been

reengineered over time to optimize the behavior of the structures and/or enhance the effective yield of the fabrication cycle.

Fabrication of sample #15 of wafer C070419B

1) Take the individualized sample #15 out of the exsiccator (together with etch test samples from the same radial range of the wafer).
2) Cleaning cascade, standard 5 min., 1 min. and 30 sec. in acetone vessels with ultrasound on, then into an isopropanol bath.
3) Drying with nitrogen gun and directly following spin coating optical resist ARP3740 with 3000 rpm (0) 5 sec. and 6000 rpm (0) 30 sec.
4) Prebaking @ 90 °C hotplate for 6 min.
5) Exposure in the mask aligner for 50 sec. with the mesa mask, see figure A.4.

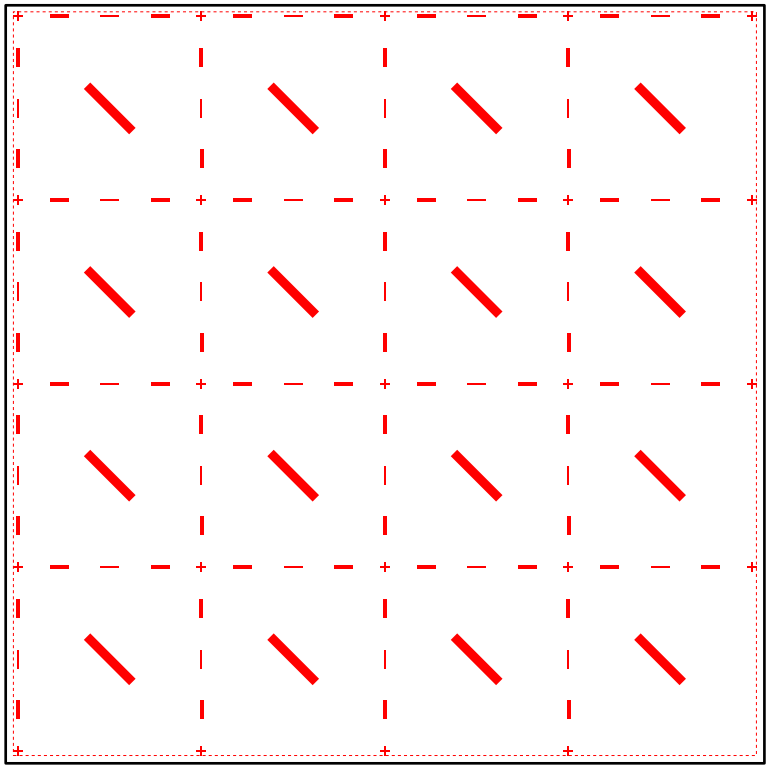

Fig. A.4: The mesa mask with all mesas oriented in 45° angles. As the GaAs crystal breaks always along [110] directions, but the easy axes of GaMnAs are nearly 45° turned, we structured all samples presented here along easy axes and thus the switching behavior of GaMnAs should be easier to understand.

6) Developing the sample in a solution of AR 300-26:H_2O (1:3) for 41 sec.
7) Postbake @ 60 °C hotplate for 3 min.
8) Etching one etch test sample, 45 sec. in HCl:H_2O (1:1) and 60 sec. in acetic acid:H_2O_2:H_2O (5:1:5) for 60 sec., resulting etch rate was 4.77 nm/sec.
9) Etching the real samples to a depth of 380 nm, etch stop and cleaning in DI water, drying with nitrogen.

10) Preconditioning of the PECVD chamber to get a constant temperature and homogeneous film thicknesses by processing two dummy samples at 108 °C and for 1 min. each.
11) Deposition of expected ≈ 340 nm SiO_2 on real sample with the assumed (indeed very longtime stable) constant deposition rate of ≈ 40 nm/sec.
12) Removing the resist and the SiO_2 on top of it in 60 °C hot acetone with ultrasound to uncover the etched mesas.
13) Check of the structural contour line with the DEKTAK. A step of 10-20 nm was visible, nearly perfect.
14) Again a cleaning cascade but only with the last two steps (1 min. and 30 sec.) was applied and the optical resist has to be spin coated onto the sample with the same parameters and bake outs, this time however the pad-mask has to be used, see fig. A.5. The exposure times and development etc. are literally the same.

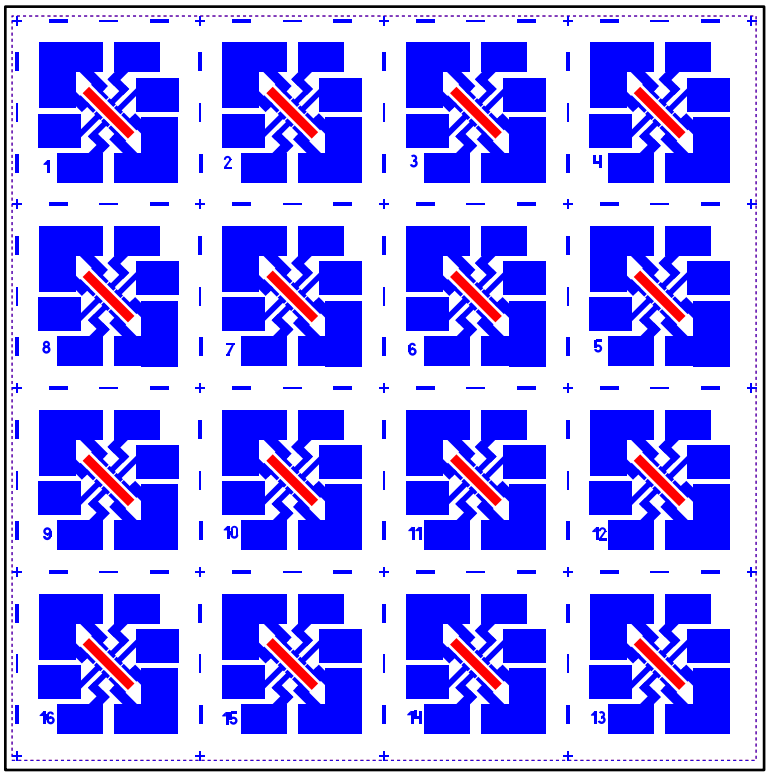

Fig. A.5: The bond pad mask with the according orientation to the mesa mask used. The alignment accuracy of this mask to the previous one has to be at least 5 µm or better across the whole sample to guarantee a feasible processing later on.

15) Now the Ti/Au bond pads had to be evaporated. Here the time for reaching base pressure is not so critical, but the contacts have to stick very firm on the underground to be easily bondable, therefore we typically sputtered for 20 sec. with argon ions and a current of 1.2 mA before evaporation.
16) Now we evaporated 15 nm titanium as a sticking layer and 150 nm gold as the real current feed material; 150 nm are a good choice to get an easy bonding process afterwards.

17) Subsequently the lift off process was performed with 60 °C acetone and a little ultrasound support.
18) Subsequently we cleaned the sample again in fresh acetone and spun on a double layer PMMA resist system.
19) 200k (7 %) with 3000 rpm (0) 5 sec. and 9000 rpm (9) 30 sec.
20) Bake out at 150 °C hotplate for 5 min.
21) 950k (2 %) with 3000 rpm (0) 5 sec. and 9000 rpm (9) 30 sec.
22) Bake out at 150 °C hotplate for 10 min.
23) EBL at LEO SEM with the GaMnAs contacts file, see fig. 4.6

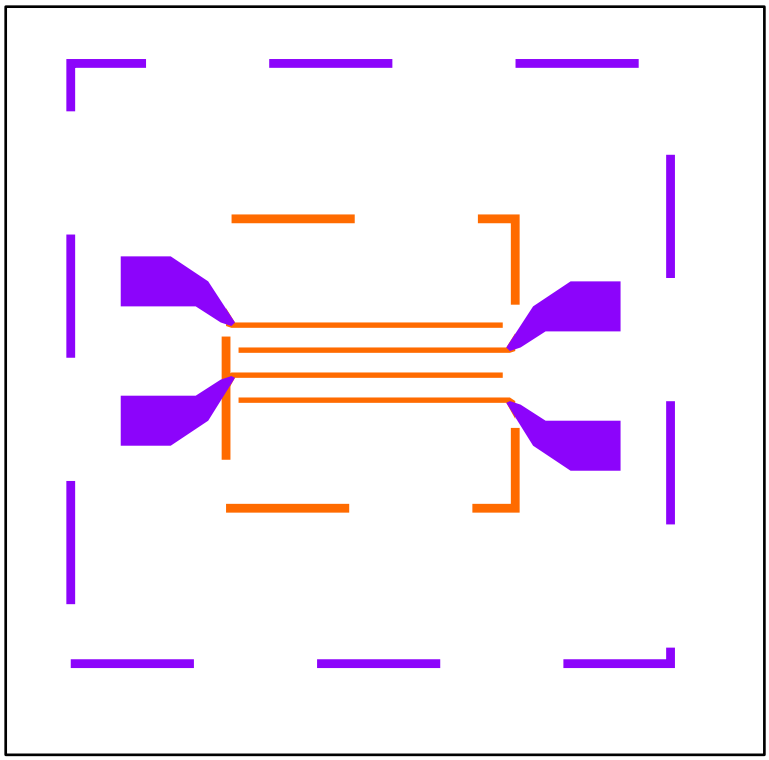

Fig. A.6: This design was used for the GaMnAs contacts of sample #15. The inner orange contact stripes are at first aligned relative to the mesa and the bond pad metallization. If the misalignment of these first two layers to each other is too big, quite some problems can occur. The outer violet structures connect the GaMnAs stripes to the big bond pad structures and are written directly after the inner contacts. Thereby the SEM has to change its field of view (FOV) from 58 µm to 120 µm (the dashed squares). At the LEO SEM this can typically be done without problems, but at the Topcon SEM a correction factor has to be integrated to account for the angular shift between different FOVs. The inner contacts were written with a dose of 390 µC/cm² and the outer ones with lower 350 µC/cm². The smaller the structures the more important it is to design the structures parallel to the horizontal coordinate axis. The reason lies within the SEM itself, it is more stable by contours along the horizontal line compared to long structures along the vertical line. If the structure is designed correctly but a scaling factor within the EBL software miscalculates the angular transition from design file to e-beam controller straight lines can turn out as small step functions, see figure Fig. A.11.

24) Developing the sample in MIBK/isopropanol (1:3) for 20 sec. and stop it thereafter in pure isopropanol for 45 sec.
25) Preconditioning of the UNIVEX A chamber with 4 hours pre-pumping and three nitrogen flushes of 2 min. each.

26) Native oxide dip in HCl:H_2O (1:1) for 40 sec. with the sample already mounted onto the UNIVEX holder.
27) Mounting of the sample into UNIVEX, evacuating and gettering with Ti leads to a base pressure of 3×10^{-6} mbar after only 25 min.
28) Evaporation of 15 nm titanium with an e-gun current of 55 mA, a rate of 2 Å/sec. and a pressure of $3.2 - 2.9 \times 10^{-6}$ mbar.
29) Evaporation of 110 nm gold with a heating current of 134-155 A, a rate of 2.3 - 1.6 Å/sec. and a pressure of $3.4 - 7.8 \times 10^{-6}$ mbar.
30) Lift-off process in 60 °C hot acetone and isopropanol bath, drying with nitrogen.
31) Etch rate determination with etch test samples, 45 sec. HCl:H2O (1:1) then the diluted acetic acid:H_2O_2:H_2O solution (15:3:50), result was 1.78 nm/sec. These test samples are etched in the same way as the real samples afterwards, see figure A.7. Typically two samples are used at the same time for the etch rate determination, while further control samples are accompanying the real samples afterwards.
32) Etching the real sample with 45 sec. HCl:H_2O and 13 sec. diluted acetic acid. Measured etch depth ≈ 25 nm, very well.

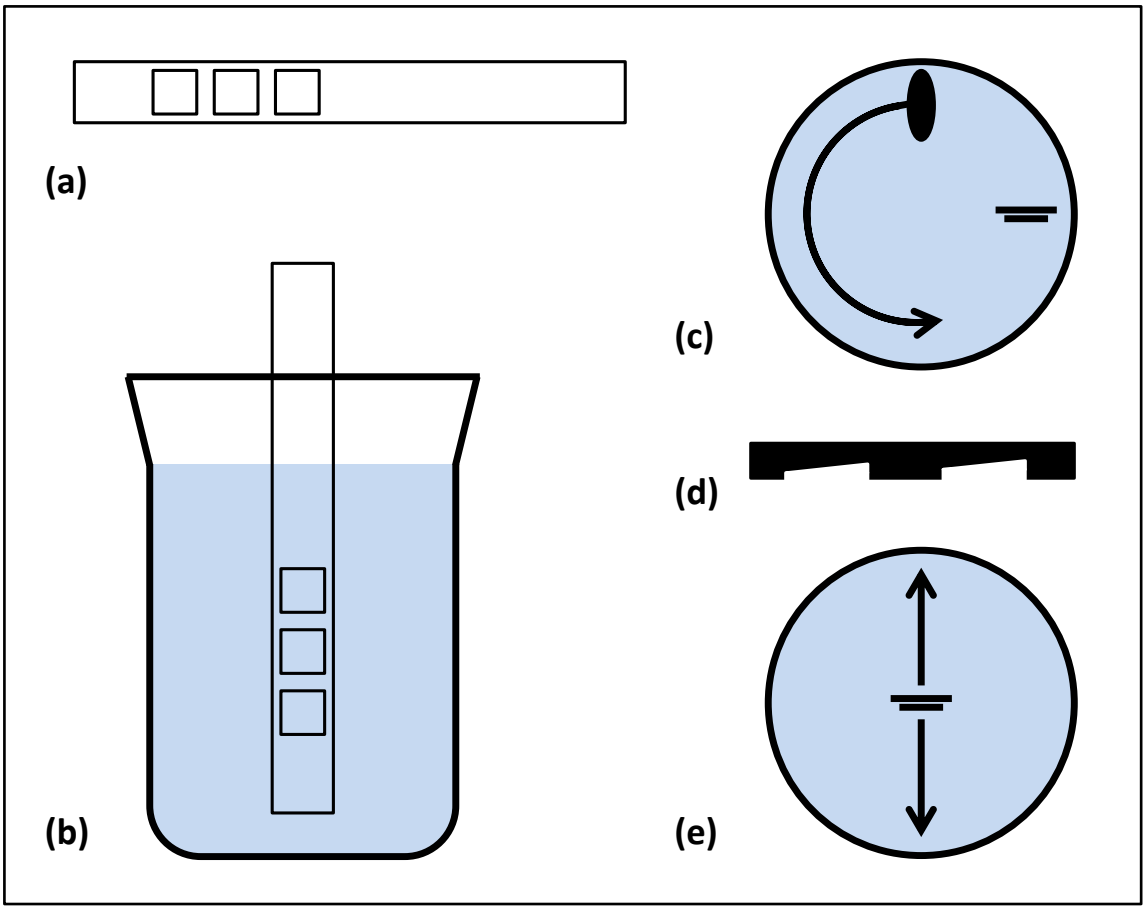

Fig. A.7: The process of wet etching. After the etch test has been done ,the real samples are glued with PMMA onto a glass substrate next to additional etch test control samples (a). The samples are etched within the acidic dilution (b) by moving the glass substrate vertically through the vessel (e) as the conventional method with magnetic stir bars (c) leads to higher etch rates on the radial outside of the vessel (d).

33) Std. cleaning cascade again.
34) Optical resist spin coating and prebake steps as above.
35) UV exposure as above but with ohmic contacts mask, see figure A.8.

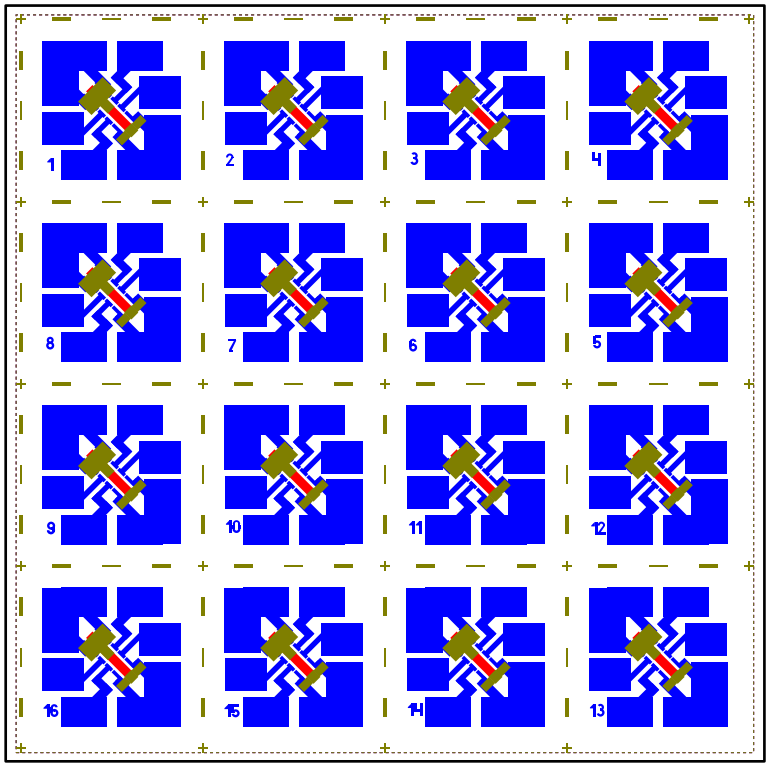

Fig. A.8: The ohmic contacts mask is used for the evaporation of the Pd/Ge contacts on top of the uncovered highly doped n^+-layer. The additional metallization needed for sample #15 of wafer C070419B was structured by a very similar mask. There the contacts were both like the smaller one on this mask. Thus the mask could be dislocated by some micrometers and the electrical contact from pads to Pd/Ge on top of the GaAs could be reestablished without touching the active area with this second layer.

36) Development and postbake as above.
37) Pre-pumping of UNIVEX and native oxide dip as above.
38) Base pressure of 4.6×10^{-6} mbar after 50 min. (as Pd blocks the e-gun for Ti no gettering is possible).
39) Evaporation of 40 nm palladium with an e-gun current of 95 mA, a rate of 1.1 - 1.5 Å/sec and a pressure of $6.1 - 7.7 \times 10^{-6}$ mbar.
40) Evaporation of 111 nm germanium with a heating current of 141-148 A, a rate of 1.1 - 3.0 Å/sec and a pressure of $7.3 - 7.9 \times 10^{-6}$ mbar.
41) Lift-off process in 60 °C hot acetone and isopropanol bath, drying with nitrogen.
42) The contacts have to be annealed to get an ohmic characteristic with reasonable low resistance for 60 min. at 225 °C in a forming gas atmosphere at ≈230 mbar.
43) Again etch tests were needed to determine the etch rate of freshly mixed acetic acid and the rest of the highly doped n^+-layer as well as the transition layer are etched away to uncover the low doped conduction

channel and confine the current to it. An etch depth of ≈ 30 nm was chosen.

44) Unfortunately due to bad lift off behavior the ohmic Pd/Ge contacts were broken at the mesa edges and no current could flow, see fig. A.9. Therefore we evaporated a second metallization with 15 nm of titanium and 85 nm of gold to save the samples and therewith current flow was recovered.

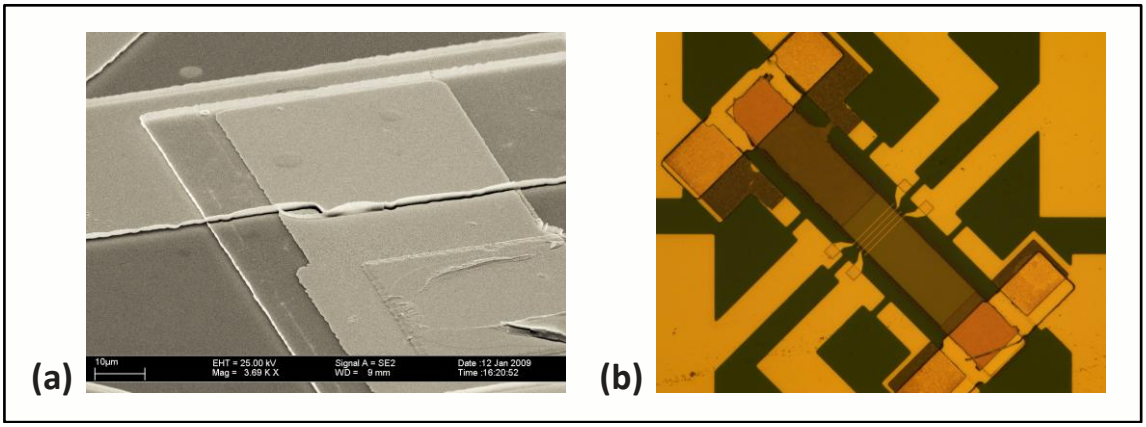

Fig. A.9: Due to an adverse combination of deposited layer thickness, resist development and humidity the lift-off process can leave a lift-off limb around the structures what disrupts the next metal layer (a). Sample #15 in an optical microscope with the second Ti/Au metallization that connects the interrupted Pd/Ge ohmic contacts to the pad metallization again (b).

45) Finally the sample was finished and singularized with the help of a diamond tip and some sticky tape.

46) It is placed onto a drop of PMMA that is positioned in the middle of a chip carrier. The PMMA is cured at the 150 °C hotplate.

47) The sample had to get some wire bonds to allow electrical measurements inside one of our cryostats. This was realized at our gold wire bonder with the parameter sets P1/T1 4.5/4.5 and P2/T2 also 4.5/4.5 and the bond tool heated to 75 °C.

Fabrication of sample #03 of wafer C070419B

This sample was structured the same way as #15. There were only some differences. The mesa mask was placed 90° turned, now the long mesa side was parallel to [100] not to [010] as before. Additionally point 11) was skipped, we didn't deposit an isolating SiO_2 layer under the current feed lines this time. This resolves an issue at the mesa edge, where the SiO_2 can make sharp edges during the lift off which can inhibit a persistent contact line. On the other hand, the missing dielectric layer leaves a much higher topology, however. For this 350 nm high step at the mesa edge this is not a big problem, but at higher steps we had at other wafers this generated serious problems. The second problem is the adhesion force of the Ti/Au and especially the annealed Pd/Ge contacts on

the SiO_2. This is way better on the pure GaAs surface. One of the main reasons we introduced this dielectric was the fear to get some parasitic effects when contacting the mesa sidewall bay the contact stripes without an isolating coating. Even though the outermost layer should have been completely depleted we did not want to take any risk here. The results from sample #03 showed however that this protection layer was electrically not necessary. The next deviant processing step was the design of the inner contacts to the GaMnAs layer, see fig. A.10.

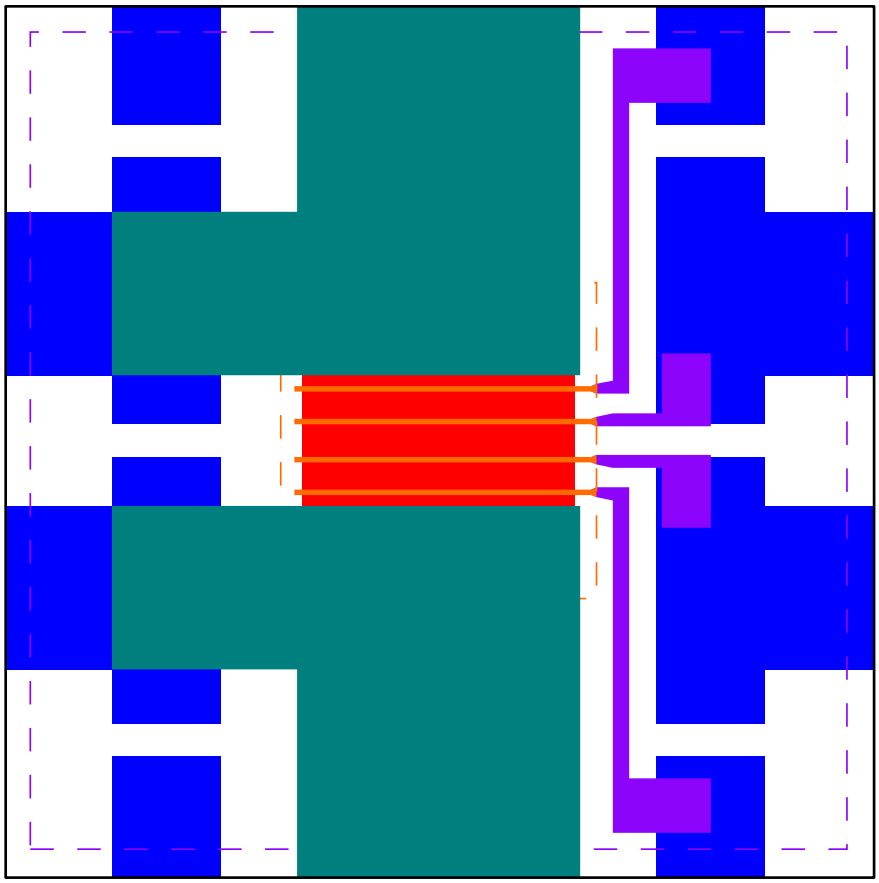

Fig. A.10: The design of sample #03 was modified a little bit. A reason for that was the use of evaporation wedges to assure reliable metallization across the mesa etch step without the dielectric adjusting layer, as shown in figure 4.4. The inner GaMnAs contacts were all connected to bond pad stripes from one mesa side. The ohmic Pd/Ge contacts were this time designed in the EBL software, as the maximum alignment failure across the whole 5mm sample had to be below 1.5µm, impossible with our optical equipment. Therefore each contact pair had to be aligned to the existing contacts and the 40 seconds of exposure on the mask aligner turn easily to 50 minutes and more at the SEM.

The center to center spacing was increased to 6 µm for the two outer contacts and 7 µm for the inner contacts. Additionally the connection to the big bond pads was done only on one side of the mesa to simplify the creation of the ohmic Pd/Ge contacts that were placed very close to the ferromagnetic contacts this time. They were structured by an EBL step this time, as the needed alignment accuracy was not possible with our optical equipment. For the big ohmic contacts the parameters of the exposure matrix used from the

software/SEM are not so important. This always looks fine. But the smaller the structures get, the more important it is to utilize the full functionality of the EBL software/SEM combination. As mentioned in fig. A.6 already, the correct alignement of the structures in the e-Draw software is important. Long and thin stripes are best aligned horizontally, as in this configuration the SEM exhibits the best stability. A long element designed vertically can suffer from severly blured edges. As x-y on the design screen is not the x-y axis of the SEM itself, the EBL software has to translate all the coordinates of the design into the real coordinates of the SEM. If there is a failure in the implementation of this algorithm, this can be seen as digital jump lines at the actually horizontally designed estructures, see fig. A.11.

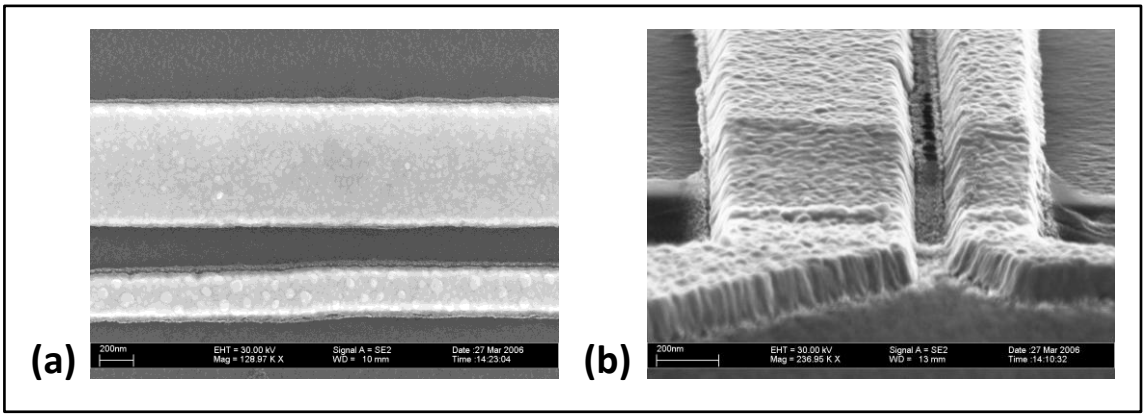

Fig. A.11: Originally designed straight edges of structures can turn out to have small steps after developing and evaporation if there is something wrong in the EBL software. The size of the steps depends on the pixel grid size one is using in the EBL file.

As we wanted to get higher spin diffusion lengths we had to use wafers with channel doping closer to the metal insulator transition. This however means thicker channels, to prevent the system from carrier depletion. This implies in turn that we run into serious trouble with our sample processing scheme at the mesa edges.

For sample #11 of wafer C080903A we had to invent a new methodology of sample preparation, therefore. In figure 4.5 we already showed a mesa etch step made by RIE with a step height of 3.5 μm. Looking to that sidewall it becomes clear, that a normal metal evaporation, even using our evaporation wedges has no chance to guarantee a closed and conducting metallic contact stripe. Therefore we tried to fill the height step conventionally with SiO_2 again and the typical results are shown in figure A.12. We get a nice and deep trench all around the mesa. The meanest thing about that is that in the top view in the SEM or optical microscope it seems as if everything will be okay. Not until you tilt the stage in the SEM you are able to identify the failure mode that allows completely no current to flow over the contacts.

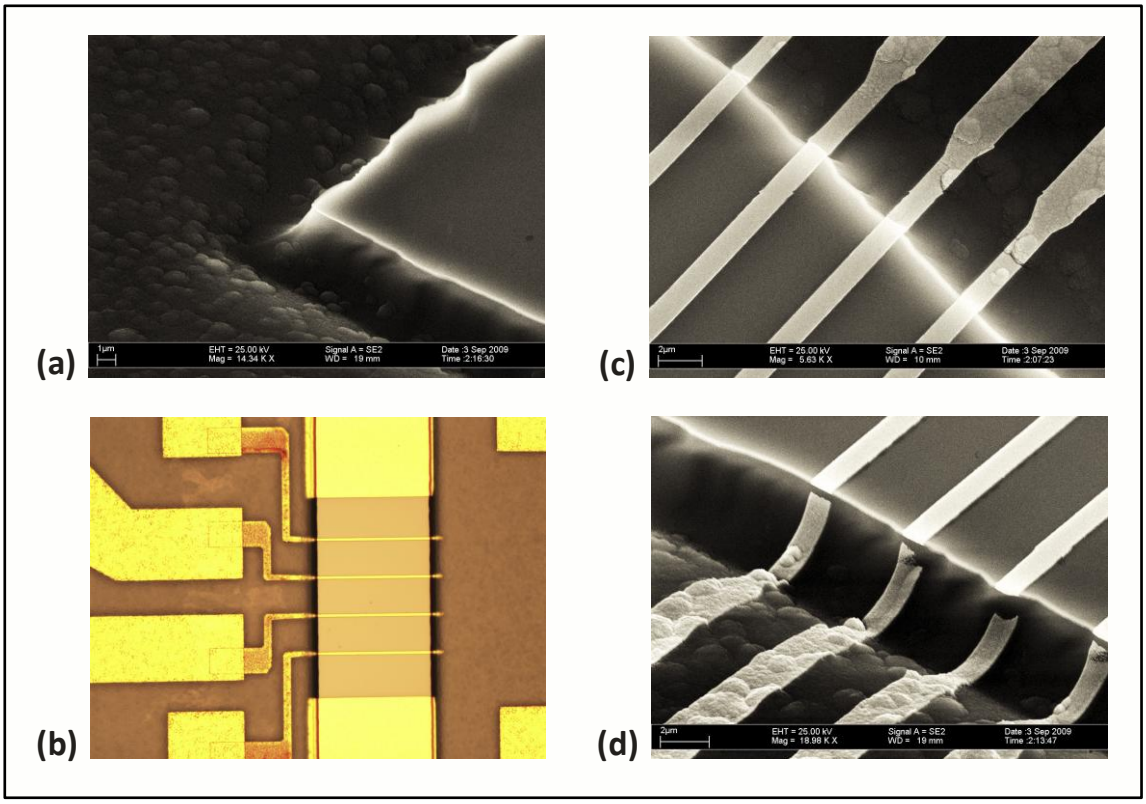

Fig. A.12: If the mesas have to be etched very deep because of a very thick transport channel, the vertical height difference has to be compensated somehow. Using SiO_2 deposition for that purpose leaves quite big trenches around the mesa (a). After the contact evaporation these seem to be quite okay in the optical microscope (b) as well as in the SEM (c). If one tilts the sample plane however, one can clearly see that there cannot flow any current (d) as all of them are broken due to the too high height step.

Thus we changed the manufacturing sequence (in very short form):

1) Define the mesa with standard lithography and wet chemical etching, but the etch depth is only around 100 nm. Just enough to get any contrast during EBL in the SEM.
2) Make the contact metallization to define the ferromagnetic GaMnAs stripes.
3) At first we tried to contact the highly doped n^+-GaAs but later we only designed Esaki contacts without any ohmics due to the everlasting problems of getting reasonable resistances.
4) At the final stadium we also designed the big bond pad structures with EBL what took several hours at the SEM for each 5×5 mm^2 sample.
5) After evaporating the metallization for the contacts we could then etch down to the semi-insulating wafer region to confine the current to the low doped conduction channel. In the figures A.13 and A14 one can see the design of the latest sample #11.

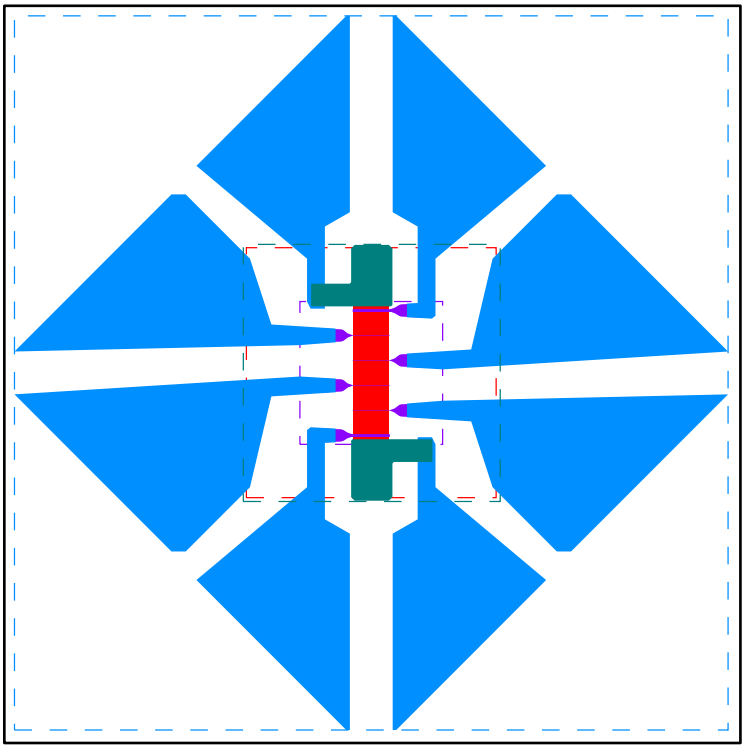

Fig. A.13: The sample #11 made of wafer C080903A was a complete redesign. As due to the 1 µm thick conduction channel new problems arised all the contacts as well as the bond pads were defined by EBL. Altogether the accumulated writing time of the EBL steps necessary for one complete 5 x 5 mm² sample was roughly 4 hours on the LEO SEM.

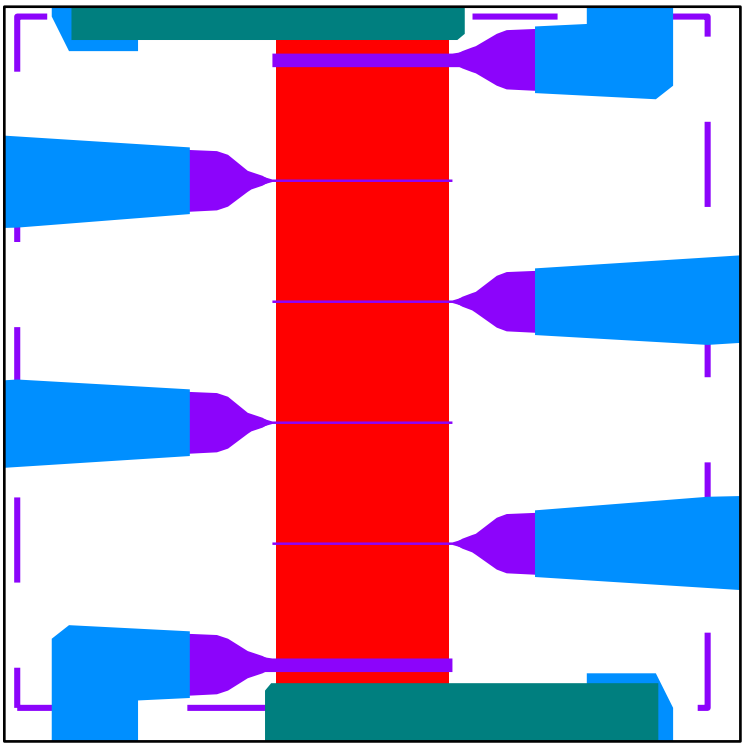

Fig. A.14: The inner contacts were written in one step in this design. Three EBL steps were necessary for sample completion. The inner GaMnAs ones -violet- the ohmic Pd/Ge contacts -green- and the big bond pads -in azure. As the ohmic contacts were later dropped for only ferromagnetic GaMnAs contacts the steps could be reduced to two, but the ohmic contacts had to be aligned separately and also the beam aperture had to be changed between the two contact steps.

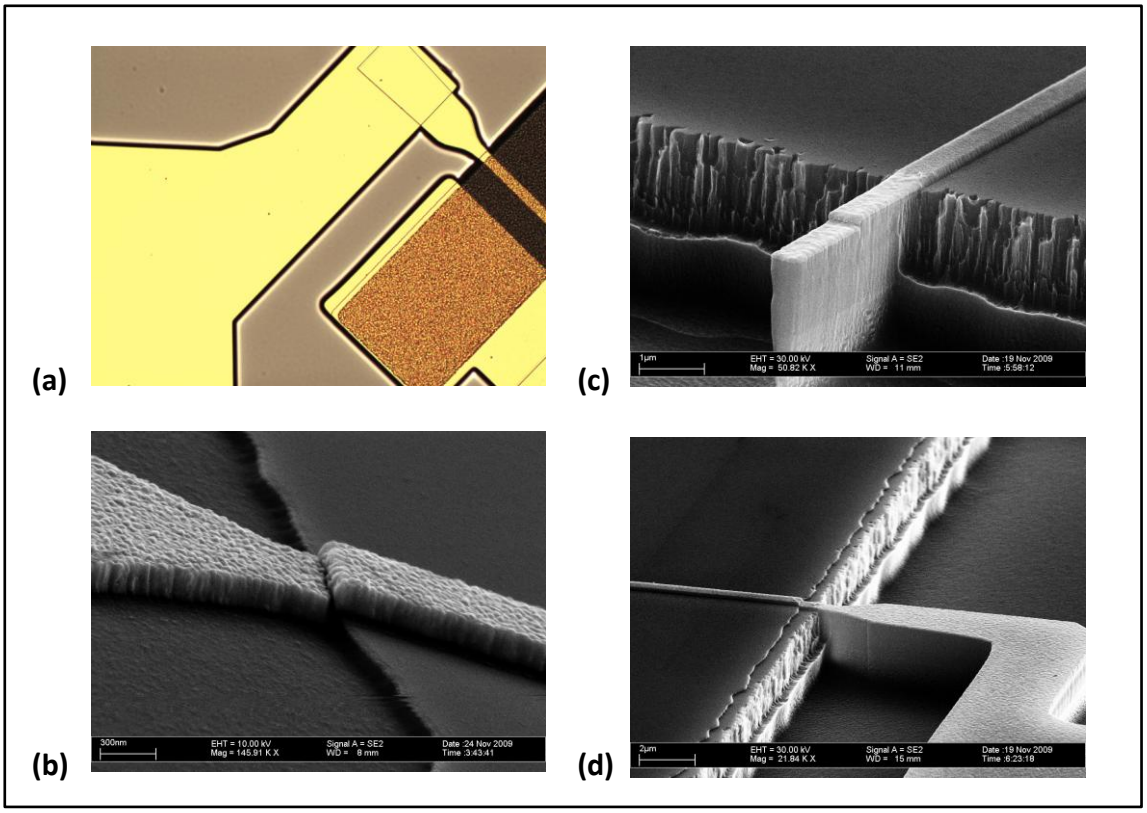

Fig. A.15: If the power at the RIE etching process is too high, the resist is burnt and cannot be removed from the mesa anymore to complete the processing of the sample (a). Despite the tiny step height of ~100 nm it can happen that the contact does carry no current (b). The quite high RF-power needed in the RIE process to get reasonable etch rates in GaAs obviously harms the metal surface, too (c). The confinement of the channel needs another alignment step in the mask aligner. The alignment accuracy is in fact not satisfactorily as can be seen by the steps in the sidewall (d).

At the end we show you just two peculiarities observed during our work. In figure A.16 one can see results of wet chemical etching. The H_2O_2 is used to oxidize the chemically very stable GaAs surface that is it etchable for typical acidic solutions. This process generates gas bubbles that can stick to topologically emerging structures and disrupt the etching at these places. If the structures that should be etched are to small in lateral dimensions they can be underetched. RIE etching uses two mechnisms to get anisotropic etching profiles. The first one is a bias voltage that accelerates the radicalized gas and plasma onto the sample. This gives a simple momentum transfer if the radicals impinge at the surface. The second mechanism relies on a polymerization of the sidewalls. This prevents the radicals from eroding the surface and therefore passivates the sidewalls. The ratio of these mechanisms can be controlled by the process parameters. If the sidewall passivation is too strong, however, after the removal of the resist these sidewalls can clap onto the mesas where they never ever can be removed, shown in figure A.17.

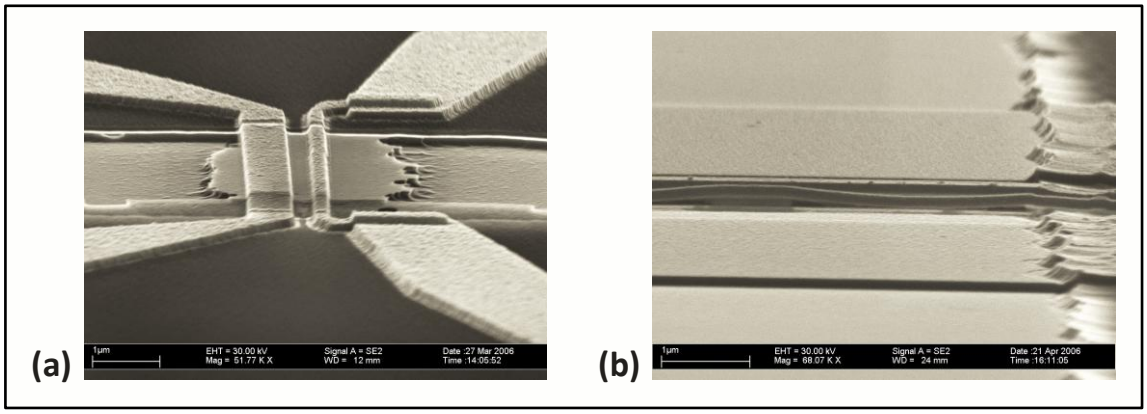

Fig. A.16: An emerging gas bubble has prohibited the etching in the vicinity of this contact structures (a). If laterally small structures are etched too deep one can build nice contact bridges from one side of the mesa to the other one (b)

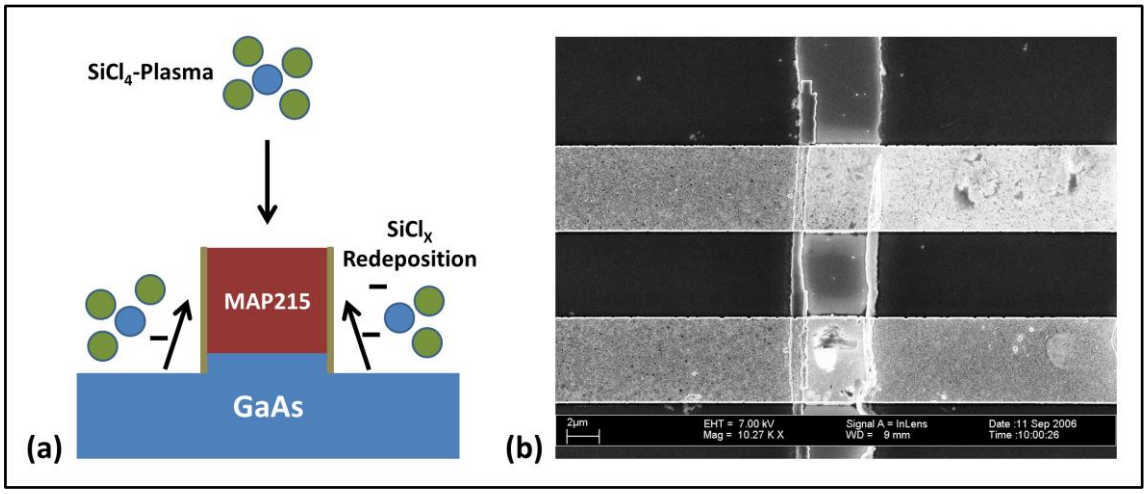

Fig. A.17: The RIE method can serve with very accurately anisotropic etching. Depending on the process parameters the sidewalls are covered with polymers during the etching process what assists the anisotropic character. If these passivation walls get too thick, however, they are not released from the sidewalls during the cleaning and stick to the mesa surface where they cannot be removed anymore.

Appendix B: Measurements

In this appendix we show the spin valve measurements already mentioned in chapter 6. We did a regular spin valve measurement along [010] and then added another 15° to the in-plane angle of the external field for every next measurement. So every sixth sweep equals an easy axis again. However the alignment of the sample in the cryostat is not perfectly accurate and additionally due to strain in the GaMnAs layers the easy axes are not perfectly orthogonal to each other. This can be seen as the exact form of the detected spin signals is not a perfect match for every 90° turn.

One again can extract the ΔV values from the non-local spin-valve measurements for all the different angles and look at the decay lengths. In figure 6.12 we showed previously some extracted decay lengths. In fact the agreement for every single measurement of the next pages with the values achieved in chapter six is extraordinarily good.

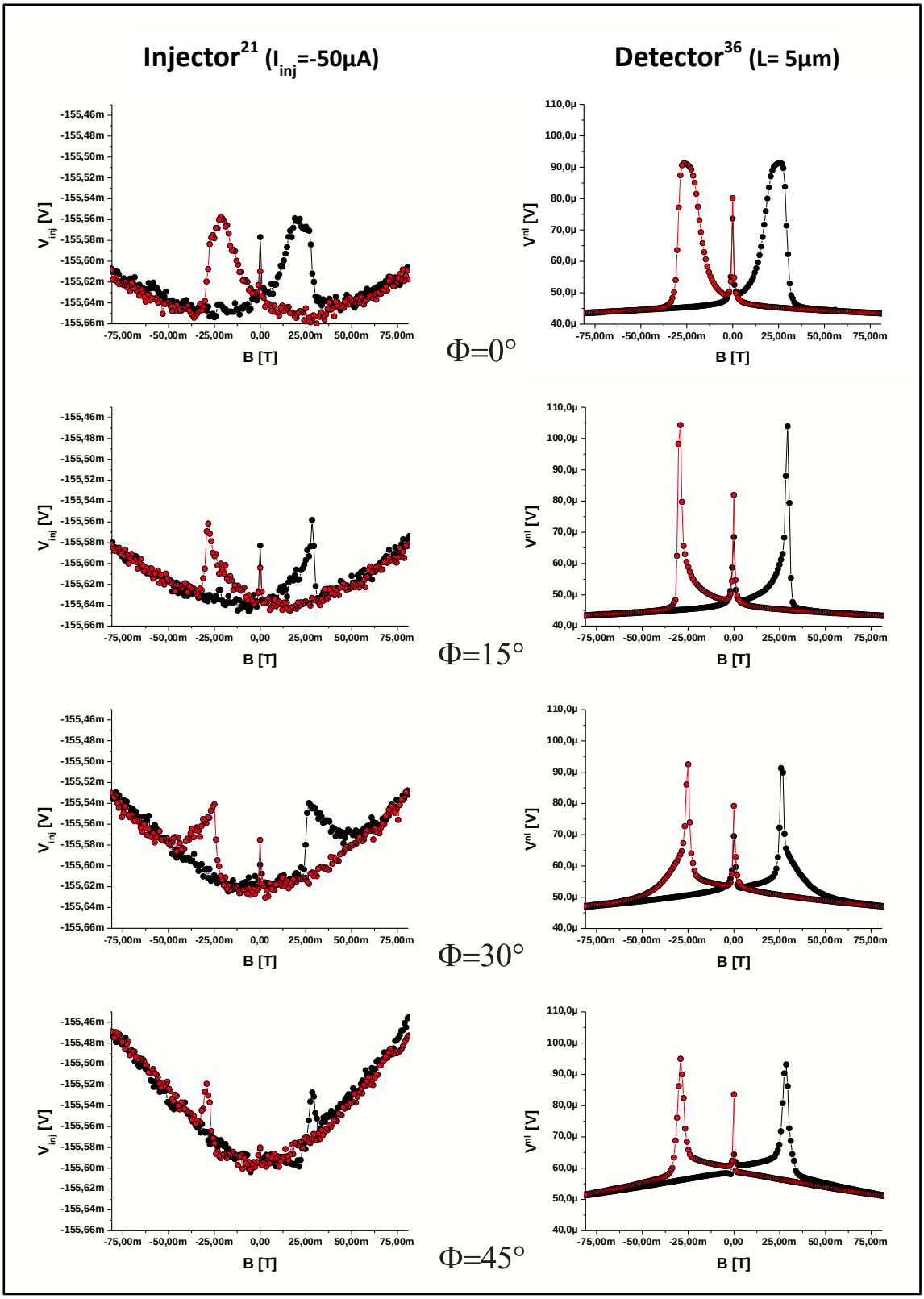

Fig. B.1: The injector voltage on the left and the nonlocal detector signal in 5 µm distance on the right for the in-plane field angles of Φ = 0°, 15°, 30° and 45°. The injector signal is a combination of channel and contact resistance. The first angles show a variation of the typical spin-valve signal to a sharply peaked characteristic.

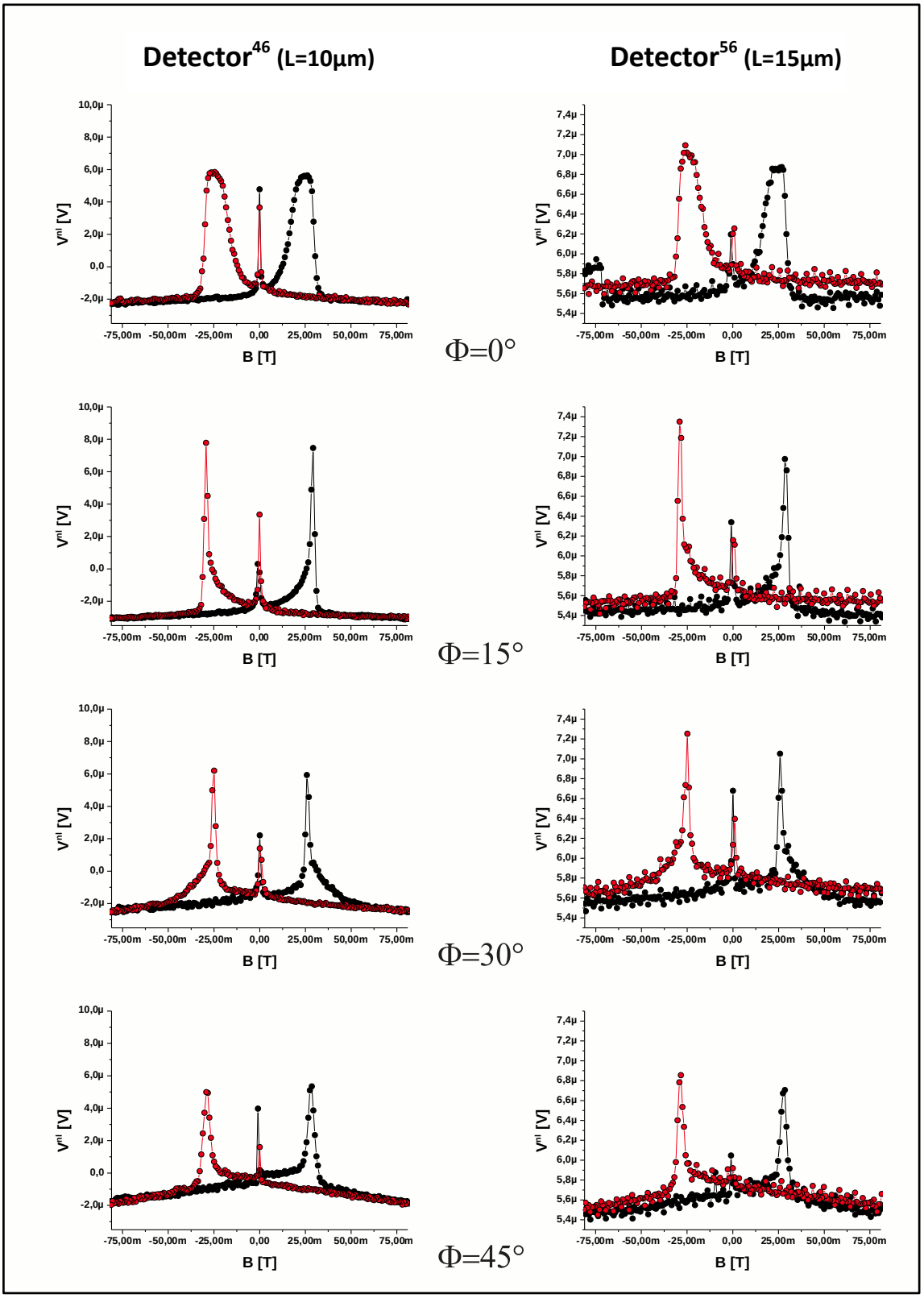

Fig. B.2: Here we see the nonlocal signals measured at the field angles of Φ = 0°, 15°, 30° and 45° in 10 and 15 µm distance respectively. The signal shape is the same as the one found at the first detector; only the signal height is clearly damped with increasing distance to the injector contact.

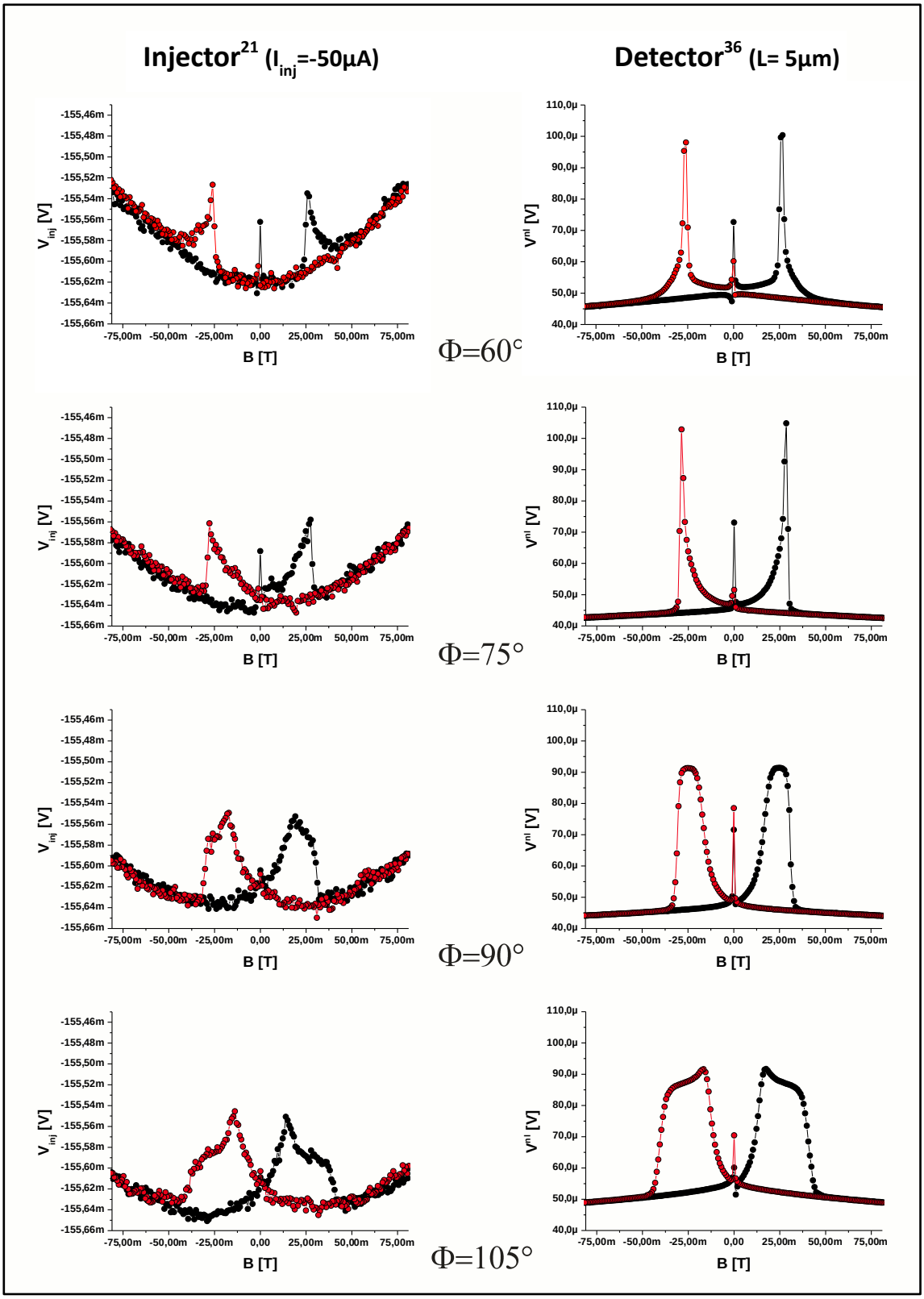

Fig. B.3: The injector voltage on the left and the nonlocal detector signal in 5 µm distance on the right for the in-plane field angles of Φ = 60°, 75°, 90° and 105°. The signal shape from 45° to 90° develops in the same way as from 45° to 0° in figure B.1, reflecting the symmetries of the GaMnAs layer. In the last row for an angle of 105° one can already expect a different evolution of the signal shape in the next quadrant.

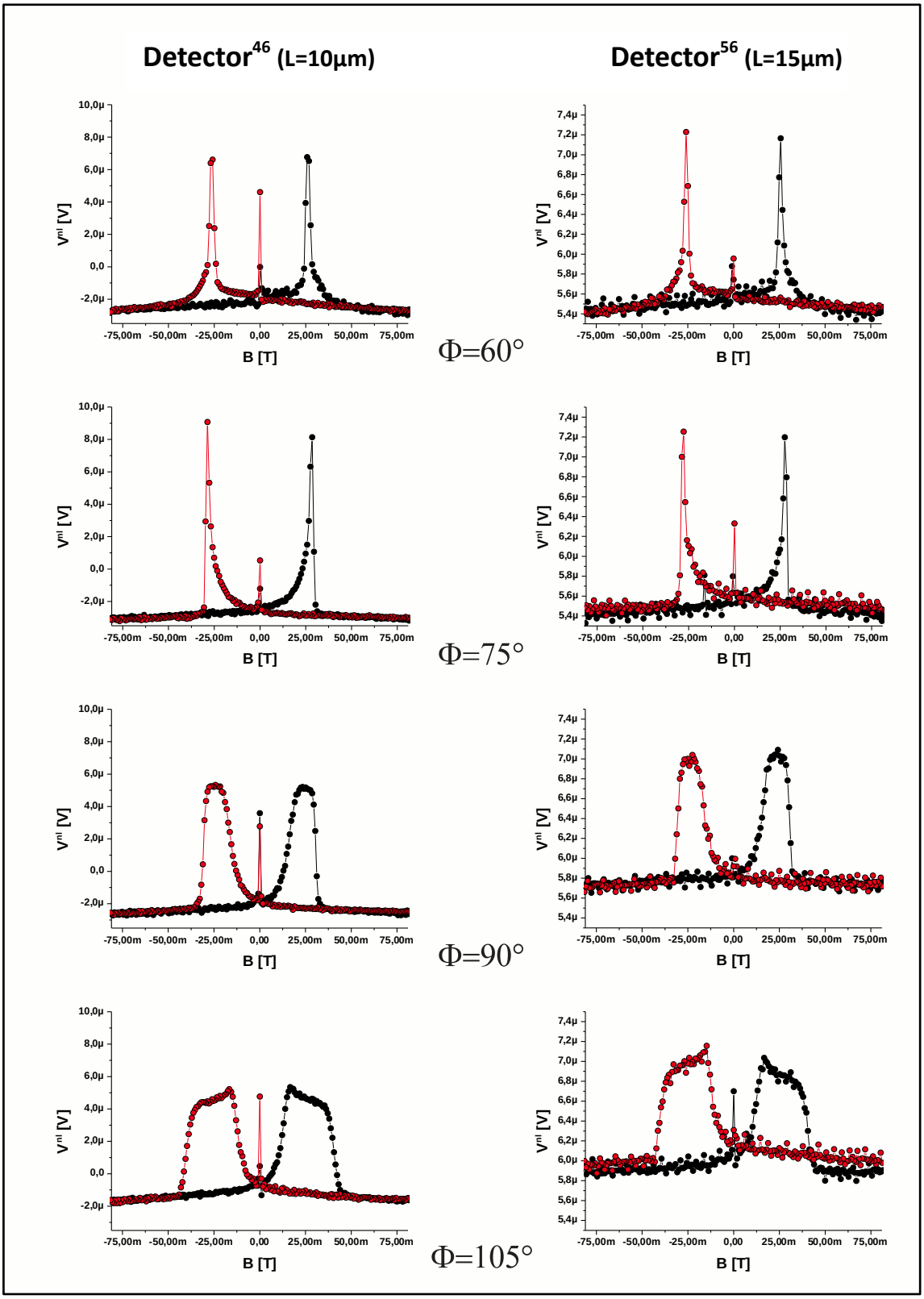

Fig. B.4: Here we see the nonlocal signals measured at the field angles of Φ = 60°, 75°, 90° and 105° in 10 and 15 µm distance respectively. The signal shape from 45° to 90° evolves backwards compared to the first 45 degrees. As in figure B.3 we can see at the lowermost row that the next quadrant will show a different development of the signal characteristic.

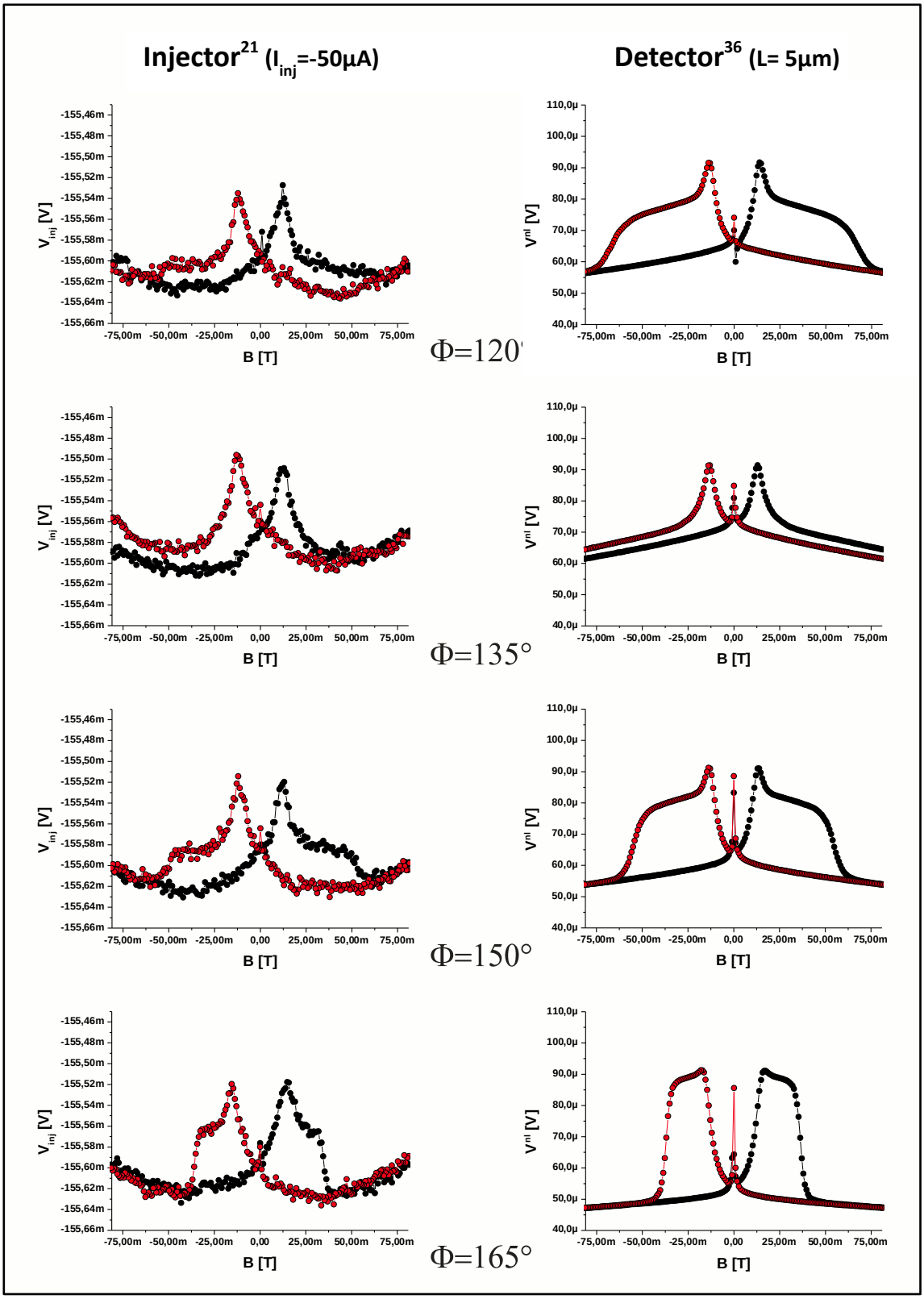

Fig. B.5: The injector voltage on the left and the nonlocal detector signal in 5 µm distance on the right for the in-plane field angles of Φ = 120°, 135°, 150° and 165°. In the second quadrant of the angular dependent field sweeps the spin-valves evolve into a much broader form as during the first 90°. Only in the *[-1-10]* direction (Φ = *135*°) a quite sharp behavior can be observed.

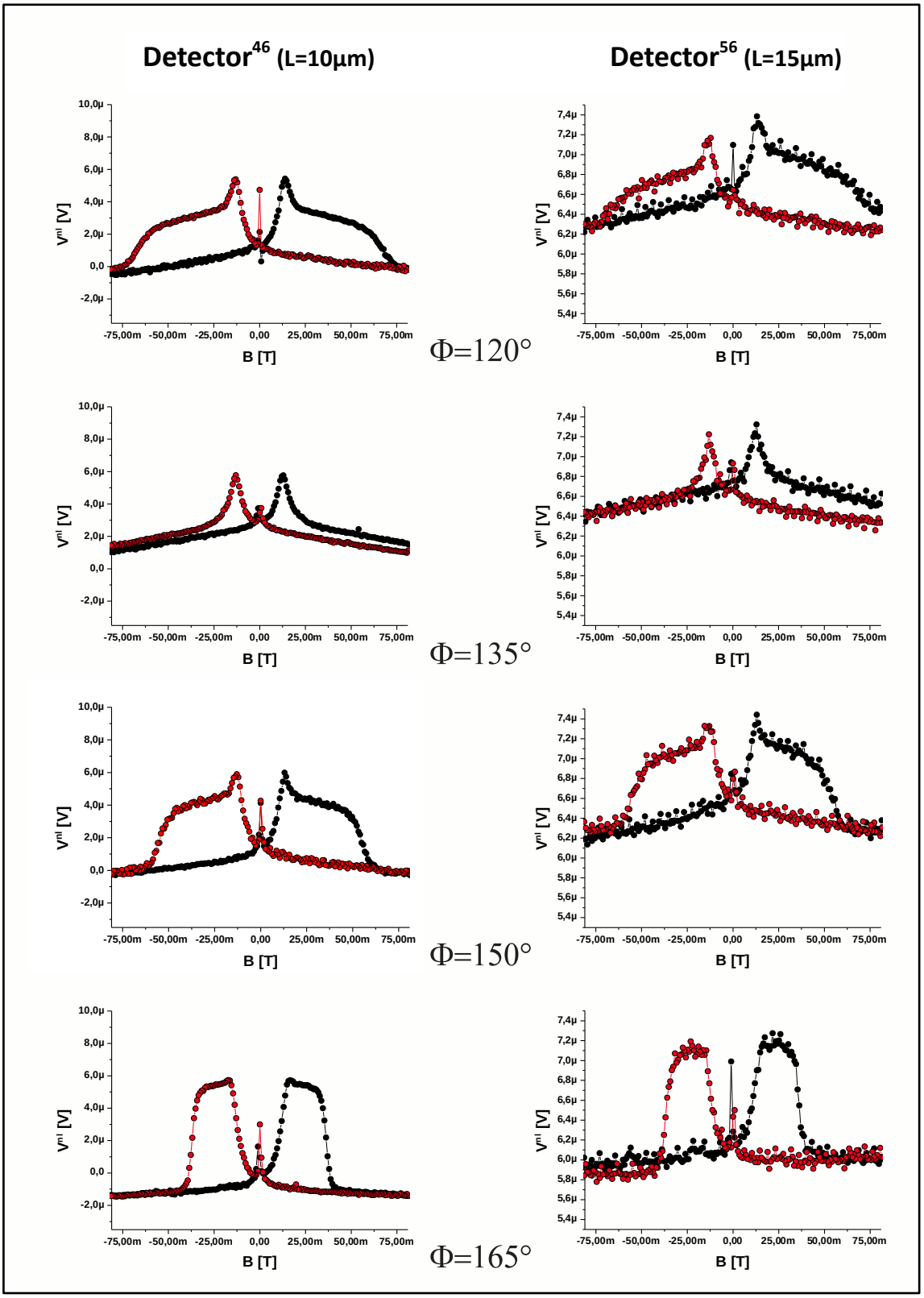

Fig. B.6: Here we see the nonlocal signals measured at the field angles of Φ = 120°, 135°, 150° and 165° in 10 and 15 µm distance respectively. In these angles the signal shapes for injector circuit and detector circuits differ very clearly if one looks at the peak to shoulder ratios of the signals.

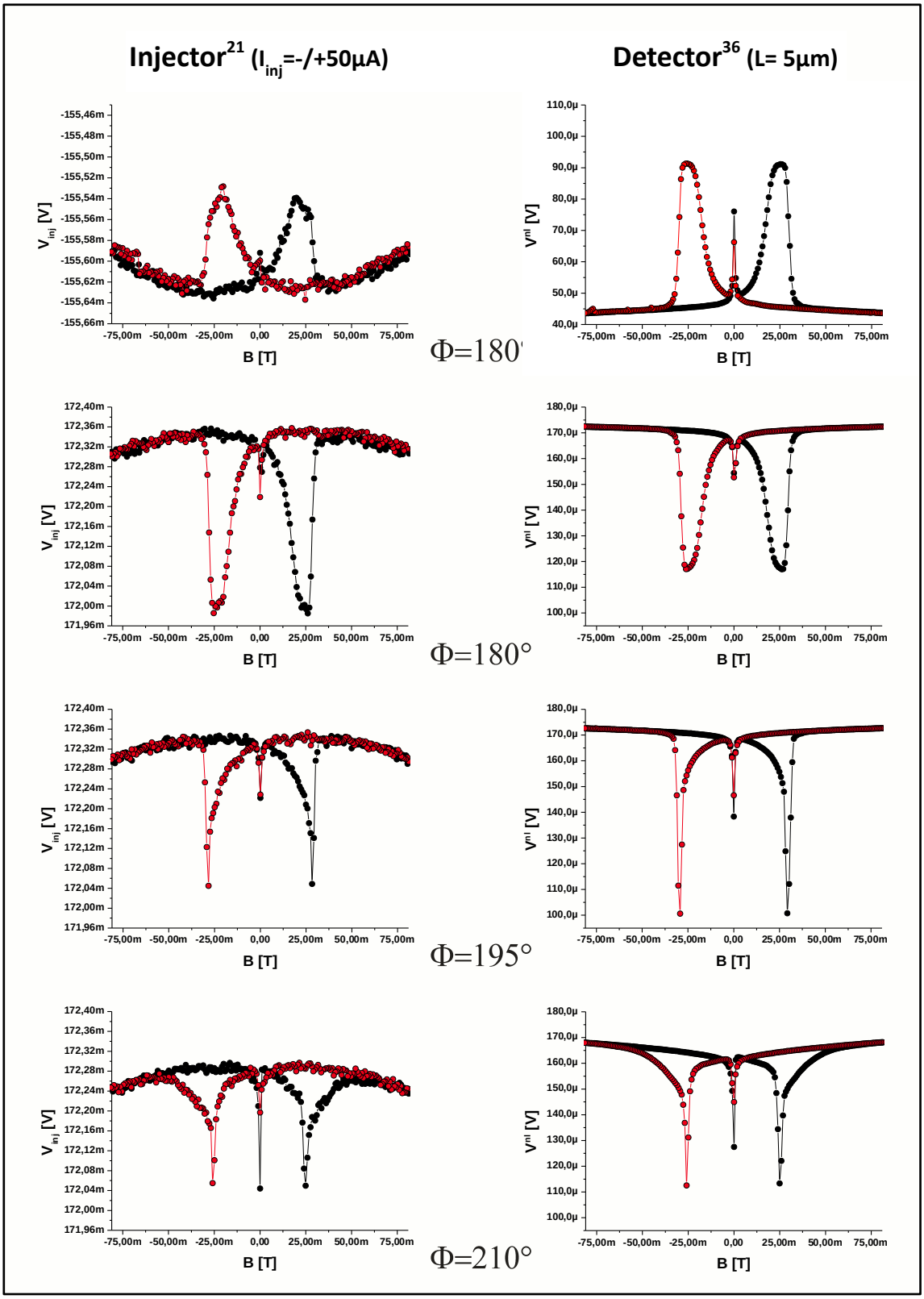

Fig. B.7: The voltage drop at the injector circuit on the left and the nonlocal detector signal in 5µm distance on the right for the in-plane field angles of Φ = 180° for the spin injection case. For spin extraction the angles Φ = 180°, 195° and 210° are shown. If one compares the signal shape for the first angles in the spin extraction case with figure 6.11, an analogous signal development can easily be discovered.

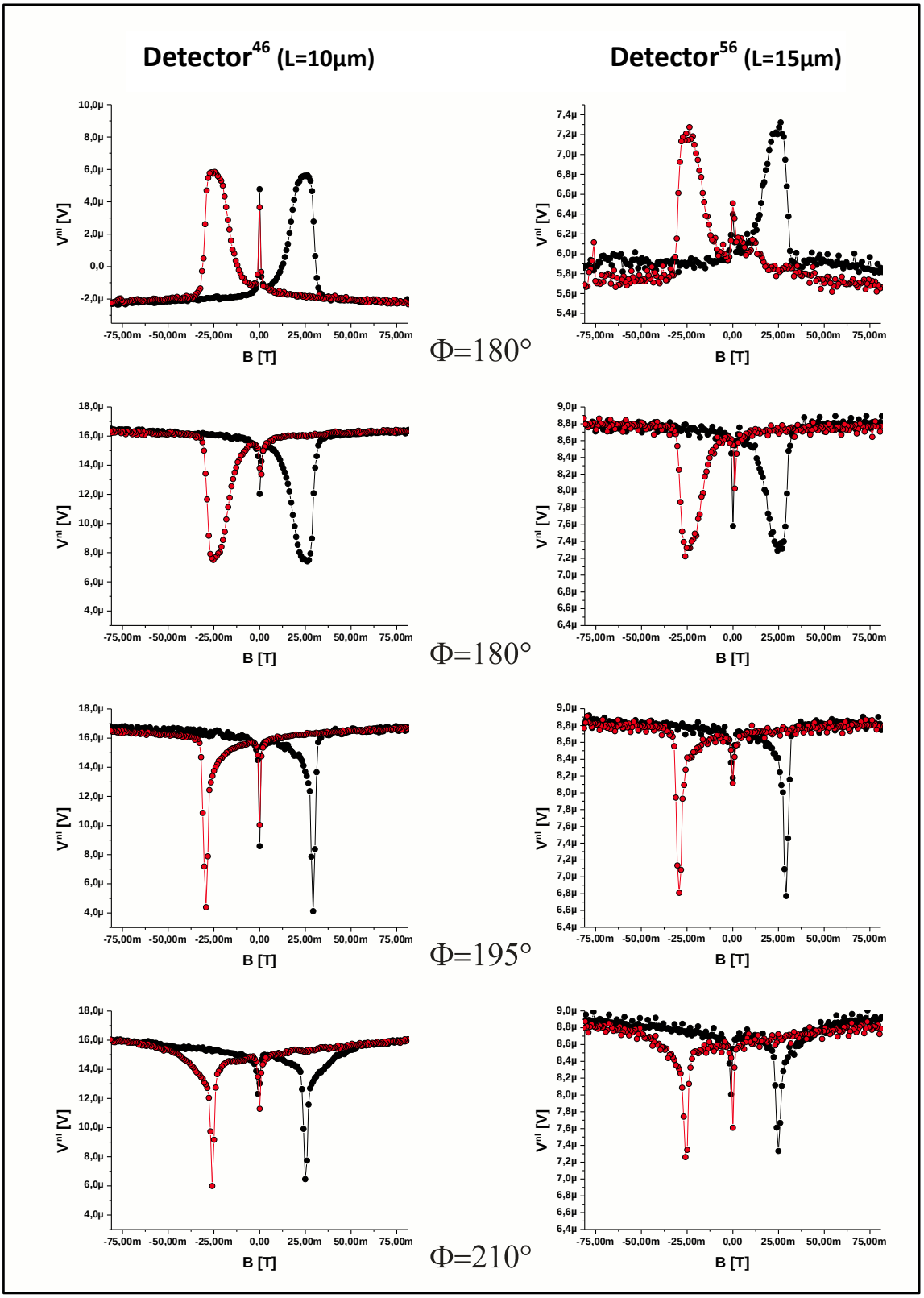

Fig. B.8:Here we see the nonlocal signals measured at spin injection at the field angle of Φ = 180° in 10 and 15 µm distance respectively. For spin extraction we show results at angles of Φ = 180°, 195° and 210°. Once again the signal shape is absolutely identical for all three detectors. This quadrant behaves equivalently to the first one with very sharp switching signals.

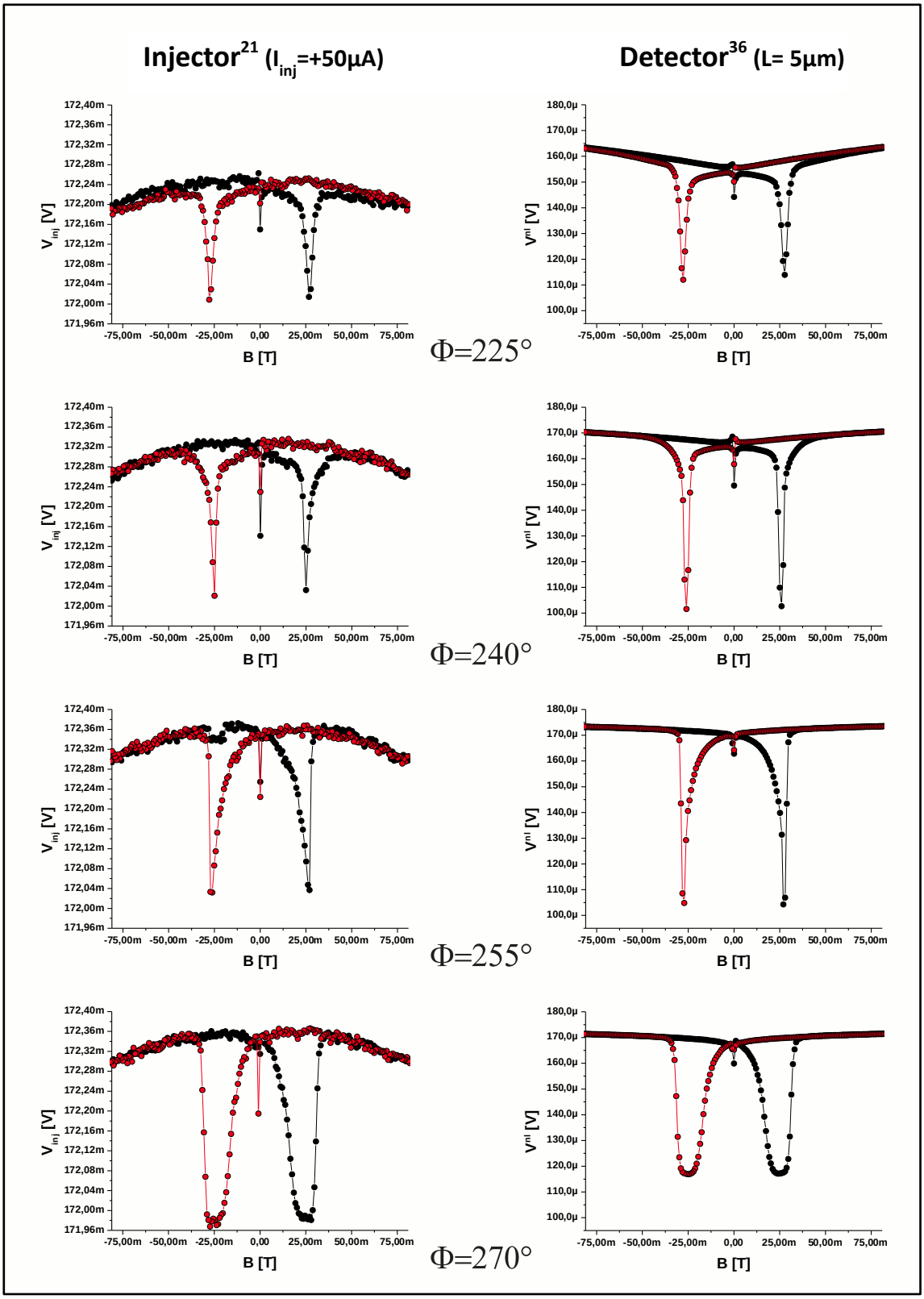

Fig. B.9:The voltage drop of the injector circuit on the left and the nonlocal detector signal in 5 µm distance on the right for the in-plane field angles of Φ = 225°, 240°, 255° and 270° are shown. As in the case of spin injection the quadrant between [0-10] and [100] directions shows a sharp cusped spin-valve signal.

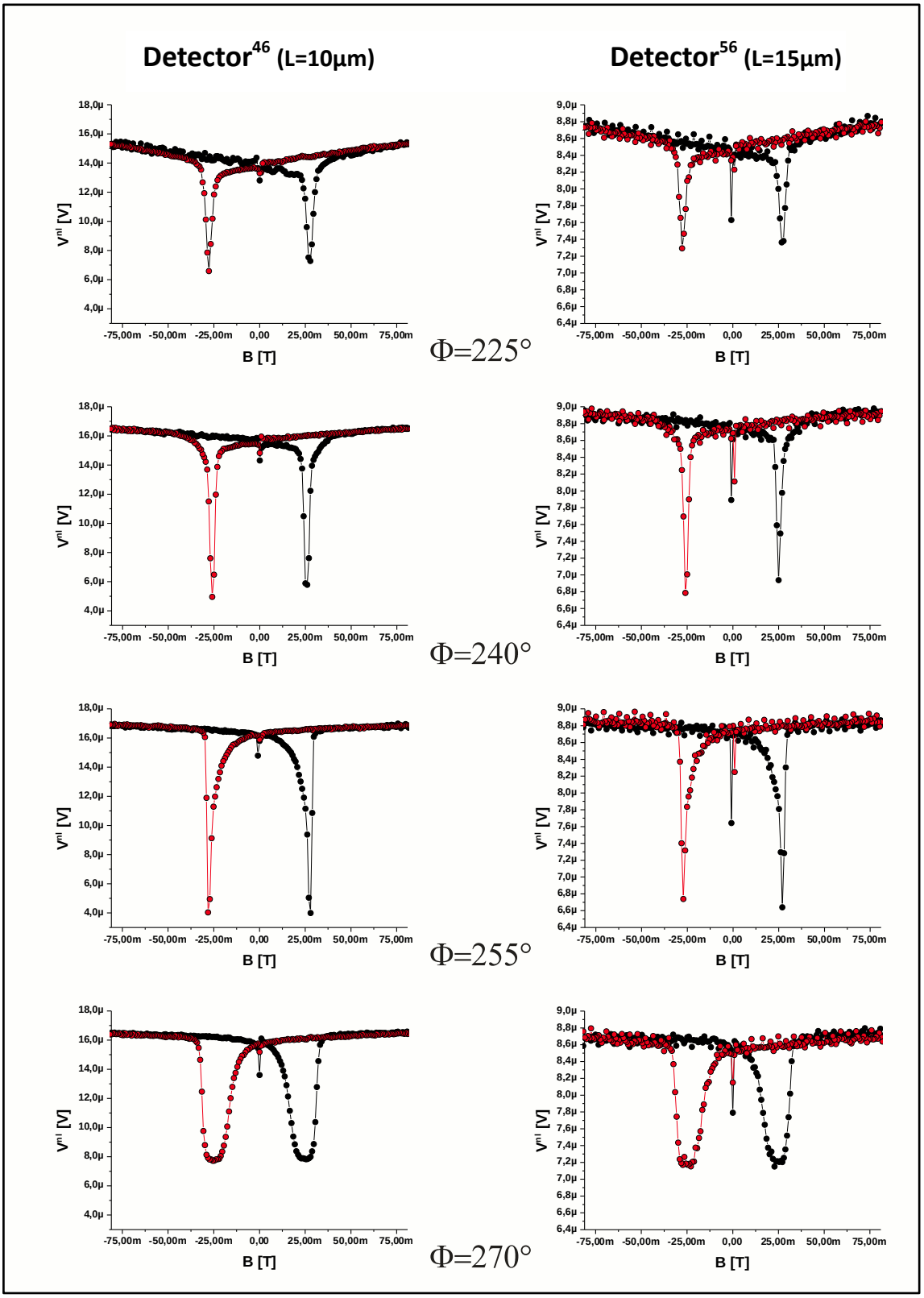

Fig. B.10: Here we see the nonlocal signals measured at the field angles of Φ = 225°, 240°, 255° and 270° in 10 and 15 µm distance respectively. The sharp cusps are a characteristic for all detectors in this quadrant.

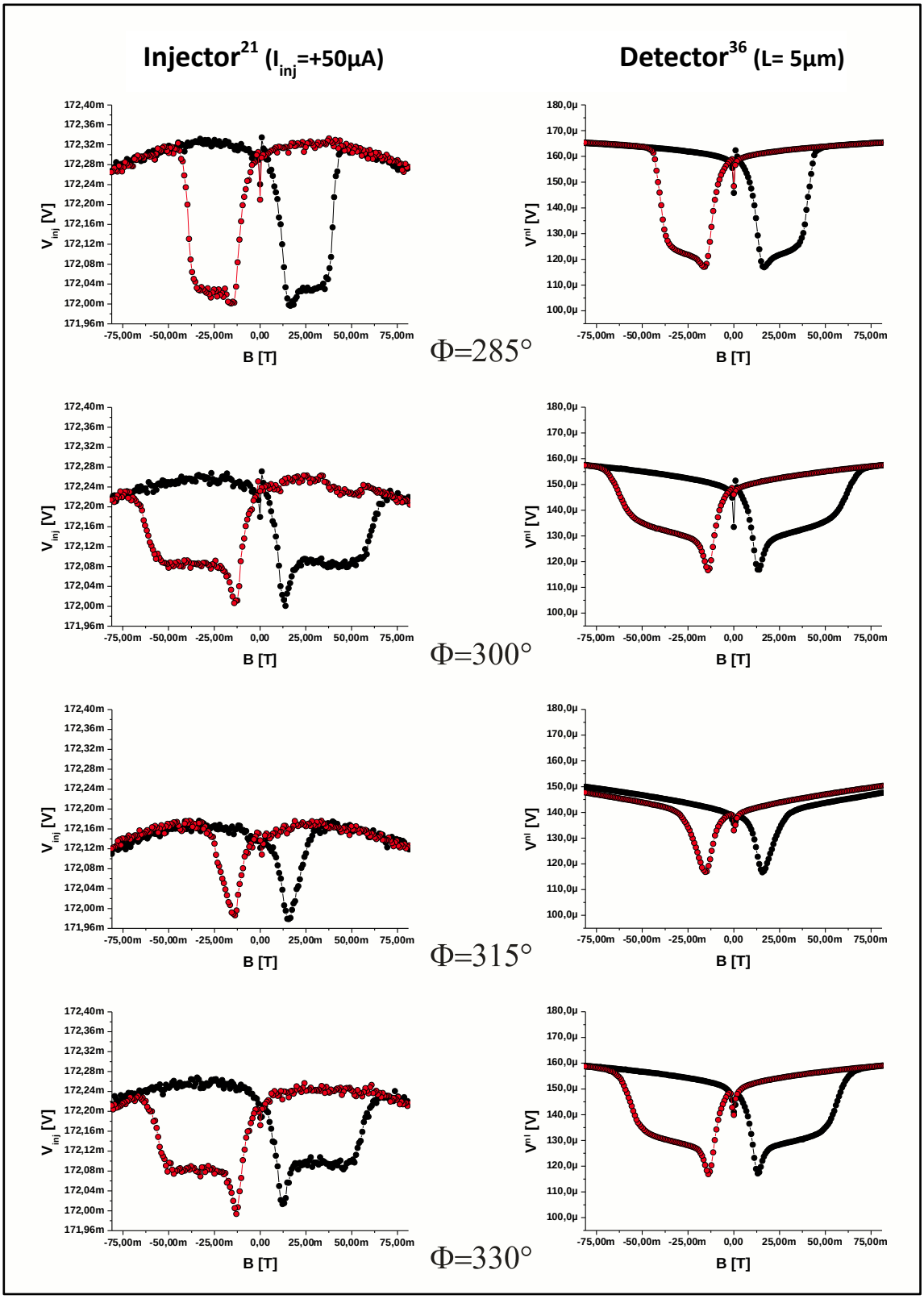

Fig. B.11: The voltage drop of the injector circuit on the left and the nonlocal detector signal in 5 µm distance on the right for the in-plane field angles of Φ = 285°, 300°, 315° and 330° are shown. Again in the range between [100] and [010] the spin-valve feature is very much broadened.

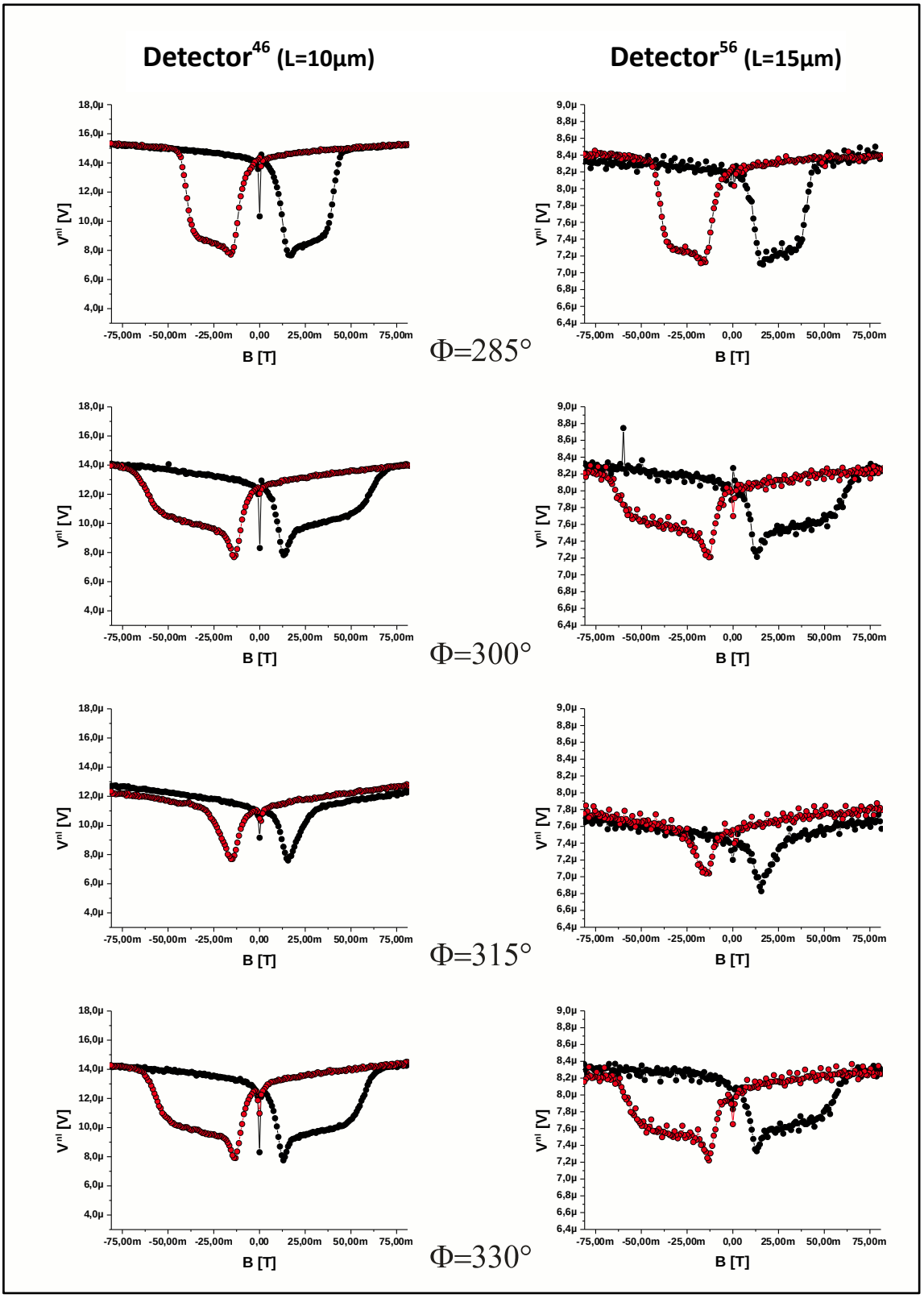

Fig. B.12: Here we see the nonlocal signals measured at the field angles of Φ = 285°, 300°, 315° and 330° in 10 and 15 µm distance respectively. The broader signal shape in this quadrant was already found in the spin injection results shown in figure B.5 and B.6.

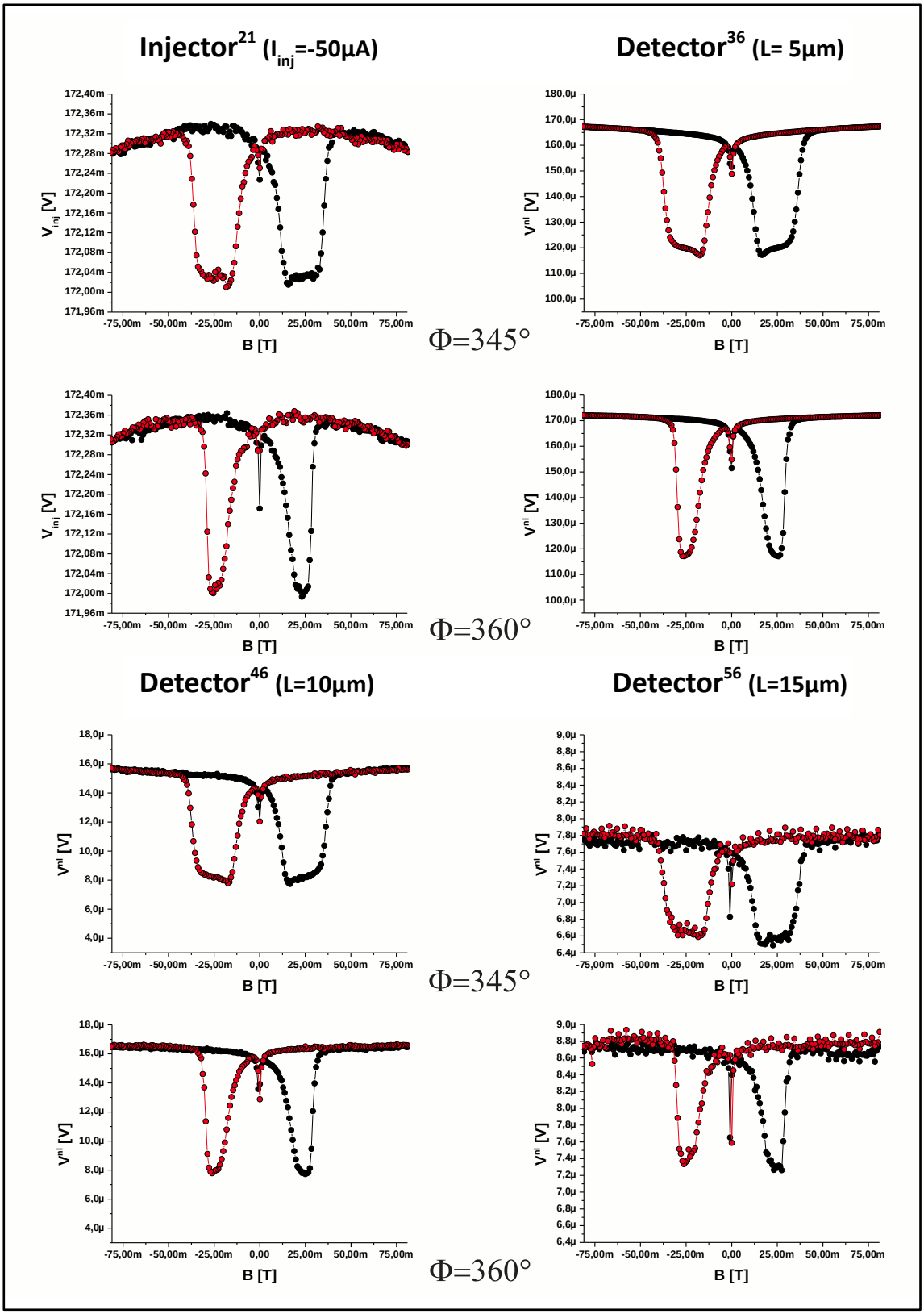

Fig. B.13: The voltage drop of the injector circuit and the nonlocal detector signal in 5, 10 and 15 µm distance for the last two angles of Φ = 345° and 360° in one graph. After one complete circle of 360° we get again the exactly same signal shape as for the 0° case with the same signal amplitudes. This shows the stability of the system, as the complete measurement time was nearly three days.

Appendix C: List of publications

Local spin valve effect in lateral (Ga,Mn)As/GaAs spin Esaki diode devices; M. Ciorga, C. Wolf, A. Einwanger, M. Utz, D. Schuh and D. Weiss; AIP Advances 1, 22113 (2011)

Bias dependence of spin injection into GaAs from Fe, FeCo, and (Ga,Mn)As contacts; B. Endres, F. Hoffmann, C. Wolf, A. Einwanger, M. Utz, D. Schuh, G. Woltersdorf, M. Ciorga, D. Weiss, C. Back and G. Bayreuther; Journal of Applied Physics 109, (2011)

In-plane anisotropy of tunneling magnetoresistance and spin polarization in lateral spin injection devices with (Ga,Mn)As/GaAs spin-Esaki diode contacts; M. Ciorga, A. Einwanger, U. Wurstbauer, D. Schuh, W. Wegscheider and D. Weiss; Physica E, Low-dimensional Systems and Nanostructures 42, 2673-2675 (2010)

Tunneling anisotropic spin polarization in lateral (Ga,Mn)As/GaAs spin Esaki diode devices; A. Einwanger, M. Ciorga, U. Wurstbauer, D. Schuh, W. Wegscheider and D. Weiss; Applied Physics Letters 95, 152101 (2009)

Mapping the magnetic anisotropy in (Ga,Mn)As nanostructures; F. Hoffmann, G. Woltersdorf, W. Wegscheider, A. Einwanger, D. Weiss and C. Back; Physical Review B (PRB) 80, 54417 (2009)

Electrical spin injection and detection in lateral all-semiconductor devices; M. Ciorga, A. Einwanger, U. Wurstbauer, D. Schuh, W. Wegscheider and D. Weiss; Physical Review B 79, 165321 (2009)

TAMR effect in (Ga,Mn)As-based tunnel structures; M. Ciorga, M. Schlapps, A. Einwanger, S. Geißler, J. Sadowski, W. Wegscheider and D. Weiss; New Journal of Physics 9, 351 (2007)

Tunneling anisotropic magnetoresistance effect in p+(Ga,Mn)As/n+GaAs Esaki diode; M. Ciorga, A. Einwanger, J. Sadowski, W. Wegscheider and D. Weiss; Phys. Stat. Sol. A 204, 186-190 (2007)

TAMR effect in (Ga,Mn)As-based tunnel structures; M. Ciorga, M. Schlapps, A. Einwanger, S. Geißler, J. Sadowski, W. Wegscheider and D. Weiss; New J. Phys. 9, 351 (2007)

References

[Adel] Postgrowth annealing under As capping: An alternative way to increase T_C; M. Adell, L. Ilver, J. Kanski, V. Stanciu, P. Svedlindh, J. Sadowski, J. Z. Domagala, F. Terki, C. Hernandez and S. Charar; Appl. Phys. Lett. **86**, 112501 (2005)

[Ade1] Effects of doping profile and post-growth annealing on spin injection from Fe into (Al,Ga)As heterostructures; C. Adelmann, J. Q. Xie, C. J. Palmstrøm, J. Strand, X. Lou, J. Wang and P. A. Crowell; J. Vac. Sci. Technol. B Volume 23, Issue 4, 1747 (2005)

[Andr] Low-temperature GaAs films grown on Ge and Ge/SiGe/Si substrates; C.L. Andre, J.J. Boeckl, C.W. Leitz, M.T. Currie, T.A. Langdo, E.A. Fitzgerald and S.A. Ringel, J. Appl. Phys. **94**, 4980-4985 (2003).

[Aron] Spin injection in metals and polarization of nuclei; A. G. Aronov; Zh. Eksp. Teor. Fiz. Pisma Red. **24**, 37, [JETP Lett. **24**, 32-34 (1976)]

[Ashc] Solid State Physics; N. W. Ashcroft and D. N. Mermin; Saunders College Publishing (1976)

[Avru] Growth of GaMnAs under near-stoichiometric conditions; V. Avrutin, D. Humienik, S. Frank, A. Koeder, W. Schoch, W. Limmer, W. Sauer and A. Waag; J. Appl. Phys. **98**, 023909 (2005)

[Awsc] Semiconductor Spintronics and Quantum Computation; D. D. Awschalom, D. Loss, N. Samarth (Editors); Springer-Verlag, Berlin, Heidelberg (2002)

[Aws1] Manipulating and storing spin coherence in semiconductors; D. D. Awschalom; Physica E (Amsterdam) **10**, 1–6 (2001)

[Baib] Giant magnetoresistance of (001)Fe/(001)Cr magnetic superlattices; M. N. Baibich, J. M. Broto, A. Fert, F. Nguyen Van Dau, F. Petroff, P. Etienne, G. Creuzet, A. Friederich, and J. Chazelas; Phys. Rev. Lett. **61**, 2472-2475 (1988)

[Band] Introduction to Spintronics; Supriyo Bandyopadhyay and Marc Cahay; CRC Press by Taylor & Francis Group, LLC, Boca Raton (2008)

[Bard] Three-electrode circuit element utilizing semiconductive materials; J. Bardeen and W. H. Brattain; United States Patent and Trademark Office, U.S. Patent 2,524,035, Issue date Oct. 3, 1950

[Bayl] Hole spin relaxation in n-modulation doped quantum wells; B. Baylac, T. Amand, X. Marie, B. Dareys, M. Brousseau, G. Bacquet and V. Thierry-Mieg; Solid State Commun. **93**, 57–60 (1995)

[Bina] Enhanced magnetoresistance in layered magnetic structures with antiferromagnetic interlayer exchange; G. Binasch, P. Grünberg, F. Saurenbach and W. Zinn; Phys. Rev. B. **39**, 4828-4830 (1989)

[Bir] Z. Eksp. Teor. Fiz.; G. I. Bir, A. G. Aronov and G. E. Pikus; Z. Eksp. Teor. Fiz. **69**, 1382 (1975); Sov. Phys. JETP **42**, 705 (1976)

[Birk] Growth of 3“ and 4“ gallium arsenide crystals by the vertical gradient freeze (VGF) method; B. Birkmann, M. Rasp, J. Stenzenberger and G. Müller; J. Cryst. Growth Vol. **211** (2000)

[Blun] Magnetism in Condensed Matter; S. Blundell; Oxford University Press, Oxford New York (2001)

[Bohr] Studier over Metallernes Elektrontheori; N. Bohr; Københavns Universitet (1911)

[Brey] Tunnel magnetoresistance in GaMnAs: Going beyond Jullière formula; L. Brey, C. Tejedor and J. Fernández-Rossier; Appl. Phys. Lett. **85**, 1996, (2004)

[Broe] Magnetic anisotropy of multilayers; F. J. A. den Broeder, W. Hoving and P. J. H. Bloemen; Journal of Magnetism and Magnetic Materials **93**, 592-570 (1991)

[Burc] Impurity Band Conduction in a High Temperature Ferromagnetic Semiconductor; K. S. Burch, D. B. Shrekenhamer, E. J. Singley, J. Stephens, B. L. Sheu, R. K. Kawakami, P. Schiffer, N. Samarth, D. D. Awschalom and D. N. Basov; Phys. Rev. Lett., **97**:087208 (2006)

[Chan] Hyperfine interactions and spin transport in ferromagnet-semiconductor heterostructures; M. K. Chan, Q. O. Hu, J. Zhang, T. Kondo, C. J. Palmstrøm and P. A. Crowell; Phys. Rev. B **80**, 161206 Rapid Communications (2009)

[Chib] Electric-field control of ferromagnetism in (Ga,Mn)As; D. Chiba, F. Matsukura, H. Ohno; Appl. Phys. Lett., **89**:162505 (2006)

[Chi1] Electric Field Effect on the Magnetic Properties of III/V Ferromagnetic Semiconductor (In,Mn)As and ((Al),Ga,Mn)As; D. Chiba, M. Yamanouchi, F. Matsukura, E. Abe, Y. Ohno, K. Ohtani and H. Ohno; Journal of Supercond., **16**:179 (2003)

[Cior] TAMR effect in (Ga,Mn)As-based tunnel structures; M. Ciorga, M. Schlapps, A. Einwanger, S. Geißler, J. Sadowski, W. Wegscheider and D. Weiss, New Journal of Physics **9**, S. 351. (2007)

[Coey] Magnetism and Magnetic Materials; J. M. D. Coey; Cambridge University Press, 2010

[Cole] Spin-disorder effects in the electrical resistivities of metals and alloys; B. R. Coles; Advances in Physics, 7:25, 40-71 (1958)

[Crai] Magnetism, Principles and Applications; D. Craik; John Wiley & Sons, New York, 1995

[Cull] Introduction to Magnetic Materials; B. D. Cullity and C. D. Graham; Wiley-IEEE. 2nd edition (2008)

[Czoc] Ein neues Verfahren zur Messung des Kristallisationsgeschwindigkeit der Metalle; J. Czochralski; Z. phys. Chem. **92**, 219-221 (1918)

[Datt] Electronic analog of the electro-optic modulator; S. Datta & B. Das; Appl. Phys. Lett. **56**, 665 (1990)

[Deby] Electrical Properties of N-Type Germanium; P. P. Debye and E. M. Conwell; Phys. Rev. 93, 693 (1954)

[Diet] Origin and control of ferromagnetism in diluted magnetic semiconductors and oxids; T. Dietl; J. Appl. Phys., **103**:07D111 (2008)

[Dorp] Nuclear spin orientation by electrical spin injection in an $Al_xGa_{1-x}As$/GaAs spin-polarized light-emitting diode; P. Van Dorpe, W. Van Roy, J. De Boeck and G. Borghs; Phys. Rev. B. **72**, 035315 (2005)

[Dor1] Voltage-controlled spin injection in a (Ga,Mn)As/(Al,Ga)As Zener diode; P. Van Dorpe, W. Van Roy, J. De Boeck, G. Borghs, P. Sankowski, P. Kacman, J. A. Majewski and T. Dietl; Phys. Rev. B. **72**, 205322 (2005)

[Dor2] Very high spin polarization in GaAs by injection from a (Ga,Mn)As Zener diode; P. Van Dorpe, Z. Liu, W. Van Roy, V. F.

Motsnyi, M. Sawicki, G. Borghs and J. De Boeck; Appl. Phys. Lett. **84**, 3495 (2004)

[Drud] Zur Elektronentheorie der Metalle; P. Drude; Annalen der Physik, 306 (3): 566 (1900)

[Dyak] Z. Eksp. Teor. Fiz.; M. I. Dyakonov, V. I. Perel; Z. Eksp. Teor. Fiz. **60**, 1954 (1971); Sov. Phys. JETP **33**, 1053 (1971)

[Dya1] Sov. Phys. Solid State 13; M. I. Dyakonov, V. I. Perel; Fiz. Tverd. Tela **13**, 3581 (1971); Sov. Phys. Solid State **13**, 3023 (1972)

[Dya2] Basics of Semiconductor and Spin Physics; M. I. Dyakonov (Editor); Spin physics in Semiconductors, Springer-Verlag Berlin Heidelberg (2008)

[Dzhi] Low-temperature spin relaxation in n-type GaAs; R. I. Dzhioev,K. V. Kavokin, V. L. Korenev, M. V. Lazarev, B. Ya. Meltser, M. N. Stepanova, B. P. Zakharchenya, D. Gammon and D. S. Katzer; Phys. Rev. B. **66**, 245204 (2002)

[Dzh1] Suppression of Dyakonov-Perel Spin Relaxation in High-Mobility n-GaAs; R. I. Dzhioev, K. H. Kavokin, V. Korenev, M. Lazarev, N. K. Poletaevx, B. P. Zakharchenya, E. A. Stinaff, D. Gammon, A. Bracker and M. Ware; Phys. Rev. Lett. **93**, 216402 (2004)

[Edmo] Mn Interstitial Diffusion in (Ga,Mn)As; K. W. Edmonds, P. Boguslawski, K. Y. Wang, R. P. Campion, S. N. Novikov, N. R. S. Farley, B. L. Gallagher, C. T. Foxon, M. Sawicki, T. Dietl, M. Buongiorno Nardelli and J. Bernhole; Phys. Rev. Lett. **92**(3), 037201 (2004)

[Eins] Über die von der molekularkinetischen Theorie der Wärme geforderte Bewegung von in ruhenden Flüssigkeiten suspendierten Teilchen; A. Einstein; Annalen der Physik **322** (8): 549-560 (1905)

[Eise] Grundlagen der Silizium-Halbleitertechnologie; I. Eisele; Seminar Institut für Physik Fakultät für Elektrotechnik und Informationstechnik Universität der Bundeswehr München; Überarbeitete Version 2006

[Ekim] Observation of optical orientation of equilibrium electrons in n-type semiconductors; A. I. Ekimov and V. I. Safarov; Pis'ma Zh. Eksp. Teor. Fiz. **13**, 251–254 [JETP Lett. **13**, 177–179 (1971)].

[Elli] Theory of the Effect of Spin-Orbit Coupling on Magnetic Resonance in Some Semiconductors; R. J. Elliot; Phys. Rev. 96, 266 (1954)

[Erve] Electrical injection and detection of spin-polarized carriers in silicon in a lateral transport geometry; O. M. J. van't Erve, A. T. Hanbicki, M. Holub, C. H. Li, C. Awo-Affouda, P. E. Thompson and B. T. Jonker; Appl. Phys. Lett. **91**. 212109 (2007)

[Fabi] Semiconductor Spintronics; J. Fabian, A. Matos-Abiaque, C. Ertler, P. Stano and I. Zutic; Acta Physica Slovaca vol. **57** No. 4 & 5. 565 – 907 (2007)

[Fab1] Theory of spin-polarized bipolar transport in magnetic p-n junction; J. Fabian, J. I. Žutić and S. Das Sarma; Phys. Rev. B **66**, 165301 (2002)

[Fert] Conditions for efficient spin injection from a ferromagnetic metal into a semiconductor; A. Fert and H. Jaffrès; Phys. Rev. B **64**, 184420 (2001)

[Fer1] Semiconductors between spin-polarized sources and drains; A. Fert, J. M. George, H. Jaffres and R. Mattana; IEEE Trans. Electronic Devices **54**, 921 (2007)

[Flem] Instrument for converting alternating electric currents into continuous currents; J. A. Fleming; United States Patent and Trademark Office, U.S. Patent 803,684, Issue date Nov 7, 1905

[Fore] Space telegraphy; L. de Forest; United States Patent and Trademark Office, U.S. Patent 879,532, Issue date Feb 18, 1908

[Gebh] The Mott Metal-Insulator Transition: Models and Methods; F. Gebhardt; Springer Tracts in Modern Physics, Volume 137, Springer Verlag Berlin, Heidelberg, New York 1997

[Gerl] Das magnetische Moment des Silberatoms; W. Gerlach, O. Stern; Zeitschrift für Physik **9**: 353–355 (1922)

[Getz] Fundamentals of Magnetism; M. Getzlaff; Springer-Verlag, Berlin, Heidelberg (2008)

[Gira] Voltage-controlled tunneling anisotropic magnetoresistance of a ferromagnetic p^{++}-(Ga,Mn)As/n^{+}-GaAs Zener-Esaki diodeitle; R. Giraud, M. Gryglas, L. Thevenard, A. Lemaître and G. Faini; Appl. Phys. Lett. **87**, 242505 (2005)

[Glas] Determination of the Local Concentrations of Mn Interstitials and Antisite Defects in GaMnAs; F. Glas, G. Patriache, L. Largeau, and A. Lemaître; Phys. Rev. Lett **93**(8), 086107 (2004)

[Goul] Tunneling Anisotropic Magnetoresistance: A Spin-Valve-Like Tunnel Magnetoresistance Using a Single Magnetic Layer; C. Gould, C. Rüster, T. Jungwirth, E. Girgis, G. M. Schott, R. Giraud, K. Brunner, G. Schmidt and L. W. Molenkamp; Phys. Rev. Lett. **93**, 117203 (2004)

[Grae] Electrically detected magnetic resonance of two-dimensional electron gases in Si/SiGe heterostructures; C. F. O. Graeff, M. S. Brandt, M. Stutzmann, M. Holzmann, G. Abstreiter and F. Schäffler; Phys. Rev. B **59**, 13242–13250 (1999)

[Gros] Spinelektronik; R. Gross and A. Marx; Walther-Meissner-Institut, Lehrstuhl für Technische Physik (2004)

[Grun] The Physics of Semiconductors; M. Grundmann; Springer-Verlag Berlin Heidelberg (2006)

[Gupt] Spin coherence in semiconductor quantum dots; J. A. Gupta, D. D. Awschalom, X. Peng and A. P. Alivisatos; Phys. Rev. B **59**, 10421–10424 (1999)

[Hall] Physics of ultra-pure germanium; E. E. Haller, W. L. Hansen and F. S. Goulding; Adv. Phys. **30**, 93-138 (1981)

[Hers] Charge and spin transport through a metallic ferromagnetic-paramagnetic-ferromagnetic junction; S. Herschfield and H. L. Zhao; Phys. Rev. B **56**, 3296 (1997)

[Hilt] Optical Orientation and Femtosecond Relaxation of Spin-Polarized Holes in GaAs; D. J. Hilton and C. L. Tang; Phys. Rev. Lett. 89, 146601 (2002)

[Hunk] Festkörperphysik; Siegfried Hunklinger; Oldenbourg Wissenschaftsverlag GmbH

[Hoff] Mapping the magnetic anisotropy in (Ga,Mn)As nanostructures; F. Hoffmann, G. Woltersdorf, W. Wegscheider, A. Einwanger, D. Weiss and C. H. Back; Phys. Rev. B **80**, 054417 (2009)

[Home] Homepage of the Department of Surfaces and Interfaces, Academy of Sciences of the Czech Republic, Prague, Institute of Physics (2006)

[Hümp] Lithographic engineering of anisotropies in (Ga,Mn)As; S. Hümpfner, K. Pappert, J. Wenisch, K. Brunner, C. Gould, G. Schmidt, L. W. Molenkamp, M. Sawicki and T. Dietl; Appl. Phys. Lett. **90**, 102102 (2007)

[Jede] Electrical spin injection and accumulation at room temperature in an all-metal mesoscopic spin-valve; F. J. Jedema, A. T. Filip and B. J. van Wees; Nature **410** (6826), 345 (2001)

[Jian] Electron-spin relaxation in bulk III-V semiconductors from a fully microscopic kinetic spin Bloch equation approach; J. H. Jiang and M. W. Wu; Phys. Rev. B **79**, 125206 (2009)

[John] Interfacial charge-spin coupling: Injection and detection of spin magnetization in metals; M. Johnson and R. H. Silsbee; Phys. Rev. Lett. **55**, 1790 (1985)

[Joh1] Thermodynamic analysis of interfacial transport and of the thermomagnetoelectric system; M. Johnson and R. H. Silsbee; Phys. Rev. B **35**, 4959 (1987)

[Joh2] Coupling of electronic charge and spin at ferromagnetic-paramagnetic metal interface; M. Johnson and R. H. Silsbee; Phys. Rev. B **37**, 5312 (1988)

[Joh3] Analysis of anomalous multilayer magnetoresistance within the thermomagnetic system; M. Johnson; Phys. Rev. Lett. **67**, 3594 (1991)

[Jull] Tunneling between ferromagnetic films; M. Julliere; Phys. Lett. A **54**, 225-226 (1975)

[Jung] Theory of ferromagnetic (III,Mn)V semiconductors; T. Jungwirth, J. Sinova, J. Mašek, J. Kučcera und A. H. Mac-Donald; Rev. Mod. Phys., **78**:809 (2006)

[Jun1] Prospects for high temperature ferromagnetism in (Ga,Mn)As semiconductors; T. Jungwirth, K. Y. Wang, J. Ma_sek, K. W. Edmonds, J. König, J. Sinova, M. Polini, N. A. Goncharuk, A. H. MacDonald, M. Sawicki, A. W. Rushforth, R. P. Campion, L. X. Zhao, C. T. Foxon and B. L. Gallagher; Phys. Rev. B, **72**:165204 (2005)

[Jun2] Character of states near the Fermi level in (Ga,Mn)As: Impurity to valence band crossover; T. Jungwirth, J. Sinova, A. H. MacDonald, B. L. Gallagher, V. Novák, K. W. Edmonds, A. W. Rushforth, R. P.

Campion, C. T. Foxon, L. Eaves, E. Olejník, J. Mašek, S.-R. Eric Yang, J. Wunderlich, C. Gould, L. W. Molenkamp, T. Dietl and H. Ohno; Phys. Rev. B, **76**:125206 (2007)

[Kats] Growth modes in two-dimensional heteroepitaxy on an elastic substrate; H. Katsunoa, H. Uemuraa, M. Uwahaa and Y. Saito; Journal of Crystal Growth, **275**, Issues 1–2, e283–e288 (2005)

[Kavo] Anisotropic exchange interaction of localized conduction-band electrons in semiconductors; K. V. Kavokin; Phys. Rev. B **64**, 075305 (2001)

[Kikk] Resonant Spin Amplification in n-Type GaAs; J. M. Kikkawa, D. D. Awschalom; Phys. Rev. Lett. **80**, 4313 (1998)

[Kik1] Room-temperature spin memory in twodimensional electron gases; J. M. Kikkawa, I. P. Smorchkova, N. Samarth and D. D. Awschalom; Science **277**, 1284–1287 (1997)

[Kime] Room-temperature ultrafast carrier and spin dynamics in GaAs probed by the photoinduced magneto-optical Kerr effect; A. V. Kimel, F. Bentivegna, V. N. Gridnev, V. V. Pavlov, R. V. Pisarev and T. Rasing; Phys. Rev. B **63**, 235201 (2001)

[Kimu] Room-Temperature Reversible Spin Hall Effect; T. Kimura, Y. Otani, T. Sato, S. Takahashi and S. Maekawa; Phys. Rev. Lett. 98, 156601 (2007)

[Kita] Spin injection with three terminal device based on (Ga,Mn)As/n+-GaAs tunnel junction; T. Kita, M. Kohda, Y. Ohno, F. Matsukura and H. Ohno; Phys. Stat. Sol. (c) **3**, No. 12, 4164-4167 (2006)

[Kohd] Bias voltage dependence of the electron spin injection studied in a three-terminal device based on a (Ga,Mn)As/n^+-GaAs Esaki diode; M. Kohda, T. Kita, Y. Ohno, F. Matsukura and H. Ohno; Appl. Phys. Lett. **89**, 012103 (2006)

[Koh1] Effect of n^+-GaAs thickness and doping density on spin injection of GaMnAs/n^+-GaAs Esaki tunnel junction; M. Kohda, Y. Ohno, F. Matsukura and H. Ohno; Physica E 32 438–441 (2006)

[Kwak] Thermally stable, low-resistance PdGe-based ohmic contacts to high–low doped n-GaAs; J. S. Kwak, H. N. Kim, H. K. Baik, J.-L. Lee, H. Kim, H. M. Park and S. K. Noh; Appl. Phys. Lett. **67**, 2465 (1995)

[Lale] Inorganic Materials Synthesis and Fabrication; J. N. Lalena, D. A. Cleary, E. Carpenter, N. F. Dean; Wiley-Interscience (2008)

[Land] L. D. Landau and E. M. Lifshitz; Theory of the dispersion of magnetic permeability in ferromagnetic bodies; Phys. Z. Sowietunion **8**, **153** (1935)

[Linn] Electronic structure of the GaAs:Mn_{Ga} center; M. Linnarsson, E. Janzén, B. Monemar, M. Kleverman and A. Thilderkvist; Phys. Rev. B, **55**(11):6938 (1997)

[Liu] Ferromagnetic resonance in $Ga_{1-x}Mn_xAs$: Effects of magnetic anisotropy; X. Liu, Y. Sasaki and J. K. Furdyna; Phys. Rev. B **67**, 205204 (2003)

[Liu1] Native point defects in low-temperature-grown GaAs; X. Liu, A. Prasad, J. Nishio, E. R. Weber, Z. Liliental-Weber and W. Walukiewicz; Appl. Phys. Lett. 67, 279 (1995)

[Look] Anomalous Hall-effect results in low-temperature molecular-beam-epitaxial GaAs: Hopping in a dense EL2-like band; D. C. Look, D. C. Walters, M. O. Manasreh, J. R. Sizelove, C. E. Stutz and K. R. Evans; Phys. Rev. B **42**, 3578-3581 (1990)

[Lou] Electrical detection of spin transport in lateral ferromagnet-semiconductor devices; X. Lou, C. Adelmann, S. A. Crooker, E. S. Garlid, J. Zhang, K. S. Madhukar Reddy, S. D. Flexner, C. J. Palmstrøm and P. A. Crowell; Nat. Phys. **3**, 197 (2007)

[Love] Low Resistivity Ohmic Contacts to Moderately Doped n-GaAs with Low Temperature Processing; M. L. Lovejoy, A. J. Howard, K. R. Zavadil, D. J. Rieger and R. J. Shul; Program EM-ThP2, http://www.osti.gov/bridge/ servlets/purl/31655-TyK1yP/webviewable/31655.pdf

[MacI] Processing and Properties of PdGe Ohmic contacts to GaAs; A. N. MacInnes, R. Morton, F. Radulescu and J. McCarthy; GaAsMANTECH Conference (2000)

[Maek] Concepts in Spin Electronics; S. Maekawa (Editor); Oxford University Press 2006

[Marc] Fluctuation-dissipation: Response theory in statistical physics; U. M. B. Marconi , A. Puglisi, L. Rondoni and A. Vulpiani; Physics Reports; Volume 461, Issues 4-6,Pages 111–195 (2008)

[Maše] Interstitial Mn in (Ga,Mn)As: Binding energy and exchange coupling; J. Mašek and F. Máca; Phys. Rev. B 69, 165212 (2004)

[Matt] The Theory Of Magnetism Made Simple; D. C. Mattis; World Scientific Publishing Co. Pte. Ltd. (2006)

[Mats] Magnetotransport properties of metallic (Ga,Mn)As films with compressive and tensile strain; F. Matsukura, M. Sawicki, T. Dietl D. Chiba and H. Ohno; Physica E, **21**:1032 (2004)

[Menz] Mikrosystemtechnik für Ingenieure; W. Menz and P. Bley; VCH, 2. Auflage (1993)

[Meye] Introductory solid state physics; H. P. Meyers; CRC Press, 2nd edition (1997)

[Monz] Strong Hall voltage modulation in hybrid ferromagnet/semiconductor microstructures; F. G. Monzon, M. Johnson and M. L. Roukes; Appl. Phys. Lett. **71**, 3087 (1997).

[Mon1] Characterization of individual nanomagnets by the local Hall effect; F. G. Monzon, D. S. Patterson and M. L. Roukes; J. Magn. Magn. Mater. **195**, pp. 19-25(7) (1999)

[Moor] Cramming more components onto integrated circuits; G. E. Moore; Electronics. 38, Nr. 8, P.114-117 (1965)

[Mose] Tunneling anisotropic magnetoresistance and spin-orbit coupling in Fe/GaAs/Au tunnel junctions; J. Moser, A. Matos-Abiague, D. Schuh, W. Wegscheider, J. Fabian and D. Weiss; Phys. Rev. Lett. **99**, 056601, (2007)

[Mott] The electrical conductivity of transition metals; N. F. Mott; Proc. R. Soc. Lond. A **153**, 699 (1936)

[Mot1] Electrons in transition metals; N. F. Mott; Advances in Physics **13**, 51, 325-422 (1964)

[Mot2] Metal-Insulator Transitions; N. F. Mott; Taylor & Francis, London, New York, Philadelphia, Second Edition 1990

[Mot3] The metal-insulator transition in extrinsic semiconductors; N. F. Mott; Advances in Physics, **21**:94, 785-823 (1972)

[Mune] Diluted magnetic III-V semiconductors; H. Munekata, H. Ohno, H.Molnar, S. von Segmüller, A. Chan, and L. L. Esaki; Phys. Rev. Lett **63**, 1849 (1989)

[Mura] Damage free and selective RIE of GaAs/AlGaAs in $SiCl_4/SiF_4$ plasma for MESFET and pseudomorphic HEMT's gate recess etching; S. K. Murad, P. D. Wang, N. I. Cameron, S. P. Beaumont and C. D. W. Wilkinson; Microelectronic Engineering Vol. 27, Issue 1-4 439 (1995)

[Myer] Antisite effct in hole-mediated ferromagnetism in (Ga,Mn)As; R. C. Myers, B. L. Sheu, A. W. Jackson, A. C. Gossard, P. Schiffr, N. Samarth and D. D. Awschalom; Phys. Rev. B **74**, 155203 (2006)

[Nano] nanonic GmbH provides elaborate software tools for designing e-beam structures (e-Draw) as well as control software to realize them on SEM systems (eLitho); www.nanonic.de

[Ohno] Electric field control of ferromagnetism; H. Ohno, D. Chiba, F. Matsukura, T. Omiya, E. Abe, T. Dietl, Y. Ohno and K. Ohtani; Nature, 408:944 (2000)

[Ohn1] (Ga,Mn)As: A new diluted magnetic semiconductor based on GaAs; H. Ohno, A. Shen, F. Matsukura, A. Oiwa, A. Endo, S. Katsumoto and Y. Iye; Appl. Phys. Lett., **69**:363 (1996)

[Ohn2] Spin dependent tunneling and properties of ferromagnetic (Ga,Mn)As; H. Ohno, F. Matsukura, T. Omiya and N. Akiba; J. Appl. Phys. **85**, 84277 (1999).

[Ohn3] Making Nonmagnetic Semiconductors Ferromagnetic; H. Ohno; Science 281, 951 (1998)

[Olen] Enhanced annealing, high Curie temperature, and low-voltage gating in (Ga,Mn)As: A surface oxide control study; K. Olejník, M. H. S. Owen, V. Novák, J. Mašek, A. C. Irvine, J. Wunderlich and T. Jungwirth; Phys. Rev. B **78**, 054403 (2008)

[Oxfo] http://www.oxford-instruments.com/products/low-temperature/Superconducting-magnets/solenoid-magnets/Pages/standard-solenoid-magnets.aspx (2012)

[Page] Low field electron-nuclear spin coupling in gallium arsenide under optical pumping conditions; D. Paget, G. Lampel, G. B. Sapoval and V. I. Safarov; Phys. Rev. B 15, 5780 (1977)

[Papp] Magnetization-switched metal-insulator transition in a (Ga,Mn)As tunnel device; K. Pappert, M. J. Schmidt, S. Hümpfner, C. Rüster, G. M. Schott, K. Brunner, C. Gould, G. Schmidt and L. W. Molenkamp; Phys. Rev. Lett. **97**, 186402 (2006)

[Paul] Über den Einfluß der Geschwindigkeitsabhängigkeit der Elektronenmasse auf den Zeemaneffekt; W. Pauli; Z. Phys. **31**, 373–385 (1925)

[Pau1] Über den Zusammenhang des Abschlusses der Elektronengruppen im Atom mit der Komplexstruktur der Spektren; W. Pauli; Z. Phys. **31**, 765–783 (1925)

[Pear] Electrical Properties of Pure Silicon and Silicon Alloys Containing Boron and Phosphorus; G. L. Pearson and J. Bardeen; Phys. Rev. 75, 865 (1949)

[Rash] Theory of electrical spin injection: Tunnel contacts as a solution of the conductivity mismatch problem; E. I. Rashba; Phys. Rev. B **62**, R16267 (2000)

[Ras1] Diffusion theory of spin injection through resistive contacts E. I. Rashba; Eur Phys. J. B **29**, 513 (2002)

[Rein] Herstellung und Charakterisierung von ferromagnetischem GaMnAs auf der GaAs (001)- und (311)A-Oberfläche; M. Reinwald; epub Regensburg urn:nbn:de:bvb:355-opus-6333

[Rost] Effekte der Physik und ihre Anwendungen; A. Rost und G. Tschuch; Book editors M. von Ardenne, G. Musiol and U. Klemradt; Wissenschaftlicher Verlag Harri Deutsch, Frankfurt, p. 509 ff. (2007)

[Rüst] Very large tunneling anisotropic magnetoresistance of a (Ga,Mn)As/GaAs/(Ga,Mn)As stack; C. Rüster, C. Gould, T. Jungwirth, J. Sinova, G. M. Schott, R. Giraud, K. Brunner, G. Schmidt and L. W. Molenkamp; Phys. Rev. Lett. **94**, 027203, (2005)

[Sah] Fundamentals of Solid-State Electronics; Chih-Tang Sah; World Scientific Publishing Co. Pte. Ltd, Singapore, (1991)

[Saik] A drift diffusion model for spin polarized transport in a two-dimensional non-degenerate electron gas controlled by spin-orbit interaction; S. Saikin; J. Phys: Condens. Matt., **16**, 5071-5081 (2004)

[Sait] Origin of the tunnel anisotropic magnetoresistance in $Ga_{1-x}Mn_xAs$/ZnSe/$Ga_{1-x}Mn_xAs$ magnetic tunnel junctions of II-VI/III-V heterostructures; H. Saito, S. Yuasa and K. Ando; Phys. Rev. Lett. **95**, 086604, (2005)

[Saka] Conduction-type conversion in Si-doped (311)A GaAs grown by molecular beam epitaxy; N. Sakamoto, K. Hirakawa and T. Ikoma; Appl. Phys. Lett. **67** 1444-46 (1995)

[Sand] ESR investigations of modulation-doped Si/SiGe quantum wells; N. Sanderfeld, W. Jantsch, Z. Wilamowski and F. Sch#ffler; Thin Solid Films **369**, 312–315 (2000)

[Sank] Spin-dependent tunneling in modulated structures of (Ga,Mn)As; P. Sankowski, P. Kacman, J. A. Majewski and T. Dietl; Phys. Rev. B **75**, 045306 (2007)

[Sche] Crystal Growth Technology; H. J. Scheel and T. Fukuda; John Wiley & Sons Ltd. England (2003)

[Schm] Fundamental obstacle for electrical spin injection from a ferromagnetic metal into a diffusive semiconductor; G. Schmidt, D. Ferrand, L. W. Molenkamp, A. T. Filip and B. J. van Wees; Phys. Rev. B **62**, R4790 (2000)

[Schu] Ultrafast optical studies of diffusion barriers between ferromagnetic Ga(Mn)As layers and non-magnetic quantum wells; R. Schulz, T. Korn, D. Stich, U. Wurstbauer, D. Schuh, W. Wegscheider and C. Schüller; Physica E 40 (2008) 2163-2165

[Shin] Stable Multidomain Structures Formed in the Process of Magnetization Reversal in GaMnAs Ferromagnetic Semiconductor Thin Films; D. Y. Shin, S. J. Chung, S. Lee, X. Liu and J. K. Furdyna; Phys. Rev. Lett. **98**, 047201 (2007)

[Sils] R. H. Silsbee; Bull. Magn. Reson. 2, 284 (1980)

[Skom] Simple Models of Magnetism; R. Skomski; Oxford Graduate Texts, Oxford University Press, Oxford New York (2008)

[Smol] Zur kinetischen Theorie der Brownschen Molekularbewegung und der Suspensionen; M. Smoluchowski; Annalen der Physik **326** (14): 756-780 (1906)

[Snid] 1D Poisson/Schrödinger program; Greg Snider; Department of Electrical Engineering, University of Notre Dame, snider.7@nd.edu

[Song] Proximity Induced Enhancement of the Curie Temperature in Hybrid Spin Injection Devices; C. Song, M. Sperl, M. Utz, M.

Ciorga, G. Woltersdorf, D. Schuh, D. Bougeard, C. H. Back, and D. Weiss; Phys. Rev. Lett. **107**, 056601 (2011)

[Staa] Spin precession in lateral all-metal spin-valves: Experimental observation and theoretical description; A. van Staa, J. Wulfhorst, A. Vogel, U. Merkt and G. Meier; Phys. Rev. B 77, 214416 (2008)

[Stil] GaInAsP Alloy Semiconductors; G. E. Stillman, L. W. Cook, T. J. Roth, T. S. Low and B. J. Skromme; John Wiley & Sons, New York (1982)

[Stöh] Magnetism, From Fundamentals to Nanoscale Dynamics; J. Stöhr, H. C. Siegmann; Solid State Series, Springer-Verlag Berlin Heidelberg (2006)

[Sze] Physics of Semiconductor Devices, Chapter 9 IMPATT Diodes; S. M. Sze and K. K. Ng; John Wiley & Sons, New York, (2006)

[Tang] Spin Injection and Transport in Micro- and Nanoscale Devices; H. X. Tang, F. G. Monzon, F. J. Jedema, A. Filip, B. J. van Wees and M. L. Roukes; Semiconductor Spintronics and Quantum Computation, Editors D. D. Awschalom, D. Loss and N. Samarth; Springer, Berlin 2002

[Tboo] Homepage of tbookdtd project; http://tbookdtd.sourceforge.net/datb-no-mathml/gaasband-web.png

[Tech] http://www.techquark.com/2009/08/spinning-electrons-to-store-data.html (2009)

[Thus] Physik der Halbleiterbauelemente; F. Thuselt; Springer Berlin Heidelberg New York (2005)

[Vale] Theory of the perpendicular magnetoresistance in magnetic multilayers; T. Valet and A. Fert; Phys. Rev. B **48**, 7099 (1993)

[Val1] Direct Electronic Measurement of the Spin Hall Effect; S. O. Valenzuela and M. Tinkham; Nature **442**, 176 (2006)

[Vign] Coulomb drag, magnetoresistance, and spin-current injection in magnetic multilayers; G. Vignale and I. D'Amico; Solid State Commun. **127**, 829 (2003)

[vFle] The theory of electric and magnetic susceptibilities; J. H. van Vleck; Clarendon Press. (1932)

[vLee] Problèmes de la théorie électronique du magnetism; H. J. van Leeuwen; Journal de Physique et le Radium 2 (12): 361–377. (1921)

[vSon] Boundary resistance of the ferromagnetic-nonferromagnetic metal interface; P. C. van Son, H. van Kempen and P. Wyder; Phys. Rev. Lett. **58**, 2271 (1987)

[Wang] Low-temperature-processed (150-175 °C) Ge/Pd-based Ohmic contacts ($\varrho_C \approx 1x10^{-6} \Omega cm^2$) to n-GaAs; L. C. Wang and P. H. Hao; Appl. Phys. Lett. **67** (4) 10.1063/1.114552 (1995)

[Wan1] Magnetism in (Ga,Mn)As Thin Films With T_C Up To 173K; K. Y. Wang, R. P. Campion, K. W. Edmonds, M. Sawicki, T. Dietl, C. T. Foxon und B. L. Gallagher; AIP Conf. Proc., 772, 333 (2005)

[Wan2] Achieving High Curie Temperature in (Ga,Mn)As; M. Wang, R. P. Campion, A. W. Rushforth K. W. Edmonds C. T. Foxon und B. L. Gallagher; arXiv:0808.1464v1 (2008)

[Welp] Magnetic Domain Structure and Magnetic Anisotropy in $Ga_{1-x}Mn_xAs$; U. Welp, V. K. Vlasko-Vlasov, X. Liu, J. K. Furdyna and T. Wojtowicz; Phys. Rev. Lett., **90**:167206 (2003)

[Weni] Control of Magnetic Anisotropy in (Ga,Mn)As by Lithography-Induced Strain Relaxation; J. Wenisch, C. Gould, L. Ebel, J. Storz, K. Pappert, M. J. Schmidt, C. Kumpf, G. Schmidt, K. Brunner and L. W. Molenkamp; Phys. Rev. Lett., **99**:077201 (2007)

[Widm] Technologie hochintegrierter Schaltungen; D. Widmann; Springer Verlag, Weinheim (1996) Band 19

[Yafe] Solid State Physics, page 1; Y. Yafet; SSP vol. 14, edited by F. Seits and D. Turnbull Academic, New York (1963)

[Zuti] Spintronics: Fundamentals and applications; I. Zutic, J. Fabian and S. Das Sarma, Rev. Mod. Phys., **76**:323 (2004)

[Zut1] Novel aspects of spin polarized transport and spin dynamics; I. Žutić; J. Supercond. **15**, 5 (2002)

[Zut2] Spin injection and detection in silicon; I. Žutić, J. Fabian and S. C. Erwin; Phys. Rev. Lett. 97, 026602 (2006)

[Zwol] DNA spintronics; M. Zwolak and M. Di Ventra; Appl. Phys. Lett. **81**, 925–927 (2002)

Acknowlegements

In the end it is an honor for me to thank all the people who have contributed in so various ways to the success of this work:

Prof. **Dieter Weiss** for giving me the possibility of doing this PHD at his chair. For providing me the clean room, equipment and material to produce the samples, the cryostats and paying the helium bills necessary for measurments.

Mariusz Ciorga for his help, time and sharing of knowledge as well as many fruitful discussions throughout the work.

Prof. **Jaroslav Fabian** for providing a nice 343-pages paper that aims directly at the heart of this work.

Ursula Wurstbauer and **Martin Utz** for growing all the MBE-wafers and Prof. **Werner Wegscheider** for providing his MBE chambers for our studies.

Matthias Sperl for doing the MOKE measurements and Prof. **Christian Back** for providing us with the necessary equipment.

Roland Völkl for doing optical comparative measurements on my samples and Prof. **Christian Schüller** for the possibility to use the laser equipment.

Uli Wurstbauer for doing AFM measurements that helped us with the wafer design.

Karl Weigert, **Thomas Solleder** and **Christian Haimerl** for helium liquefaction over all the years without any grumbling.

Uli Gürster, **Cornelia Linz**, **Michael Weigl** and **Thomas Haller** for supporting us each and every (working) day

Claudia Rahm and **Elke Haushalter** for embodying the positive spirit at our chair, solving all problems with printed forms and other stuff a physicist is unfortunately not clever enough.

All other chair-members for being every time available in case of open questions.

Philipp Kotissek for pushing me to the end.

My **parents** for enabling me nearly everything.

My **sisters** for being my sisters.

Last but surely not least **Serpil** and **Luca** for being there whenever needed…